Transactions of the ASME

EDITORIAL STAFF
Editor, J. J. JAKLITSCH, JR.
Production Editor
CORNELIA MONAHAN
Editorial Production Assistant
BETH DARCHI

FLUIDS ENGINEERING DIVISION
Technical Editor
FRANK M. WHITE (1981)
Executive Secretary
L. T. NELSON (1981)
Calendar Editor
M. F. ACKERSON

Associate Editors
Fluid Machinery
H. JAMES HERRING (1981)
BUDUGAR LAKSHMINARAYANA (1981)
Fluid Measurements
BHARATAN R. PATEL (1981)
Fluid Mechanics
RICHARD A. BAJURA (1980)
OWEN M. GRIFFIN (1981)
BRIAN E. LAUNDER (1981)
WILLIAM G. TIEDERMAN (1981)
Fluid Transients
DAVID C. WIGGERT (1980)
Polyphase Flow
CLAYTON T. CROWE (1980)
ROBERT L. STREET (1981)
Review Articles
KENNETH E. HICKMAN (1981)

FOREIGN CORRESPONDENTS
Europe and Russia
JACQUES CHAUVIN
Europe and Russia
JOHN H. HORLOCK
India and Middle East
ARUN PRASAD
Japan and China
YASUTOSHI SENOO

POLICY BOARD, COMMUNICATIONS
Chairman and Vice-President
I. BERMAN

Members-at-Large
M. J. RABINS
J. E. ORTLOFF
J. W. LOCKE
W. J. WARREN

Policy Board Representatives
Basic Engineering, F. LANDIS
General Engineering,
A. A. SEIREG
Industry, R. K. HAMPTON
Power, R. E. REDER
Research, G. P. COOPER
Codes and Stds., L. L. ELDER
Computer Technology Com.,
A. A. SEIREG
Nom. Com. Rep., S. P. ROGACKI

Business Staff
345 E. 47th St.
New York, N. Y. 10017
(212)644-7789
Mng. Dir., Pub., C. O. SANDERSON

OFFICERS OF THE ASME
President, D. N. ZWIEP
Exec. Dir. Sec'y,
ROGERS B. FINCH
Treasurer, ROBERT A. BENNETT

The Journal of Fluids Engineering (USPS 278-480) is edited and published quarterly at the offices of *The American Society of Mechanical Engineers*, United Engineering Center, 345 E. 47th St., New York, N. Y. 10017. Cable Address, "Mechaneer," New York. **Second-class** postage paid at New York, N.Y., and at additional mailing office. **CHANGES OF ADDRESS** must be received at Society headquarters seven weeks before they are to be effective. Please send old label and new address. **PRICES:** To members, $25.00, annually: *to nonmembers, $50.00. Single copies, $15.00* each. Add $1.50 for postage to countries outside the United States and Canada. **STATEMENT** from By-Laws. The Society shall not be responsible for statements or opinions advanced in papers or . . . printed in its publications (B13, Par. 4).

INDEXED by the Engineering Index, Inc.

Journal of Fluids Engineering

Published Quarterly by The American Society of Mechanical Engineers

VOLUME 102 • NUMBER 1 • MARCH 1980

Announcements and Special Notices

IN MEMORIAM – ALAN H. STENNING

by
Willem Jansen

In the fall of 1973 the community of mechanical engineers particularly those involved with turbomachinery received, with the deepest sorrow, the news of Alan Stenning's death.

The event was particularly shocking to me since Alan contributed more than anyone else to my career. A few weeks after I arrived at M.I.T., Alan helped me along as one of his students to bridge the cultural and academic gap at the school. I performed miserably as his graduate student, but Alan continued to provide help. Alan alone was responsible for persuading me not to leave when my scholarship fund ran dry after one semester. He offered me a research assistantship which really launched my career. It was the most important event in my education.

From 1960 to 1961 I worked for Alan at Northern Research. There I learned to admire his talents as an engineer without peer. The continuing growth of the firm can be traced to Alan's contributions during that period. I fondly recall the project we were engaged in that brought us both to McKeesport, Pennsylvania for fourteen days in a dilapidated hotel, surrounded by steel factories. The problem was a belligerent axial compressor that shed its blades every month due to an unexplained surge. Alan represented the user, while I represented the manufacturer. He solved the problem (fouling of the blades).

Alan and I never lost touch, whether it was at an ASME meeting or during his consulting days at Northern Research. I remember one time in 1970 during a boring conference in San Diego when one day we decided to go sailing instead of attending the conference. We toured the harbor in a rented boat and talked about writing books. Alan was philosophical and perceptive in his observations. His wise words then gave me insight I had never thought of. I enjoyed that day and felt it had been worth going to San Diego.

The following papers show examples of Alan's techniques. In broad strokes he identifies the major effects and concentrates on analyzing these. He is able to make the necessary assumptions that render the problem manageable, a rare quality among academicians. Thus without much effort he established analytically what one can expect in practice.

His grasp of fundamentals was phenomenal ("It's all Newton's Law," he was fond of saying). After a few months of study he would become an expert in the many fields he studied. He applied his techniques to such diverse topics as Partial Admission Turbines, Rotating Stall in Compressors, The Starting and Control of Nuclear Rockets (this treatise is my favorite; in only a few pages he marries Nuclear Physics to Turbomachinery to explain the fundamental behavior of Nuclear Rockets), Hydrogen Cavitation and the cause of early chemical rocket failures, and of course the distortion work.

It is true that the following papers do not provide the latest information on the subjects. For example, the collection of papers given at the AGARD Conferences of 1974 (AGARD-LS-72) provide a more up-to-date review of distortion effects and rotating stall in axial compressors. It is even doubtful if Alan would have allowed the publication of the present papers. However, the papers show Alan's technique and should be an inspiration to those who think that technology has become too difficult and one is helpless without the availibilty of a large computer.

Inlet Distortion Effects in Axial Compressors

A. H. Stenning
Department of Mechanical Engineering and Mechanics, Lehigh University, Bethlehem, Pa. 18015
(deceased)

Although uniform inlet conditions are highly desirable and system designers attempt to insure distortion-free flow entering compressors, situations frequently arise in which substantial total pressure, velocity, and angle variations exist at the compressor inlet. Aircraft gas turbines are particularly prone to inlet distortion problems due to changes in aircraft attitude and the effect of the airframe on the inlet flow conditions, but industrial insallations may also suffer from inlet distortion in cases where poorly designed bends have been installed upstream of the compressor. In this paper, problems associated with inlet distortion are discussed and some of the simpler techniques for analyzing the effects of circumferential inlet distortion are presented.

Types of Distortion

Inlet conditions may be uniform circumferentially but distorted radially, or uniform radially but distorted circumferentially, or distorted both circumferentially and radially. With any type of distorton, some portion of the blading is likely to be operating under more unfavorable conditions than would occur with uniform flow at the same mass flow rate. In consequence, a performance penalty is usually associated with distortion.

Pure radial distortion may be analyzed using the techniques presented in other papers on axisymmetric flow solutions and is essentially equivalent to the radial distortion presented to a high pressure compressor by a low pressure compressor under off-design conditions. In consequence, radial distortions will not be discussed further in this paper.

A great deal of attention has been devoted to circumferential total pressure distortion, which frequently occurs in bifurcated inlet systems. Approximate methods of analysis have been developed for predicting the effects of circumferential distortion on compressor behavior, and for predicting the attenuation or amplification of the distortion pattern.

Combined radial and circumferential distortion has so far proved extremely resistant to analysis, and designers have resorted to empirical correlations to estimate its influence on the compressor.

Even if the mean flow is uniform, the instantaneous turbulent flow pattern at the compressor face may be highly distorted (especially for supersonic inlets) and compressor response to transient distortion has been an important consideration in several recent aircraft installations.

Circumferential Total Pressure Distortion

The simplest type of circumferential distortion, and the one which has received the greatest attention, is one in which the total pressure far upstream of the compressor varies with angle θ and the static pressure far upstream is uniform (Fig. 1). The total pressure distortion then produces a corresponding distortion in velocity far upstream of the compressor.

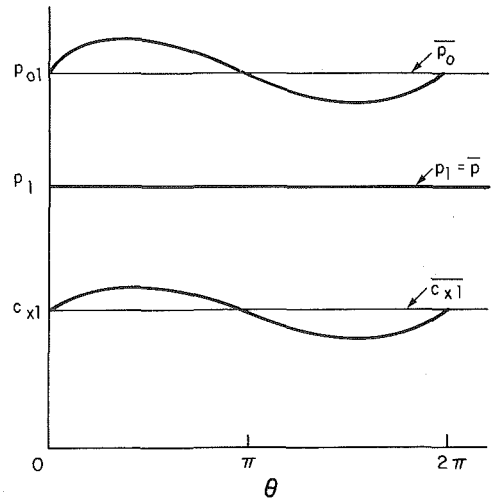

Fig. 1 Flow pattern for upstream for circumferential total pressure distortion

As a consequence of this velocity distortion, the flow coefficient c_x/U varies around the circumference of the compressor and the pressure rise across the compressor also varies around the circumference. The resulting pressure variation and flow redistribution in front of and within the compressor changes the performance characteristic of the compressor and modifies the amplitude and shape of the distortion pattern. An engineer who must use the compressor as a component in a system is interested in both the effect of the distortion on compressor performance and the attenuation or amplification of the distortion pattern as it passes through the compressor, since the distortion leaving the compressor may influence other components (such as combustion

Contributed by the Fluids Engineering Division for publication in the JOURNAL OF FLUIDS ENGINEERING. Manuscript received by the Fluids Engineering Division, January 23, 1975.

chambers) downstream. Analytical and experimental studies of inlet distortion have been aimed at obtaining a better understanding of both phenomena.

Simple Analyses of Circumferential Distortion

At the present time, it is still not possible to predict the undistorted performance of an axial compressor with complete reliability even though the use of high speed computers has greatly improved the accuracy of performance analysis. In consequence, any attempt to calculate the distorted performance and distortion attenuation of a multistage compressor starting with no information other than the geometry of the blading is unlikely to be entirely successful. If, however, methods can be developed which use the known undistorted performance characteristic as a starting point to predict the behavior of the machine with distortion then the prospects for success are greatly improved since the analysis at least begins from the right place.

A number of investigators have developed models for response to circumferential distortion which use the undistorted compressor performance or stage characteristics to predict the behavior with distortion [1 - 5]. These analyses in general are based on two assumptions.

(a) The pressure rise across any stage at any circumferential position is a function only of the local flow coefficient, and is equal to the pressure rise of the stage at that flow coefficient when operating without distortion.

$$\text{i.e.,} \quad \frac{\Delta p(\theta)}{\frac{1}{2}\rho u^2} = f\left[\frac{c_x(\theta)}{U}\right]$$

(b) The static pressure after the last stator is uniform around the circumference.

Assumption (a) has been found to be reasonably good provided that unsteady flow effects are negligible and crossflows between blade rows are small. Plourde and Stenning [3] have shown that assumption (b) is valid for high hub-tip ratio machines if the last stator maintains a constant exit flow angle round the annulus and adequate space is available for pressure adjustment downstream.

These analyses yield simple solutions when the spacing between rotors and stators is so small that crossflows can be neglected within the compressor. In this situation, the flow rate through a segment $d\theta$ of the annulus is the same at all axial positions and in consequence, according to assumption (a), the pressure rise across the compressor at that circumferential position is equal to the undistorted pressure rise corresponding to the local value of c_x/U at the inlet blading. Thus, in regions where c_x/U is higher than average the pressure rise across the compressor will be low (point 1 in Fig. 2) and in regions where c_x/U is smaller than average the pressure rise will be high (point 2 in Fig. 2) unless point 2 happens to be to the left of the surge line.

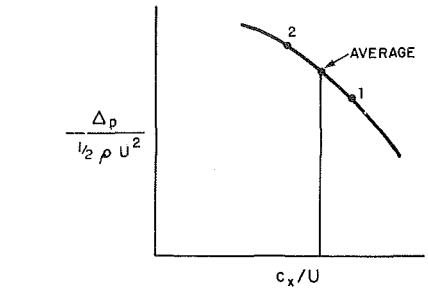

Fig. 2

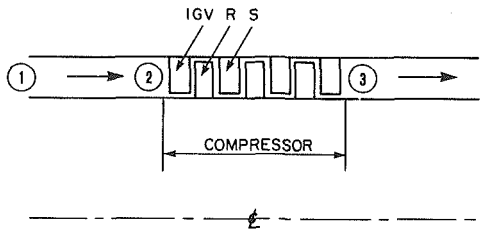

Fig. 3 Schematic of compressor

Two of the simplest "zero crossflow" analyses are discussed in the next section. The first permits an estimate of the flow redistribution upstream and the attenuation of the distortion pattern within the machine, and the second predicts the effect of circumferential distortion on the performance map.

Small Perturbation Zero Crossflow Analysis. Consider the compressor shown in Fig. 3. Far upstream, at station (1) where the static pressure is uniform around the circumference, let the tangential velocity be zero and let the axial velocity distribution be given by the expression

$$c_{x1} = \overline{c_{x1}} + \epsilon \sin(n\theta) \tag{1}$$

where $\epsilon << \overline{c_{x1}}$

$\overline{c_{x1}}$ is the average axial velocity

$c_{\theta 1} = 0$

If the inlet Mach number is small

$$p_{01} = p_1 + \frac{1}{2}\rho_1 c^2$$

$$p_{01} = p_1 + \frac{1}{2}\rho_1 \overline{c_{x1}}^2 + \rho_1 \overline{c_{x1}}\,\epsilon \sin(n\theta) \tag{2}$$

Nomenclature

A = cross sectional flow area
c = velocity
F = dimensionless parameter

$$\frac{-1}{\rho_1 \overline{c_{x1}}} \frac{\partial \Delta p}{\partial c_{x2}}$$

m = mass flow rate
M = Mach number
n = number of harmonic
p = static pressure
p_0 = total pressure
q = dynamic pressure $1/2\,\rho c^2$
r = radius
R = total pressure ratio $\overline{p_{03}}/\overline{p_{02}}$
t = time
T = temperature
T_0 = total temperature
u = axial velocity perturbation
U = blade speed
v = tangential velocity perturbation
x = axial coordinate
γ = amplitude of static pressure distortion
δ = amplitude of total pressure distortion
ϵ = amplitude of axial velocity distortion far upstream
θ = tangential coordinate
ρ = density

Subscripts

1 = far upstream
2 = compressor inlet
3 = compressor exit
x = axial
θ = tangential
L = low total pressure region
H = high total pressure region

neglecting ϵ^2 in comparison with $\overline{c_{x1}}\epsilon$. Furthermore,

$$p_{01} = \overline{p_{01}} + \delta_1 \sin(n\theta) \tag{3}$$

where $\delta_1 = \rho_1 \overline{c_{x1}} \epsilon$ and is equal to the amplitude of the total pressure distortion upstream of the compressor.

Along any streamline, the total pressure remains constant upstream of the compressor and if the induced tangential velocities are small, then the total pressure will be only a function of θ upstream of the compressor. Hence, at any θ, $p_{01} = p_{02}$, and

$$p_1 - p_2 = \frac{1}{2}\rho_1 (c_2{}^2 - c_1{}^2)$$

At ② let $c_{x2} = \overline{c_{x1}} + c_{x2}{}'$

$$c_{\theta 2} = c_{\theta 2}{}'$$

where $c_{x2}{}'$, $c_{\theta 2}{}'$ are of order ϵ.
Then

$$p_1 - p_2 = \frac{1}{2}\rho_1 [(c_{x2}{}^2 + c_{\theta 2}{}^2) - c_{x1}{}^2]$$

$$p_1 - p_2 = \rho_1 \overline{c_{x1}} [c_{x2}{}' - \epsilon \sin(n\theta)] \tag{4}$$

at any θ, neglecting terms of order ϵ^2.

At any circumferential position, the static pressure rise across the compressor is assumed to depend only on the local inlet flow coefficient c_{x2}/U, that is, only on the local inlet axial velocity. Hence, if the compressor static pressure rise is plotted as shown in Fig. 4 for the given rotational speed, as Δp $(= p_3 - p_2)$ versus c_{x2}, then the pressure rise at each circumferential position can be obtained if c_{x2} is known.

The average pressure rise across the compressor is given by $\overline{\Delta p}$ and occurs at points where $c_{x2}{}' = 0$.

At any other point θ around the annulus, the static pressure rise across the compressor can be approximated by

$$\Delta p(\theta) = \overline{\Delta p} + \frac{\partial \Delta p}{\partial c_{x2}} c_{x2}{}'(\theta) \tag{5}$$

that is, by replacing the true shape of the characteristic in the vicinity of $\overline{c_{x1}}$ by the tangent to the curve at $\overline{c_{x1}}$. This linearized approximation is valid if $c_{x2}{}' << \overline{c_{x1}}$.

Thus, along any streamline which starts far upstream and ends after the compressor we can say

$$p_3 - p_1 = (p_3 - p_2) - (p_1 - p_2)$$

$$= \overline{\Delta p} + \frac{\partial \Delta p}{\partial c_{x2}} c_{x2}{}' - \rho_1 \overline{c_{x1}} [c_{x2}{}' - \epsilon \sin(n\theta)] \tag{6}$$

But p_1 is uniform around the annulus and is equal to $\overline{p_1}$ and p_3 is uniform around the annulus and is equal to $\overline{p_3}$. Moreover, for the undistorted flow field $\overline{p_2} = \overline{p_1}$.
Hence

$$p_3 - p_1 = \overline{p_3} - \overline{p_2} = \overline{\Delta p} \tag{7}$$

That is, the static pressure rise from far upstream to far downstream is not altered by the addition of a small symmetric distortion which does not change the total mass flow rate.

Substituting (7) in (6) and solving for $c_{x2}{}'$ we obtain

$$c_{x2}{}' = \frac{\epsilon \sin(n\theta)}{1 - \dfrac{1}{\rho_1 \overline{c_{x1}}} \dfrac{\partial \Delta p}{\partial c_{x2}}} \tag{8}$$

or

$$c_{x2}{}' = \frac{\epsilon \sin(n\theta)}{1 + F} \tag{9}$$

where

$$F = \frac{-1}{\rho_1 \overline{c_{x1}}} \frac{\partial \Delta p}{\partial c_{x2}}$$

Since no crossflows are assumed to occur within the compressor, the percentage variation in axial velocity around the annulus leaving the compressor will be the same as the percentage variation around the circumference entering the compressor,

i.e.,

$$\frac{c_{x3}{}'}{\overline{c_{x3}}} = \frac{c_{x2}{}'}{\overline{c_{x1}}}$$

and

$$c_{x3}{}' = \left(\frac{\overline{c_{x3}}}{\overline{c_{x1}}}\right) \frac{\epsilon \sin(n\theta)}{1 + F} \tag{10}$$

If the compressor has been designed for constant axial velocity then $\overline{c_{x3}} = \overline{c_{x1}}$ and

$$c_{x3}{}' = c_{x2}{}' = \frac{\epsilon \sin(n\theta)}{1 + F}$$

The axial velocity distortion is attenuated upstream of the compressor if F is positive, but is amplified if F is negative, that is, if $\partial \Delta p / \partial c_x$ is positive.

Moreover, if $F = -1$, then infinite amplification of any entry distortion can occur, or *a finite circumferential distortion at the compressor inlet can be created by an infinitesimal distortion far upstream.* Since the upstream conditions are never absolutely uniform, this is an indication of the possibility of an instability in the flow. It can be shown that the existence of an infinite amplification ratio can be associated with the occurrence of rotating stall.

The attenuation or amplification of the total pressure distortion can now be calculated.

Since the static pressure at ③ is uniform around the circumference, the total pressure variation at ③ is caused by the variation in velocity at ③.

$$p_{03} = p_3 + \frac{1}{2}\rho_3 (\overline{c_{x3}} + c_{x3}{}')^2$$

if $c_{\theta 3}$ is zero. Therefore,

$$p_{03} = \overline{p_{03}} + \rho_3 \overline{c_{x3}} c_{x3}{}' \tag{11}$$

Hence, the total pressure distortion at ③ is equal to $\rho_3 \overline{c_{x3}}$ $c_{x3}{}'$. The ratio of the total pressure distortion leaving the machine to the total pressure distortion entering is

$$\frac{\delta_3}{\delta_1} = \frac{\rho_3 \overline{c_{x3}} c_{x3}{}'}{\rho_1 \overline{c_{x1}} c_{x1}{}'}$$

$$\frac{\delta_3}{\delta_1} = \frac{\rho_3}{\rho_1} \left(\frac{\overline{c_{x3}}}{\overline{c_{x1}}}\right)^2 \frac{1}{(1+F)} \tag{12}$$

For machines with high pressure ratios and hence large values of ρ_3/ρ_1, the total pressure distortion may be amplified even if F is positive.

The attenuation of the axial velocity distortion which occurs upstream of the compressor induces a static pressure distortion at the compressor face.

$$p_1 - p_2 = \rho_1 \overline{c_{x1}} [c_{x2}{}' - \epsilon \sin(n\theta)]$$

$$p_1 - p_2 = \rho_1 \overline{c_{x1}} \epsilon \sin(n\theta) \left(\frac{F}{1+F}\right) \tag{13}$$

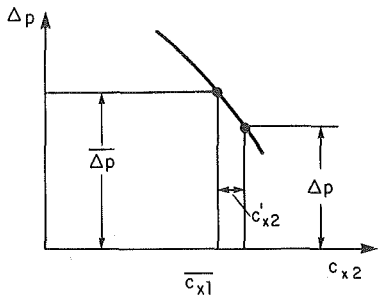

Fig. 4

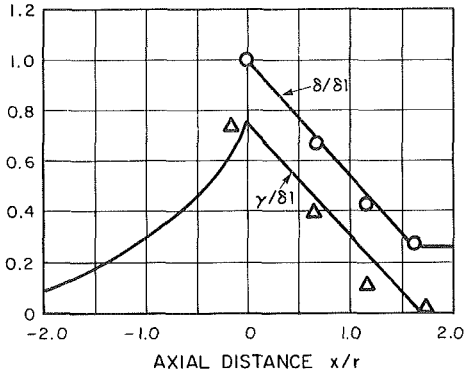

Fig. 5

The amplitude of the static pressure distortion at the compressor face is

$$\gamma_2 = \rho_1 \overline{c_{x1}} \epsilon \left(\frac{F}{1+F} \right)$$

The flow field upstream of the compressor may also be found using continuity and the fact that the vorticity along any stream-line remains constant between (1) and (2).

Let the velocity field at any point upstream of the compressor be represented by

$$c_x = \overline{c_{x1}} + \epsilon \sin(n\theta) + u \tag{14}$$

$$c_\theta = v \tag{15}$$

where u, v are of the order of ϵ and represent the effect of the compressor on the upstream flow field.

For incompressible flow ($M << 1$), continuity yields

$$\frac{\partial c_x}{\partial x} + \frac{1}{r} \frac{\partial c_\theta}{\partial \theta} = 0$$

Hence

$$\frac{\partial u}{\partial x} + \frac{1}{r} \frac{\partial v}{\partial \theta} \Big] = 0 \tag{16}$$

Conservation of vorticity along streamlines gives

$$\frac{D}{Dt} \left[\frac{\partial c_\theta}{\partial x} - \frac{1}{r} \frac{\partial c_x}{\partial \theta} \right] = 0$$

i.e.,

$$\frac{D}{Dt} \left[\frac{\partial v}{\partial x} - \frac{1}{r} \frac{\partial u}{\partial \theta} \right] = 0 \tag{17}$$

But u, v are zero at $x = -\infty$.

Hence

$$\frac{\partial v}{\partial x} = \frac{1}{r} \frac{\partial u}{\partial \theta} = 0 \tag{18}$$

everywhere upstream of the compressor.

Solutions to (16) and (18) satisfying the boundary conditions $u, v \to 0$ as $x \to -\infty$ are found in the form

$$u = A_n e^{nx/r} \sin(n\theta) \tag{19}$$

$$v = A_n e^{nx/r} \cos(n\theta) \tag{20}$$

At the compressor face, let $x = 0$. Then, at (2)

$$c_x = \overline{c_x} + \epsilon \sin(n\theta) + A_n \sin(n\theta)$$

$$= \overline{c_x} + \frac{\epsilon \sin(n\theta)}{1+F} \quad \text{from (9)}$$

Hence

$$A_n + \epsilon = \frac{\epsilon}{1+F}$$

$$A_n = -\left(\frac{F}{1+F} \right) \epsilon \tag{21}$$

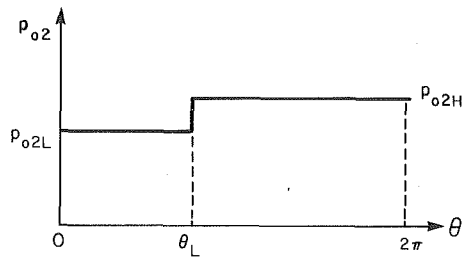

Fig. 6

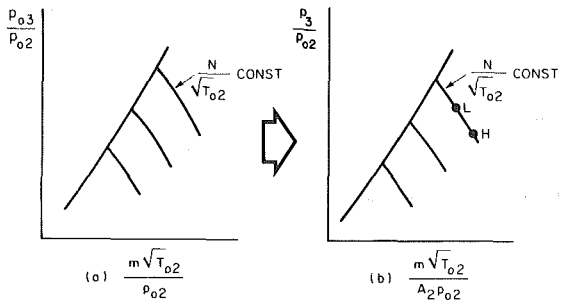

Fig. 7

and the solution for the flow field upstream of the compressor is

$$c_x = \overline{c_{x1}} + \epsilon \sin(n\theta) - \left(\frac{F}{1+F} \right) \epsilon e^{nx/r} \sin(n\theta) \tag{22}$$

$$c_\theta = -\frac{F\epsilon}{1+F} e^{nx/r} \cos(n\theta) \tag{23}$$

The above procedure was used in reference [3] and Fig. 5 shows the predicted and measured total and static pressure distortion behavior for a three stage compressor.

Parallel Compressor Model. The preceding analysis assumes that the distortion is small and hence that the average pressure rise across the compressor is unchanged by the presence of the distortion. Such an analysis is obviously incapable of estimating the influence of large inlet distortions on the compressor map.

An ingenious technique for handling large distortions known as the "parallel compressor" model has been discussed by several authors [2], [4], [6]. This approach is most suitable for the analysis of a square-wave circumferential distribution in which a portion of the compressor annulus of extent θ_L at the inlet guide vanes is supplied with low total pressure gas at p_{02L}, and the remainder of the annulus, of extent $(2\pi - \theta_L)$, is supplied with high total pressure gas at p_{02H} as shown n Fig. 6.

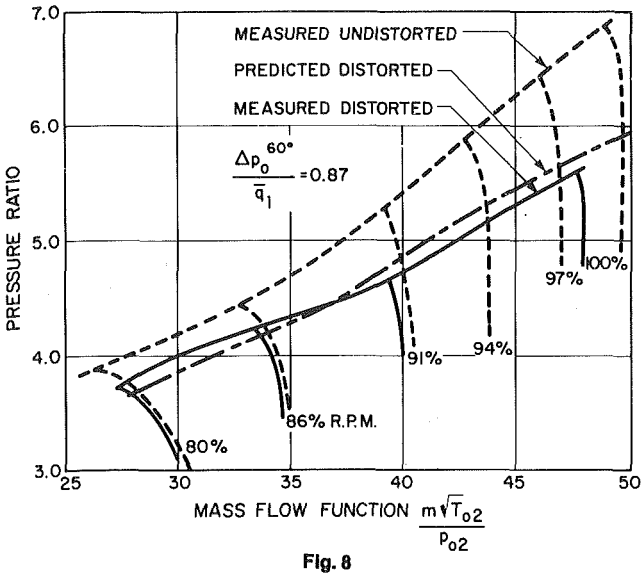

Fig. 8

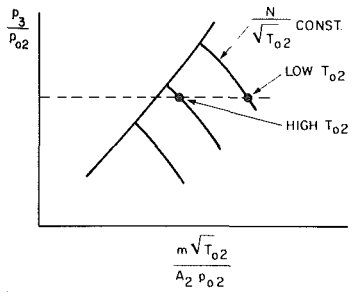

Fig. 9

If no crossflow occurs within the compressor, then the two portions of the compressor annulus act as two separate compressors in parallel, both discharging to the same exit static pressure.

The undistorted compressor map, usually plotted as p_{03}/p_{02} versus $m\sqrt{T_{02}}/p_{02}$, may be replotted as p_3/p_{02} versus $(m/A_2)(\sqrt{T_{02}}/p_{02})$ where A_2 is the inlet cross-section flow area as shown in Fig. 7, if the annulus area is known. p_3/p_{03} may be found from the exit Mach number.

Then if the sector θ_L operates at the point L on Fig. 7(b), the sector $(2\pi - \theta_L)$ operates at the point H, where

$$\left(\frac{p_3}{p_{02}}\right)_H = \left(\frac{p_3}{p_{02L}}\right)\frac{p_{02L}}{p_{02H}}.$$

The total mass flow rate is equal to $m = m_L + m_H$.

$$m = \left(\frac{m\sqrt{T_{02}}}{Ap_{02}}\right)_L \frac{\theta_L A_T}{2\pi}\left(\frac{p_{02L}}{\sqrt{T_{02}}}\right) + \left(\frac{m\sqrt{T_{02}}}{Ap_{02}}\right)_H \frac{(2\pi-\theta_L)A_T}{2\pi}\left(\frac{p_{02L}}{\sqrt{T_{02}}}\right) \qquad (24)$$

The mass averaged exit total pressure p_{03} can be calculated from the exit static pressure p_3 and the total mass flow rate.

Thus, for each operating point of the sector θ_L, there is a corresponding operating point for the sector $(2\pi - \theta_L)$, a corresponding total mass flow, total pressure ratio, and average efficiency. The compressor is assumed to go into surge when the low total pressure region crosses the surge line.

This method has proved useful for analyzing distortions

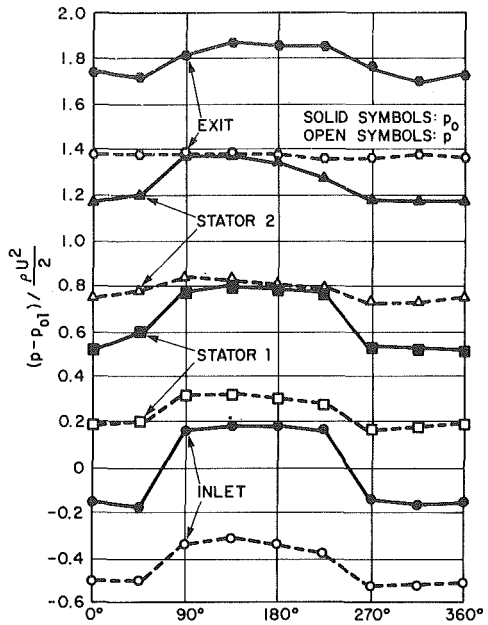

Fig. 10 Behavior of square wave distortion in a three-stage compressor

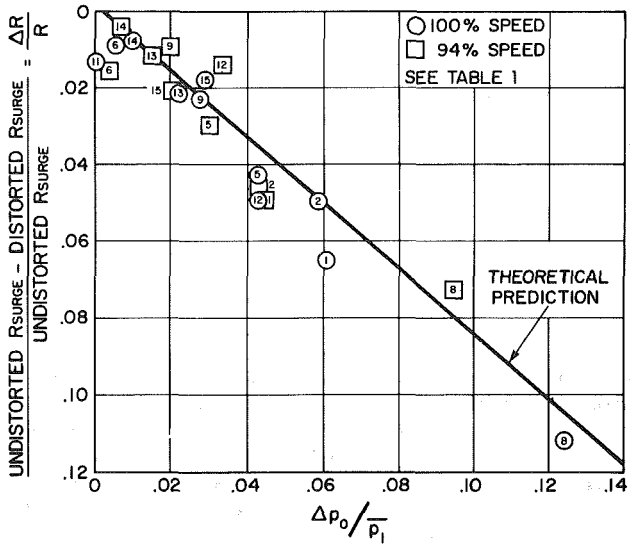

Fig. 11

greater than 60 deg in width, and Fig. 8 shows a typical compressor map with and without a 60 deg distortion, together with the surge line prediction given by the parallel compressor model [4].

Neglect of unsteady effects in the simple "parallel compressor" model makes it prone to serious errors for distortions of amplitude less than 60 deg.

The "parallel compressor" theory can also be used for the analysis of inlet temperature distortion, in which case the two portions of the annulus are operating on different corrected speed lines as shown in Fig. 9.

Actuator Disk Analyses

The assumption that the local performance of a stage depends only on the local flow coefficient is obviously a very sweeping one which must break down when velocity and pressure gradients in the θ direction are large. A rigorous analysis of inlet distortion must include the effects of the distortion on the local performance of the blade rows.

Starting with the work of Ehrich [7], a number of authors

Table 1 (reference [4]) Description of spoilers included in research program (Note: Spoiler nos. correspond to point nos. on Fig. 11.)

Spoiler No.	Description	$\frac{p_{02L}}{p_{02H}}$ at 100% speed	$\frac{\Delta p_0}{q_1}$ 60 deg	Remarks
1	1 × 90 deg	0.942	0.402	
2	1 × 45 deg	0.931	0.387	
3	1 × 22 ½ deg	–	–	test curtailed by failure
4	1 × 11 ¼ deg	–	–	not tested
5	2 × 45 deg	0.926	0.281	
6	4 × 22 ½ deg	0.977	0.036	
7	2 × 22 ½ deg	–	–	not tested
8	1 × 90 deg	0.877	0.860	
9	1 × 90 deg	0.967	0.178	
10	360 deg tip	–	–	test curtailed by high stage 1 rotor stresses
11	360 deg hub	0.952	0	
12	1 × 180 deg	0.927	0.287	
13	1 × 270 deg	0.923	0.146	
14	1 × 315 deg	0.925	0.059	
15	180 deg hub + 180 deg tip	0.934	0.185	
16	360 deg	1.0	0	covered whole annulus

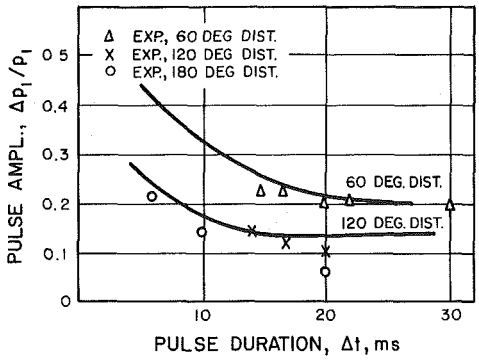

Fig. 12

have presented analyses of distortion which use the actuator disk approach to carry out a blade row by blade row calculation [8–11]. These studies give overall attenuation predictions which are similar to the zero crossflow analyses when the distance between blade rows is small. However, the shape of the distortion can be substantially modified by even small crossflows, an effect which is not predicted by the zero crossflow models.

Fig. 10 shows how a square wave distortion changes shape as it passes through a compressor [3].

Combined Circumferential-Radial Distortion

As has already been mentioned, little progress has been made in analyzing combined radial and circumferential distortion. Callahan and Stenning [12] studied flow redistribution upstream of a low hub-tip ratio fan with combined distortion using a very simple model of compressor behavior. Reid [4] suggests that radial distortion has a small effect on the surge line although it may have a strong influence on efficiency and flow. However, other researchers do not accept this view and maintain that radial distortion has a large effect on the surge line. He proposes that a distortion index $\Delta p_0/\overline{p_{02}}$ should be used based on the average inlet total pressure $\overline{p_{02}}$ and the difference Δp_0 between $\overline{p_{02}}$ and the lowest area averaged total pressure in any 60 deg sector of the annulus. Parallel compressor theory is then applied using the appropriate value of $\Delta p_0/\overline{p_{02}}$. Figure 11 shows the loss in surge pressure ratio predicted and measured using this technique for a variety of different types of distortion listed in Table 1.

Unsteady Flow Effects

When a rotor blade enters or leaves a flow distortion, it undergoes rapid changes in inlet angle of attack and relative velocity. The neglect of the resulting changes in total and static pressure and flow angle leaving the rotor is the major deficiency of all of the methods of analysis described previously. The use of even approximate techniques for calculating unsteady cascade behavior [13] gives a substantial improvement in the agreement between predicted and measured distortion attenuation and performance map modification.

Transient Distortions

The flow downstream of a supersonic inlet is highly unsteady. In consequence, even though the mean flow pattern is uniform, the instantaneous total pressure distribution may be highly distorted. It has been found that over a period of time, a short-lived distortion may appear which is of sufficient magnitude, and sufficient duration, to cause the compressor to surge. Recent investigations have been directed towards defining the critical parameters which govern this phenomenon [14–16]. Typical results from [16] are shown in Fig. 12.

References

1 Alford, J. S., "Inlet Flow Distortion Index," *Comptes Rendus des Journees Internationales de Science Aeronautique,* 1957, O.N.E.R.A.

2 Doyle, M. D.C., and Horlock, J. H., "Circumferential Asymmetry in Axial Flow Compressors," *Journal of the Royal Aeronautical Society,* Oct. 1966.

3 Plourde, G. A., and Stenning, A. H., "Attenuation of Circumferential Inlet Distortion in Multistage Axial Compressors," *Journal of Aircraft,* 1968, No. 3.

4 Reid, C., "The Response of Axial Flow Compressors to Intake Flow Distortion," ASME Paper 69-GT-29, 1969 ASME Gas Turbine Conference.

5 Mokelke, H., "The Development of Inlet Flow Distortions in Multi-Stage Axial Compressors of High Hub-Tip Ratio," SRC Turbomachinery Laboratory, Cambridge University (Presented at the 18th Congress of the International Council of the Aeronautical Sciences, Sept. 1972).

6 Roberts, F., Plourde, G. A., and Smakula, F., "Insights into Axial Compressor Response to Distortion," AIAA Paper No. 68-595, Fourth Propulsion Joint Specialist Conference, 1968.

7 Ehrich, F., "Circumferential Inlet Distortions in Axial-Flow Compressors," *Journal of the Aeronautical Sciences,* June 1957.

8 Rannie, W. D., and Marble, F. E., "Unsteady Flows in Axial Turbomachines," Comptes Rendus des Journees Internationales de Science Aeronautique, 1957, O.N.E.R.A.

9 Katz, R., "Performance of Axial Compressors with Asymmetric Inlet Flows," PhD thesis, California Institute of Technology, 1958.

10 Yeh, H., "An Actuator Disc Analysis of Inlet Distortion and Rotating Stall in Axial Flow Turbomachines," *Journal of the Aerospace Sciences,* Nov. 1959.

11 Dunham, J., "Non-Axisymmetric Flows in Axial Compressors," Mechanical Engineering Science Monograph No. 3, 1965, Institution of Mechanical Engineers.

12 Callahan, G., and Stenning, A. H., "Attenuation of Inlet Flow Distortion Upstream of Axial Flow Compressors," *Journal of Aircraft.*

13 Henderson, R. E., and Horlock, J. H., "An Approximate Analysis of the Unsteady Lift on Airfoils in Cascade," ASME *Journal of Engineering for Power,* Oct. 1972.

14 Plourde, G. A., and Brimelow, B., "Pressure Fluctuations Cause Compressor Instability," *Proceedings of the Air Force Airframe-Propulsion Compatibility Symposium,* AFAPL-TR-69-103, June 1970, Wright Patterson AFB.

15 Williams, D. D., and Yost, J. O., "Some Aspects of Inlet/Engine Flow Compatibility," Bristol Engine Division, Rolls Royce Ltd., Filton, Bristol (Presented at the 8th Congress of the International Council of the Aeronautical Sciences, Sept. 1972).

16 Jansen, W., Swarden, M. C., and Carlson, A. W., "Compressor Sensitivity to Transient and Distorted Transient Flows" (AIAA Paper No. 71-670), Presented at the AIAA/SAE 7th Propulsion Joint Specialist Conference, Salt Lake City, Utah, June 14-18, 1971.

Rotating Stall and Surge

A. H. Stenning
Department of Mechanical Engineering and Mechanics, Lehigh University, Bethlehem, Pa. 18015 (deceased)

Safe off-design operation of compressors is limited to the region in which the flow is stable. Flow instabilities can be of two types, rotating stall and surge. The first of these subjects the blading to high oscillating stresses while the second may also have a disastrous effect on the whole system of which the compressor is a component. In this paper, the properties of these two types of instability are discussed and some simple criteria for determining system stability are presented.

Flow Stability

In normal operation of a compressor without inlet distortion, the flow is essentially steady and axisymmetric, apart from the blade-to-blade pressure variations and the small scale unsteadiness associated with the moving pressure and velocity fields of the rotors. However, if the performance map of a compressor is plotted in the usual form shown in Fig. 1, as pressure ratio versus mass flow rate for different rotational speeds, a line called the stall line can be defined which separates stable operation from unstable operation. To the left of the line, the flow is no longer steady. Large oscillations of the mass flow rate may occur (called surge), or self-induced circumferential flow distortions may rotate around the annulus (called rotating stall), or a combination of both phenomena may appear (Fig. 2). Alternatively, after a few oscillations, the compressor may converge on a new steady state with very small pressure rise and mass flow rate. In this condition flow recirculation and the interaction with the rest of the system may produce a rapid temperature rise of the gas within the compressor, in extreme cases causing blades to melt within a few seconds or minutes of the occurrence of instability.

Rotating stall induces large vibratory stresses in the blading of compressors and is therefore undesirable for structural reasons although the compressor may continue to give acceptable performance. Rotating stall occurs in compressible as well as incompressible flows. Surge is usually intolerable from the point of view of system operation. No matter which type of instability appears when the stall line is crossed, it is clear that the stall line represents a limit to the safe operation of the machine under most circumstances and is therefore to be avoided. Surge only occurs in compressible flows, i.e. gaseous fluids.

In the development of a new compressor, the position of the stall line is a matter of great concern to the designer, and considerable effort is frequently devoted to moving the stall line away from the region of maximum efficiency.

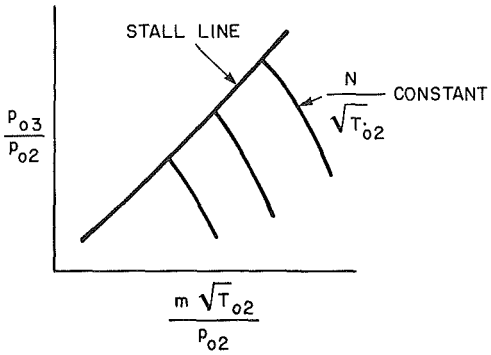

Fig. 1

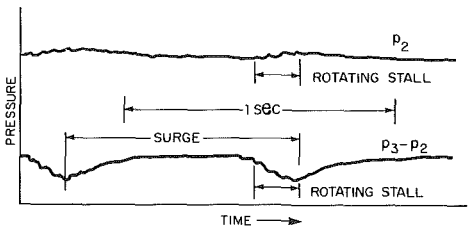

Fig. 2

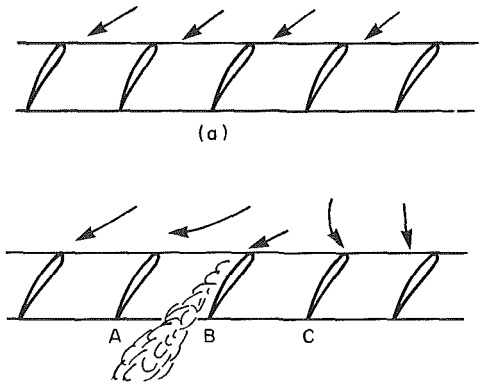

Fig. 3

Rotating Stall

When rotating stall occurs, one or more "stall cells" travel around the compressor annulus in the direction of rotation of

Contributed by the Fluids Engineering Division for publication in the JOURNAL OF FLUIDS ENGINEERING. Manuscript received by the Fluids Engineering Division, January 23, 1975.

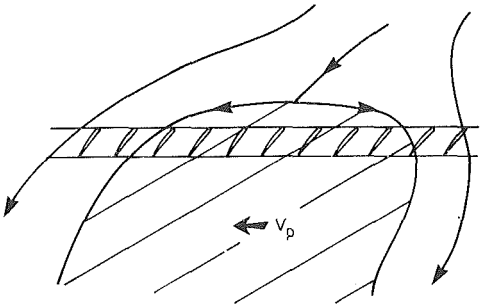

Fig. 4

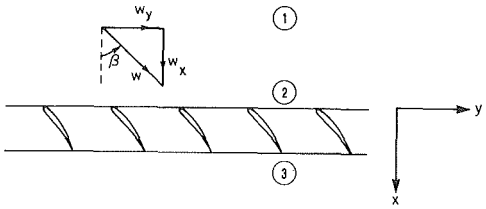

Fig. 5

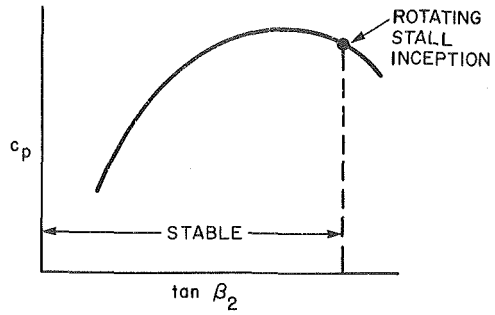

Fig. 6

the compressor, with a rotational speed which is usually close to one-half of the compressor rotational speed, although in a few rare cases stationary stall cells have been observed attached to inlet struts. Rotating stall can occur in both axial and centrifugal compressors. Within each stall cell the blades are so severely stalled that there is virtually no flow through the blade row. A stall cell may cover only a few blades, or may occupy a substantial portion of the annulus. It may appear at the root or tip of the blading or may extend over the whole blade length.

The simplest method of explaining the onset of rotating stall is illustrated in Fig. 3. Consider a row of axial compressor blades operating at a high angle of attack as shown in Fig. 3(*a*). If a flow disturbance produces a local increase in angle of attack on blade B as shown in Fig. 3(*b*), then severe flow separation may occur. The resulting blockage of the channel will divert flow away from blade B, increasing the angle of attack on blade A and reducing the angle of attack on blade C. The stall will therefore propagate from right to left and, if conditions are suitable, may build up into a fully developed stall cell as shown in Fig. 4, propagating along the cascade with velocity V_p.

Rotating stall was first observed by the group developing centrifugal compressors for the Whittle turbojet in 1938 [1]. A comprehensive list of publications on rotating stall up to 1967 has been assembled by Fabri [2], and a series of ASME papers extending from 1954 to 1972 cover many of the significant developments in the field [3-7]. In the following sections, attention will be devoted to the development of criteria for the prediction of the onset of rotating stall, to the propagation velocity, and to the number of stall cells.

Small Perturbation Analysis. A large number of analyses of rotating stall have been made in which the response of the flow entering a cascade to a small unsteady circumferentially varying disturbance is studied. The objectives of all of these analyses are to determine a criterion for the onset of rotating stall, the velocity of propagation, and (if possible) the number of stall cells. The first of these objectives has largely been attained, but small-perturbation analyses have shown only limited success in predicting the propagation speed or the number of stall cells. The following discussion describes the very simplest type of small-perturbation incompressible theory but does yield a criterion for the onset of rotating stall in a cascade which appears to be applicable to single-stage compressors and some multi-stage compressors.

Figure 5 shows an infinite two-dimensional rectilinear cascade lying on the y axis in the xy plane. At the leading edge of the cascade let $x = 0$. At station (1), $x = -\infty$. Under steady, uniform upstream flow conditions

$$w_x = \overline{w_x}$$

$$wy = \overline{w_y}$$

where w_x, w_y are the velocity components relative to the

Nomenclature

a = coefficient in Fourier expansion
A = flow area
b = coefficient in Fourier expansion
c = absolute velocity
c_p = pressure coefficient
C = $p_2 - p_{01}$
C' = $\dfrac{d(p_2 - p_{01})}{dm}$
D = coefficient
E = coefficient
F = $p_3 - p_{01}$
F' = $\dfrac{d(p_3 - p_{01})}{dm}$
g_c = coefficient in Newton's law
k = polytropic exponent
L = duct length
m = mass flow rate
n = number of harmonic
N = rotational speed
p = pressure
p_0 = total pressure
Δp = pressure rise
R = gas constant
t = time
T = temperature
u = axial velocity perturbation
U = blade speed
v = tangential velocity perturbation
V = plenum volume
V_p = stall cell propagation speed
w = relative velocity
x = axial coordinate
y = tangential coordinate
z = variable
β = flow angle relative to cascade
δ = perturbation
ϕ = perturbation velocity potential
Φ = total velocity potential
ρ = density
ψ = total pressure rise coefficient $\dfrac{p_{03} - p_{02}}{\rho U^2}$
ψ_s = total-to-static coefficient $\dfrac{p_3 - p_{02}}{\rho U^2}$

Subscripts

1 = Far upstream of blading
2 = Inlet of blading
3 = Outlet of blading

cascade. Let the static pressure rise across the cascade be of the form

$$c_p = \frac{p_3 - p_2}{\frac{1}{2}\rho w_2{}^2} = g(\tan\beta_2) \quad (1)$$

where

$$\tan\beta_2 = \frac{w_{y2}}{w_{x2}} \quad (2)$$

as shown in Fig. 6.

Consider the possibility of small unsteady disturbances in the flow such that upstream of the cascade

$$w_x = \overline{w_x} + u(x,y,t) \quad (3)$$
$$w_y = \overline{w_y} + v(x,y,t) \quad (4)$$
$$p = \bar{p} + \delta p(x,y,t) \quad (5)$$

where $u, v << \overline{w_x}, \overline{w_y}$

and $\delta p << \frac{1}{2}\rho w_x{}^2$. $u, v \to 0$ for $x \to -\infty$.

Since the flow far upstream of the cascade is irrotational, the upstream flow field is free of vorticity and we may define a potential function Φ such that

$$\Phi = \overline{w_x}x + \overline{w_y}y + \phi \quad (6)$$

where $w_x = \frac{\partial\Phi}{\partial x}$ $w_y = \frac{\partial\Phi}{\partial y}$

Hence $u = \frac{\partial\phi}{\partial x}$ and $v = \frac{\partial\phi}{\partial y}$

From continuity, $\frac{\partial u}{\partial x} + \frac{\partial v}{\partial y} = 0 \quad (7)$

Hence $\frac{\partial^2\phi}{\partial x^2} + \frac{\partial^2\phi}{\partial y^2} = 0 \quad (8)$

Solutions to (8) may be found in the form

$$\phi = \sum_{n=1}^{\infty}\left[a_n(t)\cos\frac{n\pi y}{b} + b_n(t)\sin\frac{n\pi y}{b}\right]e^{\frac{n\pi x}{b}} \quad (9)$$

representing wave-like disturbances in the flow. At $x = -\infty$, u and $v = 0$, $w_{x1} = \overline{w_x}$, $w_{y1} = \overline{w_y}$. The unsteady Bernoulli equation upstream of the cascade may be written (5)

$$\frac{\partial\phi}{\partial t} + \frac{w^2}{2} + \frac{p}{\rho} = \frac{w_1^2}{2} + \frac{p_1}{\rho} \quad (10)$$

Hence, at ②

$$\left(\frac{\partial\phi}{\partial t}\right)_2 + \frac{w_2^2}{2} + \frac{p_2}{\rho} = \frac{\bar{w}_1^2}{2} + \frac{p_1}{\rho}$$

which yields

$$\left(\frac{\partial\phi}{\partial t}\right)_2 + \overline{w_x}u_2 + \overline{w_y}v_2 + \frac{\delta p_2}{\rho} = 0 \quad (11)$$

i.e., $$\left(\frac{\partial\phi}{\partial t}\right)_2 + \overline{w_x}\left(\frac{\partial\phi}{\partial x}\right)_2 + \overline{w_y}\left(\frac{\partial\phi}{\partial y}\right)_2 + \frac{\delta p_2}{\rho} = 0 \quad (12)$$

If the unsteady cascade behavior is the same as the steady cascade behavior, then the pressure rise across the cascade in unsteady flow can be found, for small perturbations, from the expression

$$c_p = \frac{p_3 - p_2}{\frac{1}{2}\rho w_2^2} = \overline{c_p} + \frac{\partial c_p}{\partial\tan\beta_2}\delta(\tan\beta_2)$$

Hence,

$$p_3 - p_2 = \frac{1}{2}\rho w_2^2\left[\overline{c_p} + \frac{\partial c_p}{\partial\tan\beta_2}\delta(\tan\beta_2)\right] \quad (13)$$

where

$$w_2^2 = [\overline{w_x} + u_2]^2 + [\overline{w_y} + v_2]^2 \quad (14)$$

After some rearrangement, neglecting terms in u^2, v^2, it is found that if $p_2 = \overline{p_2} + \delta p_2$ and $p_3 = \overline{p_3} + \delta p_3$ then

$$\delta p_3 - \delta p_2 = \rho\overline{c_p}[\overline{w_x}u_2 + \overline{w_y}v_2] + \frac{1}{2}\rho\overline{w_2^2}\frac{dc_p}{d\tan\beta_2}\delta(\tan\beta_2) \quad (15)$$

where $$\delta(\tan\beta_2) = \delta\left(\frac{w_{y2}}{w_{x2}}\right)$$

$$= \frac{\overline{w_x}v_2 - \overline{w_y}u_2}{\overline{w_x}^2} \quad (16)$$

For an isolated cascade in rotating stall, experiments [8] indicate that the fluctuations in pressure downstream of the cascade are much smaller than the fluctuations in pressure upstream, i.e., $\delta p_3 << \delta p_2$. Setting $\delta p_3 = 0$ and substituting equation 15 in equation 12 we obtain the following equation which must be satisfied by the perturbation potential.

$$\left(\frac{\partial\phi}{\partial t}\right)_2 + D\left(\frac{\partial\phi}{\partial x}\right)_2 + E\left(\frac{\partial\phi}{\partial y}\right)_2 = 0 \quad (17)$$

where $$D = \left[(1-\overline{c_p})\overline{w_x} + \frac{\overline{w_y}}{2\cos^2\beta_2}\frac{dc_p}{d\tan\beta_2}\right] \quad (18)$$

and $$E = \left[(1-\overline{c_p})\overline{w_y} - \frac{\overline{w_x}}{2\cos^2\beta_2}\frac{dc_p}{d\tan\beta_2}\right] \quad (19)$$

Substituting equation (9) in equation (17) a pair of linear simultaneous differential equations are obtained for $a_n(t)$, $b_n(t)$.

$$\frac{da_n}{dt} + \frac{n\pi}{b}(Da_n + Eb_n) = 0 \quad (20)$$

$$\frac{db_n}{dt} + \frac{n\pi}{b}(Db_n - Ea_n) = 0 \quad (21)$$

Solutions to these equations show that when $D < 0$, disturbances die away but when $D > 0$ they grow and propagate along the cascade. The condition for inception of rotating stall is $D = 0$, for which

$$\frac{dc_p}{d\tan\beta_2} = -\frac{2(1-\overline{c_p})\cos^2\beta_2}{\tan\beta_2} \quad (22)$$

The velocity of propagation is found to be

$$V_p = \frac{\overline{w_y}(1-\overline{c_p})}{\sin^2\beta_2} \quad (23)$$

All wavelengths become unstable simultaneously. From (22) it can be seen that rotating stall cannot occur until $dc_p/d\tan\beta_2$ is negative, that is until an increase in B_2 produces a decrease in c_p. The cascade must be severely stalled for this condition to be satisfied (as shown in Fig. 5).

For isolated cascades, equation (22) appears to give a reasonably good prediction of the onset of rotating stall. However, the measured stall propagation velocities are not in good agreement with equation (23). As has been shown by Takata and Nagano [7], fully developed rotating stall is a highly nonlinear phenomenon and there is, in fact, no reason

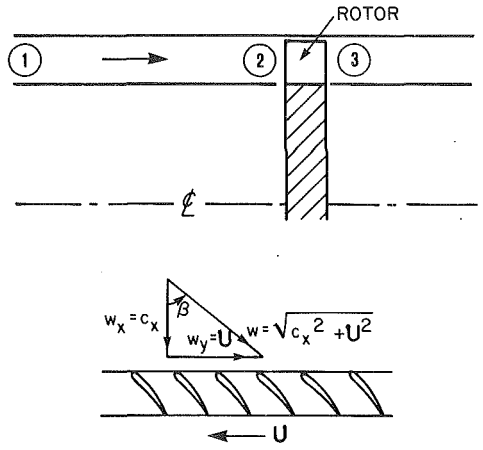

Fig. 7 Isolated rotor

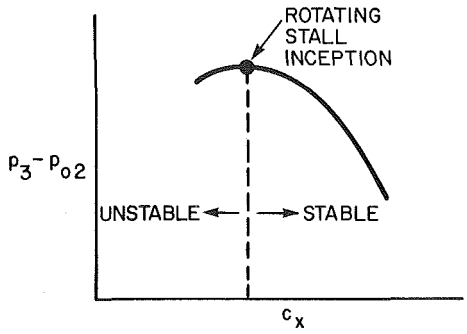

Fig. 8

to expect that a small perturbation theory will be successful in predicting V_p after the stall cells have grown to their limiting size.

An especially interesting application of simple stall propagation theory is the case of an isolated rotor illustrated in Fig. 7.

If the flow approaches the rotor with no swirl, then $\overline{c_{y2}} = 0$ and

$$\overline{w_{y2}} = U \qquad \overline{w_y} = \overline{c_x}$$

$$\overline{w^2} = \overline{c_x}^2 + U^2$$

The pressure rise across the rotor in steady flow is given by

$$\Delta p = p_3 - p_2 = c_p \frac{1}{2}\rho w_2^2 = c_p \frac{1}{2}\rho[c_{x2}^2 + U^2] \tag{24}$$

$$\frac{d\Delta p}{dc_x} = \frac{1}{2}\rho[c_x^2 + U^2]\frac{dc_p}{dc_x} + \rho c_x c_p$$

$$= \frac{1}{2}\rho w_2^2 \frac{dc_p}{d\tan\beta_2}\frac{d\tan\beta_2}{dc_x} + \rho c_x c_p \tag{25}$$

$$\frac{d\tan\beta_2}{dc_x} = -\frac{U}{c_x^2} \text{ since } \tan\beta_2 = \frac{U}{c_x} \tag{26}$$

Hence
$$\frac{d\Delta p}{dc_x} = -\frac{\rho U}{2\cos^2\beta_2}\frac{dc_p}{d\tan\beta_2} + \rho c_x c_p \tag{27}$$

When rotating stall starts,

$$\frac{dc_p}{d\tan\beta_2} = -\frac{2(1-\overline{c_p})\cos^2\beta_2}{\tan\beta_2} \tag{22}$$

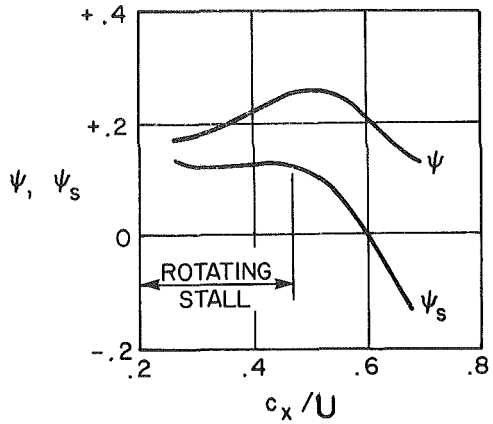

Fig. 9 Experimental compressor characteristics

Substituting equation (22) in equation (27) we find that when rotating stall begins

$$\frac{d\Delta p}{dc_x} = \rho c_x$$

or
$$\frac{1}{\rho c_x}\frac{d\Delta p}{dc_x} = 1 \tag{28}$$

This is exactly the condition at which the onset of a self-induced flow distortion was predicted by equation (10) of reference [2].

It therefore appears that the existence of an infinite amplification ratio for inlet flow distortion can be associated with the inception of rotating stall.

Moreover, $p_3 - p_2 = (p_3 - p_{02}) + p_{02} - p_2)$

$$\Delta p = (p_3 - p_{02}) + \frac{1}{2}\rho c_x^2$$

Hence
$$\frac{d\Delta p}{dc_x} = \frac{d(p_3 - p_{02})}{dc_x} + \rho c_x \tag{29}$$

When $\dfrac{d\Delta p}{dc_x} = \rho c_x$, then

$$\frac{d(p_3 - p_{02})}{dc_x} = 0 \tag{30}$$

Thus, if the rotor pressure rise characteristic is plotted in the form $(p_3 - p_{02})$ versus c_x, then rotating stall occurs at the peak of the curve shown in Fig. 8. This important result was first obtained by Dunham [9].

As a criterion for the inception of rotating stall, equation (30) appears to be useful not only for isolated rotors but also for single-stage compressors and some multistage compressors, and it has been discussed by Moritz [10]. When a multistage high pressure ratio compressor operates at low speed, rotating stall may be initiated by severe local stalling of the front stages and equation (30) does not apply.

In Fig. 9, the observed point of rotating stall inception is shown on the characteristic of a single stage compressor tested by Dunham [9]. Rotating stall started at the peak of the stagnation-to-static pressure rise coefficient ψ_s defined as $(p_{03} - p_2)/\rho U^2$. Similar good agreement has been found in many other machines.

Other authors have found that applying the above criteria to each streamtube at each blade, localized rotary stall can be predicted in multistage compressors. Surge usually follows according to [13 and 14].

Several attempts have been made to predict the number of stall cells using small perturbation stability analyses. None

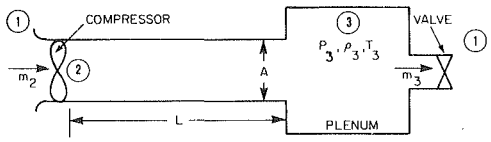

Fig. 10

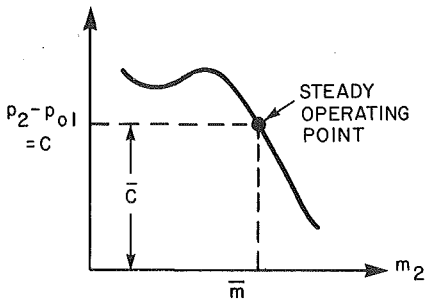

Fig. 11

has met with success and it appears that nonlinear phenomena are intimately involved in the process which determines the number of cells, as well as boundary layer delay times and fluid inertia in the cascade.

Nonlinear Analyses of Rotating Stall. When the stall cell reaches its limiting size, the axial velocity within the cell is almost zero. This fact has been used [5, 8] to derive a simple expression for the propagation speed of the cell along the cascade.

$$V_p = \overline{w_y}\left[1-\sqrt{1-\frac{(1-c_p)}{\sin^2\beta_2}}\right] \tag{31}$$

which gives better agreement with measured propagation speeds than equation (23).

Takata and Nagano [7] have recently undertaken an extremely thorough numerical solution of the nonlinear unsteady equations of motion for rotating stall which has been successful in reproducing most of the observed phenomena, and which has indicated that the number of stall cells in a complete stage is governed by the interference effects between blade rows. They have not, however, been able to explain why different numbers of stall cells appear at different operating conditions in an isolated rotor.

Surge

Surge consists of large-amplitude oscillations of the flow through the entire compressor which also produces large oscillations in compressor delivery pressure [4, 11].

The conditions which induce surge, and an estimate of the surge frequency, may be obtained from a small perturbation stability analysis of the whole system.

Small Perturbation Analysis of Surge. The essential ingredients of any surge analysis are

(*a*) a compressor
(*b*) mass storage
(*c*) fluid inertia
(*d*) a throttle

In any real system, the mass storage and the inertia are distributed throughout the system. However, the essential elements of the surge phenomenon can be extracted from the simple lumped parameter model pictured in Fig. 10. The system is lumped into four components, consisting of the compressor, a duct, a plenum and a valve. The compressor is

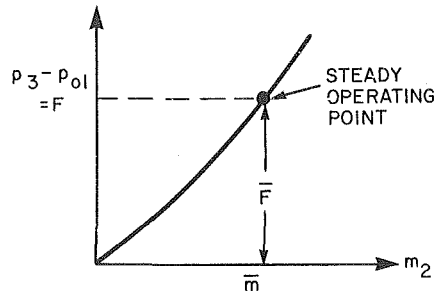

Fig. 12

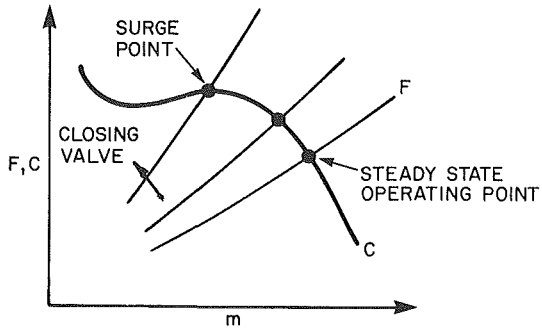

Fig. 13

assumed to have a pressure rise characteristic as represented in Fig. 11, with $p_2 - p_{01}$ some function of the mass flow rate through the compressor m_2.

$$p_2 - p_{01} = C(m_2) \tag{32}$$

The gas leaving the compressor enters a duct of length L and constant flow area A and discharges into a plenum of volume V, which it leaves through a valve. Under steady flow conditions, $m_2 = m_3 = \bar{m}$ and $p_2 = p_3 = \bar{p}$ if we neglect frictional effects in the duct.

Consider small fluctuations about a mean flow such that

$$m_2 = \bar{m} + \delta m_2 \tag{33}$$
$$m_3 = \bar{m} + \delta m_3 \tag{34}$$
$$p_2 = \bar{p} + \delta p_2 \tag{35}$$
$$p_3 = \bar{p} + \delta p_3 \tag{36}$$

Neglecting axial density changes in the duct, the momentum equation within the duct is

$$p_2 - p_3 = \frac{L}{Ag_c}\frac{dm_2}{dt} \tag{37}$$

i.e., $$(\bar{p}+\delta p_2)-(\bar{p}+\delta p_3) = \frac{L}{Ag_c}\frac{d}{dt}(\bar{m}+\delta m_2)$$

$$\delta p_2 - \delta p_3 = \frac{L}{Ag_c}\frac{d\delta m_2}{dt} \tag{38}$$

Mass conservation in the plenum requires

$$m_2 - m_3 = V\frac{d\rho_3}{dt} \tag{39}$$

If the process in the plenum is polytropic, then

$$\frac{k}{\rho_3}\frac{d\rho_3}{dt} = \frac{1}{p_3}\frac{dp_3}{dt} \tag{40}$$

where k is the polytropic exponent.

Hence, $$m_2 - m_3 = \frac{V\rho_3}{kp_3}\frac{dp_3}{dt}$$

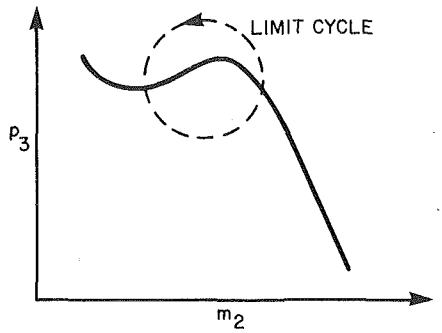

Fig. 14

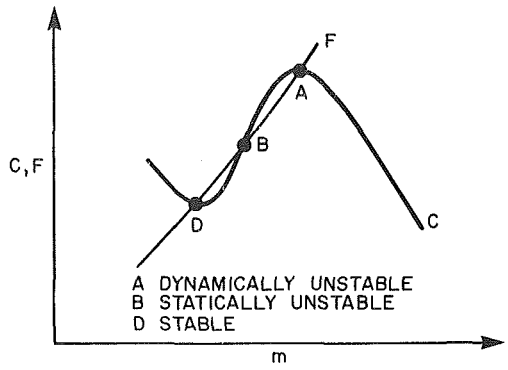

Fig. 15

$$(\bar{m}+\delta m_2)-(\bar{m}+\delta m_3)=\frac{V}{kRT_3}\frac{d}{dt}(\bar{p}+\delta p_3)$$

$$\delta m_2-\delta m_3=\frac{V}{kRT_3}\frac{d}{dt}(\delta p_3) \tag{41}$$

If we linearize the compressor characteristic in the vicinity of the steady state operating point then

$$p_2-p_{01}=C\simeq\bar{C}+\frac{dC}{dm_2}\delta m_2 \tag{42}$$

$$(\bar{p}+\delta p_2)-p_{01}=\bar{C}+\frac{dC}{dm_2}\delta m_2$$

But $\bar{p}-p_{01}=\bar{C}$

Therefore $\delta p_2=\dfrac{dC}{dm_2}\delta m_2$

$$\delta p_2=C'\delta m_2 \tag{43}$$

where $C'=\dfrac{dC}{dm_2}$

Let the pressure drop from the plenum to the atmosphere be a function of the mass flow through the valve as shown in Fig. 12.

$$p_3-p_{01}=F(m_3) \tag{44}$$

Then for small disturbances away from the steady state

$$p_3-p_{01}=\bar{F}+\frac{dF}{dm_3}\delta m_3 \tag{45}$$

$$(\bar{p}+\delta p_3)-p_{01}=\bar{F}+\frac{dF}{dm_3}\delta m_3$$

$$\delta p_3=\frac{dF}{dm_3}\delta m_3$$

$$\delta p_3=F'\delta m_3 \tag{46}$$

where $F'=\dfrac{dF}{dm_3}$

The linearized equations for surge are therefore

$$\delta p_2-\delta p_3=\frac{L}{Ag_c}\frac{d}{dt}\delta m_2 \tag{38}$$

$$\delta m_2-\delta m_3=\frac{V}{kRT_3}\frac{d\delta p_3}{dt} \tag{41}$$

$$\delta p_2=C'\delta m_2 \tag{43}$$

$$\delta p_3=F'\delta m_3 \tag{46}$$

Eliminating any three of the variables from these four equations, we find the following characteristic equation for the remaining variable z where z can be δp_2, δp_3, δm_2 or δm_3.

$$\frac{LF'V}{Ag_ckRT_3}\frac{d^2z}{dt^2}+\left(\frac{L}{Ag_c}-\frac{C'F'V}{kRT_3}\right)\frac{dz}{dt}+(F'-C')z=0 \tag{47}$$

This is a second order equation which has constant coefficients if the disturbances are small. The coefficient of d^2z/dt^2 is always positive because, for any real valve, F' is always positive. Hence, instabilities occur if the coefficient of dz/dt becomes negative (negative damping) or the coefficient of z becomes negative (negative spring rate). If the coefficient of dz/dt becomes negative, the system is dynamically unstable and will undergo oscillations of increasing amplitude (surge). If the coefficient of z is negative, the system is statically unstable.

The steady state operating point of the system is defined by the intersection of the F and C characteristics as shown in Fig. 13.

If the valve area is gradually reduced the steady state operating point moves to the left on the compressor characteristic. $F' > C'$ for all the operating points shown in the figure so that the coefficient of z is always positive. C' is initially negative. However, as soon as the peak of the compressor characteristic is passed, C' $(=dC/dm)$ becomes positive. The system damping becomes zero when

$$\frac{C'F'V}{kRT_3}=\frac{L}{Ag_c}$$

or $$C'=\frac{LkRT_3}{g_cAF'V} \tag{48}$$

and surge oscillations then begin. For any real system, this will occur very close to the peak of the curve, and long before the system becomes statically unstable. According to equation (30), rotating stall should start at the peak of the curve, just before the initiation of surge. However, the inaccuracy of equation (30) as a rotating stall criterion for multistage compressors makes it possible for surge to occur before the inception of rotating stall, or for both to appear simultaneously. High speed dynamic measurements of surge initiation in high pressure ratio compressors have indicated that surge may be triggered very rapidly by rotating stall, and that the slight dip in the compressor characteristic produced by the rotating stall may be sufficient to induce surge. In low pressure ratio machines, the stall line may be indicative of rotating stall alone, without surge, and it may be necessary to penetrate deeply into the rotating stall region before surge occurs, or in some cases the machine may not surge at all.

The radian frequency of the oscillations for small disturbances is given by

$$\omega = \sqrt{\frac{(F' - C')Ag_c kRT_3}{LF'V}} \tag{49}$$

or, since C' is nearly zero at surge

$$\omega \simeq \sqrt{\frac{Ag_c\, kRT_3}{LV}} \tag{50}$$

The surge oscillations may build up into large amplitude limit cycles illustrated in Fig. 14, or in some cases the system may find a new steady state operating condition.

In Fig. 15, a combination of valve and compressor characteristics is shown with three intersections. Point A, the point of surge initiation, is dynamically unstable. Point B is statically unstable because $F'_B < C'_B$. However, point D is stable and, depending on the way in which surge is entered and the parameters of the system, it may be possible for the machine either to surge continuously or, after a few cycles, to converge on D. In the latter event, severe compressor damage may be sustained due to excessive temperatures or to rotating stall if D is in the region where rotating stall occurs.

Summary (by editor)

This paper has brought together the phenomena of rotating stall and surge. It has been the experience of the editor that the ideas expressed here are completely borne out by successfully corrolating experimental and calculated surge conditions.

Dividing a multistage compressor into a number of streamtubes (5 to 9) and calculating rotating stall criteria for each tube and blade row, one finds that surge will occur when the streamtube close to the hub is unstable for rotating stall. At the hub where the outlet angle is nearly axial ($\beta_2 = 0$), one finds $C' \sim 0$. However surge will not occur when the shroud streamtube is unstable. Since at the shroud ($\beta \sim 45$ deg) C' $<< 0$ and only a partial rotating stall will occur. Only when half of the upper streamtubes are in rotating stall, then surge will occur.

These rules, verified in this paper, are significant when designing high efficiency compressors, while maintaining adequate surge margin.

References

1 Chesire, L. J., "The Design and Development of Centrifugal Compressors for Aircraft Gas Turbines," *Institution of Mechanical Engineers Proceedings,* 1945, Vol. 153 (War Emergency Issue No. 12).

2 Fabri, J., "Rotating Stall in Axial Flow Compressors," Internal Aerodynamics (Turbomachinery), Institution of Mechanical Engineers, 1967.

3 Iura, T., and Rannie, W. D., "Experimental Investigations of Propagating Stall in Axial Flow Compressors," *Trans. ASME,* Mar. 1954.

4 Emmons, H. W., Pearson, C. E., and Grant, H. P., "Compressor Surge and Stall Propagation," *Trans. ASME,* Apr. 1955.

5 Stenning, A. H., and Kriebel, A. R., "Stall Propagation in a Cascade of Airfoils," *Trans. ASME,* May 1958.

6 Emmons, H. W., Kronauer, R. E., and Rockett, J. A., "A Survey of Stall Propagation Experiment and Theory," *ASME Journal of Basic Engineering,* 1959, p. 409.

7 Takata, H., and Nagano, S., "Nonlinear Analysis of Rotating Stall," *ASME Journal of Basic Engineering,* Oct. 1972.

8 Stenning, A. H., Seidel, B. S., and Senoo, Y., "Effect of Cascade Parameters on Rotating Stall," NASA TM 3-16-59W, Apr. 1959.

9 Dunham, J., "Non-Axisymmetric Flows in Axial Compressors," Institution of Mechanical Engineers, Mechanical Engineering Science Monograph No. 3, Oct. 1965.

10 Moritz, R. R., Rolls Royce Ltd., Derby, England. Lecture to Von Karman Institute, Rhode-Saint-Genese, Belgium, Feb. 1970.

11 Huppert, M. C., and Benser, W. A., "Aerodynamic Design of Axial-Flow Compressors," Chapters 12, 13, NASA SP-36, 1965.

12 Stenning, A. H., "Inlet Distortion Effects in Axial Compressors," preceding paper.

13 Nenni, J. P., and Ludwig, G. R., "A Theory to Predict the Inception of Rotating Stall in Axial Flow Compressors," AIAA Paper No. 74-528, American Institute of Aeronautics and Astronautics.

14 Jansen, W., and Smith, G. E., "Propulsion System Flow Stability Program (Dynamic), Phase I Final Technical Report, Part X. Explicit Stall Prediction Model - Theory and Comparison of Computed and Experimental Results," (AFAPL-TR-68-142), Air Force Aero Propulsion Laboratory, Wright-Patterson Air Force Base, Ohio, Dec. 1968.

M. H. Tennant

Research Engineer,
Savannah River Laboratory,
E.I. du Pont de Nemours & Co.,
Aiken, S.C.
Mem. ASME

F. J. Pierce

Professor.
Mem. ASME

J. E. McAllister

Instructor.

Mechanical Engineering,
Virginia Polytechnic Institute
and State University,
Blacksburg, Va. 24061

An Omnidirectional Wall Shear Meter

An omnidirectional wall shear meter has been developed which is capable of the direct measurement of both magnitude and direction of wall shear stress. Linearity, resolution, and accuracy have been demonstrated analytically and experimentally by static and dynamic calibration. The floating element device works on the cantilevered beam principle. Eddy current probes, set at right angles to the beam and to each other, sense the magnitude and direction of deflection which can be calibrated against known force loadings. The device is used to measure wall shear stress in three-dimensional flows, and was specifically developed as a means of validating proposed three-dimensional near-wall similarity laws.

Introduction

In 1954 Clauser [1] made a significant contribution to the study of two-dimensional turbulent boundary layers by showing that wall shear stress can be inferred from the near-wall velocity field using the two-dimensional near-wall similarity law,

$$u^+ = \frac{1}{K} \ln y^+ + C, \tag{1}$$

commonly known as the "law of the wall." Derivable from first principles, the law of the wall has been repeatably verified by comparison with direct measurements of wall shear stress [2–16]. Although some question as to the exact values of K and C remain [17], the wide applicability of this simple expression is quite remarkable.

Verification of the two-dimensional near-wall similarity law experimentally can only be accomplished by "direct" wall shear stress measurements, viz., measurements with floating element devices. In essence, a small area of the wall is isolated and the force acting on the area is measured. Note in particular that the existence of a near-wall similarity law is a *prerequisite* for use of "indirect" measurement techniques such as heated elements, Preston tubes, and the like. Given the validity of a near-wall similarity law, indirect techniques derive their usefullness from their simplicity compared with the floating element technique where extreme care is required to avoid the numerous potential error sources [3, 6, 11, 18–20].

Unlike the two-dimensional case, no three-dimensional near-wall similarity law can be formulated from first principles. Although several three-dimensional near-wall similarity laws have been postulated [21–28] none have been experimentally verified by direct measurements. Additional complexities are added for the three-dimensional case because the velocity profile is not collateral and the wall shear direction cannot be determined *a priori*. The only direct measurements of wall shear stress in a three-dimensional flow reported to date are five data by Pierce and Krommenhoek [18] using a one-dimensional device, where the wall shear direction was inferrred using the heated element technique.

A floating element device capable of simultaneous measurement of wall shear stress magnitude and direction is needed to provide a means of testing the validity of any three-dimensional near-wall similarity law [28–30]. In turn, a valid three-dimensional near-wall similarity model might provide a means of determining wall shear stress, an often important component of drag, from near-wall velocity data, and would aid in the development of more precise and efficient closure methods of analytical modeling of three-dimensional turbulent flows. An omnidirectional floating element device has been developed and used successfully for three-dimensional turbulent flow studies [31].

Description of Apparatus

A schematic of the omnidirectional floating element device is shown in Fig. 1. A 2.86 cm circular disk is supported by a 1.59 mm diameter steel rod, 21.6 cm in length. The disk is separated from the surrounding wall by a 0.127 mm gap. Vertical misalignment of the disk can be limited to less than 0.025 mm. As air moves over the wall, the disk is allowed to move as the local wall shear and secondary forces dictate. A viscous damper filled with 10,000 cs oil is provided to limit oscillations of the disk. The entire device is sealed with respect

Contributed by the Fluids Engineering Division and presented at the Winter Annual Meeting, New York, N.Y., December 3–7, 1979, of THE AMERICAN SOCIETY OF MECHANICAL ENGINEERS. Manuscript received by the Fluids Engineering Division, February 12, 1979. Paper No. 79-WA/FE-22.

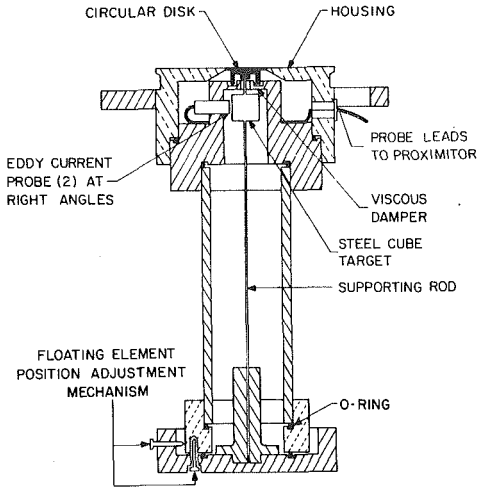

Fig. 1 Omnidirectional wall shear stress measurement device

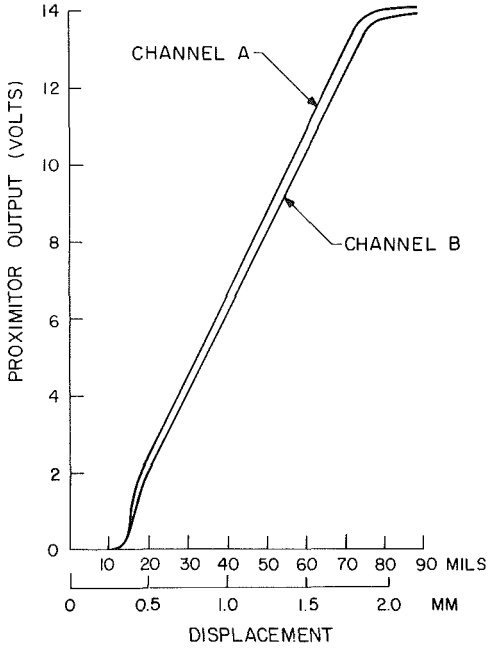

Fig. 2 Displacement calibration for eddy current proximity probes

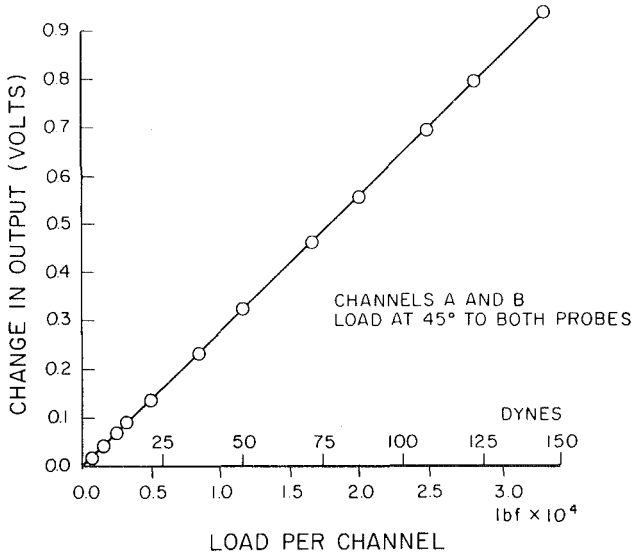

Fig. 3 Floating element static calibrations

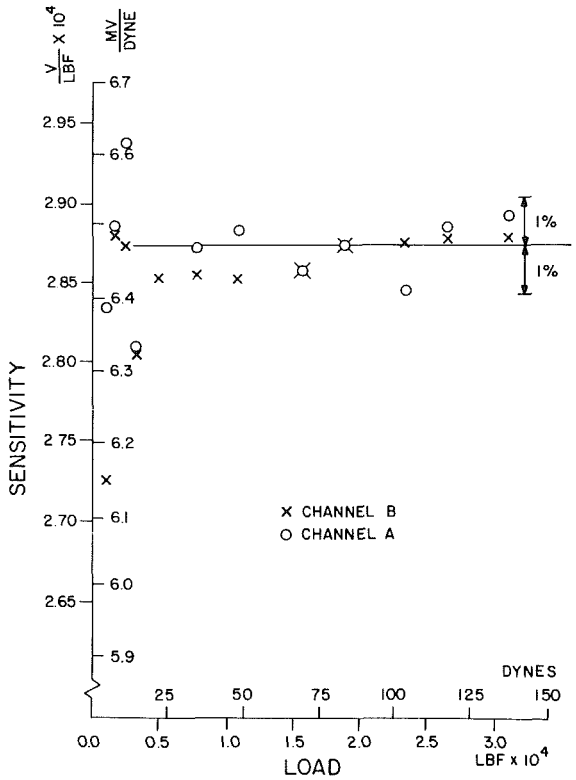

Fig. 4 Floating element sensitivities

to the environment to minimize flow through the gap between the disk and adjacent meter surface.

Two eddy current devices, labeled channels A and B, sense displacement of a 2.0 cm steel cube supported by the rod. These sensors are located at right angles and produce d-c voltage outputs whose resolution indicates both the magnitude and direction of the wall shear stress.

Characteristics of Operation

The floating element mechanism was modeled analytically using the Line Solution Developer (LSD) [32]. This computer program is based on line-solution technology (transfer matrices or initial parameter theory) that allows for an accurate static solution for the deformation of elastic solids. The complex coupling of shear and normal forces as well as bending moments can be modeled. Results indicate that the floating element mechanism should behave linearly over displacements substantially greater than designed in the meter. Eccentric moments due to weight imbalances in the target or disk, preexisting bends in the supporting rod, and

Nomenclature

C, K = constants
$\mathrm{Re}_{\mathrm{unit}}$ = unit Reynolds number at tunnel entrance, U/ν
u = local velocity
u^+ = $u/\sqrt{\tau_w/\rho}$
U = free-stream velocity
y = distance from the wall
y^+ = $y\sqrt{\tau_w/\rho}\,/\nu$
ρ = density
τ_w = wall shear stress
ν = kinematic viscosity

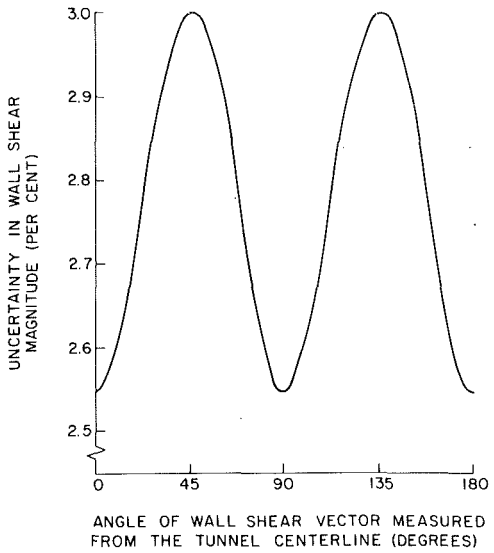

Fig. 5 Calculated uncertainty in wall shear magnitude measurements (estimated at 15:1)

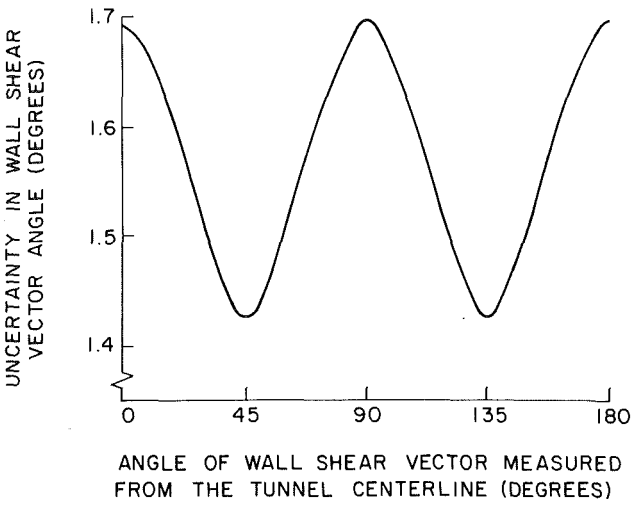

Fig. 6 Calculated uncertainty in wall shear vector angle measurements (estimated at 15:1)

the nulling method used in static calibration have no effect on the linearity or sensitivity of the mechanism.

Bently Nevada model 2388-3000 series eddy current proximitors and model 300 probes were chosen as displacement sensors. For this study, the drift characteristics were measured at constant temperatures to be 0.028 μm/5 min and 0.070 μm/5 min for channels A and B, respectively. This drift represents a change in the sensed load of less than 0.03 and 0.08 dynes/5 min for channels A and B, respectively.

Fig. 2 shows the effect of displacement on proximitor output. A steel target was displaced from each proximitor in 0.0254 mm increments using a precision micrometer. The proximitors are operated in the linear 5 to 8 volt range when installed.

Calibration-Static

The static calibration technique requires that small masses of predetermined weight be placed in a pan suspended by a thread connected through a pulley to a small post extending from the center of the floating element. Two vibrators are used on the pulley and calibration stand in order to minimize dry friction. The additional weight of the pan and thread is negated before the masses are added by adjusting the

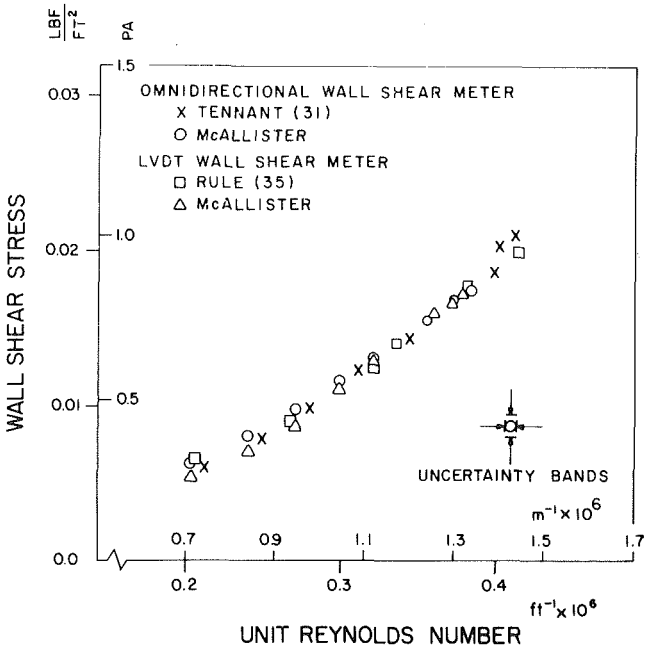

Fig. 7 Comparison of omnidirectional wall shear meter with LVDT Meter [35]

calibration stand level in order to recenter or rezero the floating element. By plotting the proximitor outputs versus the loading, calibration curves are obtained.

Fig. 3 shows a typical calibration curve. Using a least squares fit, the coefficient of determination (33), r^2, was calculated to be 0.9999. The values of r^2 may range from 0.0 to 1.0 and indicates how closely the linear relation fits the experimental data. The closer r^2 is to 1.0, the better the fit.

In Fig. 4, the sensitivity calculated for each calibration point is plotted verus load. Fig. 4 reveals that: 1) considerable more scatter in the data occurs for small loadings than larger loadings, 2) that the sensitivities for channels A and B are approximately the same at 6.469 mV/dyne, and 3) all data, except for loadings below 10 dynes, fall within a ± 2 percent error band while data above 25 dynes fall within a ± 1 percent error band. The increased scatter and uncertainty in the calibration sensitivities determined from the lighter loads are to be expected since dry friction and other secondary forces become large when compared with the load. For repeated calibration curves before and after use of the meter, proximitor sensitivities remain within one percent.

A Kline-McClintock [34] uncertainty analysis of wall shear stress magnitude and direction was completed. The uncertainties in signal conditioning, element area, relative probe alignment, and static calibration were considered in evaluating overall uncertainty in wall shear meaurements with the omnidirectional meter. If the wall shear vector, whose magnitude is assumed to be 0.85 Pa, is allowed to rotate 180 deg relative to the tunnel center line, the uncertainty in the magnitude and direction of wall shear stress can be plotted versus the angle of rotation, as shown in Figs. 5 and 6. The nonuniformity shown in Fig. 6 occurs when the shear force is aligned in the direction of either channel A or B. A 0.015 percent uncertainty due to drift and a fixed uncertainty of two percent due to disk misalignment with the meter housing are included with the Kline-McClintock results in Fig. 5. In Fig. 6 a 0.2 deg uncertainty due to drift and fixed uncertainties of one deg resulting from misalignment of the omnidirectional meter with the tunnel center line and one deg from disk misalignment with the meter housing are included with the Kline-McClintock results. Uncertainties associated with pressure gradients are currently being investigated.

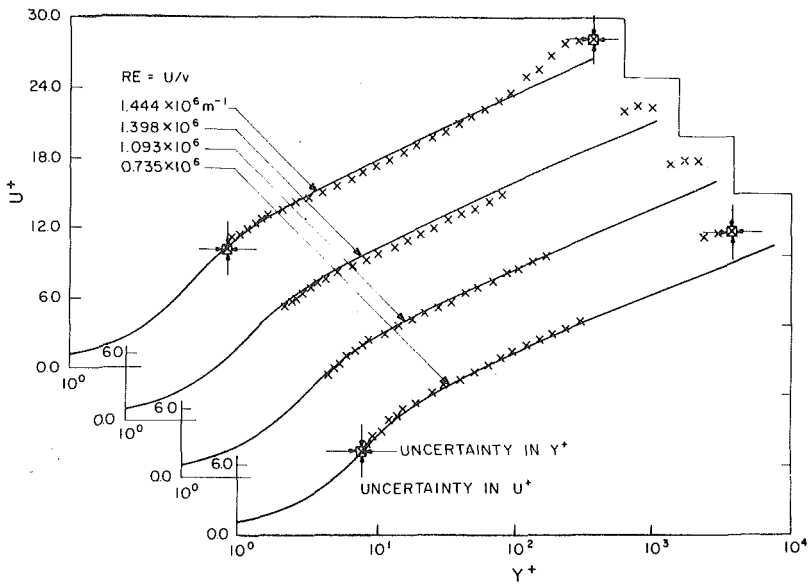

Fig. 8 Two-dimensional similarity plots (with uncertainty estimates at 20:1)

Calibration-Dynamic

At least for small to moderate pressure gradient flows, the ability of a device to measure the magnitude and direction of wall shear stress in three-dimensional flows may be tested in a two dimensional flow. In this case the shear meter is aligned so that each channel measures an approximately equal component of the local wall shear stress with both mangitude *and* direction of the wall shear stress calculated from the response of the two separate channels. This is the same procedure that is used in a three-dimensional case with the exception that in such a case with the approximate wall shear stress direction not known *a priori,* the force components on each channel would likely be different in magnitude. Thus, the resolution of both the wall shear stress magnitude *and* direction in a two-dimensional flow is an effective test of the instrument's capability to perform in a three-dimensional flow.

The omnidirectional floating element device was installed in a large-scale, low turbulence wind tunnel and subjected to a nominally two-dimensional flow. The device was carefully aligned so that each proximity probe was displaced 45 degrees from the tunnel center line. Wall shear stress and velocity profile measurements were obtained at various tunnel speeds. Seventeen wall shear measurements were taken. Since the flow was nominally two-dimensional, the wall shear angle should have been at 45 degrees to each proximitor. The maximum difference from 45 degrees was $+0.5$, -1.0 degrees with a mean average of -0.25 degrees and a standard deviation of 0.55 degrees. The maximum difference among wall shear measurements at any given unit Reynolds number was 2.5 percent, although the difference was typically less than one percent.

Using the same wind tunnel, Rule [35] obtained direct measurements of wall shear stress using the floating element device developed by Pierce and Krommenhoek [18]. Their device allows for movement of the floating element in one direction only, and utilizes an LVDT for sensing displacement. Comparison with Rule's data for varying unit Reynolds number is shown in Fig. 7. McAllister completed his measurements approximately 1½ years after Tennant and Rule. During this period, both floating element meters were disassembled, inspected, and realigned. Additionally, the method of proximitor output measurement was changed from VFC-counter combination to a more state-of-the-art, 5½ digit, d-c voltmeter with a slight increase in accuracy in this measurement. The repeatability in Fig. 7 shows each meter's reliability to obtain data without any dependence on a particular operator.

The law of the wall is well established for two-dimensional flows, and therefore provides a means of further verifying the omnidirectional wall shear meter measurements. Near-wall velocity data for a nominally two-dimensional, slightly negative pressure gradient (13.6 Pa/m) was carefully measured using a specially designed total pressure probe [35]. Two-dimensional similarity plots are shown in Fig. 8. The solid curves represent the two-dimensional similarity law in Spalding's third-order form [36] with NPL constants [37]. Spalding's law simply combines the law of the wall, given by equation (1), with the governing expression for the viscous sublayer region, $u^+ = y^+$, through an assumed smooth transition. The X's represent the velocity data non-dimensionlized by the measured values of wall shear stress. For measured wall shear values consistent with the law of the wall, the symbols and the solid curves coincide. Some of the velocity measurements between the logarithmic and wake regions were omitted to reduce data acquisition time.

Utilizing the Kline-McClintock [34] analysis again, uncertainties for the data shown in Fig. 8 can be determined. Considering the combined uncertainties in velocity probe location, manometer accuracy, drift, wall shear stress measurements, and the fixed uncertainties due to the circular disk's misalignment, uncertainty limits may be placed on each data point. Four such uncertainty bands are shown in Fig. 8.

Acknowledgments

Research for this paper was supported by a grant from the National Science Foundation.

References

1 Clauser, F., "Turbulent Boundary Layers in Adverse Pressure Gradients," *Journal of Aeronautical Science,* Vol. 21, No. 2, Feb. 1954, pp. 91–108.

2 Granville, P. S., "A Modified Law of the Wake for Turbulent Shear Layers," Naval Ship Research and Development Center - 4639, Bethesda, Md., May 1975.

3 Brown, K. C., and Joubert, P. N., "The Measurement of Skin Friction In Turbulent Boundary Layers with Adverse Pressure Gradients," *Journal of Fluid Mechanics,* Vol. 35, Part 4, 1969, pp. 732–757.

4 Dhawan, S., "Direct Measurements of Skin Friction," NACA TN 2567, 1952.

5 Dickinson, J., and Ozarapoglu, V., "The Determination of Turbulent Skin Friction," Progress Report DRB 9550-23 Universite Laval, Canada, 1969.

6 Everett, H. U., "Calibration of Skin Friction Balance Discs for Pressure Gradient," Defense Research Laboratory, DRL-426, CF-2708, Aug. 1958.

7 Fowke, J. G., "Development of a Skin-Friction Balance to Investigate Sources of Error in Direct Skin-Friction Measurements," M.S. thesis, University of Virginia, 1969.

8 Franklin, R. E., "A Force-Displacement Indicator for a Drag Balance," Ministry of Aviation, Aeronautical Research Council, C.P. No. 549, London, 1961.

9 Furuya, Y., Nakamura, I., Osaka, H., and Honda, H., "The Spanwise Non-Uniformity of Nominally Two-Dimensional Turbulent Boundary Layer II—Wall Shear Stress and Flow Field," *JSME Bulletin,* Vol. 18, July 1975, pp. 673–680.

10 Kempf, G., "Neue Ergebnisse der Widerstands forschung," *Werft Reederei Hafen,* Vol. 10, 1929, pp. 234–239.

11 Miller, B. L. P., "The Measurement of Wall Shearing Stress in Turbulent Boundary Layers," Ph.D. thesis, University of Leicester, Great Britain, Aug. 1972.

12 Morsy, M. G., "An Instrument for the Direct Measurement of the Local Shear Stress on Circular Cylinders," *Journal of Physics, Part E-Scientific Instruments,* Vol. 7, Feb. 1974, pp. 83–86.

13 Paros, J. M., "Application of the Force-Balance Principle to Pressure and Skin Friction Sensors," *16th Annual Technical Meeting Proceedings,* Institute of Environmental Science, 1970, pp. 363–368.

14 Schultz-Grunow, F., "New Frictional Resistance Law for Smooth Plates," NACA TM 956, 1950.

15 Smith, S. L., Lawn, C. J., and Hamlin, M. J., "The Direct Measurement of Wall Shear Stress in an Annulus," C.E. G.B. RD/B/N 1232, 1968.

16 White, J. K., and Franklin, R. E., "Measurements of Skin-Friction in an Annulus by the Floating Element Technique," A.R.C. 25 661, F.M. 3419, Feb. 24, 1964.

17 Pierce, F. J., and Gold, D. S., "Near-Wall Velocity Measurements for Wall Shear Inference in Turbulent Flows," *Flow Measurements in Open Channels and Closed Conduits,* NBS Special Publication 484, Vol. 2, Oct. 1977, pp. 621–648.

18 Pierce, F. J., and Krommenhoek, D. H., "Wall Shear Stress Diagnostics in Three-Dimensional Turbulent Boundary Layers," Interim Technical Report No. 2, ARO-D Project 6858E, Virginia Polytechnic Institute and State University, Sept. 1968.

19 Allen, J. M., "Experimental Study of Error Sources in Skin Friction Balance Measurements," ASME JOURNAL OF FLUIDS ENGINEERING, Vol. 99, Mar. 1977, pp. 192–204.

20 O'Donnell, F. B., Jr., "A Study of the Effect of Floating-Element Misalignment on Skin-Friction-Balance Accuracy," Defense Research Laboratory, DRL-515, CR-10, Mar. 1964.

21 Johnston, J. P., "On the Three-Dimensional Turbulent Boundary Layer Generated by Secondary Flow," ASME *Journal of Basic Engineering,* Vol. 82, Mar. 1960, pp. 233–248.

22 Coles, D., "The Young Person's Guide to the Data," *Proceedings Computation of Turbulent Boundary Layers - 1968,* AFOSR-IFP-Stanford Conference Vol. II, 1968, pp. 1–45.

23 East, L. F., and Hoxey, R. P., "Low-Speed Three-Dimensional Turbulent Boundary Layer Data," Parts I and 2, Aeronautical Research Council R & M 3653, Mar. 1969.

24 Hornung, H. G., and Joubert, P. N., "The Mean Velocity in Three-Dimensional Turbulent Boundary Layers," *Journal of Fluid Mechanics,* Vol. 15, Part 3, 1963, pp. 368–384.

25 Prahlad, T. S., "Wall Similarity in Three-Dimensional Turbulent Boundary Layers," *AIAA Journal,* Vol. 6, No. 9, 1968, pp. 1772–1774.

26 Perry, A. E., and Joubert, P. N.,, "A Three-Dimensional Turbulent Boundary Layer," *Journal of Fluid Mechanics,* Vol. 22, Part 2, 1965, pp. 285–304.

27 Chandrashekhar, N., and Swamy, N. V. C., "Wall Shear Stress Inference for Three-Dimensional Turbulent Boundary Layer Velocity Profiles," ASME *Journal of Applied Mechanics,* Vol. 43, Mar. 1976, pp. 20-27.

28 van den Berg, B., "The Law of the Wall in Two- and Three-Dimensional Turbulent Boundary Layers," National Aerospace Laboratory, The Netherlands, TR 72111 U, Jan. 1973.

29 Nash, J. F., and Patel, V. C., *Three Dimensional Turbulent Boundary Layers,* SBC Technical Books, 1972.

30 Chandrashekhar, N., "Some Studies on Three-Dimensional Turbulent Boundary Layers," PhD Dissertation, Department of Applied Mechanics, Indian Institute of Technology, Madras, India, Oct. 1974.

31 Tennant, M. H., "Near-Wall Similarity in Three-Dimensional Turbulent Boundary Layers," PhD dissertation, Virginia Polytechnic Institute and State University, Blacksburg, Va., Nov. 1977.

32 Pilkey, W. D., *Manual for the Response of Structural Members,* IIT Research Institute, Vols. I and II, Aug. 1969.

33 Burr, I. W., *Applied Statistical Methods,* Academic Press, 1974.

34 Kline, S. J., and McClintock, F. A., "Describing Uncertainties in Single-sample Experiments," *Mechanical Engineering,* Jan. 1953, p. 3.

35 Rule, J. A., Jr., "Near-Wall Similarity and Wall Shear Stress Measurements in a Two-Dimensional Wind Tunnel," M.S. thesis, Virginia Polytechnic Institute and State University, Blacksburg, Va., Aug. 1976.

36 Spalding, D. B., "A Single Formula for the Law of the Wall," ASME *Journal of Applied Mechanics,* Vol. 83, Sept. 1961, pp. 455–458.

37 Staff of the N.P.L., "On the Measurement of Local Surface Friction on a Flat Plate by Means of Preston Tubes," A.R.C. R & M 3185, May 1958.

Piston Vibration in Piston-Cylinder Systems

I. Etsion
Mem. ASME

M. Magen

Department of Mechanical Engineering,
Technion—Israel Institute of Technology,
Haifa, Israel

The motion of a cylindrical piston falling in a liquid filled vertical cylinder is analyzed. It is found that concentric motion is impossible and that flow induced vibration is always associated with such piston-cylinder systems. If the clearance over radius ratio is larger than a certain critical value, β_{cr}, severe wobble and piston-cylinder contact occurs. For clearance over radius ratio less than β_{cr} stable periodical oscillation with a constant amplitude takes place and the piston never contacts the cylinder wall. Reasonable agreement is achieved between the theoretical results and previous experimental observation.

Introduction

Piston-cylinder systems are widely used in fluids engineering applications. Among these are spool valves, piston pumps, various actuators, capsule-pipeline transportation, viscometers and timing devices, and, of recent interest, the free piston in some versions of the stirling engine.

Piston-cylinder systems have been analyzed in the past mainly with respect to hydraulic lock [1, 2], or leakage losses past the piston [3]. However, in all these analyses the piston is considered stationary. Few works that deal with moving pistons indicate some sort of fluctuations which may lead to unstable motion. In [4] a moving piston having a constant axial velocity is analyzed based on the assumption of steady state conditions. However, it is claimed that contact between the piston and cylinder wall is repeatedly occurring. The possibility of unstable piston motion is pointed out in [5] and shown experimentally in [6].

Unstable motion of pistons is also reported in [7]. In this experimental work pistons of length over radius ratio $L/r_0^* = 2$ were allowed to fall in a water filled vertical glass tube. It was found that cylindrical pistons can move within the tube stable or unstable depending on their clearance to radius ratio β. When the ratio β is smaller than a critical value β_{cr} the piston moves downward smoothly, however, when $\beta > \beta_{cr}$ wobble starts and the piston repeatedly hits the tube wall.

In still another experimental work [8], a periodical change in surface finish appearance during the process of hydrostatic extrusion of aluminum bars is reported. This uneven bamboo-type appearance of the surface could be the result of an unstable motion of the driving piston.

All these observations call for a rigorous dynamic analysis of pistons motion in cylinders. Previous analyses of stationary pistons or incomplete dynamic analyses like [5] cannot provide solutions to the real nature of piston motion. In all these analyses the fluid forces and moments exerted on the piston are obtained from solutions of the Reynolds equation of hydrodynamic lubrication [9]. In these solutions the clearance ratio β is neglected being usually very small.

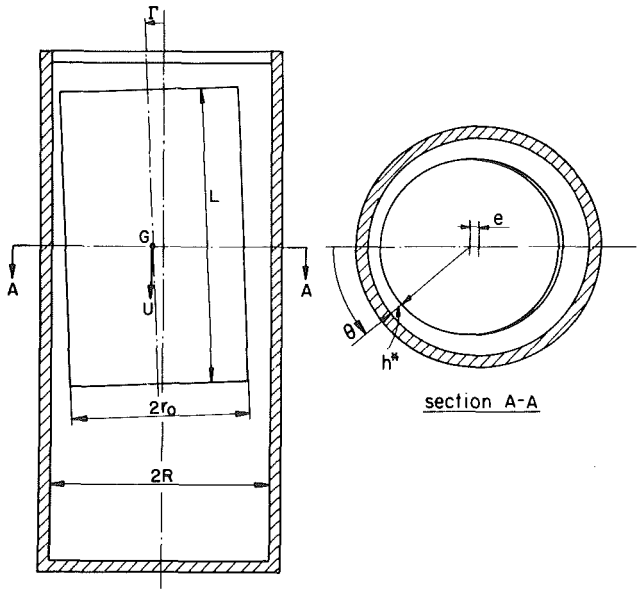

Fig. 1 Piston in cylinder

However, as was observed in [7] β is the main parameter affecting motion stability. Hence, it should be retained in any dynamic analysis of piston-cylinder system.

The aim of this work is to present a dynamic analysis for the motion of a cylindrical piston falling freely in a liquid filled vertical cylinder. The critical parameter β_{cr} will be found for various piston-cylinder-fluid combinations, and in the case of stable pistons the nature of their motion will be presented. The theoretical results will then be used to explain the experimental finding in [7].

The Modified Reynolds Equation

Consider the piston in Fig. 1 with a length over radius ratio $\alpha = L/r_0^*$, clearance ratio $\beta = C/r_0^*$, eccentricity e, and tilt angle relative to the tube axis Γ. The piston is falling in the fluid filled vertical cylinder with an axial velocity U and can oscillate in a plane containing the piston and cylinder axes.

Contributed by the Fluids Engineering Division for publication in the JOURNAL OF FLUIDS ENGINEERING. Manuscript received by the Fluids Engineering Division, June 27, 1979.

The normalized Navier-Stokes equations for the flow around the piston are in polar coordinates

$$\left.\begin{aligned} R_e\left[u_r\frac{\partial u_x}{\partial y}+0(\beta)\right] &= -6\frac{\partial p}{\partial x}+\frac{\partial^2 u_x}{\partial y^2}+\frac{\beta}{r}\frac{\partial u_x}{\partial y}+0(\beta^2) \\ \beta R_e\left[u_r\frac{\partial u_r}{\partial y}+0(\beta)\right] &= -6\alpha\frac{\partial p}{\partial y}+\beta\left[\frac{\partial^2 u_r}{\partial y^2}+\frac{\beta}{r}\frac{\partial u_r}{\partial y}+0(\beta^2)\right] \\ R_e\left[u_r\frac{\partial u_\theta}{\partial y}+0(\beta)\right] &= -6\frac{\alpha}{r}\frac{\partial p}{\partial \theta}+\frac{\partial^2 u_\theta}{\partial y^2}+\frac{\beta}{r}\frac{\partial u_\theta}{\partial y}+0(\beta^2) \end{aligned}\right\} \quad (1)$$

The continuity equation is in dimensionless form

$$\frac{\partial}{\partial y}(ru_r)+\beta\frac{\partial u_\theta}{\partial \theta}+\frac{\beta}{\alpha}r\frac{\partial u_x}{\partial x}=0 \quad (3)$$

Proper integrations of equations (2), using the no slip condition on the boundaries, give the components of the velocity vector $\mathbf{u}$ in the form

$$\left.\begin{aligned} u_x &= u'_x\left[1-\frac{\ln(1+\beta y)}{\ln(1+\beta h}\right]+\frac{3}{\beta}\frac{\partial p}{\partial x}\left[y\left(1+\beta\frac{y}{2}\right)-h\left(1+\beta\frac{h}{2}\right)\frac{\ln(1+\beta y)}{\ln(1+\beta h)}\right] \\ u_r &= u'_r\left[1-\frac{\ln(1+\beta y)}{\ln(1+\beta h\ )}\right] \\ u_\theta &= u'_\theta\left[1-\frac{\ln(1+\beta y)}{\ln(1+\beta h\ )}\right]-\frac{6\alpha}{\beta}\frac{\partial p}{\partial \theta}\left[y-h\frac{\ln(1+\beta y)}{\ln(1+\beta h\ )}\right] \end{aligned}\right\} \quad (4)$$

The dimensionless fluid velocity vector is $\mathbf{u} = \beta\mathbf{u}^*/V$ where V is a characteristic velocity. The dimensionless pressure is $p = p^*/P_s$ where P_s is the axial driving force divided by the piston cross section area. Hence,

$$P_s = L(\rho_p-\rho_f)g$$

The characteristic velocity V is related to P_s by

$$V=\frac{C^3}{6\mu r_0^* L}P_s$$

and the Reynolds number Re is

$$\mathrm{Re}=\rho_f\frac{Vr_0^*}{\mu}$$

Thus for typical clearances, C, Re $<<$ 1. Applying the assumptions of lubrication theory [9], but retaining terms of order β in (1), we have

$$\left.\begin{aligned} \frac{\partial^2 u_x}{\partial y^2}+\frac{\beta}{r}\frac{\partial u_x}{\partial y} &= 6\frac{\partial p}{\partial x} \\ \frac{\partial^2 u_r}{\partial y^2}+\frac{\beta}{r}\frac{\partial u_r}{\partial y} &= 0 \\ \frac{\partial^2 u_\theta}{\partial y^2}+\frac{\beta}{r}\frac{\partial u_\theta}{\partial y} &= 6\frac{\alpha}{r}\frac{\partial p}{\partial \theta}. \end{aligned}\right\} \quad (2)$$

In equation (4) $\mathbf{u}'$ is the dimensionless velocity vector of an arbitrary point (x, θ) on the piston surface. Using a dimensionless axial velocity of the piston in the form $\lambda = U/V$, a dimensionless eccentricity $\epsilon = e/C$, and a dimensionless tilt $\gamma = \Gamma L/2C$, and noting that the tilt angle Γ is very small, the components of $\mathbf{u}'$ are

$$\left.\begin{aligned} u'_x &= \beta\left(\lambda+\frac{\beta}{\alpha^2}\dot{\epsilon}\gamma-\frac{\dot{\gamma}}{\alpha^2}\cos\theta\right) \\ u'_r &= \frac{\beta}{\alpha}\left[-2\beta\lambda\gamma+\frac{1}{2}(\dot{\epsilon}+2\dot{\gamma}x)\right]\cos\theta \\ u'_\theta &= \frac{\beta}{\alpha}\left[2\beta\lambda\gamma-\frac{1}{2}(\dot{\epsilon}+2\dot{\gamma}x)\right]\sin\theta \end{aligned}\right\} \quad (5)$$

Substituting equations (4) and (5) into equation (3) integrating and neglecting terms of $0(\beta^2)$ we finally have the modified Reynolds equation in the form

$$\begin{aligned} \frac{\partial}{\partial x}\left[h^3\left(1+\frac{\beta h}{2}\right)\frac{\partial p}{\partial x}\right]+\alpha^2\frac{\partial}{\partial \theta}\left[h^3\left(1-\frac{\beta h}{2}\right)\frac{\partial p}{\partial \theta}\right] = \\ (4\beta\lambda\gamma-\dot{\epsilon}-2\dot{\gamma}x)\ \cos\theta+\beta\left(\lambda-\frac{\dot{\gamma}}{\alpha^2}\cos\theta\right)\frac{\partial h}{\partial x} \\ -\frac{\beta}{2}(\dot{\epsilon}+2\dot{\gamma}x)\frac{\partial}{\partial \theta}(h\ \sin\theta) \end{aligned} \quad (6)$$

In equation (6) h is a dimensionless film thickness $h = h^*/C$.

Nomenclature

C = radial clearance, $R - r_0^*$
e = eccentricity
F^* = force
F = dimensionless force, $F^*/\pi r_0^{*2}P_s$
h^* = film thickness
h = dimensionless film thickness, h^*/C
$h_{\min}$ = time dependent dimensionless minimum film thickness
h_{mm} = lowest value of $h_{\min}$ during periodical oscillation
I^* = piston moment of inertia
L = piston length
M^* = moment
M = dimensionless moment, $M^*/\pi r_0^{*2}L\,P_s$
m^* = piston mass
m = dimensionless mass $m^*V^2/2\pi r_0^{*2}L\,P_s\beta$
N = number of piston lengths travelled by piston during one complete cycle of stable motion
n = system parameter, $\rho_p(\rho_p-\rho_f)gr_0^{*3}/72\,\mu^2$
P_s = driving force per unit cross section area, $L(\rho_p-\rho_f)g$
p^* = pressure
p = dimensionless pressure, p^*/P_s
p_e = dimensionless pressure differential across piston
q = leakage
R_e = Reynolds no., $\rho_f Vr_0^*/\mu$
r^* = radius
r = dimensionless radius,

Its expression, accurate up to an order β, is

$$h = 1 - (\epsilon + 2\gamma x)\ \cos\theta - \frac{\beta}{2}(\epsilon + 2\gamma x)^2\ \sin^2\theta \tag{7}$$

The boundary conditions of equation (6) are

$$p = 0 \text{ at } x = -1/2$$

$$p = p_e \text{ at } x = 1/2$$

where p_e is a dimensionless pressure differential across the piston. Also because of symmetry about the plane of motion we have

$$\frac{\partial p}{\partial \theta} = 0$$

$$\text{at } \theta = 0 \text{ and at } \theta = \pi$$

The Governing Equations of Piston Motion

Pressures and shear stresses produce forces and moments on the piston which together with the buoyancy and gravity control the piston motion. Consider a coordinate system $ON_1N_2N_3$ fixed to the cylinder axis (see Fig. 2). The piston is moving in the plane ON_1N_2, hence, the force vector in this system has the components F_1^* F_2^* while the moment vector has only one component M_3^*. If τ_x^* and τ_θ^* are the axial and tangential shear stresses, respectively, and p^* is the pressure on a surface element ds, then

$$\left.\begin{aligned} F_1^* &= \int_s [\tau_x^*\ \cos\Gamma + (\tau_\theta^*\ \sin\theta + p^*\ \cos\theta)\ \sin\Gamma]ds - \pi r_0^{*2} p_e^*\ \cos\Gamma \\ F_2^* &= \int_s [\tau_x^*\ \sin\Gamma - (\tau_\theta^*\ \sin\theta + p^*\ \cos\theta)\ \cos\Gamma]ds - \pi r_0^{*2} p_e^*\ \sin\Gamma \\ M_3^* &= -\int_s [(p^* x^* + \tau_x^* r_0^*)\ \cos\theta + \tau_\theta^* x^*\ \sin\theta]ds \end{aligned}\right\} \tag{8}$$

Evaluating the shear stress on the piston surface and neglecting terms of order β^2 we have [10]

$$\left.\begin{aligned} F_1 &= -p_e - \frac{\beta}{\pi}\int_0^\pi \int_{-1/2}^{1/2} \left(h\frac{\partial p}{\partial x} - 4\gamma p\ \cos\theta\right) dx d\theta \\ F_2 &= -\frac{2\alpha}{\pi}\int_0^\pi \int_{-1/2}^{1/2} \left(p\ \cos\theta - \frac{\beta h}{2}\frac{\partial p}{\partial \theta}\sin\theta\right) dx d\theta - \frac{2\beta\gamma}{\alpha} p_e \\ M_3 &= -\frac{2\alpha}{\pi}\int_0^\pi \int_{-1/2}^{1/2} \left[\left(px - \frac{\beta}{2\alpha^2} h\frac{\partial p}{\partial x}\right)\cos\theta - \frac{\beta h}{2} x\frac{\partial p}{\partial \theta}\sin\theta\right] dx d\theta \end{aligned}\right\} \tag{9}$$

The three equations of motion are

$$m^* \dot{U}^* = F_1^* + W^*$$

$$m^* \ddot{e} = F_2^*$$

$$I^* \ddot{\Gamma} = M_3^*$$

where I^*, the piston moment of inertia, is $I^* = m(L^2/12 + r_0^{*2}/4)$.

Using the dimensionless forces, moment, axial velocity λ, and a dimensionless time in the form

$$t = \frac{V}{2L\beta} t^*$$

the dimensionless equations of motion become

$$\left.\begin{aligned} m\dot{\lambda} &= F_1 + 1 \\ m\ddot{\epsilon} &= 2\alpha F_2 \\ m\ddot{\gamma} &= \frac{12\alpha^3}{3 + \alpha^2} M_3 \end{aligned}\right\} \tag{10}$$

Substituting (9) in (10) we obtain three equations with four time dependent unknowns ϵ, γ, λ, and p_e. The fourth equation needed to complete the set is obtained from the flow rate pass the piston. Consider a control volume ABCD as in Fig. 3. The rate of change of pitson's volume in this control volume equals the leakage across the section AB. Hence,

$$\pi r_0^{*2}(U\ \cos\Gamma + \dot{e}\ \sin\Gamma) = -q \tag{11}$$

The leakage q across the section AB is the same as the leakage across any section parallel to AB. Thus,

$$q = \int_{r_o^*}^{r_o^* + h^*} \int_0^{2\pi} (u_x^*)_{x^*=0} r^* d\theta dr^* \tag{12}$$

Nomenclature (cont.)

r^*/r_0^*
r_0^* = piston radius
R = cylinder radius
t^* = time
t = dimensionless time, $Vt^*/2L\beta$
t_p = dimensionless period time
U = axial velocity
$\mathbf{u}^*$ = velocity vector
$\mathbf{u}$ = dimensionless velocity vector, $\beta\mathbf{u}^*/V$
$\mathbf{u}'$ = dimensionless velocity vector on piston surface
V = characteristic velocity, $C^3 P_s/6\mu r_0^* L$
W^* = driving force, $\pi r_0^{*2} L(\rho_p - \rho_f)g$
x^*, y^* = coordinates
x, y = dimensionless coordinates, x^*/L, y^*/C
α = length ratio, L/r_0^*
β = clearance ratio, C/r_0^*
Γ = tilt angle
γ = dimensionless tilt angle, $\Gamma L/2C$
δ = $\alpha[(1 - \beta/2)/(1 + \beta/2)]^{1/2}$
ϵ = dimensionless eccentricity, e/C
θ = angular coordinate measured from plane of minimum film thickness
λ = dimensionless axial velocity, U/V
μ = viscosity
ρ_f = fluid density
ρ_p = piston density
τ^* = shear stress
τ = dimensionless stress, τ^*/P_s

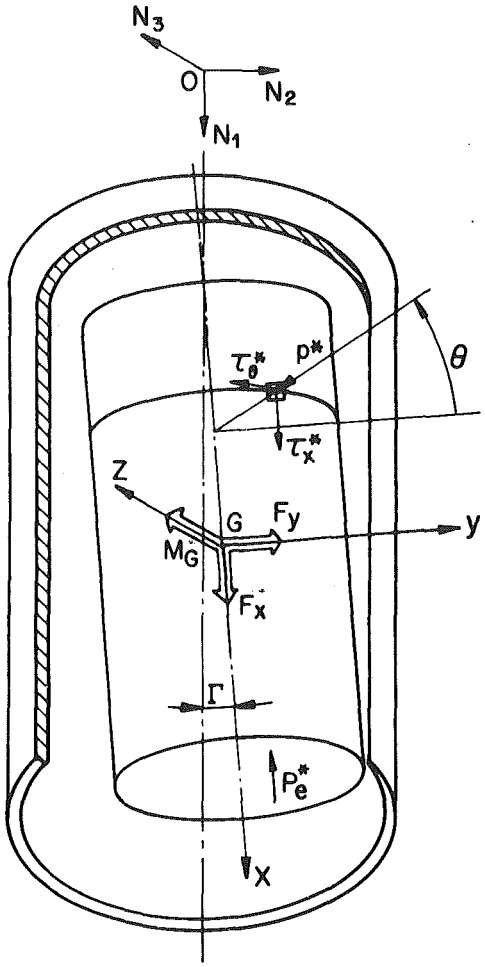

Fig. 2 Pressure and shear stress components

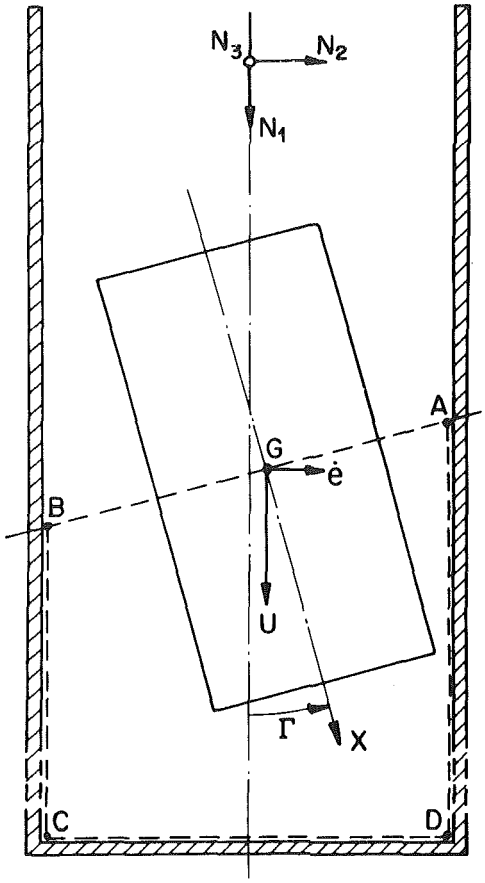

Fig. 3 Control volume for leakage calculation

Substituting equation (12) in (11) and using equations (4) and (5) for $(u_x)_{x=0}$, integrating over y, and neglecting terms of order β^2, we finally obtain

$$\frac{1}{\pi}\int_0^{\pi}\left[h^3\left(1+\frac{\beta h}{2}\right)\frac{\partial p}{\partial x}\right]_{x=0}d\theta=\lambda(1+\beta)+\frac{\beta\gamma}{\alpha^2}\dot{\epsilon}+\frac{\beta}{2\alpha^2}\epsilon\dot{\gamma} \tag{13}$$

Equations (9), (10), (13) and equation (6) with its boundary conditions completely define the functions ϵ, γ, p_e and λ.

Motion Stability

The modified Reynolds equation, equation (6), gives the pressure p as a function of ϵ, γ, λ, and p_e which are all time dependent. The pressure p can then be used in (9) to find F_1, F_2, and M_3 which are substituted in (10). Equations (10) and (13) are then solved simultaneously giving ϵ, γ, λ, and p_e as functions of the time t. This approach is straightforward, but very costly in terms of computer time. Hence, we shall examine cases where analytical solution of the modified Reynolds equation are possible. One such case is that of small perturbations about the concentric equilibrium position of the piston. The other case is that of a short piston where the circumferential pressure gradient in (6) can be neglected compared to the axial one [11].

Small Perturbation Analysis. Consider the case of a concentric piston, that is $\epsilon = \gamma = 0$. Under these conditions we have $h = 1$, axisymmetry prevails and equation (6) becomes

$$\left(1+\frac{\beta}{2}\right)\frac{\partial^2 p_0}{\partial x^2}=0$$

Hence

$$p_0 = p_{e0}\left(x+\frac{1}{2}\right)$$

where p_0 and p_{e0} are the pressure distribution and pressure differential, respectively, for the concentric case.

From equations (9) we obtain

$$F_1 = -p_{e0}(1+\beta)$$

and

$$F_2 = M_3 = 0$$

which by substituting in (10) give

$$1 - p_{e0}(1+\beta) = 0$$

From (13) we have

$$p_{e0}\left(1+\frac{\beta}{2}\right)=\lambda_0(1+\beta)$$

Hence, for $\beta^2 << 1$

$$p_{e0} = 1-\beta \tag{14}$$

$$\lambda_0 = 1-\frac{3}{2}\beta \tag{15}$$

From (14) and (15), it is clear that the concentric position is an equilibrium one with p_{e0} and λ_0 constants. Assuming small perturbations ϵ and γ about this equilibrium, that is

$$\lambda = \lambda_0 + \lambda_1 = 1 - \frac{3}{2}\beta + \lambda_1$$

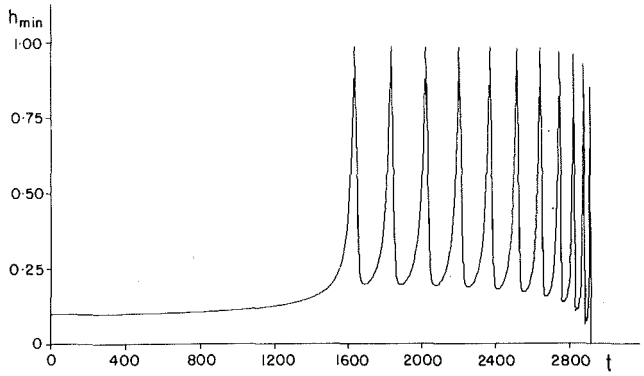

Fig. 4 Minimum film thickness, h_{min}, as function of time. Unstable piston $\beta > \beta_{cr}$

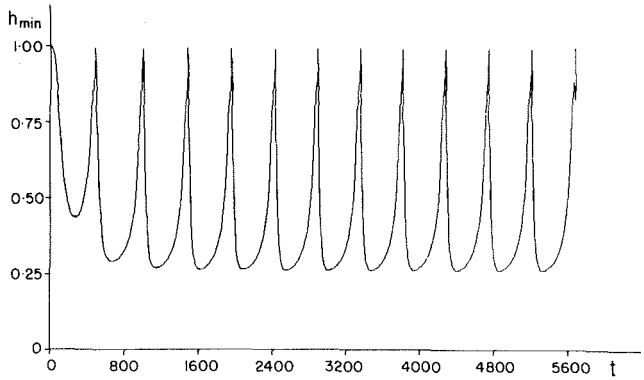

Fig. 5 Minimum film thickness, h_{min}, as function of time. Stable piston $\beta < \beta_{cr}$

$$p_e = p_{e0} + p_{e1} = 1 - \beta + p_{e1}$$

$$h = h_0 + h_1 = 1 + h_1$$

$$p = p_0 + p_1 = (1-\beta)\left(x + \frac{1}{2}\right) + p_1$$

where λ_1, p_{e1}, h_1, and p_1 are very small compared to unity as ϵ and λ are. Equation (6) can now be solved analytically [12]. The pressure p is substituted in (9) and (13) which, after linearization give a set of four linear equations. Solving this set it can be shown [12] that the perturbations ϵ_1 and γ_1 are increasing in time. That is, the equilibrium of the concentric position is unstable.

Short Piston Finite Perturbations. As was shown by the small perturbations analysis the concentric position is unstable. Thus, two possible cases exist. A stable case where the piston oscillates with constant amplitudes of ϵ and γ without touching the cylinder, and an unstable case where the oscillation amplitude increases in time until the piston hits the cylinder wall. Evidently, finite perturbations analysis is needed but the problem can be simplified by assuming a short piston, thus, enabling analytical solution of equation (6).

For short pistons $\alpha^2 << 1$ hence, by neglecting terms of order α^2 and β compared to unity but retaining terms of order β/α^2 equation (6) becomes

$$\frac{d}{dx}\left(h^3 \frac{dp}{dx}\right) = -\left(\dot{\epsilon} + 2\dot{\gamma}x - \frac{2\beta}{\alpha^2}\gamma\dot{\gamma}\cos\theta\right)\cos\theta \qquad (16)$$

The boundary conditions for equation (16) are

$$p = 0 \quad \text{at} \quad x = -1/2$$

and

$$p = p_e \quad \text{at} \quad x = 1/2$$

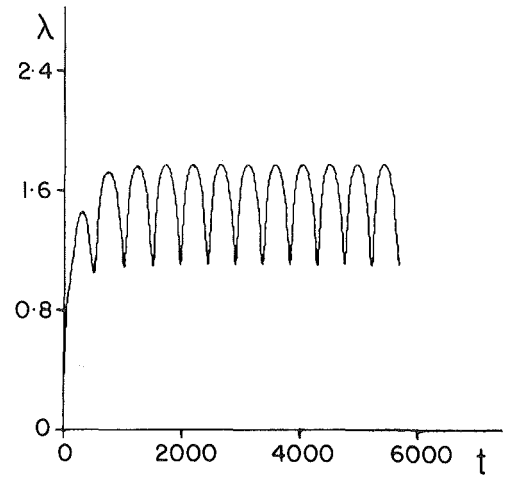

Fig. 6 Dimensionless axial speed, λ, as function of time. Stable piston $\beta < \beta_{cr}$

The film thickness, with terms of order β neglected, is

$$h = 1 - (\epsilon + 2\gamma x)\cos\theta \qquad (17)$$

In order to simplify the writing we shall define the parameters

$$s = \frac{\gamma\cos\theta}{1 - \epsilon\cos\theta}$$

$$h' = 1 - 2sx$$

$$\delta_1 = \gamma^3\cos^2\theta$$

$$\delta_2 = \frac{\alpha^2\gamma^2}{2\beta}\cos\theta$$

Using these parameters equation (16) can be written in the form

$$\frac{d}{dx}\left(h'^3 \frac{dp}{dx}\right) = -\frac{s^3}{\delta_1}(\dot{\epsilon} + 2\dot{\gamma}x) + \frac{s^3}{\delta_2}\dot{\gamma} \qquad (18)$$

The solution of (18) with the proper boundary conditions of (16) is

$$p = p_e \frac{(1-s)^2}{4s}\left[\left(\frac{1+s}{h'}\right)^2 - 1\right] + \frac{s}{8}\left(\frac{\dot{\epsilon}}{\delta_1} - \frac{\dot{\gamma}}{\delta_2}\right)\left(\frac{2}{h'} - \frac{1-s^2}{h'^2} - 1\right) + \frac{\dot{\gamma}}{8\delta_1}\left\{\frac{2}{h'} - \frac{1-s^2}{h'^2} - 1 + \ln h' + \frac{1}{s}\left(\frac{1-s^2}{2h'}\right)^2 \ln\frac{1+s}{1-s} + \frac{1}{4s}[(1-s)^2\ln(1+s) - (1+s)^2\ln(1-s)]\right\} \qquad (19)$$

Substituting equation (19) in (9), neglecting terms of order β compared to β/α^2, integrating and using equations (13) and (10) give a set of four nonlinear differential equations [10] for the time dependent variables $\gamma, \epsilon, \lambda$, and p_e. This set is solved numerically [12] using Runge-Kutta technique and the functions γ, ϵ, λ, and p_e are obtained for each time point t.

From (17) it is clear that the minimum film thickness, h_{min}, between the piston and cylinder wall occurs at either $\theta = 0$ or $\theta = \pi$ and at $x = 1/2$ or $x = -1/2$, Hence, the time dependent function h_{min} is

$$h_{min}(t) = 1 - |\epsilon(t)| - |\gamma(t)| \qquad (20)$$

The criterion for stable motion is $h_{min} > 0$ at all t. If h_{min} vanishes, that means piston-cylinder contact and such case is considered an unstable.

Table 1 Summary of the results for stable motion
$\alpha = 0.5$

n	m	$\beta \times 10^3$	ϵ_{max}	$\gamma_{max} \times 10^3$	h_{mm}	λ_{av}	N
10^{10}	2	10.0	0.890	47.0	0.110	2.06	132
	4	11.5	0.904	49.6	0.096	2.08	157
	6	12.5	0.911	50.7	0.089	2.09	183
	8	13.2	0.917	51.7	0.083	2.10	203
	10	13.8	0.920	52.6	0.080	2.10	220
	12	14.3	0.925	53.4	0.076	2.10	238
	14	14.8		Unstable, $\beta = \beta_{cr}$			
10^8	2	25.1	0.914	63.8	0.086	2.06	334
	4	28.9	0.921	65.4	0.079	2.09	376
	6	31.3	0.926	66.1	0.074	2.10	422
	8	33.1	0.929	66.6	0.071	2.10	457
	10	34.7	0.932	67.0	0.068	2.11	492
	12	35.9	0.934	67.4	0.066	2.11	528
	14	37.1		Unstable, $\beta = \beta_{cr}$			

Results and Discussion

Examples of two cases, one unstable the other stable, are presented in Figs. 4 and 5 which show the time behavior of h_{min}. The pistons in both cases have length over radius ratio $\alpha = 2$ and a system parameter $n = 10^8$ where n is defined as

$$n = m\frac{\alpha}{\beta^5} \tag{21}$$

The parameter n is used to eliminate the effect of β in m which by

$$m^* = \pi r_0^2 L \rho_p$$

and by the definition of P_s and V is given as

$$m = \frac{\rho_p(\rho_p - \rho_f)g}{72\mu^2} r_0^{*} \frac{\beta^5}{\alpha} \tag{22}$$

Hence, from (21) and (22)

$$n = \frac{\rho_p(\rho_p - \rho_f)}{72\mu^2} g r_0^{*3} \tag{23}$$

The only difference between the two cases shown in Figs. 4 and 5 is in the clearance parameter β. The unstable piston has $\beta = 0.058$ while the stable one has a slightly smaller value $\beta = 0.056$. These two cases were chosen to demonstrate the critical value β_{cr} which for $\alpha = 2$ and $n = 10^8$ is about $\beta_{cr} = 0.057$. In the case shown in Fig. 4, where $\beta > \beta_{cr}$, the minimum film thickness h_{min} vanishes at $t = 2900$. In the other case, Fig. 5, where $\beta < \beta_{cr}$ the piston oscillates periodically with h_{min} always larger than a certain value h_{mm} which remains constant in time and is $h_{mm} = 0.26$. Fig. 6 presents the time variation in λ for the stable piston and it is seen that oscillation about an average velocity $\lambda = 1.3$ takes place. Figs. 5 and 6 are typical of any stable case that is, whenever $\beta < \beta_{cr}$ a periodical motion takes place.

The falling distance of a stable piston along the cylinder axis during one period can be calculated from

$$N = \frac{1}{L}\int_0^{t_p^{*}} U dt^* \tag{24}$$

where N is a dimensionless distance expressed as the number of piston's lengths travelled during one period. Using the normalized velocity and time equation (24) becomes

$$N = 2\beta \int_0^{t_p} \lambda dt \tag{25}$$

About 50 different cases were examined. These include pistons of length over radius ratios $\alpha = 0.5$ and $\alpha = 2$, and system parameters values $n = 10^8$ and $n = 10^{10}$. At each combination of α and n various clearance parameters β were analyzed starting from large β which assures unstable motion, $h_{min} = 0$. The parameter β was then gradually decreased until the first value of β that gives stable motion was found. A search for β_{cr} was then performed in the interval between the β values corresponding to the last unstable and first stable case. After β_{cr} was found some more stable cases with $\beta < \beta_{cr}$ were examined. The values of ϵ_{max} and γ_{max} corresponding to the amplitudes of $\epsilon(t)$ and $\gamma(t)$, respectively, where found along with the value h_{mm} which gives the minimum film thickness during the periodical oscillation. Also the average velocity λ_{av}, and the dimensionless falling distance N corresponding to the period time t_p were calculated. The results of 24 stable cases are presented in Table 1 for pistons of $\alpha = 0.5$ and in Table 2 for pistons of $\alpha = 2$. The critical values β_{cr} are also indicated for each set of α and n.

From the tables it can be seen that as β decreases the oscillation amplitudes of ϵ and γ decrease too and h_{mm} increases as expected. Also as β decreases the average velocity λ_{av} and the falling distance N during one period decrease.

An interesting result is the small value of γ_{max} which indicates that the piston oscillates while its axis remains almost parallel to the cylinder axis. For $\alpha = 0.5$ the amplitude of ϵ is quite large, in the range of 0.9 for all values of β examined. The critical value β_{cr} is $\beta_{cr} = 0.015$ for $n = 10^{10}$ and $\beta_{cr} = 0.037$ for $n = 10^8$. The average axial velocity is about twice its value in a concentric position.

For $\alpha = 2$ the amplitudes of both ϵ and γ are smaller, ϵ_{max} is in the range of 0.6 to 0.7 and γ_{max} is almost zero. Since the oscillation amplitude is smaller than in the case $\alpha = 0.5$ the average velocity λ_{av} is closer to unity, being only 50 percent higher than the concentric piston velocity.

Although the finite perturbations analysis assumes short piston, that is, small α, results for $\alpha = 2$ were also obtained to enable comparison with the experiments reported in [7]. The validity of the results for $\alpha = 2$ can be evaluated based on the results in [11] where it is found that for $\gamma = 0$ the short piston analysis can be used as a good approximation for finite pistons provided the eccentricity ϵ is not too large. For $\alpha = 2$ the upper limit of ϵ for valid approximation is according to [11] around 0.7. Hence, the results obtained here are considered acceptable for the stable cases when $\gamma_{max} \simeq 0$ and $\epsilon_{max} < 0.7$. However, the accurate value of β_{cr} is somewhat suspected for $\alpha = 2$ since at $\beta = \beta_{cr}$ $h_{min} = 0$ and neither γ nor ϵ are small.

Another difficulty in comparing the present analytical results with these of ref. [7] is due to a very slow convergence of the numerical solution at $\alpha = 2$ when $m < 8$. The piston-cylinder system in [7] had $n = 3.7 \times 10^6$ for which a critical clearance parameter β_{cr} was found between 0.0179 and 0.0264. Hence, from $m = n\beta^5/\alpha$, even for $\beta = 0.0264$ the dimensionless mass in [7] was only $m = 0.024 << 8$. In the case of very small values m the solution of the set of eqs. (10) requires singular perturbation approach [13]. This, however, would exceed the space limitation of a single paper.

In trying to overcome the above mentioned difficulty it was found that the most important parameter affecting convergence of the numerical solution is m. When plotting h_{mm} versus m, a critical value m_{cr} can be found similar to β_{cr}. That is whenever $m > m_{cr}$ the piston is unstable and whenever $m < m_{cr}$ the piston is stable. However, as opposed to β_{cr}, the critical value m_{cr} is not very much affected by the system parameter n. Figure 7 presents results of h_{mm} as function of m. As can be seen from the figure at $\alpha = 0.5$ $m_{cr} = 14$ and at $\alpha = 2$ $m_{cr} = 32$ almost regardless of n. This interesting finding enables one to obtain the value of β_{cr} for any desired n from an already know β_{cr}^{*} corresponding to n^*.

Since for a given α, $m_{cr} = m_{cr}^{*}$ and is independent on n we have from (21)

$$n\beta_{cr}^5 = n^*\beta_{cr}^{*5}$$

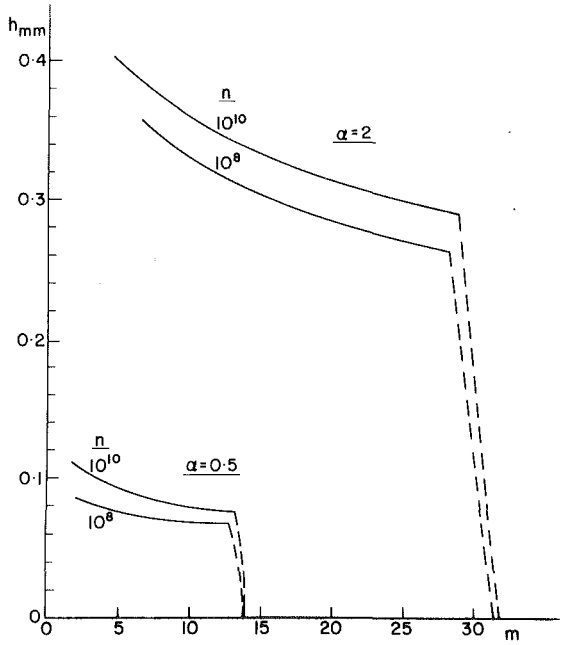

Fig. 7 Dimensionless minimum clearance, h_{min}, as function of dimensionless mass, m

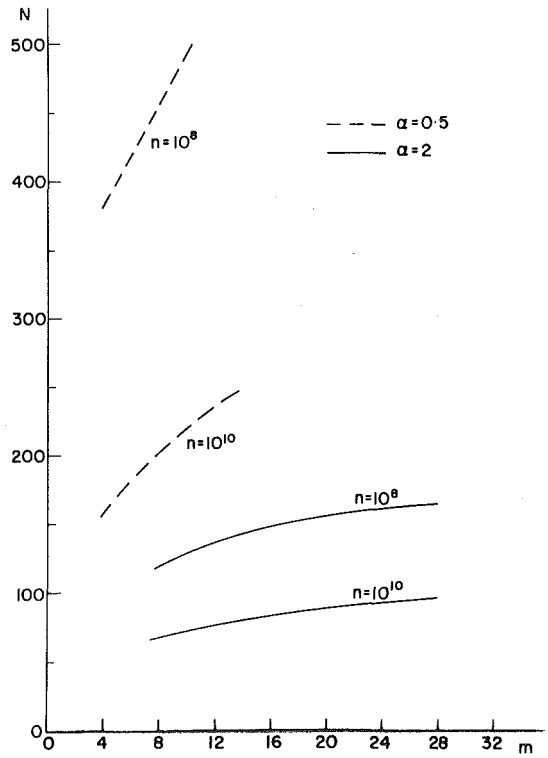

Fig. 8 Dimensionless falling distance, N, in each period as function of dimensionless mass, m

or

$$\beta_{cr} = \beta^*_{cr}\left(\frac{n^*}{n}\right)^{1/5} \tag{26}$$

Using this approach one would find for $n = 3.7 \times 10^6$ and $\alpha = 2$ a value $\beta_{cr} = 0.11$ which is about 4 times higher than β_{cr} found in [7]. This discrepency is probably due to a large error introduced by the short piston approximation as h_{mm} approaches zero. Nevertheless, for the stable cases where ϵ_{max} does not exceed 0.7 the results of the short piston approximation seem to be reasonably valid even at $\alpha = 2$.

Table 2 Summary of the results for stable motion
$\alpha = 2.0$

n	m	$\beta \times 10^3$	ϵ_{max}	$\gamma_{max} \times 10^3$	h_{mm}	λ_{av}	N
10^{10}	8	17.4	0.627	2.05	0.373	1.44	66.9
	12	18.9	0.654	2.14	0.347	1.48	75.7
	16	20.0	0.671	2.19	0.329	1.50	82.2
	20	20.9	0.686	2.23	0.314	1.52	87.5
	24	21.7	0.698	2.26	0.302	1.53	91.8
	28	22.4	0.708	2.30	0.292	1.54	95.2
	32	23.0		Unstable, $\beta = \beta_{cr}$			
10^8	8	43.7	0.658	3.27	0.342	1.49	121
	12	47.4	0.683	3.37	0.317	1.52	135
	16	50.2	0.701	3.43	0.299	1.54	146
	20	52.5	0.715	3.50	0.285	1.55	154
	24	54.5	0.727	3.56	0.273	1.56	160
	28	56.2	0.737	3.64	0.263	1.56	163
	32	57.7		Unstable, $\beta = \beta_{cr}$			

Fig. 8 presents the dimensionless falling distance, N, in each complete cycle. The variation of N is almost linear having a decreasing slope as n or α increase. The distance travelled during each complete cycle is quite large being at $\alpha = 2$, for example, always greater than 50. As n decreases the distance N increases.

In [7] pistons about 1.5 cm long were released in a water filled vertical tube and their motion examined along a falling distance of about 50 cm. When β was less than the critical value no evidence of any oscillation was detected and it was concluded that for $\beta < \beta_{cr}$ the pistons were moving smoothly down the tube. The present analytical results are in line with this observation since the falling distance in [7] was only about 30 piston lengths while the calculated N for the tests with $n = 10^6$ is at least 150. Hence, in [7] the falling distance was only 20 percent of one complete cycle and since $\gamma \simeq 0$ (see Table 2) the change in ϵ could not be noticed over the short distance examined.

Conclusions

The governing equations for the motion of a piston closely fitted in a cylinder are derived based on the assumptions of lubrication theory. It is found that a piston driven by an axial force in a cylinder filled with an incompressible fluid has an equilibrium in the concentric position provided the axial force is the only external force acting on it. However, this equilibrium is unstable and as a result concentric motion is impossible, leading to an oscillating motion.

Stability of the oscillations is determined by a critical value of the clearance ratio β_{cr}. If $\beta > \beta_{cr}$ the oscillation amplitude increases in time. If $\beta < \beta_{cr}$, stable oscillation with constant amplitude takes place. In this case the piston is moving almost parallel to the cylinder axis changing its eccentricity periodically. The distance travelled by the piston during one complete cycle is usually very long being of the order 10^2 of its length.

The short piston approximation gives good insight into the phenomenon of flow induced vibration in piston-cylinder systems. The theory fairly well agrees with experiment in that both show unstable motion when the clearance ratio is above a critical value β_{cr}.

The theoretical values of β_{cr} are too high compared with experimental results. This is probably due to large errors introduced by the short piston approximation at high eccentricities associated with unstable pistons. Another limitation of the present analysis is the extremely small time steps required in the numerical computation whenever the dimensionless mass m (equation (22)) is small. It is believed that better correlation can be achieved by testing piston-cylinder systems with larger system parameters n or larger

mass m, and by solving the complete Reynolds equation for a finite length piston.

References

1 Blackburn, J. F., "Contribution to Hydraulic Control," TRANS, ASME, Vol. 75, Aug. 1953, pp. 1175-1180.

2 Hessey, M. F., Martin, B. P., and Brighton, D. K., "Hydraulic Lock Forces On Tapered Pistons," *Proceedings of the Institution of Mechanical Engineers,* Vol. 184, Part 1, 1969-1970, pp. 983-992.

3 Dransfield, P., and Bruce, D. M., "Leakage Flowrate Past Pistons of Oil Hydraulic System Components," *Journal of Aircraft,* Vol. 5, Mar.-Apr. 1968, pp. 156-160.

4 Grag, V. K., "Capsule-Pipelining An Improved Theoretical Analysis," ASME JOURNAL OF FLUIDS ENGINEERING, Vol. 99, Dec. 1977, pp. 763-771.

5 Yamaguchi, A., and Tanioka, Y., "Motion of Pistons in Piston Type Hydraulic Machines: Theoretical Analysis," *Bull. of the JSME,* Vol. 19, Apr. 1976, pp. 402-407.

6 Yamaguchi, A., and Tanioka, Y., "Motion of Pistons in Piston-Type Hydraulic Machines: Experiments," *Bull. of the JSME,* Vol. 19, Apr. 1976, pp. 408-412.

7 Etsion, I., and Hamrock, B. J., "Optimum Step Design for Centering of Pistons Moving in an Incompressible Fluid," ASME JOURNAL OF FLUIDS ENGINEERING, Vol. 99, Dec. 1977, pp. 675-680.

8 Kulkarny, K. M., and Schey, J. A., "Hydrostatic Extrusion with Controlled Follower Block Clearance," ASME *Jour. of Lub. Tech.* Vol. 97, Jan. 1975, pp. 25-34.

9 Pinkus, O., and Sternlicht, B., *Theory of Hydrodynamic Lubrication,* McGraw-Hill, 1961.

10 Etsion, I., and Magen, M., "Flow Induced Vibration in Piston-Cylinders Systems," TME 358 Technion-Israel Institute of Technology, May 1979.

11 Etsion, I., and Pinkus, O., "The Hydrodynamics of a Plug Bearing," ASME *Jour. of Lub. Tech.,* Vol. 98, July 1976, pp. 433-440.

12 Magen, M., "Dynamic Analysis of Piston Motion Within a Tube," M.Sc. thesis, Technion-Israel Institute of Technology, Apr. 1979.

13 Cole, J. D., *Perturbation Methods in Applied Mathematics,"* Blasdell Publishing Co., 1968.

Sensitizing the Dissipation Equation to Irrotational Strains

K. Hanjalić[1]
B. E. Launder
Department of Mechanical Engineering,
University of California,
Davis, Calif. 95616

The paper recommends the addition of an extra term to the conventional approximate transport equation for the turbulence energy dissipation rate. The term may be interpreted as emphasizing the role of irrotational deformations in promoting energy transfer across the spectrum or, equivalently, of augmenting the influence of normal strains. Calculations, including the new term, are reported for the plane and round jet, and for several turbulent boundary layers. In the cases considered the addition of the new term significantly improves agreement with experiment.

Introduction

The 1970's have seen a distinct changeover in the approaches used to approximate the Reynolds stresses in the numerical simulation of turbulent shear layers. At the beginning of the decade the models in use were commonly based on the notion of a universal profile of mixing length across the shear flow under study - or on some other equally rudimentary assumption. Even the calculation procedure of Bradshaw, Ferriss and Atwell [1], which was perhaps the first practical scheme to incorporate stress-transport ideas, assumed a universal length-scale distribution across the boundary layer. In the early years of the 70's, however, several publications appeared (e.g., references [2–6]) which discarded the universal-length-scale concept in favor of a length scale obtained from the solution of a rate equation. The most popular approach, adopted *inter alia* by references [2–5] has been to solve an approximate transport equation for the dissipation rate of turbulence energy, ϵ. The local length scale is then proportional to $k^{3/2}/\epsilon$, where k is the local turbulent energy.

The influential Stanford Conference on Turbulent Boundary Layers (see Kline, et al. [7]) took place before the appearance of this new generation of turbulence models. A few years later, however, Ng and Spalding [8] made predictions of all the Stanford test cases using three models of turbulence: a version of the mixing length hypothesis; that of reference [1]; and a two-equation model in which the local effective viscosity was taken proportinal to $\rho k^2/\epsilon$. The main conclusion drawn from this comparison was that, given the uncertainties in the initial conditions and in the two-dimensionality of the data near separation, none of the models could be identified as superior to the other two - at least, not on the basis of that group of shear flows.

A corollary that is sometimes added to the above result is that the two-dimensional boundary layers chosen for the Stanford Conference provided a too narrow range for model-refinement purposes. The idea is that by extending one's field of view to include wall jets, free shear flows and even homogeneous flows, one may deveop a model of such generality that the problem of predicting the turbulent boundary layer will automatically be dealt with. Several groups of workers, including the present writers, have at least partly accepted this philosophy. On the face of it, this direction of development has been rather successful. A study for the Langley Free Shear Flows Conference showed decisive superiority for models that obtained the length scale from transport equations [9] while more recently the second-moment closure of Launder, Reece, and Rodi [10] was successfully applied to predict the development of a plane-strain distortion, a jet, a wake, the fully-developed flow in a plane channel and the boundary layer on a flat pate at high Reynolds numbers.

Thus, it could be said that models existed which predicted at least *certain* representatives from several different classes of turbulent flow. Whether or not this meant that the models would work, let us say, for *all* the boundary layers in the Stanford Conference Proceedings (Coles and Hirst [11]) was not examined at the time. With hindsight, however, it may be said that several discouraging portents were available. Rodi and Spalding [3] had reported that the length scale equation used to predict the plane mixing layer and the plane and radial jets did not produce "realistic results" when applied to the round jet in stagnant surroundings[2], while in reference [10], the calculated growth rate of the far wake was markedly too low. Rodi [12] had shown an even more serious discrepancy in predictions of momentumless wakes, i.e., those generated by self-propelled bodies. Now, the far wakes differ from the successfully predicted shear flows of [10] by virtue of the relatively large importance of convective transport. In the round jet, mean and turbulent velocities decay rapidly in the stream-wise direction. One might therefore infer that, whenever external conditions produced either rapid changes or large imbalances between generative and destructive agencies, available models were liable to give anomalous results.

[1] On leave from Masinski fakultet, Sarajevo 71000, Yugoslavia.

Contributed by the Fluids Engineering Division of THE AMERICAN SOCIETY OF MECHANICAL ENGINEERS and presented at the Fluids Engineering Conference, Niagara Falls, N. Y., June 18–20, 1979. Manuscript received by the Fluids Engineering Division, February 14, 1979.

[2] More recently Launder and Morse [15] found that the closure of [10] predicted a rate of growth for the round jet that was 50 percent too high.

Of the flows included in the Stanford Conference, two that proved elusive to accurate prediction were boundary layers recovering from strong disturbances and those held near equilibrium in a prolonged adverse pressure gradient. At the outset of the present study computations were made of representative boundary layers of this type using the stress-transport model of [10]. As we had feared, the calculations (which will be discussed later) showed the same kind of discrepancies as the earlier study of reference [8]. The main errors in the predictions were attributable to the dissipation rate transport equation since, if *ad hoc* adjustments were made to the dissipation rate to produce the correct turbulence energy level, broadly the correct mean field development was predicted. Our attention was therefore directed towards diagnosing and removing the weaknesses in the model. A promising approach that the authors have been developing entails providing different sets of response equations for different parts of the turbulence energy spectrum; the preliminary results of this study are reported in references [13] and [14]. In the course of evolving that fairly elaborate description, however, it appeared that a very simple modification to the commonly employed dissipation rate equation would also achieve significant improvement in predictive accuracy in several situations. Here we discuss the rationale for the modification and show the benefits of including it in several flows that were hitherto poorly predicted.

The Proposed Dissipation Rate Equation

The energy dissipation rate is usually calculated from a transport equation of the following form:

$$\frac{D\epsilon}{Dt} = c_{\epsilon 1}' \frac{P_k \epsilon}{k} - c_{\epsilon 2} \frac{\epsilon^2}{k} + \mathfrak{D}_\epsilon \tag{1}$$

where P_k denotes the generation rate of turbulence energy (by mean shear, buoyancy, etc.,) and $\mathfrak{D}_\epsilon$ is the net diffusion rate of ϵ arising from inhomogeneities in the flow. The quantities $c_{\epsilon 1}'$ and $c_{\epsilon 2}$ are usually taken as constants: reference [9] for example suggests the values 1.43 and 1.92, respectively, when equation (1) is used in conjunction with a two-equation viscosity model while, in the stress-transport closure of [10], the corresponding values are 1.44 and 1.90. These very similar pairs of constants have arisen from matching the decay of grid turbulence (which fixes $c_{\epsilon 2}$ in the range 1.80–1.95) and then optimizing $c_{\epsilon 1}'$ to obtain the best agreement with the measured rates of spread for a number of well-documented free shear flows.

Equation (1) is the simplest conceivable form of transport equation that will produce at least qualitatively correct behavior for ϵ. The equation must have both a source and a sink term in order that large generation rates of turbulence energy lead to high dissipation rates and, if energy generation is switched off, the dissipation rate diminishes fast enough to prevent the turbulence energy becoming negative. Qualitatively correct responses are one thing, quantitatively correct predictions quite another. It would therefore be unreasonable to expect much in the way of generality from this basic form - indeed, the degree of success that has been reported seems quite remarkable.

There have been several proposals for extending the width of applicability of (1). Some of these introduce non-local characteristics of the flow, (reference [9] for example) while others retain strictly local properties but introduce additional invariant parameters of the mean or turbulence field. Lumley and his colleagues (e.g., reference [16]) allow the quantity $c_{\epsilon 2}$ to be a function of the anisotropy of the Reynolds stress tensor.[3] The anisotropy responds less rapidly than does P_k to changes in mean strain and its presence in the equation modifies the sensitivity of ϵ to changes in external conditions.

Pope [17] introduced a term which may be interpreted as an additional generation rate of ϵ due to the stretching of mean vorticity (Pope argues that, though the stretching of *turbulent* vortex lines is really what one is interested in, the large-scale turbulent motions tend to be aligned with the vorticity in the mean flow). The term is zero in a plane two-dimensional flow because the mean vortex lines do not change their length. In an axisymmetric round jet, however, they are stretched as the jet enlarges downstream; the additional term thus raises the level of ϵ and consequently reduces the Reynolds stresses and the spreading rate. No other tests of this modification have yet been reported.

The present proposal has certain similarities with the above though it has been arrived at from a different line of exploration. In [14] the writers propose a transport equation for the rate of energy transfer out of the energy containing motions (which, except in local equilibrium, is *not* the same as the energy dissipation rate). The equation originally had an exactly parallel form to (1). We found, however, that to predict correctly the variation of turbulence energy in irrotational flows through a nozzle a substantially higher coefficient was needed for the equivalent of $c_{\epsilon 1}'$ than for, let us say, the plane jet or mixing layer. The idea that energy transfer rates across the spectrum were preferentially promoted by irrotational deformations seemed at least plausible.

Now, since energy in transit across the spectrum ends up as energy dissipated, there is the implication that equation (1) should also benefit from a term that promotes higher rates of dissipation for irrotational than for rotational strains. This characteristic can be imparted to equation (1) by introducing on the right-hand side a term proportional to:

$$k \frac{\partial U_i}{\partial x_j} \frac{\partial U_l}{\partial x_m} \epsilon_{ijk} \epsilon_{lmk} \tag{2}$$

[3] The anisotropy may be defined as $(\overline{u_i u_j} - 2/3\, k\, \delta_{ij})\ (\overline{u_i u_j} - 2/3\ k\ \delta_{ij})/k^2$.

[4] Our own experiences, admittedly based on a narrow range of shear flows, have been that introduction of the anisotropy brings only marginal benefits. The multi-scale approaches described in [13] and [14] seem better able to simulate the spectral time lag between changes in the large-scale energy-containing eddies and responses in the time-scale dissipative motions.

Nomenclature

c_f = skin friction coefficients ($\tau_w / \frac{1}{2}\rho U_m^2$)
$c_{\epsilon 1}$, $c_{\epsilon 1}'$ = empirical coefficients in dissipation
$c_{\epsilon 2}$, $c_{\epsilon 3}$ = rate transport equation
$\mathfrak{D}_\epsilon$ = net diffuson rate of ϵ
H = boundary layer shape factor (ratio of displacement: momentum thicknesses)
k = turbulent kinetic energy (kinematic) $\overline{u_i u_i}/2$
p = static pressure
$\overline{v^2}$ = y-direction component of Reynolds normal stress
U = streamwise mean velocity
U_i = component of mean velocity, tensor notation
U_m = maximum mean velocity at particular station (free stream velocity for boundary layers, centerline velocity for jets)
U_0 = reference free stream velocity upstream of deceleration
U_τ = friction velocity, $(\tau_w/\rho)^{1/2}$
u_i = turbulent component of

where ϵ_{ijk} stands for the third-order alternating tensor and the multiplicative coefficient must be *negative*. For two-dimensional thin shear flows (with the possible exception of flows following curved paths) the term sensibly reduces to $k(\partial U/\partial y)^2$ or, equivalently, to:

$$\left(\frac{k^2}{\epsilon}\frac{\partial U}{\partial y}\right)\cdot\frac{\partial U}{\partial y}\cdot\frac{\epsilon}{k}.$$

Now, within the framework of the $k \sim \epsilon$ viscosity model

$$\frac{k^2}{\epsilon}\frac{\partial U}{\partial y} \propto -\overline{uv} \tag{3}$$

and so the original term appearing in (2) may be replaced by

$$c'_{\epsilon 3}\overline{uv}\frac{\partial U}{\partial y}\frac{\epsilon}{k} \tag{4}$$

where $c'_{\epsilon 3}$ is a *positive* coefficient to be determined. On adding (4) to the first term on the right side of equation (1) and decomposing P_k into its component parts, the total contribution due to mean strain emerges as:

$$\frac{\epsilon}{k}\left(-c_{\epsilon 1}\overline{uv}\frac{\partial U}{\partial y} - c_{\epsilon 3}(\overline{u^2}-\overline{v^2})\frac{\partial U}{\partial x}\right) \tag{5}$$

where $c_{\epsilon 1} \equiv (c'_{\epsilon 1} - c'_{\epsilon 3})$ and $c_{\epsilon 3} \equiv c'_{\epsilon 1}$. Now, since $c'_{\epsilon 3}$ is a positive quantity, $c_{\epsilon 1}$ is smaller than $c_{\epsilon 3}$. We can thus reinterpret the new term as augmenting the effect of normal strain generation relative to that due to shear strain.[5] The complete dissipation rate transport equation may be written

$$\frac{D\epsilon}{Dt} = -c_{\epsilon 1}\overline{uv}\frac{\partial U}{\partial y}\frac{\epsilon}{k} - c_{\epsilon 2}\frac{\epsilon^2}{k} - c_{\epsilon 3}(\overline{u^2}-\overline{v^2})\frac{\partial U}{\partial x}\frac{\epsilon}{k} + \mathfrak{D}_\epsilon \tag{6}$$

We note that $c_{\epsilon 1}$ should take approximately the same value as $c'_{\epsilon 1}$ in equation (1) since, if the effects of streamwise changes in U are negligible (as, for example, in fully-developed channel flow), equations (1) and (6) are identical in form. In the present study, following [10], we take $c_{\epsilon 1} = 1.44$ and $c_{\epsilon 2} = 1.90$ while $c_{\epsilon 3}$ is given the value 4.44.

Two types of shear flows have so far been examined: free jets in stagnant surroundings (axisymmetric and plane geometries) and boundary layers in adverse pressure gradients. The latter have been computed with the Reynolds stress closure of reference [10] using equation (6) in place of the original dissipation equation and (as in [10]) with diffusive transport represented by

$$\mathfrak{D}_\epsilon = 0.15\frac{\partial}{\partial y}\left(\frac{\overline{v^2}k}{\epsilon}\frac{\partial \epsilon}{\partial y}\right) \tag{7}$$

The jets have been computed using the simpler $k \sim \epsilon$ viscosity closure. Our reason for doing so was partly that experience has shown mean field characteristics of self-preserving free shear flows to be predicted equally as well with that model as with the more elaborate Reynolds stress transport model (Morse, private communication) and partly that, for the axisymmetric jet, the stress-transport equations are rather tricky to solve numerically with the finite-difference scheme used here [15], [18]. With the $k \sim \epsilon$ model diffusion of ϵ is approximated as

$$\mathfrak{D}\epsilon = 0.09\frac{\partial}{\partial y}\left(\frac{k^2}{\epsilon}\frac{\partial \epsilon}{\partial y}\right) \tag{8}$$[6]

while the normal-stresses appearing in (6) and in (10) below are expressed in terms of the turbulence energy by

$$(\overline{u^2}-\overline{v^2}) = 0.33k \tag{9}$$

The kinetic energy equation and the stress-strain relation are standard:

$$\frac{Dk}{Dt} = -\overline{uv}\frac{\partial U}{\partial y} - (\overline{u^2}-\overline{v^2})\frac{\partial U}{\partial x} - \epsilon + 0.09\frac{\partial}{\partial y}\left(\frac{k^2}{\epsilon}\frac{\partial k}{\partial y}\right) \tag{10}$$

$$-\overline{uv} = 0.09\frac{k^2}{\epsilon}\frac{\partial v}{\partial y} \tag{11}$$

The Patankar-Spalding [18] finite-difference procedure used as the basis for the numerical computations adopts a normalized stream function, ω, as cross-stream variable. Consequently the most accessible $\partial U/\partial x$ is that along a line of constant ω. It is emphasized that this is not the appropriate x derivative for use in equations (6) and (10); rather, one needs the rate of change along a constant $-y$ line. This derivative has been obtained in the course of computations by assuming the shape of the velocity profile to be invariant between the upstream and downstream end of any forward step, as proposed by Launder and Morse [15]. Predictions of the shear flows reported below have been obtained using 28 cross-stream nodes. In the case of boundary-layer computations, the node adjacent to the wall was located far enough from the surface to lie in fully turbulent fluid. The wall shear stress was obtained from the streamwise velocity at this node using the well known semi-logarithmic law of the wall.

Near-wall boundary conditions for the other dependent variables were obtained from local-equilibrium estimates as described in reference [10].

Discussion of Computed Results

The computed and measured behavior for the jets are compared in Figs. 1-4 and in Table 1. The self-preserving mean velocity profiles shown in Figs. 1 and 2 are in satisfactory accord, the only noticeable difference between the measured and calculated behavior being a calculated approach to the free-stream conditions that is too slow near the edge of the plane jet. The corresponding kinetic energy profiles, shown in Figs. 3 and 4, also display satisfactory

[5] In speaking of "normal" and "shear" strains one should strictly add that this applies to a coordinate system in which one axis points in the direction of the mean velocity vector.

[6] The value of the diffusion constant in (8) was raised from the "standard" value of 0.07 in order to improve the shape of the turbulence energy profile towards the edges of the jet.

Nomenclature (cont.)

velocity, tensor notation
$\overline{u_iu_j}$ = kinematic Reynolds stress, tensor notation
uv = turbulent shear stress
u^2 = streamwise component of Reynolds normal stress
x = coordinate direction parallel to free stream
x_i = Cartesian coordinate, tensor notation
y = cross-stream distance coordinate (denotes radius from symmetry axis for round jet)
$y_{1/2}$ = cross-stream distance from plane or axis of symmetry to point where mean velocity is half axis value
β = pressure gradient parameter $(\delta^*/\tau_w)dp/dx$
δ = boundary layer thickness
δ^* = boundary layer displacement thickness
ϵ = rate of dissipation of kinematic turbulence energy
ρ = density
τ_w = local wall shear stress

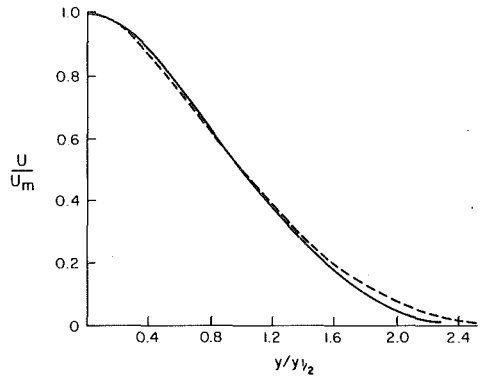

Fig. 1 Mean velocity profiles in plane jet in stagnant surroundings:
___ measurements, Robins [21]
------ predicted

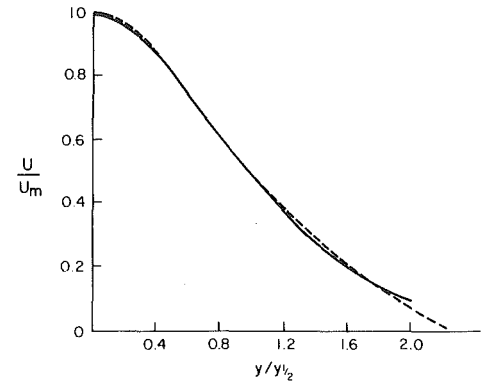

Fig. 2 Mean velocity profiles in round jet in stagnant surroundings
___ measurements, Rodi [19]
------ predicted

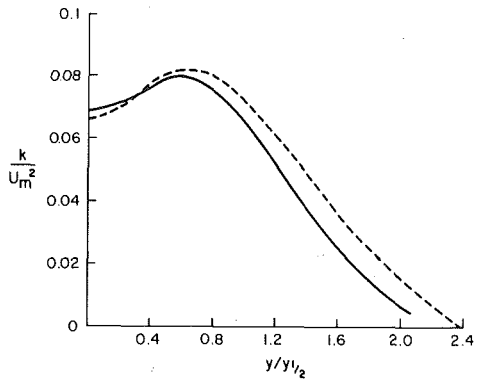

Fig. 3 Turbulence energy profiles in plane jets in stagnant surroundings
___ measurements, Bradbury [20]
------ predicted

accord in view of the difficulties of obtaining accurate turbulence levels in these high-intensity flows. One notes in particular that the difference in the shape of the energy profiles between the round and plane jet is correctly reproduced by the numerical computations. The most interesting characteristic of the results appears in Table 1 which lists the rates of spread of the two flows as obtained from experiments, from the proposed form of the $k \sim \epsilon$ model and from the $k \sim \epsilon$ model without normal strain amplication. With the original model, the calculated rate of spread is 5 percent higher for the round jet than for the plane one; experiments suggest, however that the spread of the round jet is the slower by fully 20 percent. The present computations show a great improvement over the original $k \sim \epsilon$ model; the

Table 1 Rates of spread of plane and round jets

	$dy_{½}/dx$		
Flow	Expt.	Standard[7] $k-\epsilon$ model	Present model, equation (6)
Plane jet	0.110	0.109	0.116
Round jet	0.86–0.90	0.115	0.098

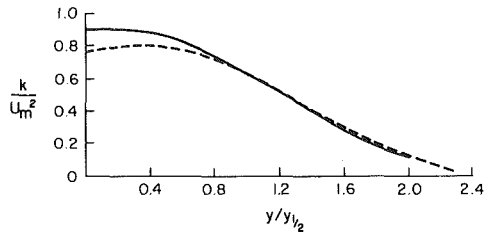

Fig. 4 Turbulence energy profiles in round jet in stagnant surroundings
___ measurements, Rodi [19]
------ predicted

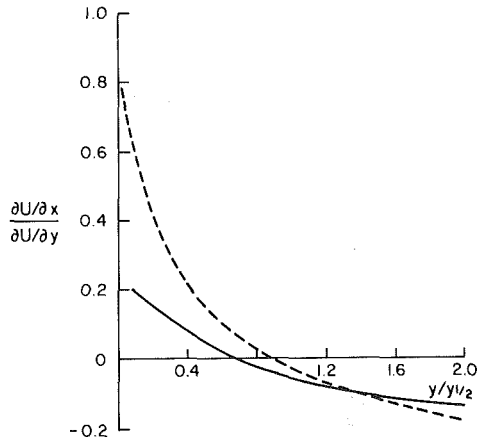

Fig. 5 Ratio of streamwise: cross velocity gradients in jets
___ plane jets; ------ round jet

rate of spread of the round jet is now some 17 percent below that of the plane jet. Interestingly the effect of introducing the extra term reduces the growth of the round jet but increases that of the plane jet. The reason for this contrasting behavior may be inferred from Fig. 5 which shows the predicted variation of axial:cross-stream velocity gradients in the two flows. In both flows $\partial U/\partial x$ is negative near the plane or axis of symmetry and positive toward the outer edge. In the case of the round jet, however, the strength of the velocity decay in the near-axis region is far greater than for the plane jet. Now, when $\partial U/\partial x$ is negative the generation due to normal strains is positive, creating higher levels of ϵ and lower energy and shear-stress levels. In the outer region of the jet all these features are reversed; the net outcome, however, is that the overall level of ϵ is increased and, by virtue of the lower effective viscosities, the rate of spread is reduced. For the plane jet the region of negative $\partial U/\partial x$ extends only to $0.65y_{½}$; over the remainder of the shear flow fluid is accelerating and this produces a net *increase* in the rate of spread.

Turning to the wall boundary layers, Fig. 6 shows excellent agreement of the mean velocity and Reynolds stress profiles with Klebanoff's [22] measurements for zero streamwise pressure gradient. This comparison serves to indicate that in a slowly developing flow with a uniform external-stream velocity the modification introduced to the ϵ equation has negligible effect: the predicted pattern is sensibly the same as

[7] With $c_{\epsilon 1} = 1.42\, c_{\epsilon 2} = 1.92$.

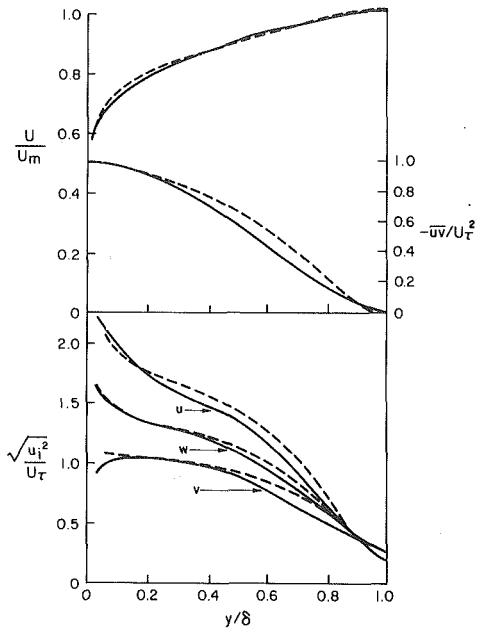

Fig. 6 Mean velocity, shear stress and turbulence intensity profiles in flat plate boundary layer: ____ measurement, Klebanoff [22]; ------ predicted

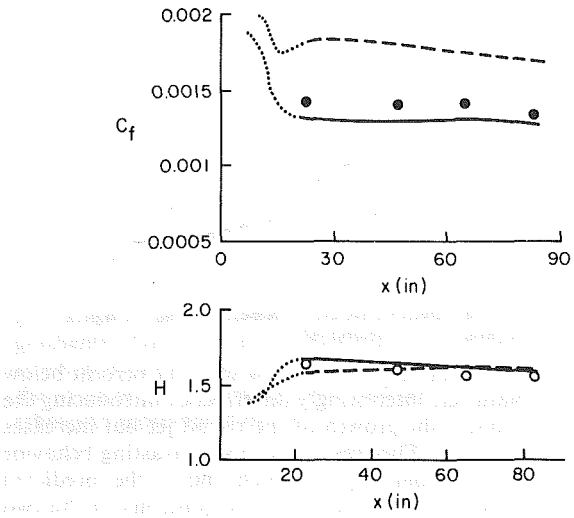

Fig. 7 Skin friction and shape factor in equilibrium boundary layer in adverse pressure gradient o, • measurements, Bradshaw [23],
____ present predictions
------ predictions with model of reference [10]

reported in reference [10]. The next boundary layer considered is the Stanford Conference Flow 2600-1, an equilibrium boundary layer in adverse pressure gradient measured by Bradshaw [23]. In this flow the free stream velocity varies as $x^{-0.255}$. Fig. 7 shows the variation with streamwise distance of the skin friction coefficient, and the shape factor, H. The initial conditions for the computations corresponded to those for zero pressure gradient. There is thus a rapid initial variation in c_f and H as the boundary layer relaxes to its equilibrium condition from about $x = 20$ in. onwards. The original model of reference [10] produces levels of wall shear stress that are abut 40 percent too high; by comparison, the predictions obtained with the modified ϵ equation are on average 7 percent too low. Both versions predict generally satisfactory agreement with the measured shape factor, though here, too, the variation produced with equation (6) is superior.

Bradshaw [24] produced a further set of experiments in

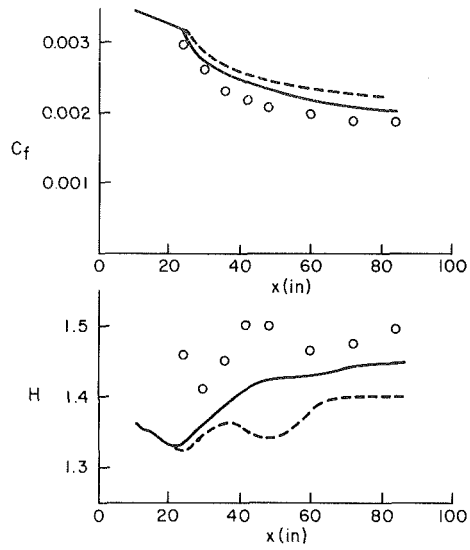

Fig. 8 Shape factor and friction factor in non-equlibrium layer in adverse pressure gradient o measurements, case "A", Bradshaw [24]
____ present predictions
------ predictions using model of reference [10]

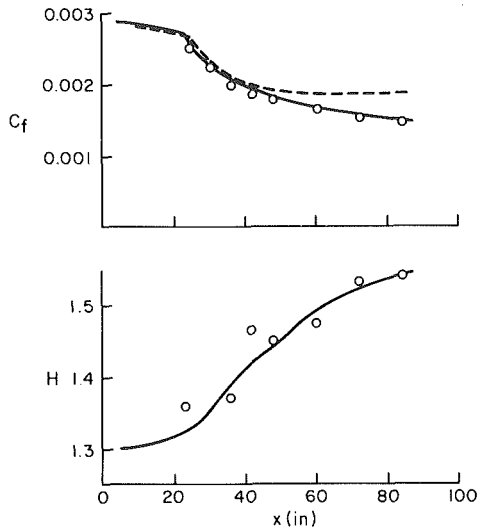

Fig. 9 Shape factor and friction factor in non-equilibrium layer in adverse pressure gradient o measurements, case "C," Bradshaw [24]
____ present predictions
------ predictions using model of reference [10]

which an initial region of uniform free stream velocity preceded the application of the adverse pressure gradient. Three cases were studied in which the effects of different initial boundary layer thickness were examined. Here we report comparisons for the two extreme cases. Figs. 8 and 9 show the development of the experimental values of c_f and H together with the predicted variations obtained with the standard ϵ equation and with equation (6). For the case of the thicker initial boundary layer (layer C) shown in Fig. 9 the present dissipation equation produces a variation in almost complete agreement with the data. The standard ϵ equation, however, leads to the attainment of a self-preserving flow at about $x = 55$ in., beyond which the level of skin friction coefficient remains invariant. Consequently, at the final measuring station, the calculated wall stress is 30 percent too high. Agreement would evidently have deteriorated further had the region of adverse pressure gradient been continued.

The level of agreement is less satisfactory in the case of layer "A" where the boundary layer displacement thickness at the start of the adverse pressure gradient was only 40

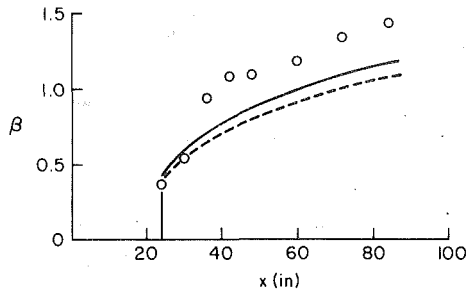

Fig. 10 Development of pressure gradient parameter β ($\equiv (\delta^*/\tau_w)\, dp/dx$) for case "A"
o experiments, Bradshaw [24]
____ present predictions
------ predictions using model of reference [10]

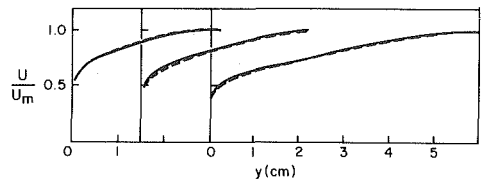

Fig. 11 Developments of mean velocity profiles for case "C." Profiles shown at x = 24 in; 36 in. and 72 in.
____ measurements, Bradshaw [24]
------ present predictions

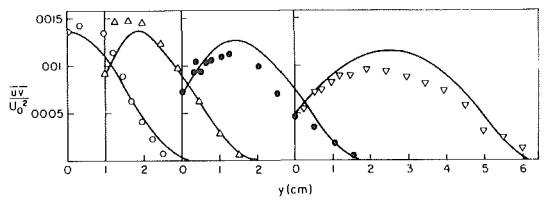

Fig. 12 Development of shear stress profiles for case "C." Profiles shown at x = 24 in.; 36 in.; 48 in. and 72 in. o 7 • Δ measurements, Bradshaw [24]; ____ present predictions

percent of that for layer "*C*." The experiments exhibit a more rapid decrease in c_f than either of the calculated variations, though here, too, the modified ϵ equation comes substantially closer to the measurements than does the original version. It seems at least possible that there is some further factor involved, however. The experimental data show initially a more rapid rise in shape factor for the layer "*A*" than for layer "*C*." This is unexpected since the *same* external pressure gradient habitually produces a greater effect on thick boundary layers than on thin ones. A possible explanation might be that, due to the thinner boundary layer in the case of layer "*A*," the initial deceleration was more severe[8]. The consequences of such an eventuality may be conveniently discussed in terms of the pressure gradient parameter 8 whose variation for case "*A*" is shown in Fig. 10.

We note first, that if β were invariant with x, the boundary layer would be said to be in equilibrium (see, for example, [25]) and the levels of c_f and H would also be nearly constant; the larger β, the lower the value of c_f. Now, in the present case β grows continuously with distance downstream. If, locally, the adverse pressure gradient were steeper than estimated the displacement thickness would grow faster than the calculated value even if the model were perfect. Thereafter, when the pressure gradient returned to the estimated value, a short distance downstream, the level of β would still be larger than the calculated value because the displacement thickness would be greater and the shear stress lower. Through this double-edged effect it seems that situations may arise where the calculated boundary layer is never able to "catch up" with the actual development. From Fig. 10 it is clear that the error in β develops suddenly between the 30 in. and 36 in. stations and remains of virtually the same magnitude over the rest of the test section.

Figs. 11 and 12 show the development of the mean velocity and shear stress profiles for case "*C*" as measured in reference [24] and as calculated with the modified ϵ equation. There is generally a satisfactory agreement between the two though difference of up to 20 percent between the measured and calculated shear stress are present in the central region of the boundary layer.

Concluding Remarks

The comparisons of the previous section have shown that a minor modification to the dissipation rate equation has brought substantial improvement to the prediction of boundary layers in adverse pressure gradients and has gone a long way towards accounting for the round jet paradox. In closing, however, it behooves us to caution potential users against expecting too much from the present formulation. In its present state the ϵ equation is still a highly simplistic model that will certainly fail badly in some situations. By way of example, the present equation has done nothing to improve the rate of spread of the plane wake. The present version, like the original $k \sim \epsilon$ model, produces as asymptotic growth rate about 35 percent less than the measurements.

Perhaps the most useful lesson the writers have learned is that the ϵ equation (which had remained virtually unchanged for seven years) can quite easily and rationally be improved to allow the applied strtain field to exert subtle yet unexpectedly large effects on the level of the energy dissipation rate. (We had formerly intended to abandon entirely single-scale approaches in favor of the multi-scale framework developed in references [13] and [14].) One may expect that the addition of further terms, such as those proposed by Pope [17] or Lumley [26] will further extend the range of shear flows describable by a single set of transport equations.

Acknowledgments

The work reported herein has been supported by NASA Ames Experimental Fluid Mechanics Division under research grants NSG 2256. The continued interest of the NASA Scientific Staff, particularly Dr. J. G. Marvin and Dr. M. W. Rubesin is appreciated.

Our thanks are due also to L. S. Majesky who prepared the camera-ready manuscript with her customary precision.

Authors' names appear alphabetically.

References

1 Bradshaw, P., Ferriss, D. H., and Atwell, N. P., "Calculation of Boundary Layer Development Using the Turbulent Energy Equation," *Journal of Fluid Mechanics,* Vol. 28, 1967, p. 593.

2 Daly, B. J., and Harlow, F. H., "Transport Equations in Turbulence," *Physics of Fluids,* Vol. 13, 1970, p. 2634.

3 Rodi, W., and Spalding, D. B., "A Two-Parameter Model of Turbulence and its Application to Free Jets," *Wärme-und-Stoffübertrangung,* Vol. 3, 1970, p. 85.

4 Hanjalić, K., and Launder, B. E., "A Reynolds Stress Model of Turbulence and its Application to Thin Shear Flows," *Journal of Fluid Mechanics,* Vol. 2, 1972a, p. 609.

5 Jones, W. P., and Launder, B. E., "The Prediction of Laminarization with a Two-Equation Model of Turbulence," *International Journal of Heat and Mass Transfer,* Vol. 15, 1972, p. 301.

6 Launder, B. E., and Spalding, D. B., "The Numerical Computation of Turbulent Flow," *Computer Methods in Applied Mechanics and Engineering,* Vol. 3, 1974, p. 269.

7 Kline, S. J., Morkovin, M. V., Sovran, G., and Cockrell, D. J. (editors), "Computation of Turbulent Boundary Layers," *Proc. AFOSR - IFP - Stanford Conference,* Mechanical Engineering Department, Stanford University.

8 Ng, K. H., and Spalding, D. B., "A Comparison of Three Methods of

[8] Reference [24] reports only a single free-stream velocity variation for the three tests.

Predicting the Hydrodynamic Behavior of Two-Dimensionai Turbulent Walls," Imperial College Mechanical Engineering Department Report BL/TN/A/32, 1970.

9 Launder, B., E., Morse, A., Rodi, W., and Spalding, D. B., "The Prediction of Free Shear Stress Flows - A Comparison of the Performance of Six Turbulence Models," *Proc. Langley Free Shear Flows Conf.*, NASA SP 320.

10 Launder, B. E., Reece, G. J., and Rodi, W., "Progress in the Development of a Reynolds Stress Turbulence Closure," *Journal of Fluid Mechanics,* Vol. 68, 1975, p. 537.

11 Coles, D. E., and Hirst, E. A. (editors), "Computation of Turbulent Boundary Layers, Vol. 2: Compiled Data," *Proc. AFOSR - IFP - Stanford Conference,* Mechanical Engineering Department, Stanford University.

12 Rodi, W., "The Prediction of Free Turbulent Boundary Layers by Use of a Two-Equation Model of Turbulence," PhD thesis, University of London, Faculty of Engineering.

13 Launder, B. E., and Schiestel, R., "Sur l'utilisation d'échelles temporelles multiples en modélisation des ecoulements turbulents," C. R. Acad. Sci., Paris, 286A, 709, 1978.

14 Hanjalić, K., and Launder, B. E., "Turbulent Transport Modelling of Separating and Reattacing Shear Flows - I. Basic Multi-Scale Development and Its Application to Thin Shear Flows," Mechanical Engineering Report TF/78/9, University of California, Davis, 1978.

15 Launder, B. E., and Morse, A., "Numerical Prediction of Axisymmetric Free Shear Flows with a Second-Order Reynolds Stress Closure," *Proc. 1st Symposium on Turbulent Shear Flow,"* Springer Verlag, New York, 1979.

16 Lumley, J. L., and Newman, G. R., "The Return to Isotropy of Homogeneous Turbulence," *Journal of Fluid Mechanics,* Vol. 82, p. 161.

17 Pope, S. B., "An Explanation of the Turbulent Round-Jet/Plane Jet Anomoly," Report FS/77/12, Department of Mechanical Engineering, Imperial College, June 1977.

18 Patankar, S. V., and Spalding, D. B., *Heat and Mass Transfer in Bounary Layers,* 2nd Edition, Intertext, London.

19 Rodi, W., "A Review of Experimental Data of Uniform Density Free Turbulent Boundary Layers," *Studies in Convection,* 1, 1975, p. 79.

20 Bradbury, L. J., S., "The Structure of the Self-Preserving Turbulent Plane Jet," *Journal of Fluid Mechanics,* 23, 1965, p. 31.

21 Robins, A., "The Structure and Development of a Plane Turbulent Free Jet," PhD thesis, University of London, 1971.

22 Klebanoff, P. S., "Characteristics of Turbulence in a Boundary Layer with Zero Pressure Gradient," NACA Report 1277, 1955.

23 Bradshaw, P., The Turbulence Structure of Equlibrium Boundary Layers," *Journal of Fluid Mechanics,* 29, 1967, p. 625.

24 Bradshaw, P., "The Response of a Constant-Pressure Turbulent Boundary Layer to the Sudden Application of an Adverse Pressure Gradient," Aero. Research Council Rep. & Mem. 3575, 1969.

25 Clauser, F. H., "Turbulent Boundary Layers in Adverse Pressure Gradients," *Journal of Aeronautical Science,* 21, 1954, p. 91.

26 Lumley, J. L., "Computational Modeling of Turbulent Flows," *Adv. in Applied Mechanics,* Vol. 18, 1978, pp. 123–126, Academic Press.

Impulsive Motion of a Sphere at Supersonic Speeds

Stephen S. H. Chang
Lockheed Missiles and Space Company, Sunnyvale, Calif. 94088

This paper presents an analytical transient solution to the subsonic flow near the stagnation region of a sphere which starts impulsively at a constant supersonic speed. The analysis is based upon a series expansion in time of the flow variables and of the shape of the moving shock. The coefficients of the series are determined analytically by substituting the series into the differential equations of motion and the standard Rankine-Hugoniot jump conditions. The series is extended over 30 terms at stagnation point and up to nine terms near the sonic point. The first four terms are in agreement with the known solutions. By recasting them in Euler's transformation, the series is analytical beyond their natural region of convergence. The results match the experiments and are in agreement with the known steady-state numerical solutions.

Introduction

Consider an impulsively started sphere at supersonic speeds in a uniform stationary flow-field. At time $t = 0$, an attached bow shock wave forms instantaneously in front of the sphere. At subsequent times, the bow shock wave moves away from the body surface until a stationary detached shock wave is formed. The flow field in the nose region between the moving shock wave and the stationary body surface is subsonic. The behavior of the transient process in that region and the time requirement to establish a stationary shock wave are of considerable interest in connection with the use of a high speed test facility, such as shock tube applications, gas gun shots, and the like.

Cabannes [1] carried the first two terms of a series solution by expanding the series in time of the motion of an obstacle at supersonic speeds in a stationary flow field, but the shock stand-off distance was in error by a factor of four in comparison with experiments. Bausset [2, 3] extended Cabannes' solution to the first four terms in the expansion but failed to find the time required for establishing a stationary detached shock wave. Miles, Mirels, and Wang [4] obtained the trajectory of the detached shock wave in front of an impulsively started flat-nosed, semi-infinite cylinder but gave no experimental verification of their results. Unfortunately, all of their analyses are limited to the transient solutions for the shock front at the stagnation region and no other useful information such as the transient behavior of the surface pressure is provided; hence, their results are limited in their application.

For a blunt-body problem, it is known that a singular limiting line appears upstream of the bow shock wave [5, 6]. When a sphere begins to move forward impulsively at supersonic speeds, in the early stages, the velocity of the shock wave at the stagnation region is much faster than that downstream. When the shock front reaches 80 percent of the stand-off distance, the shock velocity at the stagnation region is considerably slower than that downstream. Thus the shock wave begins to fluctuate. Because of the existence of the upstream singularity which is closer to the fluctuating shock wave near the sonic point than the stagnation region of the body surface, the series begins to diverge after few terms of expansion. The expansion of such a series must be terminated before any large divergence to occur. Now, with a limited number of terms of the series for obtaining a meaningful set of solutions, some techniques must be developed. The mathematical expression for an arbitrary nose shape is cumbersome. For simplicity, we limit our analysis to the sphere only. An extension of this method to the other nosetips is straightforward. A nonspherical nose, for example the paraboloid, may yield a more accurate solution. The objectives of this paper are to extend the Cabannes' series to the higher order, to examine the effect of the singularity in the transient flow, and to develop a method for improving the series solution within the region of interest.

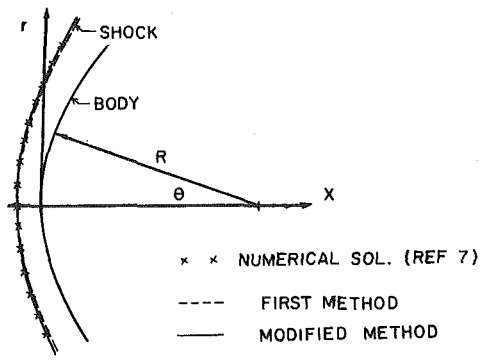

Fig. 1 Shock configuration after stabilization ($M_\infty = \infty$ and $\gamma = 1.4$)

Formulation of the Problem

Let our basic frame of reference be the spherical coordinate system (R, θ, φ) with the origin at the center of the sphere (Fig. 1). Then, the appropriate governing differential equations describing the flow field within the shock layer are

Contributed by the Fluids Engineering Division for publication in the JOURNAL OF FLUIDS ENGINEERING. Manuscript received by the Fluids Engineering Division, January 1, 1979.

the standard conservation equations.

$$\rho_t + \frac{1}{R^2}(\rho v R^2)_R + \frac{1}{R\sin\theta}(\rho u \sin\theta)_\theta = 0$$

$$u_t + v u_R + \frac{u}{R}u_\theta + \frac{uv}{R} + \frac{1}{\rho R}p_\theta = 0 \qquad (1)$$

$$v_t + v v_R + \frac{u}{R}v_\theta - \frac{u^2}{R} + \frac{1}{\rho}p_R = 0$$

$$(p/\rho^\gamma)_t + v(p/\rho^\gamma)_R + \frac{u}{R}(p/\rho^\gamma)_\theta = 0.$$

Let $F(R, \theta, t) = 0$ be the trajectory of the moving shock wave. The boundary conditions at the shock wave are given by the standard Rankine-Hugoniot relations of a perfect gas

$$p_s(R,\theta,t) = \frac{2}{\gamma+1}\left(\frac{M_n}{M_\infty}\right)^2 - \frac{\gamma-1}{\gamma+1}\frac{1}{\gamma M_\infty^2}$$

$$\rho_s(R,\theta,t) = 1/\left[\frac{\gamma-1}{\gamma+1} + \frac{2}{\gamma+1}\frac{1}{M_n^2}\right] \qquad (2)$$

$$u_s(R,\theta,t) = \sin\theta + \frac{2}{\gamma+1}\left[\frac{M_n}{M_\infty} - \frac{1}{M_n M_\infty}\right]\frac{R_\theta}{(R^2+R_\theta^2)^{1/2}}$$

$$v_s(R,\theta,t) = -\cos\theta - \frac{2}{\gamma+1}\left[\frac{M_n}{M_\infty} - \frac{1}{M_n M_\infty}\right]\frac{R}{(R^2+R_\theta^2)^{1/2}}$$

where

$$M_n = M_\infty(F_t - \cos\theta - \frac{R_\theta}{R}\sin\theta)/\left[1+(R_\theta/R)^2\right]^{1/2}.$$

The boundary condition on the body surface is simply given by

$$v_b(R,\theta,t) = 0 \qquad \text{at } R = R_b = 1. \qquad (3)$$

Method of Solution

First Method. First, we expand the equation for the shock wave as follows;

$$F(R_s,\theta,t) = R_s(\theta,t) - [R_b + f_1(\theta)t + f_2(\theta)t^2 + f_3(\theta)t^3 + \ldots] = 0. \qquad (4)$$

Substituting the foregoing expression into equations (2) and equating like powers of t result in series equations for the flow variables , p_s, ρ_s, u_s, and v_s.

Similarly, we expand all flow variables, p, ρ, u, and v, in powers of t, take derivatives with respect to t and θ, and set them at $R = R_s$, for example, the normal velocity component

$$\frac{\partial}{\partial t}v_s = v_t + v_R R_t = \sum_{n=1} n\, v_{n+1} t^{n-1}$$

$$\frac{\partial}{\partial\theta}v_s = v_\theta + v_R R_\theta = \sum_{n=1} v_n' t^{n-1} - \sum_{n=1} u_n t^{n-1}. \qquad (5)$$

Substituting the foregoing expressions, v_t, v_θ, u_t, u_θ, p_t, p_θ, ρ_t, and ρ_θ, into equation (1) yields a system of ordinary differential equations for u_R, v_R, ρ_R, and p_R; for example,

$$v_R = \frac{-(AR_s/\rho)E_1 - (\gamma p R_s R_{s\theta}/\rho)E_2 + (A^2 - \gamma p R_{s\theta}^2/\rho)E_3}{A(A^2 - \gamma p R_s^2/\rho - \gamma p R_{s\theta}^2/\rho)}$$

$$\text{at } R = R_s \qquad (6)$$

where $A = (v - R_{st})R_s - uR_{s\theta}$,

$$E_1 = -\gamma p(2v + u\cot\theta) - R_s\frac{\partial}{\partial t}p_s - u\frac{\partial}{\partial\theta}p_s - \gamma p\frac{\partial}{\partial\theta}u_s,$$

$$E_2 = -uv - R_s\frac{\partial}{\partial t}u_s - u\frac{\partial}{\partial\theta}u_s - \frac{\partial}{\partial\theta}p_s/\rho,$$

$$E_3 = u^2 - R_s\frac{\partial}{\partial t}v_s - u\frac{\partial}{\partial\theta}v_s.$$

Using

$$v_s(\theta,t) = v_b + v_R\,|_{R=R_b}(R_s - R_b) \qquad (7)$$

and equation (3), we equate the terms of like powers of t to zero and obtain a system of algebraic equations which determine the coefficients for the shock wave. Once the coefficients, f_n, in equation (4) are known, then the other flow variables may be obtained accordingly.

The algebraic expressions for these coefficients are cumbrous. We write only the first few terms for illustration

$$f_1 = -\cos\theta + \frac{\cos\theta}{2\beta}\left\{1 + \left[\left(\frac{2\beta}{M_\infty\cos\theta}\right)^2 + 1\right]^{1/2}\right\},$$

$$f_2 = -\frac{1}{2}f_1'\sin\theta + \frac{f_1}{2\beta}\frac{-2\gamma p_1\cos\theta + p_1'\sin\theta - 2\alpha_1\sin^2\theta}{2f_1\alpha_1 + (2f_1\alpha_1 - \gamma p_1)[1 + 1/(\alpha_1 M_\infty)^2]},$$

$$f_3 = -\frac{1}{3}(f_2' - f_1'f_1)\sin\theta + \frac{v_{R1}f_2 - \beta\alpha_1[f_1'^2 - \alpha_2^2/(\alpha_1^2 M_\infty)^2]}{3\beta[1 + 1/(\alpha_1 M_\infty)^2]},$$

$$f_4 = -\frac{1}{4}[f_3' - f_2'f_1 - f_1'(f_2 - f_1^2)]$$

Nomenclature

F, f = shock function
M = Mach number
p, P = pressure normalized by $\rho_\infty V_\infty^2$
t, T = time normalized by R_b/V_∞
V = velocity normalized by V_∞
u, v = velocity components normalized by V_∞
ρ = density normalized by ρ_∞
γ = ratio of specific heats
ξ = parameter
x, r, φ = cylindrical coordinate system (Fig. 1)
R, θ, φ = spherical coordinate system
Δ, δ = stand-off distance normalized by R_b
λ = $t/(\beta + t)$,
β = constant listed in Table 2
$( )' = ( )_\theta$ = derivative with respect to θ
$( )_R$ = derivative with respect to R
$( )_t$ = derivative with respect to t

Subscripts

∞ = free stream condition
s = condition at the shock front
b = condition on the body surface
n = normal component

$$+\frac{v_{R1}f_3-\beta\alpha_1\{2f_2'(f_2'-f_1'f_1)+f_1'^2\alpha_2/\alpha_1-[2\alpha_2\alpha_3-\alpha_2^3/\alpha_1]/(\alpha_1^2M_\infty)^2\}}{4\beta[1+1/(\alpha_1M_\infty)^2]}, \tag{8}$$

where

$$\alpha_1 = f_1+\cos\theta, \qquad \alpha_2 = 2f_2+f_1'\sin\theta,$$

$$\alpha_3 = 3f_3+(f_2'-f_1'f_1)\sin\theta, \qquad \beta = 2/(\gamma+1),$$

$$p_1 = \beta\alpha_1^2-\frac{\gamma-1}{\gamma+1}/(\gamma M_\infty^2), \qquad p_2 = 2\beta\alpha_1\alpha_2,$$

$$v_{R1}=\frac{(p_2+2\gamma p_1\cos\theta+p_1'\sin\theta)/\rho_1+f_1(v_2-2\sin^2\theta)}{f_1^2-\gamma p_1/\rho_1}$$

$$v_2=\beta\alpha_2\left[1+\frac{1}{(\alpha_1M_\infty)^2}\right], \qquad \rho_1=1/\left[\frac{\gamma-1}{\gamma+1}+\frac{\beta}{\alpha_1^2M_\infty^2}\right]$$

Here the assumption for a spherical nose, $R_b = 1$, is made, otherwise the above expressions become very complicated.

For the case $\gamma = 1.4$, $\theta = 0$, $R_b = 1$, and $M_\infty = \infty$, we have

$$R_s-1=\Delta=\frac{1}{5}t-\frac{14}{75}t^2+\frac{392}{3375}t^3-\frac{2744}{50625}t^4+\frac{76832}{3796875}t^5$$

$$-\frac{1075648}{170859375}t^6+\frac{4302592}{2562890625}t^7-\frac{15059072}{38443359375}t^8+\cdots.$$

$$p_b=\frac{6}{5}-\frac{56}{75}t+\frac{2744}{3375}t^2-\frac{32928}{50625}t^3+\frac{4994080}{11390625}t^4$$

$$-\frac{45177216}{170859375}t^5+\frac{7800599296}{53820703125}t^6-\frac{58188254208}{807310546875}t^7\cdots. \tag{9}$$

Here the first two terms for R_s were found by Cabannes and the next two extended by Bausset.

The algebraic expressions in terms of the rational numbers of integer arithmetic are limited for the case $M_\infty = \infty$ and $\theta = 0$ because of existence of a square root for f_1 in equation (8). The computation for $M_\infty \neq \infty$ is carried out up to 30 terms by a computer in floating-point arithmetic. The rate of convergence for the higher Mach numbers is faster than that of the lower ones. Even at a Mach number as low as 1.2, these number of terms are sufficient.

The series in equation (9) may be written as:

$$R_s-1=\Delta=\frac{3}{28}\left[1-\exp(-\frac{28}{15}t)\right]$$

$$p_b=\frac{5}{6}\left[1+\frac{1}{5}\exp\left(-\frac{28}{15}t\right)\right]^2 \tag{10}$$

$$\rho_b=6. \qquad \text{for } \gamma=1.4,\ M_\infty=\infty,\ \text{and } \theta=0.$$

The foregoing expressions for an arbitrary Mach number and γ are lengthy. For sake of brevity, we present these for $M_\infty = \infty$, $\gamma = 1.4$, and $\theta = 0$. From equations (2) and (10), we may see that the density behind the shock wave is constant, $\rho_s = \rho_b = 6$; a stationary shock wave, $d/dt\ R_s = 0$, may be formed as $t \to \infty$; and the shock stand-off distance, Δ at $t = \infty$ is equal to 0.107, which is about 20 percent less than the known finite difference solution of Van Dyke and Gordon, $\Delta = 0.128$ [7], and about 9.3 percent less than the constant density solution of Lighthill, $\Delta = 0.1183$ [8]. The stagnation pressure at $t = \infty$ is equal to 0.8333, which is about 10 percent less than the known solution of Van Dyke and Gordon, $p_b = 0.9197$. The inaccuracy of the above results is primarily due to the one-step forward finite difference expansion of the solution from the shock front to the body surface (equation (7)). Consequently, the detailed variations of the flow field within the shock layer are not adequately considered. The pressure gradient on the body surface,

$$\frac{d}{dt}p\Big|_{R=R_b}$$

at $M_\infty = \infty$ and $\theta = 0$ is equal to zero, hence, $p_s = p_b$. The pressure behind the shock front is usually less than that on the body surface, therefore, the underestimation on the stagnation pressure is expected. The velocity of the shock wave decreases monotonically. If we assume that a stationary shock front is established when the shock wave reaches 99 percent of the stationary position, then the time required to establish a stationary shock front at $M_\infty = \infty$, $\gamma = 1.4$, and $\theta = 0$ is equal to 2.467.

At $\theta > 0$, no close form expression as shown in equation (10) may be found. The series begins to diverge after a few terms of expansion (9 or 10 terms for $M_\infty = \infty$, at $\theta = 30$ deg where the sonic line is located, and fewer terms for the lower Mach numbers). The slow convergence of the series near the sonic point, particularly at low Mach numbers, is a problem frequently encountered in solving the blunt-body problem [5, 6, 9]. As pointed out by Van Dyke, the difficulty is due to the existence a singular limiting line which is closer to the sonic point than the body surface. Such difficulty can, sometimes, be improved or removed by mapping the singularity away from the region of interest. Since the errors of the present exact solutions at the stagnation point are on the order of 10 percent, no effort is made to improve the solutions near the sonic point.

Modified Method. For a continuous and differentiable function there exists a ξ, for $R_b < \xi < R_s$, such that

$$f'(\xi)=\frac{f(R_s)-f(R_b)}{R_s-R_b} \tag{11}$$

Let $\xi = R_b$, it gives a forward difference equation (equation (7)), and $\xi = R_s$, a backward difference equation. When the value of $f'(\xi=R_b)$ is markedly different from that of $f'(\xi=R_s)$, and higher derivatives are not present, it is desirable to set $\xi = \frac{1}{2}(R_s + R_b)$. Equation (7) is then replaced by

$$v_s(\theta,t)=v_b+v_R(\xi)\Big|_{\xi=\frac{1}{2}(R_s+R_b)}\cdot(R_s-R_b) \tag{12}$$

Here the series for v_R ($\xi = R_b$) is finite, and that for v_R ($\xi = R_s$) is infinite and has a small radius of convergence. Hence, the series for v_R ($\xi = \frac{1}{2}(R_s + R_b)$) is also infinite and has a modest radius of convergence. Let $t = \bar{t}$ at $\xi = \frac{1}{2}(R_s + R_b)$. Then the value of $\bar{t}$ may be found from the inverse function of the equation defining the shock wave. Unfortunately, the inverse function of the shock wave converges very slowly and it is difficult to find $\bar{t}$ from few terms of series expansion. To remedy this we may estimate the value of $\bar{t}$ from the known solution as shown in Fig. 2 or from equation (10). It is found that $\bar{t}$ is approximately equal to $t_s/4$, where t_s is the time for the shock wave to reach its stationary position. (According to the first method it is the time for the shock wave to reach 99 percent of the stationary position.) Also, a small deviation of $\bar{t}$ does not affect solution significantly. After two or three iterations, we may find $\bar{t}$ accurate to three significant figures.

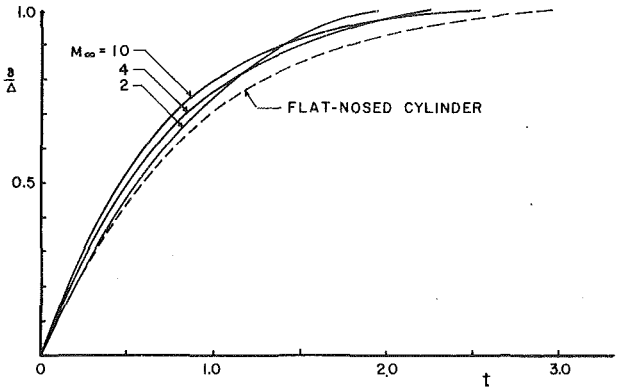

Fig. 2 Shock wave trajectories ($\gamma = 1.4$)

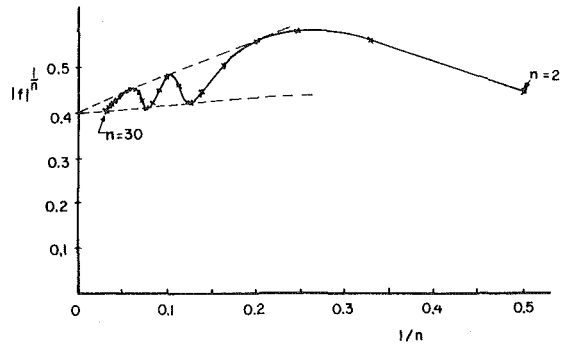

Fig. 3 Cauchy root test for the shock wave ($M_\infty = \infty$, $\gamma = 1.4$, and $\theta = 0$)

Table 1 lists the ratios of $t_s/\bar{t}$. Now, replacing $\bar{t}$ in v_R (ξ) of equation (12) by t and equating like powers of t to zero result in a sequence of algebraic equations which determine the coefficients for the shock wave and other flow variables. The computations were carried out by using a double-precision routine on a CDC76 machine. The series is extended up to 30 terms at the stagnation point and 9 terms near the sonic point.

Any analytic function has a power series development at every regular point. The convergence within a circle extends to the nearest singularity. A function in any region, or even on a line segment, is ordinarily defined uniquely in a much larger region of the complex plane and can be completed by the process of analytic continuation. For a given series, the radius of convergence can be assessed by its coefficients. One of the most useful methods is a graphical version of the Cauchy root test. According to this test, the radius of convergence, R, of power series, $\Sigma f_n t^n$, is

$$R = \lim_{n \to \infty} |f_n|^{1/n}$$

The limit is most accurately estimated from a finite number of coefficients by plotting the roots, $|f_n|^{1/n}$, versus $1/n$ and by extrapolating the $1/n$ to zero to find R. Fig. 3 is the plot of the first 30 terms of series defining the shock wave at the stagnation point showing a damped oscillation toward a limit at 0.4. The sign of the series alternates regularly with the exception of the first and eighth terms. This indicates that the nearest singularity does not lie in the region of physical interest, but rather in its analytical continuation upstream of shock wave. (We also attempted using D'Alembert's ratio test, advanced by Van Dyke [10], and found the amplitude of the damped oscillation several times larger than the root test; it is more difficult to find an accurate value at the point of interception). Once the point of interception is found, the series can be improved by using the Euler transformation, recasting the series in powers of a new variable, $\lambda = t/(0.4 +$

Table 1 Ratios of t_s/t

M_∞	$\gamma = 5/3$	$\gamma = 1.4$	$\gamma = 1.2$
10	4.42	4.96	5.75
6	4.28	4.75	5.48
4	3.95	4.42	5.05
3	3.44	4.09	4.68
2	2.85	3.55	3.98

Table 2 Locations of the nearest singularities β

M_∞	$\gamma = 5/3$	$\gamma = 1.4$	$\gamma = 1.2$
10	0.488	0.408	0.358
6	0.505	0.425	0.378
4	0.534	0.454	0.397
3	0.568	0.487	0.429
2	0.642	0.560	0.500

t), instead of t. For example,

$$R_s = 1 + f_1(\theta)\lambda + f_2(\theta)\lambda^2 + f_3(\theta)\lambda^3 + \ldots$$

This implies that we mapped the nearest singularity away from the region of interest. Table 2 lists the values of the nearest singularities we have found by means of the Cauchy root test.

Results and Discussions

Figure 1 presents the bow shock at $M_\infty = \infty$ and $\gamma = 1.4$, after a nearly stationary position is reached. The dotted line is based upon the first method, in which the shock stand-off distance increases monotonically until a maximum value of 0.107 is reached at $t = \infty$. The solid line is based upon the modified method at the first occasion when $d/dtR_s = 0$ at $\theta = 0$. The shock stand-off distance from the modified method is equal to 0.119 which agrees with the constant density solution of Lighthill, $\Delta = 0.1186$ [8]. When the velocity of the shock wave at $\theta = 0$ becomes zero and that at $\theta > 0$ does not. After $d/dtR_s = 0$ at $\theta = 0$, the shock front begins to oscillate. In the first several oscillations, the shock stand-off distance at $\theta = 0$ could be as low as 0.1 and as high as 0.15 with an average value of 0.119. At a much later time the amplitude of the oscillations becomes larger particularly at the downstream region near the sonic point. There is no occasion that the entire shock front becomes stationary simultaneously. These difficulties arise from the downstream singularities other than the one we have found. The solution from the modified method shows a significant improvement over the first method at the sonic point as well as the stagnation region. Fig. 4 gives the complete set of the stand-off distances for $\gamma = 1.2$, 1.4, and 5/3; and Mach numbers from 2.0 to 10. Also presented are the experimental data of Syshchikova, Berezkina, and Semenov [11] for carbon dioxide and the numerical solutions of Van Dyke and Gordon [7]. The present solutions match reasonably well with the experimental data and are in good agreement with the numerical solutions at higher Mach numbers.

Figure 2 represents the trajectories of the shock wave at various Mach numbers. Also shown is the numerical solution of Mils, Mirels, and Wang [4] for a flat-nosed infinite cylinder. The initial velocity of the present solutions follows a nearly straight line trajectory and is proportional to the Mach numbers. The conclusion is in agreement with the experimental data of Syshchikova, Berezkina, and Semenov [11]. After the shock wave reaches approximately 80 percent of the stand-off distance, the velocity for the higher Mach numers becomes much slower. Fig. 5 shows the time required to reach the various locations of the shock front. Also shown are the experimental results of Syshchikova, et al., and the

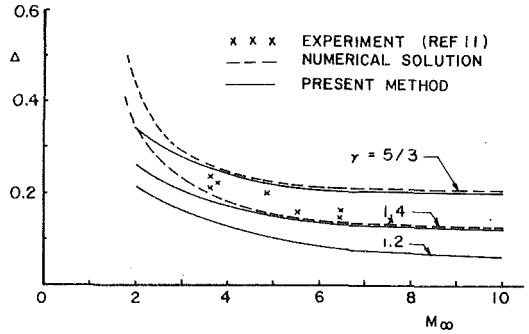

Fig. 4 Shock wave stand-off distances

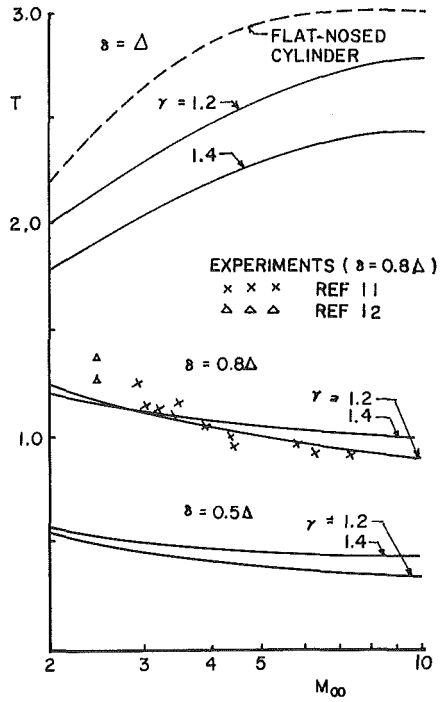

Fig. 5 Bow shock formation time

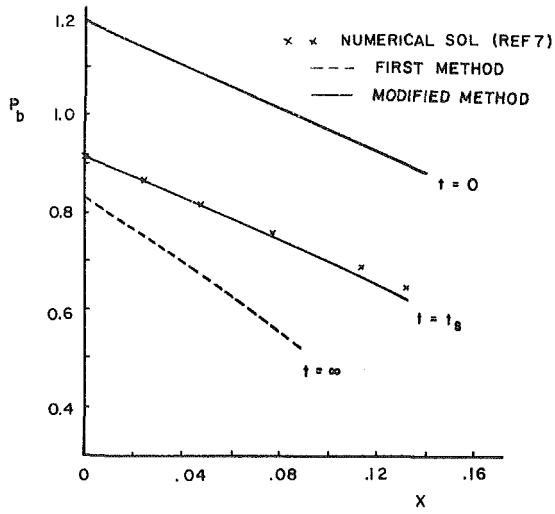

Fig. 6 Surface pressure ($M_\infty = \infty$ and $\gamma = 1.4$)

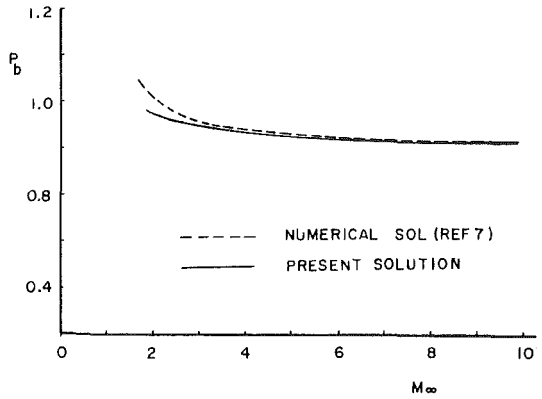

Fig. 7 Stagnation pressure ($\gamma = 1.4$)

numerical solution of Miles, et al. Because of three dimensional relief effect, we expect that the shock formation time for the sphere shall be less than that of the flat-nosed cylinder. The shock wave approaches its final steady-state position asymptotically at a very slow rate. It is difficult to measure the time at which the shock front reaches its final steady-state position. Therefore, the available experimental data were taken at the time when the shock front reaches 80 percent of the steady-state position ($\delta = 0.8\ \Delta$). At a first glance, we found that the time required from the experiments was too high. After careful studies on the series of the shadowgraph pictures (Fig. 1 [11]), we found that the time recorded on the experiments was started when the incident shock wave hits the tip of sphere. Immediately afterward, the shock wave moves away from the sphere at $\theta = 0$. In the downstream region, $\theta > 0$, the shock wave moves continuously toward the surface of sphere. It reflects back after hitting the surface of sphere at a much later time. In the analytical model, we assume that, at $t = 0$, an attached stationary shock wave stands on the front of the obstacle. Thus, we are confident to state that the average time required from the experiments was twice longer than that of the analytical model. Because of this reasoning, the experimental data were scaled down by a factor of two. Here, it is interesting to note that the time required to establish a stationary shock wave is proportional to the Mach number, this conclusion agrees with the Miles, Mirels, and Wang's analysis. The time to reach 80 percent of the stand-off distance is inversely proportional to the Mach number, and matches well with the experimental data. The present solutions are also compared with the experimental data of Zienkiewicz and Malloch [12]. Because their experiments were conducted at low Mach numbers, the agreement is relatively poor (Fig. 5).

Figure 6 depicts the surface pressures for $M_\infty = \infty$ and $\gamma = 1.4$ for both methods. The results from the modified method are in agreement with the known numerical solutions. Fig. 7 shows the surface pressure at the stagnation point for $\gamma = 1.4$. The comparison is more favorable in the region of the higher Mach numbers.

References

1 Cabannes, H., "Étude du Départ d'un Obstacle dans un Fluide au Repos," *La Recherche Aeronautique,* Vol. 36, Nov.-Dec. 1953, pp. 7-12.

2 Bausset, M. Max., "Étude du Départ d'un Obstacle dans un Fluide au Repos," *C. R. Academy of Science,* Paris, Vol. 261, Nov. 1965, pp. 4613-4616.

3 Bausset, M. Max., "Sur le Probleme de l'Onde de Choc Détachée dans les Écoulements Stationnaires," *C. R. Academy of Science,* Paris, Vol. 261, Dec. 1965, pp. 4983-4986.

4 Miles, J. W., Mirels, H., and Wang, H. E., "Time Required for Establishing Detached Bow Shock," *AIAA,* Vol. 4, No. 6, June 1966, pp. 1127-1128.

5 Van Dyke, M. D., *Perturbation Methods in Fluid Mechanics,* Academic Press New York, 1964.

6 Chang, S. S-H., "A Theory of Supersonic Flow Past Steady and Oscillating Blunt Bodies of Revolution," *AIAA,* Vol. 9, No. 9, Sept. 1971, pp. 1754-1762.

6 Van Dyke, M., and Gordon H., "Supersonic Flow Past a Family of Blunt Axisymmetric Bodies," NASA Report No. 1, 1959.

8 Lighthill, M. J., "Dynamics of a Dissociating Gas," Part I, *Journal of Fluid Mechanics,* Vol. 2, 1957, pp. 1-32.

9 Schwarts, L. W., "Series Solution for the Planer Axisymmetric Blunt Body," *The Physics of Fluids,* Vol. 18, No. 12, Dec. 1975, pp. 1630-1638.

10 Van Dyke, M., "Extension of Goldstein's Series for the Oseen Drag of a Sphere," *Journal of Fluid Mechanics,* Vol. 44, No. 2, 1970, pp. 365-372.

11 Syshchikova, M. P., Berezkina, M. K., and Semenov, A. N., "Formation of Frontal Shock Waves at Blunt Bodies in Shock Tubes," *Soviet Physics - Technical Physics 9,* May 1965, pp. 1549-1553.

12 Zienkiewicz, H. K., and Malloch, I. D., "Establishment of the Bow-Wave in the Supersonic Flow of Carbon Dioxide Past a Sphere," *The Aeronautical Quarterly,* Vol. 12, Feb. 1968, pp. 51-58.

Velocity Characteristics of Confined Coaxial Jets With and Without Swirl

M. A. Habib

J. H. Whitelaw

Imperial College of Science and Technology,
Mechanical Engineering Dept.,
London, England

Measured values of the velocity characteristics of turbulent, confined, coaxial-jet flows have been obtained, without swirl, for ratios of maximum annulus to pipe velocities of 1.0 and 3.0 and with a swirl number of 0.23 for a velocity ratio of 3.0. They were obtained by a combination of pressure probes, hot-wire and laser-Doppler anemometry. The results are compared with calculations, based on the solution of finite-difference forms of the steady, Navier-Stokes equations, and an effective-viscosity hypothesis. The measurements allow the influence of confinement and swirl to be quantified and show, for example, the increased tendency towards centerline recirculation which results from both. The results with the three types of instrumentation allow a comparison within the corner recirculation region which reveals that serious errors of interpretation of mean-velocity measurements need not arise. The two-equation model, although able to represent the non-swirling flow is less appropriate to the swirling flow and the reasons are indicated.

1 Introduction

The velocity characteristics of confined coaxial jets are of particular relevance to furnace and combustor flows and the previous investigations of Table 1 were carried out with these applications in mind. These previous measurements encompass a wide range of flows and were obtained by a combination of pressure probes, hot-wire and laser-Doppler anemometers. As indicated by Becker and Brown [8], for example, pressure probes are subject to errors in regions of significant flow fluctuations. Similarly, the analysis of hot-wire signals becomes increasingly uncertain as the turbulence intensity increases above around 20 percent. Measurements obtained by laser-Doppler anemometry are also subject to uncertainty and, for those of references [3 and 4] the finite width of the filters used to analyze the Doppler signals limited the precision of mean-velocity results to, at best, ± 2.5 percent with correspondingly larger errors in normal stresses. Nevertheless, in regions of recirculation, such as are found in confined jet flows and in contrast to pressure and hot-wire probes, the unobtrusive method provides answers with determinable precision.

The present measurements were obtained in the same geometrical configuration as that of reference [7] but included a swirling-flow arrangement and used laser-Doppler anemometry. The coaxial jets, with and without swirl, were identical to those used for the unconfined-jet investigation of Ribeiro and Whitelaw [9]. Thus, the results of references [7, 9] and this paper allow comparison of velocity characteristics of confined coaxial jets with and without swirl and confinement. The present laser-Doppler anemometer results obtained without swirl also allow a detailed comparison between the two techniques in regions of flow recirculation and high turbulence intensity. A small range of measurements were also obtained with a three-hole pressure probe and are included in the comparison of measurement techniques.

The flow configuration and instrumentation are described briefly in the following section which also includes an assessment of possible measurement errors. The results are presented in the two subsections of Section 3. The first subsection presents the results obtained without swirl and included a detailed comparison of the present results and the previous hot-wire results of reference [7]. The measurements are intended mainly to facilitate understanding of isothermal confined flows with and without swirl and provide a basis for the understanding of related combusting flows. In addition, they are relevant to calculation methods such as that described in references [7 and 10] and the Discussion of Section 4 included comments which assists an evaluation of the corresponding turbulence models.

2 Flow Configuration, Instrumentation and Error Analysis

Figure 1 presents a line diagram of the geometrical arrangement and a block diagram of the laser-Doppler instrumentation. The co-axial pipe arrangement is identical to that of reference [7, 9 and 11]; the confining chamber to that of reference [7]; and the swirler to that of reference [9]. Measurements were obtained with the two velocity ratios ($\bar{U}_a/\bar{U}_p$) and swirl numbers indicated in Table 2; the velocity ratios and Reynolds numbers are based on maximum velocities.

The three-hole pressure probe was similar to that described in reference [12]; it was calibrated in the potential core of a

Contributed by the Fluids Engineering Division of THE AMERICAN SOCIETY OF MECHANICAL ENGINEERS and presented at the Winter Annual Meeting, New York, N. Y., December 2-7, 1979. Manuscript received at ASME Headquarters August 17, 1979.

Table 1 Previous measurements in confined-jet flows

Author	Ref.	d_o/D_e	d_i/d_o	d_p/d_i	$\bar{U}_a/\bar{U}_p$	S	L/D_e	Instrumentation
Wingfield (1967)	1	0.355	0.526 and others	0.327	3.127	0.0	6	pitot probe
Mathur, et al. (1967)	2	0.402 square duct	0.324	0.0	∞	0.193 0.415 and others	5.0	pitot probe
Baker, et al. (1974)	3	0.183	0.218	$\simeq 1.0$	2.32	0.0 0.52	3.0	L.D.A.
Baker, et al. (1974)	4	0.183	0.218	$\simeq 1.0$	2.32	0.5	3.0	L.D.A.
Pai, et al. (1975)	5	0.25	0.262	0.8	0.35	0.0	8.5	Prandtl probe hot-wire anemometer
Owen (1976)	6	0.7	0.714	$\simeq 1.0$	12.0	0.0	9.6	L.D.A.
Habib and Whitelaw (1978)	7	0.356	0.485	0.745	3.0 1.0	0.0	4.76	hot-wire anemometer

Table 2 Flow conditions

$\bar{U}_a/\bar{U}_p$	S	Re_a	Re_p
3.0	0	77,500	18,800
3.0	0.23	76,000	18,540
1.0	0	50,500	35,500

round jet for the range of pitch angle experienced in the coaxial jet flows and introduced radially from the circumference of the cylinder. The total pressure measurements were obtained after the two static pressures had indicated the correct alignment of the total pressure hole. It may be expected to allow precise measurements at low turbulence intensities and to give high values, with an error proportional to the turbulence intensity squared. Thus, with intensities of around 60 percent it will yield values of mean velocity which are approximately 10 percent high.

The laser-Doppler anemometer comprised an Argon laser (Spectra Physics Model 164) operated at 488 nm and 200 mW. The laser beam passed through a water-filled acousto-optic cell which provided zero and first order beams with a frequency difference of 21 MHz [13]. The beams were separated to a distance of 71.5 mm, made parallel and focussed to their intersection by a 200 mm focal-length lens. Forward-scattered light was collected with a 100 mm diameter lens of focal length 150 mm and focussed to a pin-hole in front of a photomultiplier cathode (EMI 9815B). The optical components were secured to a 2 m long optical bench located as a milling table which allowed translation in two horizontal and orthogonal directions with a precision of better than 0.1 mm. The more important characteristics of the optical arrangement are indicated on Table 3. The plenum chambers of the annulus and pipe flow were seeded equally with a small quantity of atomized silicone oil.

Table 3 Optical characteristics

Half angle between incident light beams	11.1 deg
Frequency difference	21 MHz
Transform relationship	0.752 MHz/m/s
Length of intersection volume at e^{-2} locations	0.3 mm
Diameter of part of intersection volume observed by photodetector	0.095 mm
Magnification of light-collection arrangement	1.5

The signal from the photomultiplier was passed to an oscilloscope and to a spectrum analyzer (Hewlett Packard Model 9553B/8552A/141T) which was swept with bandwidths of 30, 100 and 300 kHz. A microprocessor evaluated the mean and rms velocity values, as described in reference [14] with the equations

$$\bar{U} = \frac{\lambda}{2\ \sin\ (\phi/2)} \bar{f} = \frac{\lambda}{2\ \sin\ (\phi/2)} \int P(f) f\ df \tag{1}$$

and

$$\overline{u^2} \equiv \overline{(U-\bar{U})^2} = \left(\frac{\lambda}{2\ \sin\ (\phi/2)}\right)^2 \int P(f)\ \ (f-\bar{f})^2 df \tag{2}$$

where

$$\int P(f)\ df = 1.0.$$

Nomenclature

D_e = the enclosure inner diameter
d_i = the annulus inner diameter
d_o = the annulus outer diameter ($=2r_2$)
d_p = the inner diameter of the central pipe
f = frequency
k = kinetic energy of turbulence
L = the model furnace length
P = probability density function
R_e = Reynolds number
R = the model furnace radius
r = radius
S = swirl number, defined as:

$$S \equiv \frac{\int_0^{r_2} r^2 \bar{U}\bar{W} dr}{r_2 \int_0^{r_2} r(\bar{U}^2 - \tfrac{1}{2}\bar{W}^2) dr}$$

U = axial velocity
u = axial velocity fluctuation
v = radial velocity fluctuation
W = tangential velocity
w = tangential velocity fluctuation
ϵ = the rate of turbulence dissipation
μ_{eff} = effective viscosity
λ = light wave length
ϕ = crossing beam angle
ρ = fluid density

Subscripts

a = annulus flow
$\mathfrak{L}$ = the value at the centre-line
0 = axis location at the inlet of the enclosure
P = pipe or pipe flow

Superscripts

$-$ = mean value

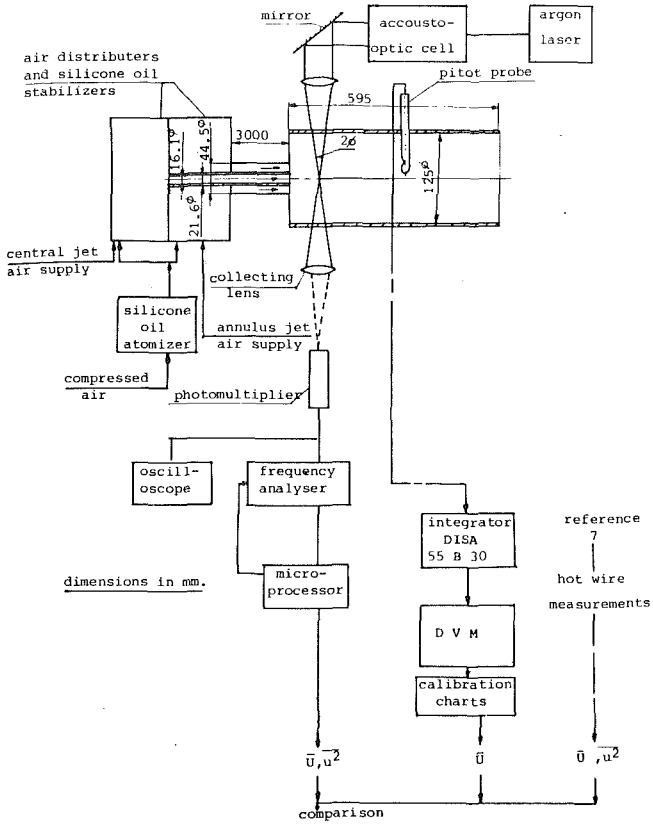

Fig. 1 Layout of the measurement techniques; ____ Laser-Doppler anemometry, _ _ _ Hot-wire anemometry, ___ Pitot tube

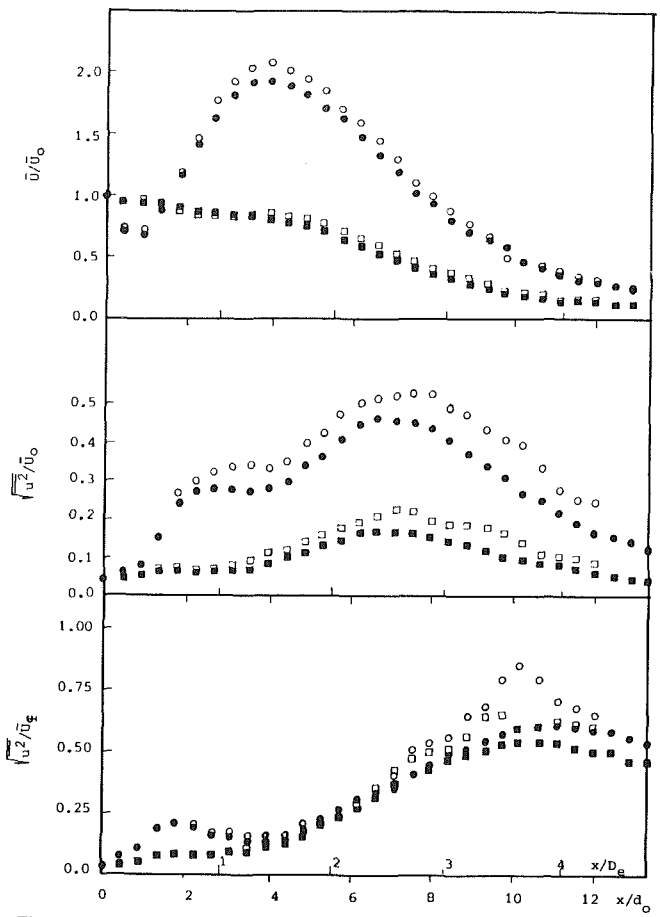

Fig. 2 Axial profiles ($S=0.0$) o, $\bar{U}_a/\bar{U}_p = 3.0$, □, $\bar{U}_a/\bar{U}_p = 1.0$; open symbols, laser; closed symbols, hot wire

In general, laser-Doppler anemometers with signal processing based on averaging of a number of individual frequency measurements may be subject to errors due to gradient and particle broadening, to incorrect measurement of signal frequency, to the number of signals used to form the average, to the method of averaging and to photodetector averaging. The optical errors experienced in the present flow are negligible and the spectrum analyzer reduces frequency-measurement uncertainty to that associated with the bandwidth of the filter which, with mean-measured frequencies in the range from 17 MHz to 60 MHz, did not exceed 1.0 percent. The number of signals used to form the averages ranged from 6,000 to 25,000 and, in accordance with the calculations of reference [15] implies uncertainties of less than 1.8 percent in mean velocity and 1.7 percent in rms values. As indicated in reference [16] the averaging characteristics of the photomultiplier will bias the signal towards lower velocities but, with the present frequency shift, the effect may be expected to be small and negligible in the case of the rms values. An opposite bias stems from the method of averaging and, in view of the shape of the measuring volume and the various time characteristics of the electronic-processing instrumentation cannot be exactly determined. It is clear, however, from the results of reference [17] that the two effects are likely to be nearly equal for the present combination of optical and signal-processing instrumentation and no corrections have been applied.

3 Results

Without Swirl. Fig. 2 represents distributions of the mean axial velocity, the rms values of the axial velocity fluctuations normalized with the maximum pipe-exit velocity and the corresponding turbulence intensities for the two velocity ratios. The previous hot-wire measurements of reference [7] are reproduced on the same figure. As can be seen, the two sets of results of Fig. 2 are in general accord and confirm the corresponding conclusions of reference [7]. The magnitude of the differences in mean velocity does not exceed 10 percent of the maximum velocity for either flow. The maximum discrepancy between the rms values obtained by the two techniques is of the order of 17 percent of the maximum rms values for each flow and is associated with the higher intensities and lower mean velocity values. In view of the rectification characteristic of the hot wire, it is to be expected that measured mean values should be high and rms quantities low in regions of turbulence intensity greater than around 30 percent. Also any overall bias of the laser-Doppler anemometer results should cause the mean velocities to be high in regions of turbulence intensity greater than around 20 percent but have little effect on the second moments. The discrepancies in mean values for $x/D_e < 2$, where the turbulence intensity is between 10 and 25 percent is probably associated partly with the method of analyzing the hot-wire signals and partly from a small overall bias to the laser results. In this region, the correct result can be expected to lie between the two curves and closer to the hot wire measurements. In the downstream region, where the turbulence intensity is high, both sets of mean values may be slightly high and the correct rms values should again be between the two sets of results but closer to the laser measurements.

Radial profiles of the axial component of mean velocity and the corresponding rms values are presented on Figs. 3 (a) and

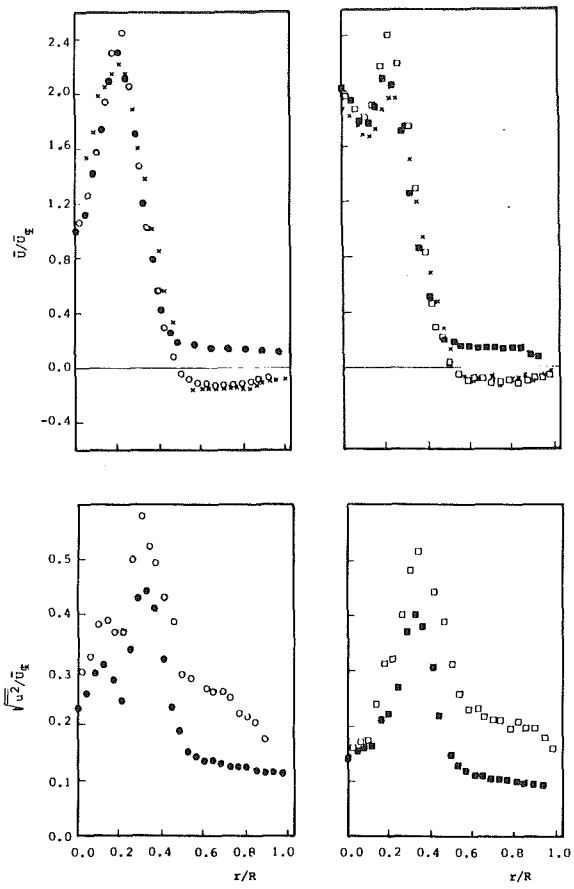

Fig. 3(a) Radial profiles ($S=0.0$, $x/D_e=0.616$) x, pitot tube results, otherwise as in Fig. 2

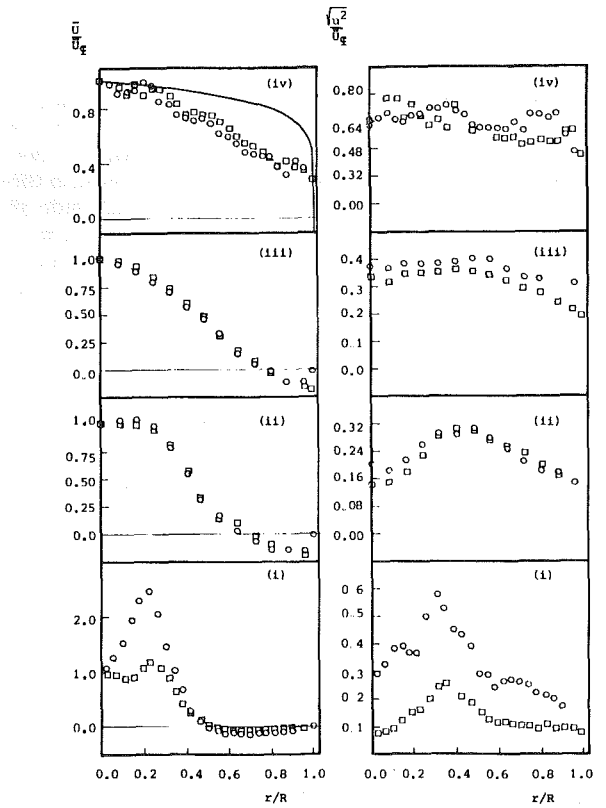

Fig. 3(b) Radial profiles ($S=0.0$) (i) $x/D_e=0.616$; (ii) $x/D_e=1.43$; (iii) $x/D_e=2.23$; (iv) $x/D_e=3.67$; ____, fully developed pipe flow; otherwise as in Fig. 2.

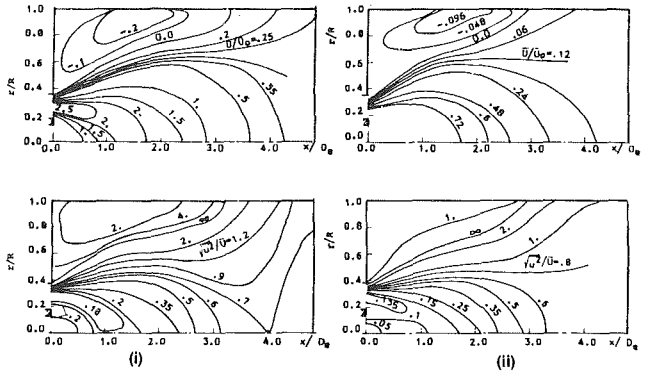

Fig. 3(c) Contours of the mean velocity and turbulence intensity ($S=0.0$ (i) $\bar{U}_a/\bar{U}_p=3.0$; (ii) $\bar{U}_a/\bar{U}_p=1.0$

3(b). As can be seen from Fig. 3(a), the results obtained by the three measuring techniques at an upstream station are in reasonable agreement provided the hot-wire results obtained in the region of recirculation are recognized as corresponding to negative values. Although the intensities in the recirculation region are very large, the magnitude of the differences in measured values of mean velocity is small (<3 percent) of the maximum velocity and around 40 percent of the local value: the differences in values of rms values are considerably larger with the hot-wire, as expected, giving the erroneously low results.

The results of Fig. 3(b) at four x-locations, may be compared with the previous hot-wire results and support the conclusions of reference [7]. The mean velocity contours of Fig. 3(c) represent a considerable interpolation of the results of Fig. 3(b) but indicate a recirculation region which increases in length with increased velocity ratio. This increase in length is related to the increase in the total axial momentum, which is associated with the higher velocity ratio. The contours of turbulence intensity clearly indicate the extensive region of high values.

The pattern of the results is similar to that observed by previous authors, for example, references [1 and 3]. From examination of these results, it can be deducted that the length of the recirculation region is dependent on velocity ratio and on the dimensions of the geometry. For example, the increase in the velocity ratio from 1.0 to 3.0 (increase in the total axial momentum by a ratio of 2.067) increases the length from $2.96D_e$ to $3.28D_e$ which corresponds to $9.2h$ and $10.2h$, respectively where h is equal to $(R-d_o/2)$. The present configuration is similar to the backward-facing step, see for example, Bradshaw and Wong [18], where similarity is held between h and the step height. The unity velocity ratio case has a rather uniform velocity distribution and therefore the length of the recirculation zone, $9.2h$, can be compared with that of the backward-facing step of reference [18] i.e. $6h$. The difference is likely to stem from differences in the geometry and axial momentum and a slight difference in the boundary layer thickness at the obstacle position.

The agreement between the three sets of measurements is imperfect but this is unlikely to alter any fluid-dynamic conclusion. It can be expected, however, that both the laser and hot-wire anemometers will measure high modulus values of mean velocity and low rms values. In the region between the centre line and r/R of approximately 0.2, the turbulence intensity is comparatively small and the discrepancies may be attributed to the relative large length of the hot-wire sensor (1.25 mm). In the high turbulence region of recirculation, the laser-anemometer results can be expected to be within 20 percent of the correct mean values and it is useful to note that the pressure probe, in spite of possible interference effects, yields similar results.

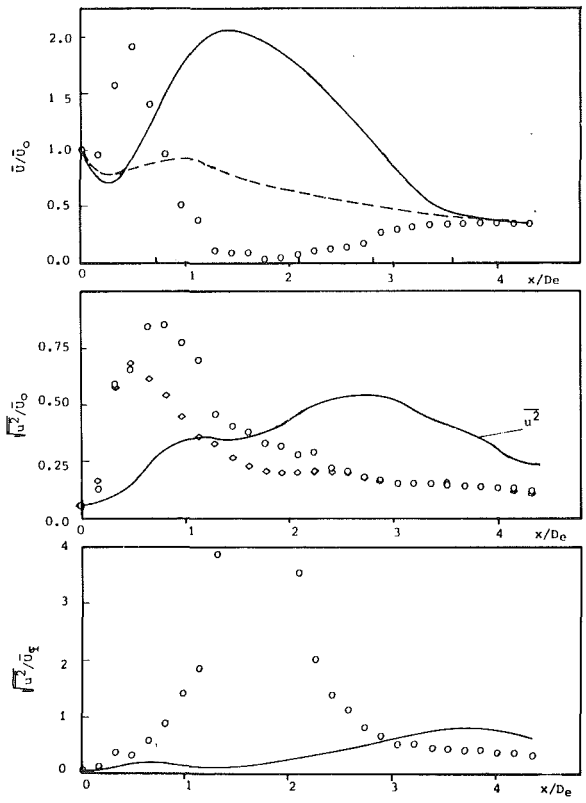

Fig. 4(a) Axial distributions ($\bar{U}_a/\bar{U}_p = 3.0$) o, $\overline{u^2}$ ◇, $\overline{v^2}$ and $\overline{w^2}$ (S = 0.23); —, (S = 0.0); _ _ _, reference [9] (free jet, S = 0.26), U_a/U_p = 1.4)

With Swirl. the laser-Doppler anemometer results of Fig. 2 are reproduced on Fig. 4 (a) which presents the measurements of mean axial velocity, the corresponding rms values and the turbulence intensities for a swirl number of 0.23. As previously observed by Ribeiro and Whitelaw [9] for their corresponding unconfined flow, the maximum rms velocity is closer to the jet exit plane with the swirl; a region of low velocity exists further downstream as the jet spreads more rapidly away from the centre line in the present flow. The axial distributions of the rms values of the two components of fluctuating velocity are similar in form with the circumferential component of very slightly lesser magnitude. This is again in accord with the free-coaxial jet. The maxima in the intensities are very much larger in the confined flow and are again located closer to the exit plane. The intensity of the free flow asymptotes to a value of around 0.25 and the present flow exhibits a similar tendency although from higher rather than lower values. Radial distributions of the axial and circumferential velocity components and the corresponding rms values are presented in Figs. 4(b) and (c). They are consistent with the greater spreading rate of the swirling flow. The distributions of mean axial velocity and normal stresses are already near uniform at x/D_e of 3.67. At the upstream stations, the influence of the swirl on the mean velocity is obvious and results in a rapid change in the profile shape between x/D_e of 0.616 and 1.43. In particular, the near zero velocity on the centre line at x/D_e of 1.43 is accompanied by a relatively high velocity at r/R of 0.8: the normal stress is already near-uniform at this location. The distributions of swirl velocity show a similar trend to the axial velocity except near to the pipe exit. Indeed, at the three downstream measuring stations, the distributions are similar to those of solid body rotation with near-uniform normal-stress profiles.

4 Calculations

Equations representing conservation of mass, momentum,

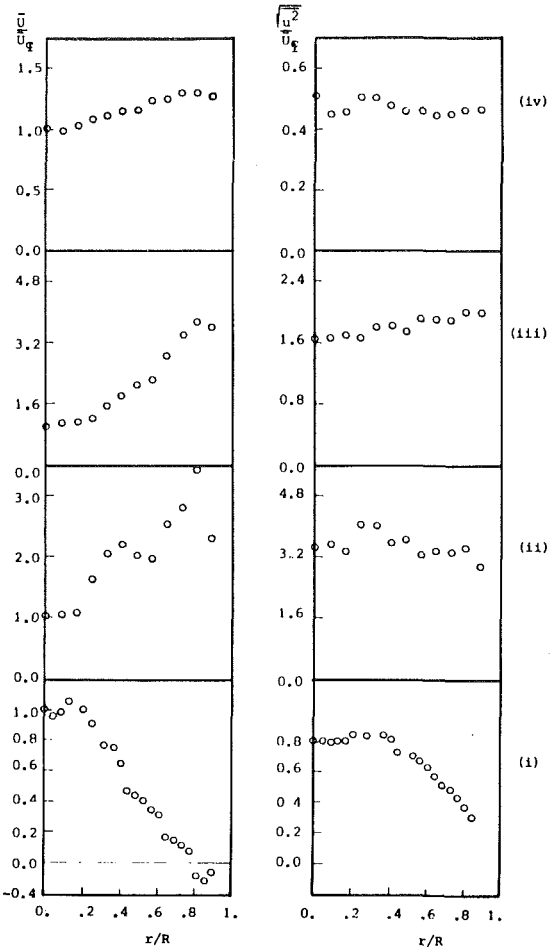

Fig. 4(b) Radial distributions of axial mean velocity and normal stress (S = 0.23); notation as in Fig. 3(b)

turbulent kinetic energy and its rate of dissipation were represented in the general form

$$\frac{\partial}{\partial x_j}(\bar{U}_j\Phi) - \frac{\partial}{\partial x_j}\left(\Gamma_\Phi \frac{\partial \Phi}{\partial x_j}\right) = S_\Phi \qquad (3)$$

and solved numerically. Details of the numerical scheme and the two-equation turbulence model may be found, for example, in references [19 and 20].

The boundary conditions corresponded to experiment wherever possible. Thus, the initial values of the components of mean axial and swirl velocity were known together with the respective normal stresses; the radial component of mean velocity was presumed zero. The initial values of dissipation rate were determined on the basis of a mixing length, i.e. $l = 0.03R$, where R is the radius of pipe or annulus and isotropy of the dissipating eddies is assumed. Symmetry and zero velocity on all walls were assumed and the flow was taken as fully developed at a downstream location where the results presented here were uninfluenced.

Typical results are presented on Figs. 5 and 6 for mean velocities and intensities respectively. The centre-line mean velocity distributions of Fig. 5 show simple trends with the poorer agreement for the swirling flow.

The results of Fig. 5 allow comparison between measured and calculated centre-line distributions of mean velocity for swirl numbers of zero and 0.23. As already indicated in reference [7] the general trends of the non-swirling flow are correctly represented but the velocity minimum and maximum have been underpredicted together with the length of the recirculation region. This result is consistent with the findings of reference [21] for bluff-body stabilized flows, where un-

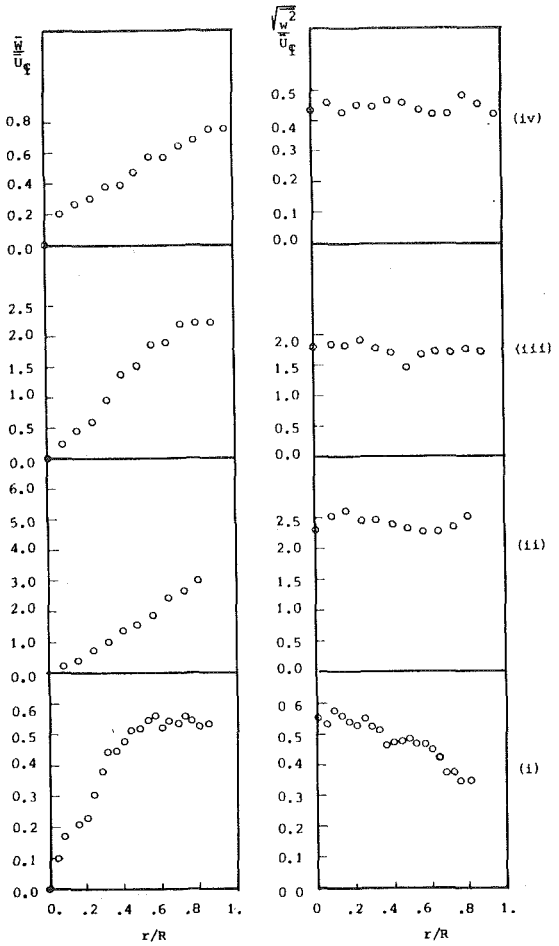

Fig. 4(c) Radial distributions of tangential velocity and normal stress ($S = 0.23$); notation as in Fig. 3(b).

derprediction was found to be of similar magnitude with the two-equation and with stress models. The swirling flow does not have the same initial region of recirculation but, instead, has a downstream region of near-zero velocity. Again, the maximum and minimum of the measurements are not well represented. Extensive numerical tests have shown that these results are essentially grid independent and, although numerical errors may still exist due to stream lines which diagonally cross the cells, they are unlikely to be the cause of the downstream discrepancies in either flow, particularly since the maximum cell Peclet number was 0.88.

In the non-swirling flow, the 20 percent discrepancy at x/D_e of 2 is associated mainly with the underprediction of turbulent diffusion. In the swirling case, the problem is compounded by additional streamline curvature and the need for additional generation terms in the equation for the transport of the Reynolds stresses. Bradshaw [22] has shown that eddy viscosity models do not represent this added generation and Morse [23] found it necessary to make the dissipation-equation constant $C_{\epsilon 1}$ a function of the Richardson number to represent his free swirling-jet flows.

The inability of the two-equation model to represent the velocity minimum on the centre-line of Fig. 5 is certainly associated with curvature effects and the inappropriateness of the presumed isotropic viscosity. As indicated by Rodi [24] and Gibson [25], for example, the assumption of a constant value for C_μ is inappropriate in curved flows; it has been shown to decrease rapidly with increasing Richardson number and to decrease with the ratio of turbulent production to dissipation. This suggests the need for the use of a model which does not require the specification of a value for C_μ, i.e.

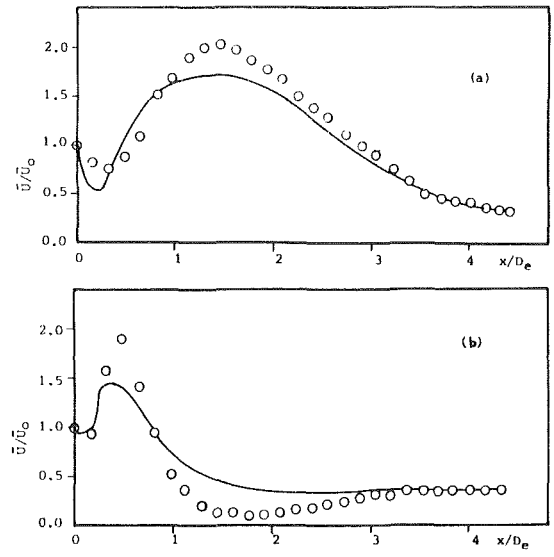

Fig. 5 Measured and calculated distributions of the mean velocity. o, Measurements; ____, Calculations, (a), $S = 0.0$; (b), $S = 0.23$.

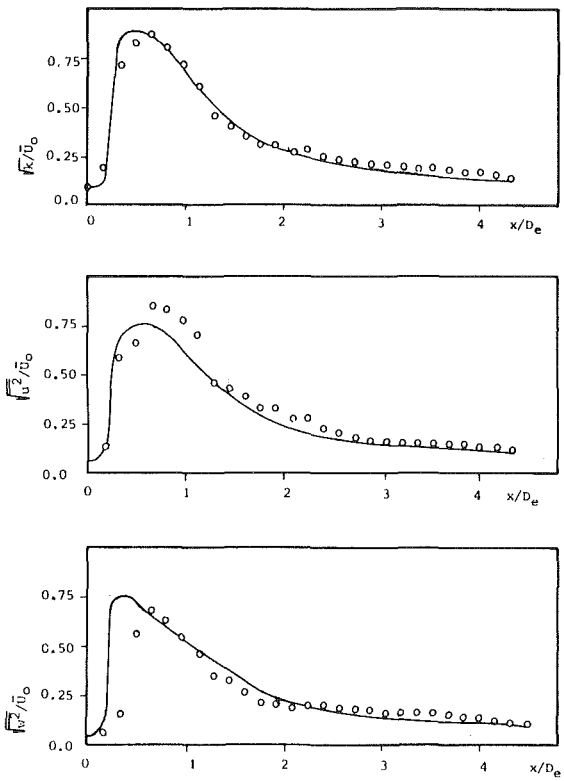

Fig. 6 Measured and calculated distributions of the kinetic energy of turbulence and normal stresses ($S = 0.23$) o, Measurements; ____, Calculations

a model based on the Reynolds stresses, but this requires the solution of equations for all six stresses in the present case. An algebraic-stress-model aproach may provide a more palatable solution, if the magnitude of the present discrepancies is considered important.

Fig. 6 indicates measured values of the two components of the rms of the velocity fluctuations and the kinetic energy. The agreement between the calculated and measured distributions of turbulence energy is excellent and suggests that the corresponding transport equation is a reasonable

representation. The two normal stresses are different by around 50 percent and this degree of anisotropy, of itself is probably insufficient to account for the discrepancy in the mean-flow results. The problem is consistent with that of reference [21] in that the extent of recirculation is underpredicted; also in common with the bluff-body calculations of reference [21] tests with reasonably-different values of initial-flow variables have shown that they are not responsible for the present discrepancies. In the present case the low production associated with the near centre-line region ensures that C_μ will be different from the prescribed value and probably leads to an incorrect representation of shear stress. This was certainly true of the non-swirling results of reference [7].

5 Discussion

The measurements allow a comparison between two obstrusive and one unobstrusive measuring techniques in regions of recirculation. Fig. 3(*a*) indicates discrepancies in the mean-velocity results on the recirculating region and at the velocity maximum. The hot-wire results are clearly incorrect but stem from a simple misinterpretation of the flow direction which can readily be appreciated. If rectified, they are in reasonable agreement with the laser anemometer results: the magnitude of the disagreement is of the order of 50 percent in some regions, due largely to the errors associated with the hot wire at the high values of local turbulence intensity but this represents less than 2 percent of the maximum velocity and is adequate for many purposes. Similarly, there are discrepancies between the pressure probe and laser-anemometer results but they are of the same magnitude. At least in this flow, the effect of probe interference does not appear to be of major significance. The low values of velocity associated with the Pitot tube and the velocity maximum are due, at least in part, to the spatial average observed by the probe.

The measured values of the rms of the velocity fluctuations show an expanded trend in the recirculating flow. The hot wire rectifies negative velocities and leads to values which are low whenever negative velocities are present. This is particularly noticeable in the region of recirculation, as previously observed by Simpson, Strickland and Barr [26], but is also present in the other regions of the flow where intensities are large. This is also shown by Fig. 2: the magnitude of the discrepancies are, however, seldom sufficiently great to permit erroneous fluid mechanic conclusions.

The present results indicate, with swirl, a region of near-recirculation on the centre line and between one and three furnace diameters downstream of the exit plane. Thus, as the swirl number is increased from zero, this tendency towards recirculation grows and will ultimately be realised as shown for example in reference [3] with a swirl number of 0.5. The intermediate swirl number of 0.23 provides a flow which is probably more difficult to present by calculation methods in that the near recirculation region is located away from solid surfaces. Calculations, in the absence of swirl, avoid the complexity of the related dependent variables and associated terms. With a swirl number of 0.5, the initial region of recirculation is tied to the exit geometry and the downstream flow is more easily represented.

The calculation of the non-swirling flow is imperfect but possibly adequate for many purposes. The representation of the swirling flow is less adequate and, even though the problem may exist over a limited range of swirl numbers, improvements are desirable. Empirical adjustments to constants may produce better results but a more satisfactory approach is to determine the extent to which an algebraic stress model, which allows for a non-isotropic viscosity, improves the calculations and to progress to a stress-transport model if required.

Acknowledgment

Financial support from the AERE, Harwell, is gratefully acknowledged.

References

1 Wingfield, G. A., "Mixing and Recirculation Patterns from Double Concentric Jet Burners Using an Isothermal Model," *Journal Inst. Fuel,* Vol. 40, 1967, p. 456.

2 Mathur, M. L., and MacCallum, N. R. L., "Swirling Air Jets Issuing from Vane Swirlers, Part 2 Enclosed Jets," *Journal Inst. Fuel,* Vol. 40, 1967, p. 238.

3 Baker, R. J., Hutchinson, P., Khalil, E. E., and Whitelaw, J. H., "Measurements of Three Velocity Components in a Model Furnace with and without Combustion," 15th Int. Symposium on Combustion, 1974, p. 553.

4 Baker, R. J., Hutchinson, P., and Whitelaw, J. H., "Velocity Measurements in the Recirculation Region of an Industrial Burner Flame by Laser Anemometry with Light Frequency Shifting," *Combustion and Flame,* Vol. 23, 1974, pp. 57-71.

5 Pai, B. R., Richter, W., and Lowes, T., "Flow and Mixing in Confined Axial Flows," *J. Inst. Fuel,* Vol. 48, 1975, p. 185.

6 Owen, F. K., "Measurement and Observations of Turbulent Recirculating Flows," *AIAA Journal,* Vol. 14, 1976, p. 1556.

7 Habib, M. A., and Whitelaw, J. H., "Velocity Characteristics of a Confined Coaxial Jet," ASME JOURNAL OF FLUIDS ENGINEERING, Vol. 101, 1979, p. 521.

8 Becker, H. A., and Brown, A. P. G., "Response of Pitot Probes in Turbulent Streams," *Journal of Fluid Mechanics,* Vol. 62, 1974, pp. 84-114.

9 Ribeiro, M. M., and Whitelaw, J. H., "Coaxial Jets with and without Swirl," Imperial College, Dept. of Mech. Eng. Reports FS/78/25, 1978, To be published in *Journal of Fluids Mechanics.*

10 Khalil, E. E., Spalding, D. B., and Whitelaw, J. H., "The Calculation of Local Flow Properties in Two-Dimensional Furnaces," *Institute of Journal Heat Mass Transfer,* Vol. 18, 1975, p. 775.

11 Durão, D. F. G., and Whitelaw, J. H., "Turbulent Mixing in the Developing Region of Coaxial Jets," JOURNAL OF FLUIDS ENGINEERING, Vol. 95, 1973, p. 467.

12 Hiett, G. F., and Powell, G. E., "Three-Dimensional Probe for Investigation of Flow Patterns," *The Engineer,* Vol. 213, 1962, p. 165.

13 Durão, D. F. G., and Whitelaw, J. H., "The Performance of Acousto-Optic Cells for Laser-Doppler Anemometry," *Journal Phys. E. Sci. Instruments,* Vol. 8, 1975, p. 776.

14 Durão, D. F. G., Laker, J., and Whitelaw, J. H., "Digital Processing of Frequency-Analysed Doppler Signals," *Proc. LDA Symposium. The Accuracy of Flow Measurements by Laser-Doppler Methods,* Copenhagen, 1975, p. 364.

15 Yanta, W. J., "Turbulence Measurements with a Laser Velocimeter," Naval Ordnance Laboratory, Maryland, Report TR 73-94, 1973.

16 Durão, D. F. G., and Whitelaw, J. H., "Relationship between Velocity and Signal Quality in Laser-Doppler Anemometry," *J. Phys. E.,* Vol. 12, 1979, p. 47.

17 Durão, D. F. G., Laker, J., and Whitelaw, J. H., "Bias Effects in Laser-Doppler Anemometry," Imperial College, Fluids Section Report FS/79/5, 1979, To be published in *J. Phys. E.*

18 Bradshaw, P., and Wong, F. Y. F., "The Reattachment and Relaxation of a Turbulent Shear Layer," *Journal of Fluids Mechanics,* Vol. 52, 1972, p. 113.

19 Habib, M. A., and Whitelaw, J. H., "Measured Velocity Characteristics of Confined Coaxial Jets with and without Swirl," Imperial College, Dept. of Mech. Eng., Report FS/78/46, 1978.

20 Gosman, A. D., and Ideriah, F. J. K., TEACH-T, "A General Computer Program for Two-Dimensional, Turbulent, Recirculating Flows," Department of Mech. Eng., Imperial College, London, 1976.

21 Pope, S. B., and Whitelaw, J. H., "The Calculation of Near-Wake Flows," *Journal of Fluid Mechanics,* Vol. 73, 1976, p. 9.

22 Bradshaw, P., "Effect of Streamline Curvature on Turbulent Flow," AGARDograph, Vol. 169, 1973.

23 Morse, A., Private Communication.

24 Rodi, W., "A New Algebraic Relation for Calculating the Reynolds Stresses," *Z. Ang. Math.* Vol. 56, 1976, p. 219.

25 Gibson, M. M., "An Algebraic Stress and Heat-Flux Model for Turbulent Shear Flow with Streamline Curvature," *Int. J. Heat Mas Transfer,* Vol. 21, 1978, p. 1609.

26 Simpson, R. L., Strickland, J. H., and Barr, P. W., "Features of a Separating Turbulent Boundary Layer in the Vicinity of Separation," *Journal of Fluid Mechanics,* Vol. 79, 1977, p. 553.

Dependence of Shock Characteristics on Droplet Size in Supersonic Two-Phase Mixtures[1]

W. J. Comfort III
Mechanical Engineer.

C. T. Crowe[2]
Professor.

University of California,
Lawrence Livermore Laboratory,
Livermore, Calif. 94550

In a dispersed two-phase flow, the mixture chokes at a velocity well below the vapor choking velocity, as shown by the velocity at the throat of a converging-diverging, two-phase, supersonic nozzle. The formation and abruptness of a normal shock wave in a two-phase mixture depends strongly on the coupling between phases, particularly upon droplet size. As droplet size becomes small, the mixture behaves as a continuum, and sharp discontinuities can occur at velocities above the two-phase choking velocity but below the vapor sonic velocity. An approximate analysis is performed to incidate the droplet size at which continuum behavior might be expected to occur. A numerical model, which includes the drag, buoyancy, Basset force, and the force associated with the virtual mass effect, is used to show droplet-size dependence in two-phase normal shock waves. For the examples presented, continuum behavior apparently is approached at droplet diameters between 1 and 2 μm, even through normal shock waves.

Introduction

High-velocity two-phase flows represent an increasingly common consideration in technology. Examples include: nuclear reactor phenomenology, rocket motor flows, gas-droplet flows in various combustion processes, water ingestion by jet engines during storms, and two-phase turbomachinery. The present paper results from work on understanding the potential loss mechanisms associated with a turbomachine designed to operate on very wet two-phase mixtures [1].

Significant shock-associated losses can occur in high-velocity two-phase-mixture flows when the fluid velocity exceeds the choking velocity of the two-phase mixture. The mass fraction of droplets in the mixture strongly affect the two-phase choking velocity as shown in Fig. 1. We define the two-phase choking velocity as the homogenous sound velocity of the mixture:

$$c=\sqrt{\frac{\partial p}{\partial \rho}}\Big|_s \tag{1}$$

In a dispersed flow the mixture chokes at a velocity well below the vapor choking velocity. This phenomenon is exhibited by the velocity at the throat of a converging-diverging two-phase nozzle. Because the choking velocity is strongly affected by the mass fraction of dispersed liquid droplets in the mixture, even relatively low velocity flows can be supersonic with respect to the two-phase choking velocity. The formation and severity of a normal shock wave in a two-phase mixture depends strongly on the coupling between phases – particularly droplet size. As droplet size becomes smaller, the mixture behaves as a continuum, and sharp discontinuities can occur at velocities above the two-phase choking velocity but below the sonic velocity of the vapor.

In this paper we discuss the mechanisms of coupling between phases and suggest an approximate analysis for predicting the droplet size that causes the mixture to behave as a continuum through a normal shock wave. Through the use of a two-phase numerical model for calculating sub- and supersonic flows, including shock waves, we calculated examples of the dependence of shock behavior of a two-phase mixture. Comparisons of shock behavior as a function of droplet size are made for flows above the two-phase choking velocity but below the vapor choking velocity and for those above the vapor choking velocity.

Previous work in the area of two-phase shocks has been concentrated on predicting the relaxation region immediately following the maximum gradient in the continuum velocity, e.g. [2, 3]. Such calculations were strictly one-dimensional. In this work, the quasi-one-dimensional formulation (including area change) and the solution of the hyperbolic form of the equations through the normal shock wave makes it possible to

[1] This work was performed under the auspices of the U.S. Department of Energy by Lawrence Livermore Laboratory under contract No. W-7405-Eng-48.

[2] Present address: Washington State University, Department of Mechanical Engineering, Pullman, Wash. 99164.

Contributed by the Fluids Engineering Division and presented at the Winter Annual Meeting, San Francisco, Calif., December 10-15, 1978, of THE AMERICAN SOCIETY OF MECHANICAL ENGINEERS. Manuscript received by the Fluids Engineering Division, October 15, 1978.

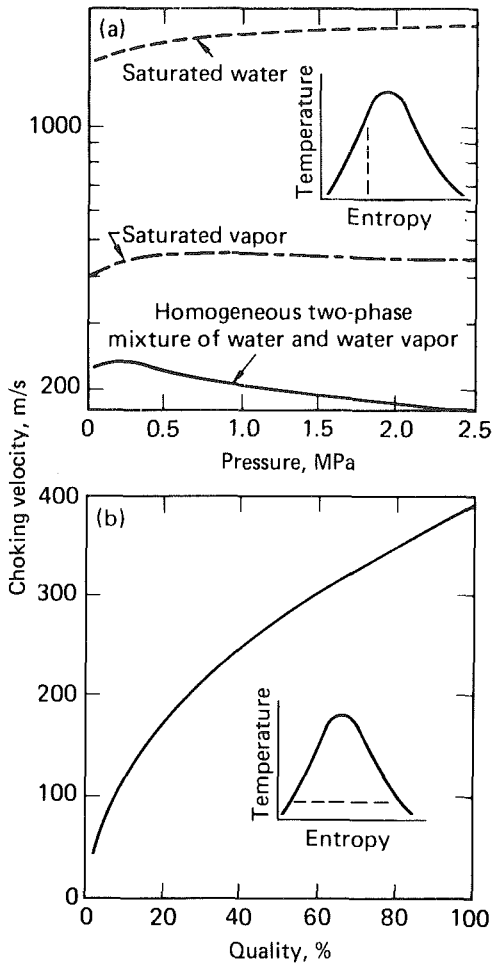

Fig. 1 Change in the continuum choking velocity:
***(a)* versus pressure at constant entropy (3.22 kJ/kg°C)**
***(b)* versus quality, the ratio of vapor mass to flow rate, at constant pressure (0.012 MPa)**

determine the location of the shock as well as the flow conditions both upstream and downstream. In addition, the virtual mass effect, the Basset force, the buoyant force, as well as the drag force, are included.

Approximate Analysis

The momentum coupling between the fluid and the droplet motion arises from the aerodynamic force on the droplet. The drag force consists of four components, the conventional steady-state drag (Stokes law or extensions thereof), the virtual mass effect, the buoyancy force, and the Basset force. The virtual mass term arises from the relative acceleration of fluid produced by droplet motion. The buoyancy force results from the pressure gradient in the fluid. The Basset force results from the unsteady viscous layer developing on the droplet. Typically, in flows where the vapor density is much less than the droplet material density, the buoyancy, virtual mass, and Basset forces are small compared to the steady-state drag force. However, for vapor-droplet flow through a shock wave, the pressure gradients and accelerations are such that these terms cannot be neglected *a priori.*

To estimate the interdependence of droplet size and a shock wave, we first assume that the steady-state drag force is dominant. We need to determine the droplet size when coupling through a normal shock is so strong that continuum behavior prevails. A measure of the responsiveness of a droplet to a change in vapor velocity is the time for a droplet released from rest to achieve 67 percent of the vapor velocity. This characteristic time is estimated, assuming Stokes law is valid, by:

$$\tau_d = \frac{\rho_d D^2}{18\ \mu_v}. \tag{2}$$

For a 1-μm droplet, the time constant is of the order of microsceconds. A droplet of this size moving at 500 m/s travels less than a millimeter through a shock before losing the majority of its momentum to the vapor phase. Thus the vapor-droplet mixture acts essentially like a continuum and produces a well-defined discontinuity. A 10-μm droplet, on the other hand, has a characteristic time two-orders-of-magnitude larger than that of the 1-μm droplet and travels 100 mm before losing most of its momentum to the vapor phase. On the basis of response time, it is expected that mixture continuum behavior would be approached as droplet size approaches 1 μm.

Numerical Model

To calculate the detailed dependence of two-phase shock behavior on droplet size and to include the effects of the various forces acting on the droplet, we used a numerical model [4] for calculating two-phase dispersed droplets in vapor flows. The quasi-one-dimensional model is based on: (*a*) an iterative solution of the time-dependent (hyperbolic) Eulerian equations for continuity, momentum, and energy for the two-phase mixture, (*b*) on the coupling of the numerical integration of the Lagrangian equation of momentum for droplets and the continuity equation for the droplet phase, and (*c*) on the equation of state for water. The Eulerian equations are integrated by use of the MacCormack algorithm [5]; the Lagrangian droplet equation is integrated using an

Nomenclature

A = area
a = acceleration modulus
c = homogeneous two-phase mixture sound velocity
C = droplet drag coefficient
D = droplet diameter
e = specific internal energy
$\mathbf{E}$ = E vector
h = specific enthalpy
$\mathbf{H}$ = H vector
K = empirical constant
m = mass flow rate
p = pressure
Re = droplet Reynolds number = $U_v D \rho_v / \mu$
t = time
U = velocity
$\mathbf{U}$ = U vector
X = mass of vapor/unit mass of mixture
Z = distance
α = relative acceleration
ϵ = spacial-differencing step selector = 1 or 0
μ = viscosity
σ = surface tension
ρ = mixture density

Subscripts

B = Basset
d = droplet phase
e = exit
i = spacial index
n = present time index
o = reference
P = buoyancy
s = isentropic
V = virtual mass
v = vapor phase

Superscripts

C = corrector
P = predictor

implicit form of the trapezoidal rule. the model includes phase velocity nonequilibrium and phase change. Phase change is based on the local pressure, using the saturation properties for water. Temperature nonequilibrium between phases can be included [6] but is considered unnecessary for the purposes of this discussion.

The two-phase-mixture equations of continuity, momentum, and energy (in the Eulerian reference frame and written in vectorized conservative form) are given by:

$$\frac{\partial \mathbf{U}}{\partial t} + \frac{\partial \bar{E}}{\partial Z} + \bar{H} = 0 \ , \tag{3a}$$

where:

$$\mathbf{U} = \begin{bmatrix} \rho A \\ \rho A[XU_v + (1-X)U_d] \\ \rho A\left[X\left(\frac{U_v^2}{2} + e_v\right) + (1-X)\left(\frac{U_d^2}{2} + e_d\right)\right] \end{bmatrix}, \tag{3b}$$

$$\mathbf{E} = \begin{bmatrix} \rho A[XU_v + (1-X)U_d] \\ \rho A[XU_v^2 + (1-X)U_d^2] + pA \\ \rho A\left[XU_v\left(\frac{U_v^2}{2} + h_v\right) + (1-X)U_d\left(\frac{U_d^2}{2} + h_d\right)\right] \end{bmatrix}, \tag{3c}$$

$$\mathbf{H} = \begin{bmatrix} 0 \\ -P\frac{dA}{dZ} \\ 0 \end{bmatrix}. \tag{3d}$$

To orient the reader who is unfamiliar with this form of the equations, we should point out that the mixture continuity equation results from substituting the first term (component) of the **U** (3*b*), **E** (3*c*), and **H** (3*d*) vectors into (3*a*). The momentum and energy equations result in a similar manner from substituting the second and third components, respectively.

The MacCormack Predictor-Corrector finite difference equations are written as follows:

Predictor:

$$\mathbf{U}_{i,n+1}^{p} = \mathbf{U}_{i,n}^{C} - \frac{\Delta t}{\Delta Z}\left[(1-\epsilon)\mathbf{E}_{i+1,n}^{C} - (1-2\epsilon)\mathbf{E}_{i,n}^{C} - \epsilon\mathbf{E}_{i-1,n}^{C}\right] + \Delta t\mathbf{H}_{i,n}^{C} \tag{4a}$$

Corrector:

$$\mathbf{U}_{i,n+1}^{C} = \frac{1}{2}\left(\mathbf{U}_{i,n}^{C} + \mathbf{U}_{i,n+1}^{p}\right) - \frac{1}{2}\frac{\Delta t}{\Delta Z}\left[\epsilon\mathbf{E}_{i+1,n+1}^{p} + (1-2\epsilon)\mathbf{E}_{i,n+1}^{p} + (\epsilon-1)\mathbf{E}_{i-1}^{p}\right] - \frac{1}{2}\Delta t\mathbf{H}_{i,n+1}^{p} \tag{4b}$$

For an individual droplet, the momentum equation derived in the Lagrangian reference frame is given by

$$\frac{\pi D^3}{6}\rho_d U_d \frac{dU_d}{dZ} = \sum F_d, \tag{5}$$

where $\sum F_d$ represents the total forces acting on the droplet,

$$\sum F_d = F_D + F_B + F_P + F_V, \tag{6}$$

where F_D, the drag force, is given by

$$F_D = \frac{\pi D^2}{8}\rho_v C(U_v - U_d)\ |U_v - U_d|\ ; \tag{7}$$

the Basset force by

$$F_B = K_B D^2\sqrt{\pi\rho_v\mu_v}\int_0^{t_n}\frac{1}{\sqrt{t_n - t}}\frac{d(U_v - U_d)}{dt}\,dt\ ; \tag{8}$$

the buoyant force by

$$F_p = -\frac{\pi D^3}{6}\frac{dp}{dZ}; \tag{9}$$

and the force associated with the virtual mass effect by

$$F_V = K_V\rho_v\frac{\pi D^3}{6}\frac{d}{dt}(U_v - U_d). \tag{10}$$

The empirical constants K_V and K_B [7] are:

$$K_V = 1.05 - 0.066/(a^2 + 1.02), \tag{11}$$

$$K_B = 2.88 + 3.12/(a+1)^3, \tag{12}$$

where a is defined as

$$a = |(U_v - U_d)^2/(\alpha D)|, \tag{13}$$

and α is the local difference in acceleration between the vapor and the droplet:

$$\alpha = \frac{d}{dt}(U_v - U_d). \tag{14}$$

The droplet drag coefficient [8] is given by

$C = 3.271 - 0.8893\ (\ln \mathrm{Re}) + 0.03417\ (\ln \mathrm{Re})^2 + 0.001443\ (\ln \mathrm{Re})^3$, $0.1 < \mathrm{Re} < 2 \times 10^4$;

$$C = \frac{24}{\mathrm{Re}},\quad 0 < \mathrm{Re} < 0.1. \tag{15}$$

Because thermal equilibrium between phases is assumed, only one additional equation, other than the equation of state, is required to complete the solution. We can use either the energy or the continuity equation associated with the droplets. In this case, we have chosen the continuity relation which is

$$D_{i+1} = D_i\left[\left(\frac{1-X_{i+1}}{1-X_i}\right)\left(\frac{\rho_{i+1}}{\rho_i}\right)\left(\frac{\rho_{d_i}}{\rho_{d_{i+1}}}\right)\times\left(\frac{U_{d_{i+1}}}{U_{d_i}}\right)\left(\frac{A_{i+1}}{A_i}\right)\right]^{1/3}. \tag{16}$$

Finally, we use the equation-of-state relations (saturation properties as a function of pressure). The first group (17) is solved with the mixture equations, while the second (18) is used with the droplet equations.

$$\rho_v = \rho_v(p), \rho_d = \rho_d(p), h_v(p), h_d = h_d(p), e_v = e_v(p), e_d = e_d(p). \tag{17}$$

$$\mu_v = \mu_v(p), \sigma = \sigma(p). \tag{18}$$

The numerical solution scheme is described in Fig. 2. The mixture equations (3) are solved with the equation-of-state functions (17) to determine mixture density, vapor velocity, vapor mass fraction, and pressure. The droplet equations (5) and (16) are then solved for droplet velocity and droplet diameter. The process continues iteratively until the problem converges and steady state is reached. Further details of the numerical scheme and the boundary conditions are given in [4]. A short discussion of the handling of the Basset force, however, is in order, because it has not been previously described for this numerical scheme. The integration of the

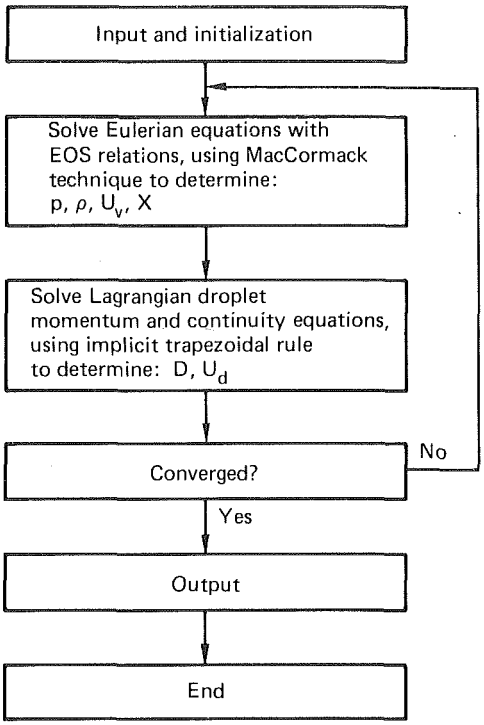

Fig. 2 Numerical solution scheme

"history" of the droplet (8) was accomplished by approximating the droplet and vapor velocity across a calculation cell as linear with time; summing the expression

$$F_{B_{i+1}} = 2K_{B_i} D_i^2 \sqrt{\pi \rho_{v_i} \mu_{v_i}}\, \alpha_i \sum_i \left(\sqrt{t_n - t_i} - \sqrt{t_n - t_{i+1}}\right), \quad (19)$$

where

$$t_n = \sum_i \frac{2(Z_{i+1} - Z_i)}{(U_{d_i} + U_{d_{i+1}})};$$

letting the initial time in the problem be zero; and summing to the present time, t_n, for each spacial step of the integration of equation (5). The evaluation of the Basset force represents no technical difficulty, though it is costly in computer time – slowing the solution by approximately a factor of two.

Calculational Results

A diverging channel is necessary to stabilize the location of the shock in these calculations, because the problem is inviscid except for droplet drag. The converging-diverging nozzle from which the diverging sections are taken has a stagnation pressure and mass-flow-rate ratio of 360 psia and 14 percent, respectively.

Figure 3 shows profiles for the portion of the diverging section where an isentropic homogeneous expansion produces velocities above the two-phase choking velocity but below the vapor sonic velocity. The maximum isentropic velocity occurring in this section would be approximately Mach 2 relative to the homogeneous-mixture choking velocity and Mach 0.7 relative to the vapor sonic velocity. Figure 4 shows profiles for the portion of the diverging section where the isentropic velocity occurring in this section would be approximately Mach 1.2 relative to the vapor sonic velocity and Mach 3.3 relative to the two-phase choking velocity. The reference values for velocity and area in *a* and *b* of Figs. 3 and 4 are associated with the exit conditions of the nozzle shown in Fig. 4(*a*), this velocity being the isentropic velocity of the mixture.

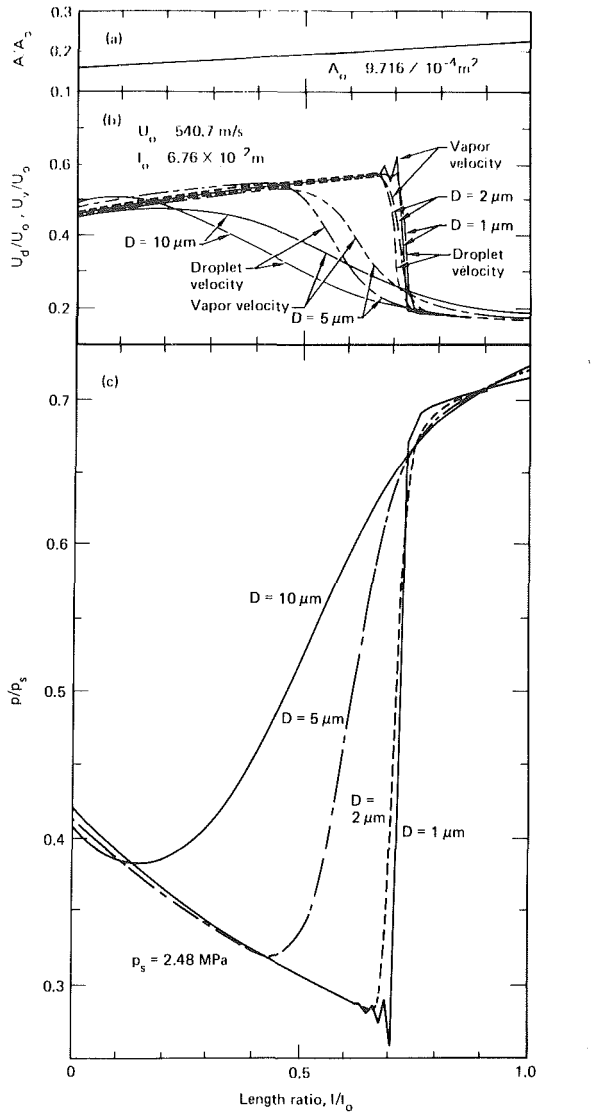

Fig. 3 Two-phase shocks for various droplet sizes at flow velocities above the two-phase choking velocity but below the vapor sonic velocity:
***(a)* area profile**
***(b)* velocity profile**
***(c)* pressure profile**

A shock is induced in the nozzle by specifying a subsonic exit boundary condition [4] that requires selection of the exit vapor velocity. A normal shock can thus form, provided the Rankine-Hugoniot conditions for a normal shock have been met or exceeded. It should be noted that these calculations do not allow direct comparison of shock phenomena having the exact same initial conditions entering the shock. The shock and postshock relaxation regions in two-phase flow are generally wide enough to affect the result because of the area change in the diverging nozzle.

Figure 3 shows the nozzle profile (*a*), velocity profile (*b*), and resultant pressure profile (*c*) for the liquid and vapor phases for four different droplet sizes. The vapor velocity at the exit was the same for all four calculations. For the 1-μm-dia droplet, a sharp discontinuity in velocity is seen, indicating shock-like behavior. As the droplet diameter was increased to first 2, then 5, and finally 10μm, the flow disturbances became increasingly gradual.

Figure 4 shows the results for a shock occurring at a velocity higher than the vapor choking velocity. The nozzle profile and the pressure and velocity profiles are shown for three different droplet sizes. In contrast to the case in Fig. 3,

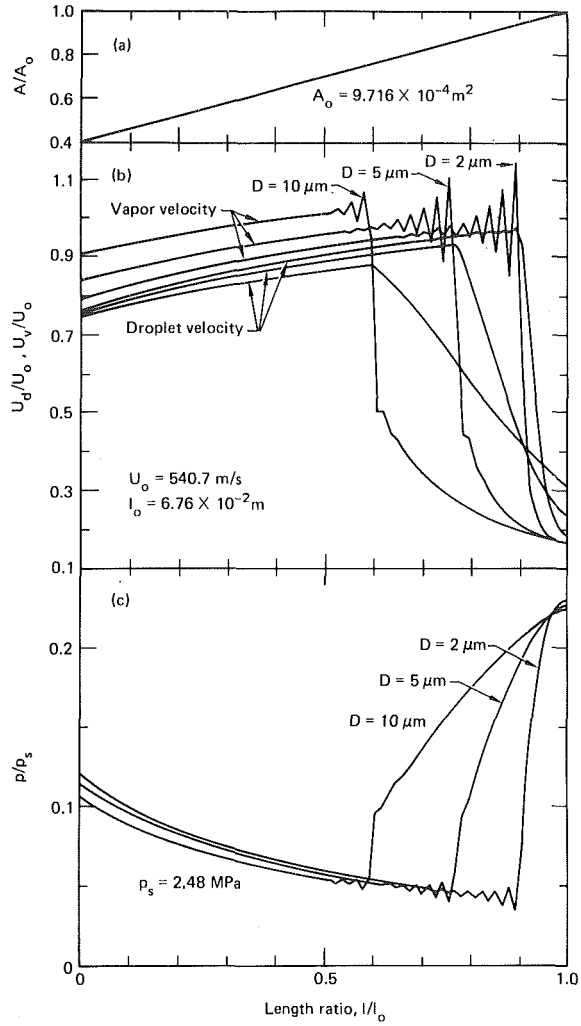

Fig. 4 Two-phase shocks for various droplet sizes at flow velocities that are supersonic relative to the vapor:
***(a)* area profile**
***(b)* velocity profile**
***(c)* pressure profile**

the vapor velocity continues to increase until the shock occurs. The result is a sharp discontinuity for all droplet sizes.

In all calculations shown, the steady-state drag force is predominant. The Basset force is typically less than 10 percent of the total force of the droplet except through the shock region where it briefly reaches as much as 60 percent of the total forces on the droplet. The buoyant force is approximately 5 percent of the total forces for the results shown in Fig. 3 and 1 percent for the results of Fig. 4. The force associated with the virtual-mass effect is at least an order-of-magnitude smaller than the buoyant force.

Discussion

For the flow conditions in the examples used here, continuum behavior appears to be approached with droplets of 1 to 2 μm in diameter. In the low-velocity cases, where the fluid was above the mixture choking velocity and below the vapor sonic velocity, the abruptness of the shock or flow discontinuity is strongly dependent upon droplet size. Discontinuous behavior occurs at velocities below the vapor choking velocity. However, when the droplets become large enough to render continuum behavior a poor approximation, the information is carried upstream in the vapor so that the discontinuity is modified. When the vapor sonic velocity is exceeded, the shock does not "see" upstream and cannot be modified until it occurs, which is consistent with supersonic-fluid behavior. In this case, the shock itself is not significantly affected by the size of the droplet except for modification of the relaxation region following the discontinuity. If the droplet size is greater than 2 μm and the flow is supersonic relative to the vapor, the relaxation region following the shock is very broad, compared to the lower velocity cases. This results from both the high velocity (great momentum and kinetic energy in the droplet field) and the large change in the vapor velocity across the discontinuity.

It is notable that the buoyant force is more significant in the low velocity cases. This is a result of higher vapor density in the low-velocity than in the high-velocity cases. Though the buoyant force is small compared to the drag and Basset forces, it apparently should not be neglected, particularly in regions where vapor densities are high.

Summary

We have presented calculations showing the dependence of two-phase shock behavior on droplet size. For the examples given, continuum behavior of the mixture appears to be approached for droplets of 1 and 2 μm in diameter, even through a normal shock wave. There is a significant difference in the effect of droplet size on discontinuities occurring in flows that are supersonic relative to the vapor and in those that are subsonic relative to the vapor but supersonic relative to the choking velocity of the mixture. In the droplet-momentum equation, we have included the steady-state drag force, the Basset force, the virtual-mass effect, and the buoyant force. Except in the very limited region of the shock wave, the steady-state drag force is dominant. To properly predict the significance of flow discontinuities in two-phase mixtures where flow velocities exceed the two-phase mixture choking velocity, we must include knowledge of the droplet size.

References

1 Comfort, W. J. III, "Modeling the Performance of a Two-Phase Turbine Using Numerical Methods and the Results of Nozzle, Static Cascade, and Windage Experiments," *Proceedings of the Symposium on Polyphase Flow in Turbomachinery,* ASME Winter Annual Meeting, San Francisco, Calif., Dec. 1978.

2 Kriebel, A. R., "Analysis of Normal Shock Waves in Particle Laden Gas," ASME *Journal of Basic Engineering,* Vol. 86, 1964, pp. 655-665.

3 Narkis, Y., and Gal-Or, B., "Two-Phase Flow Through Normal Shock Wave," The American Society of Mechanical Engineers, Paper No. 75-FE-25, ASME Winter Annual Meeting, 1975.

4 Comfort, W. J. III, Alger, T. W., Giedt, W. H., and Crowe, C. T., "Calculation of Two-Phase Dispersed Droplet-In-Vapor Flows Including Normal Shock Waves," Report UCRL-78426, Lawrence Livermore Laboratory, Livermore, Calif., Jan. 1978 (prepared for submission to the JOURNAL OF FLUIDS ENGINEERING).

5 MacCormack, R. W., "The Effect of Viscosity in Hypervelocity Impact Cratering," AIAA Paper 69-354, AIAA Meeting, Cincinnati, Ohio, 1969.

6 Crowe, C. T. and Comfort, W. J. III, "Atomization Mechanisms in Single Component, Two Phase, Nozzle Flows, Report UCRL-79656, Lawrence Livermore Laboratory, Livermore, California, 1978. (See also *Proceedings of the First International Conference on Liquid Automization and Spray Systems,* Tokyo, Japan, Aug. 29-31, 1978.)

7 Odar, F., "Verification of the Proposed Equation for Calculation of Forces on a Sphere Accelerating in a Viscous Fluid," *Journal of Fluid Mechanics,* Vol. 25, No. 3, 1966, pp. 591-592.

8 Elliot, D. G., and Weinberg, E., "Acceleration of Liquids in Two-Phase Nozzle," NASA Technical Report 32-987, Jet Propulsion Laboratory, California Institute of Technology, July 1, 1968.

Predicted and Measured Pressure Drop in Parallel Plate Rotary Regenerators

I. L. Maclaine-Cross
Lecturer,
Broken Hill Division,
University of New South Wales,
Broken Hill, New South Wales, Australia

C. W. Ambrose
Senior Lecturer,
Department of Mechanical Engineering,
Monash University,
Clayton, Victoria, Australia

The flow in the passages of parallel plate rotary heat exchangers or regenerators is laminar and fully developed. Laminar flow theory should allow an accurate prediction of heat and mass transfer and pressure drop. Previously measured values of pressure drop have been 20 percent higher than predicted. Pressure drop is predicted here by considering the passage cross section rectangular and correcting for flow acceleration, property variations, and inlet and outlet pressure drop. The pressure drops measured on a parallel plate sensible heat regenerator were within 3 percent of theory and on a prototype parallel plate total heat regenerator within 4 percent.

1 Introduction

In regenerators or regenerative heat and mass exchangers, heat and any number of chemical components are transferred from one fluid stream to a porous matrix, and then from the porous matrix to other fluid streams. Many authors have contributed to the theory of heat and mass transfer in regenerators and the literature is reviewed elsewhere [1].

A variety of passage shapes and seals have been used in rotary regenerators. The parallel plate rotary regenerators manufactured in Australia have advantages for air conditioning applications [2]. Flow and pressure drop tests on a sensible and a total heat regenerator of this type are described here.

The frame of these regenerators is usually made of aluminium (Fig. 1). Channel section spokes are fastened to either side of a hollow hub mounted on a drive shaft. The spokes are filled with rectangular spacers from the hub to an outer cover cylinder of aluminium sheet. The matrix is made by winding a reel of film or woven cloth spirally over the spacers as they are inserted in the spokes. The film used for the sensible heat regenerator tested was 76 μ m thick polyethylene terephthalate (Mylar). The total heat regenerator was made using 89 μm thick cloth woven from polyethylene terephthalate fibre threads (Terylene) and was impregnated with a small amount of lithium chloride solution. The overall dimensions of the regenerator rotors tested were outer cover diameter 1.273 m, hub diameter 457 mm and depth between faces 135 mm.

The seals between the rotor and housing are all clearance seals. They are designated axial, radial, and tangential depending on their orientation to the axis of the rotor (Fig. 1). The axial and radial seals prevent leakage from the upper to the lower regenerator flow streams. This leakage was between 3 and 5 percent of the upper flow stream for the tests. The tangential seal prevents part of a flow stream from leaking past the regenerator matrix, between the rotor circumference and housing. For the upper tangential seal, this leakage was between 3 and 8 percent of the upper flow stream for the tests.

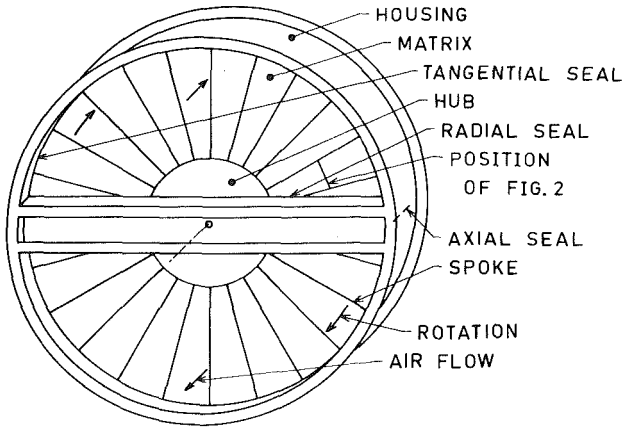

Fig. 1 Two stream counterflow air conditioning regenerator

A sensible heat regenerator matrix passage half way between the hub and outer cover is shown with dimensions in Fig. 2. The passage cross sections are isosceles trapezoids with the axis of symmetry intersecting the rotor axis. In applications of these regenerators, the passage Reynolds number is always less than 1000. For the tests the Reynolds number was always less than 400. The flow in the passages is thus laminar and also fully developed at exit. Since the mean aspect ratio w/b of the passages is 121, they may be considered as parallel plates for many design purposes. For the purpose of these tests the cross sections will be considered rectangular.

Dunkle and Maclaine-Cross [2] reported test results on a 1.98 m diameter sensible heat regenerator similar to the one previously described. For a flow of 4.11 m^3/s, they measured a pressure drop of 119 Pa, 20 percent higher than they predicted. The improvement obtained here (section 4) was partly due to an improved theory (section 2) but mainly to an

Contributed by the Fluids Engineering Division for publication in the JOURNAL OF FLUIDS ENGINEERING. Manuscript received by the Fluids Engineering Division, March 19, 1979.

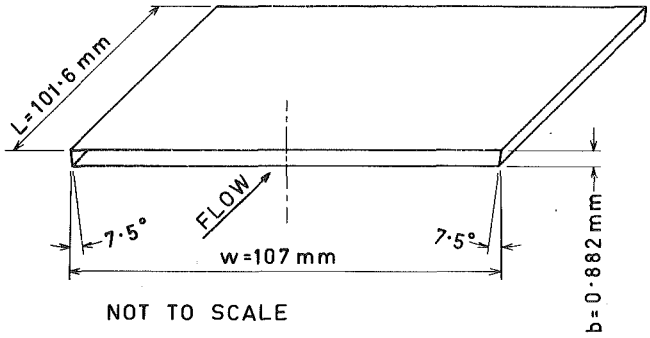

Fig. 2 Typical parallel plate rotary regenerator matrix passage

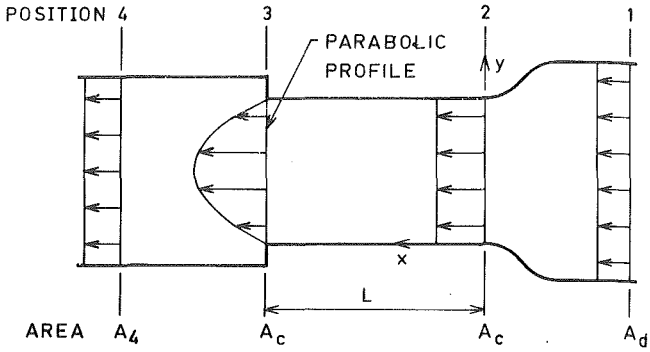

Fig. 3 Assumed one dimensional flow through regenerator for calculating inlet and outlet pressure drop

improved test rig and more careful experimental technique (section 3).

2 Theory of Flow in Parallel Plate Regenerators

2.1 Fully Developed Laminar Flow in Rectangular Passages. The pressure drop ΔP in the matrix passages for constant property, laminar flow, fully developed at exit, may be determined from

$$\Delta P = 2f_\infty \text{ Re } \mu u L/D_h^2 + K\rho u^2/2 \quad (1)$$

where f_∞ is the local Fanning friction factor for fully developed flow and K is a flow development pressure drop coefficient. In the tests, the last full term contributed between 2 and 5 percent of the total pressure drop.

For rectangular passages f_∞ Re is given by [4, 5]. For Re > 600, Beavers, et al. [6] have shown experimentally that K is a constant. For Re $\rightarrow$ 0, the creeping flow solution predicts that $K \sim C/\text{Re}$ where C is a constant depending on the inlet conditions. For the Reynolds numbers and large aspect ratios encountered in parallel plate regenerators, it is satisfactory to use a constant value of K obtained for parallel plates. $K = 24/35 \simeq 0.686$ will be used here following Lundgren, et al. [7] but other authors have given values between 0.60 [6] and 0.85 [8]. Finite difference solution of the Navier-Stokes equation [9] gives values close to the approximate theory of Lundgren, et al. [7] and allows the effect of low Reynolds number and plate thickness to be included.

2.2 Variable Property Effects. The absolute pressure variation along a regenerator passage in air conditioning applications is less than 0.2 percent and in the experiments was always less than 0.1 percent. The effect of pressure variations on density and viscosity will have an entirely negligible effect on pressure drop.

When heat was transferred in the experiments, the absolute temperature variation along the passage was up to 10 percent. The density and viscosity vary with temperature in the flow direction and normal to it. The right-hand side of equation (1) may be corrected for these effects as described in the following two paragraphs.

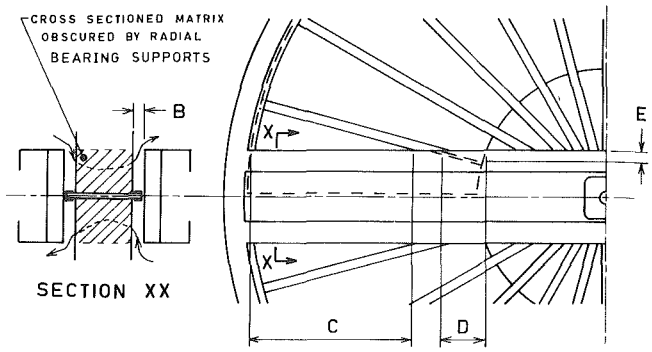

Fig. 4 Radial seal detail for estimating free flow area of passages

The viscosity and velocity in the first term should be evaluated for the bulk mean fluid temperature averaged in the flow direction through the matrix T_m. For counterflow regenerators $T_m \simeq (T_2 + T_3)/2$ where T_2 and T_3 are the temperatures evaluated at the positions shown in Fig. 3. The density and velocity in the second term should be evaluated at the fluid inlet temperature T_2. The fluid acceleration on heating or deceleration on cooling may be accounted for by adding a third term $\rho_m u_m^2 (T_3 - T_2)/T_m$, which may be derived using conservation of momentum and the ideal gas law. For the tests, this term's magnitude was between 0 and 0.7 percent of the matrix pressure drop.

The variation of density and viscosity normal to the flow direction may be corrected for following Kays and Perkins [10]. For gases, they multiplied the local friction factor by $(T_w/T_b)^m$ where T_w is the local wall absolute temperature, T_b is the local bulk fluid absolute temperature and $m = 1.00$ for heating and $m = 0.81$ for cooling. The average value in the flow direction x of this correction may be obtained as follows:

Nomenclature

a = matrix plate thickness (m)
A_c = effective minimum free flow area of matrix passages for one fluid stream (m^2)
A_d = cross-sectional area of regenerator ducts (m^2)
A_s = area of gap in clearance seals (m^2)
A_4 = unobscured cross sectional area of matrix, passages and spokes (m^2)
b = matrix plate spacing (m)
B,C,D,E = regenerator dimensions defined in Fig. 4 (m)
C_d = clearance seal discharge coefficient (dimensionless)
D_h = hydraulic diameter ($= 2b/(1 + b/w)$ for rectangular passages)
f = $\Delta P D_h/(2\rho u^2 L)$ Fanning friction factor (dimensionless).
f_∞ = local fanning friction factor for fully developed flow (dimensionless)
K = pressure drop coefficient for entrance effect inside passage (dimensionless)
L = passage length in flow direction (m)
m = coefficient in equation (3) (dimensionless)
P = static pressure (N/m^2)
Q_s = seal leakage volume flow rate (m^3/s)

$$\int_{x=0}^{x=L}\left(\frac{T_w}{T_b}\right)^m \frac{dx}{L} = \int_{x=0}^{x=L}\left(1+\frac{T_w-T_b}{T_b}\right)^m \frac{dx}{L} \quad \text{(Rearranging)}$$

$$\simeq \int_{x=0}^{x=L}\left(1+m\frac{T_w-T_b}{T_b}\right)\frac{dx}{L} \quad \left(\text{Bionomial expansion, } \frac{T_w-T_b}{T_b} < 2 \text{ percent in experiments}\right)$$

$$= \int_{x=0}^{x=L}\left(1+\frac{mL}{\Lambda T_b}\frac{\partial T_b}{\partial x}\right)\frac{dx}{L} \quad \left(\text{For passage energy conservation [1], } T_w - T_b = \frac{L}{\Lambda}\frac{\partial T_b}{\partial x}\right)$$

$$= 1 + \frac{m}{\Lambda}\ln\frac{T_3}{T_2} \quad \text{(integrating)}$$

$$\simeq 1 + \frac{m}{\Lambda}\frac{T_3-T_2}{T_m} \quad \left(\ln\frac{T_3}{T_2} \simeq \frac{T_3-T_2}{T_m} \text{ with error less than 0.04 percent for experiments}\right)$$

This approximate average value may be used as a coefficient to correct the first term of equation (1). $|m(T_3-T_2)/\Lambda T_m|$ was between 0 and 1 percent for the tests.

Applying the above four corrections to equation (1) gives the following approximate equation for the matrix pressure drop with variable property effects

$$P_2 - P_3 = \left(1+m\frac{T_3-T_2}{\Lambda T_m}\right) f_\infty \, \mathrm{Re}\frac{2\mu_m u_m L}{D_h{}^2} + K\frac{\rho_2 u_2{}^2}{2} + \frac{T_3-T_2}{T_m}\rho_m u_m{}^2 \tag{2}$$

When mass was transferred in the experiments the maximum difference in humidity ratio or moisture content was 0.01 kg water/kg dry air. The variation of density and viscosity in the flow direction resulting from this would be less than 0.6 and 0.2 percent, respectively. The viscosity and velocity in the first term of the right hand side of equation (1) should be evaluated for the bulk mean fluid absolute humidity averaged in the flow direction as for temperature above. The density and velocity in the second term should be evaluated at the fluid inlet absolute humidity. The effects of mass transfer on pressure drop through the acceleration correction, the variation of density and viscosity normal to the flow direction and distortion of the velocity profile [11] were each estimated to be less than 0.1 percent and were neglected.

2.3 Inlet and Outlet Pressure Drop. In the tests, the mean static pressure was measured as the average of four wall tappings [14] at positions 1 and 4. For each of the two streams through the regenerator, positions 1 and 4 were 308 mm upstream and downstream respectively of the regenerator housing. The assumed flow and velocity profiles through the test regenerator are shown schematically in Fig. 3.

The inlet flow is assumed to be a frictionless contraction from the duct cross sectional area A_d at position 1 to the regenerator free flow area A_c at position 2. By Bernoulli's equation and continuity at the inlet

$$P_1 - P_2 = \frac{\rho_2 u_2{}^2}{2}\left(1-\left(\frac{A_c}{A_d}\right)^2\right) \tag{3}$$

The flow leaves the passage at position 3 and is assumed to expand abruptly from the free flow area A_c to an area A_4 at the downstream static pressure measuring position 4. A_4 is the cross section area of the matrix, passages and spacers for each stream which is not obscured by the radial seal. By conservation of momentum and continuity at the outlet assuming a parabolic velocity profile at position 3 and a uniform velocity at position 4 as shown in Fig. 3.

$$P_3 - P_4 = \frac{\rho_3 u_3{}^2}{2}\left(2\left(\frac{A_c}{A_4}\right)^2 - 2.4\frac{A_c}{A_4}\right) \tag{4}$$

The measured static pressure difference between positions 1 and 4 may be predicted using equations (2, 3, 4) since $P_1 - P_4 = P_1 - P_2 + P_2 - P_3 + P_3 - P_4$. The inlet and exit pressure drop may be increased by blockage due to fraying of the edges of the cloth and other effects [3].

Kays and London [5] calculate the pressure drop across heat exchangers using entrance and exit total pressure loss coefficients K_c and K_e. Equations (2), (3) imply that $K_c = K = 0.686$ but [5, Fig. 5-3] gives $K_c = 0.55$ for the sensible heat regenerator tests where $\sigma = A_c/A_d = 0.796$. This difference in entrance loss coefficient K_c results from different assumptions about the inlet flow pattern. The tests (section 4) were not sufficiently accurate to distinguish between the two values of K_c but computer studies [9] suggest the present authors' assumptions are appropriate for high A_c/A_d. Equation (4) implies the same values of K_e as those given by [5, Fig. 5-3] if A_4 is taken as an equivalent exit duct area.

2.4 Estimation of the Effective Minimum Free Flow Area of the Passages A_c. The gap of width B between the matrix and radial bearing supports restricts the flow where the matrix is obscured by the support (Fig. 4). The actual flow at a given pressure drop is considerably less than would be estimated by assuming $2A_c$ equal to the total cross sectional area of the matrix passages. The variation in the effective value of A_c

Nomenclature (cont.)

Re = $\rho u D_h/\mu$ Reynolds number (dimensionless)
T = absolute temperature (K)
T_b = local bulk fluid absolute temperature (K)
T_w = local absolute temperature at the passage wall (K)
u = mean velocity in matrix passages (m/s)
w = width of matrix passages (m)
x = distance in the fluid flow direction (m)
ΔP = pressure drop in matrix passages for constant property flow at T_m (N/m^2)
ΔP_s = pressure drop across clearance seal (N/m^2)
Λ = number of heat transfer units for matrix stream with heat transfer alone [3] or appropriate dimensionless length for heat and mass transfer [1] (dimensionless)
μ = dynamic viscosity (Ns/m^2)
ρ = density (kg/m^3)

Subscript m denotes a quantity evaluated for the bulk mean fluid temperature or state averaged in the flow direction through the matrix. Subscripts, 1, 2, 3, and 4 indicate the measuring positions shown in Fig. 3.

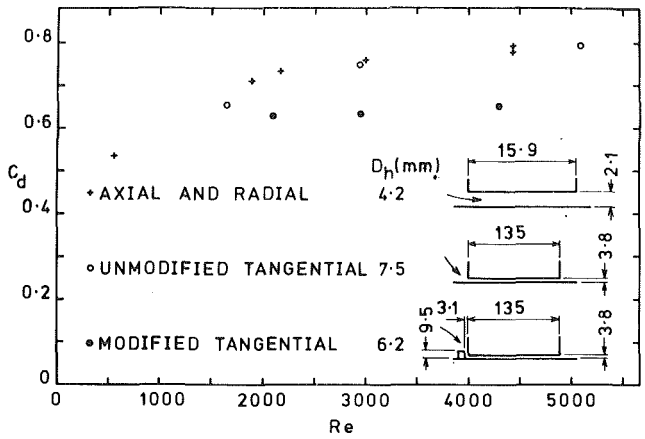

Fig. 5 Clearance seal discharge coefficients C_d

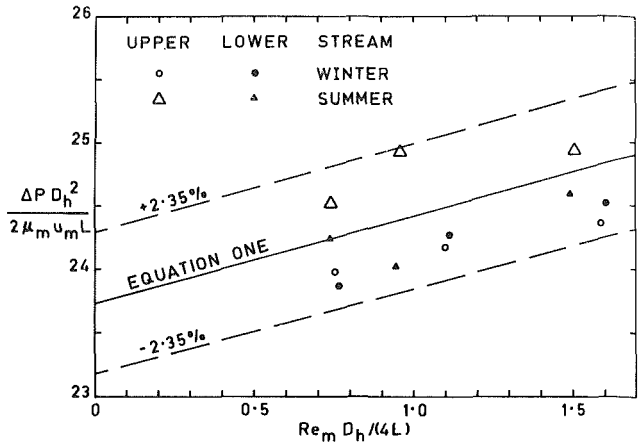

Fig. 6 Dimensionless pressure drop results for parallel plate sensible heat regenerator

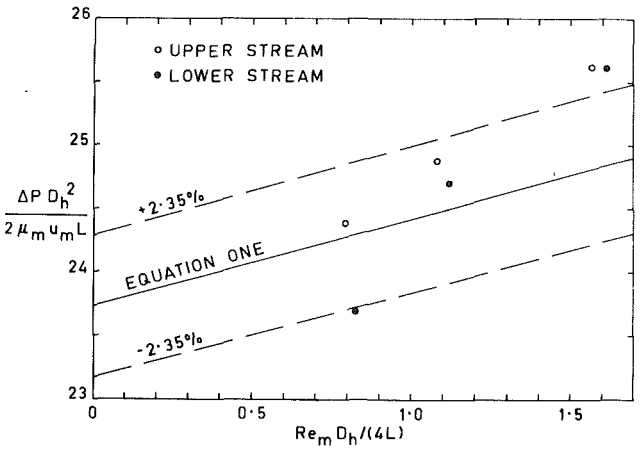

Fig. 7 Dimensionless pressure drop results for parallel plate total heat regenerator

with spoke position is certainly less than one percent, as variation in pressure drop with spoke position was only just detectable at low flow and rotational speed.

By considering the average of two limiting cases of a simplified flow pattern, it was estimated that (3.4 BC + DE)$b/(a + b)$ should be added to the unobscured passage cross-sectional area for a stream to calculate the minimum free flow area of the passage A_c. This addition was four percent of A_c for the regenerators tested. The limiting cases suggest an error in the addition of ± 30 percent so the corresponding error in A_c *is* ± 1.2 percent.

3 Measurements on Parallel Plate Regenerators

3.1 Measurement of Matrix Plate Spacing. The matrix plate thickness a was measured on a folded sample of the film or woven cloth retained during manufacture of the regenerator. Two radii on opposite sides of a rotor diameter were selected with approximately half the matrix area at smaller radii and half at greater. At each such radius, fifty passages were counted out radially every tenth one being marked by slipping a strip of paper 20 mm × 160 mm into the matrix so it protruded on either side. The counting was checked. The overall thickness of fifty passages and fifty one matrix plates was measured using vernier calipers at each radius on either side of the wheel. The thickness of fifty one matrix plates was subtracted and the results divided by fifty. The four results were averaged to give b. The measured values of b, 882 ± 3 μm for the sensible heat regenerator and 869 ± 3 μm for the total heat regenerator were significantly less than the nominal value 914 μm.

3.2 Measurement of Clearance Seal Leakage. Dunkle and Maclaine-Cross [2] recommended that seal leakage flow Q_s be calculated from the formula

$$Q_s = C_d A_s (2\Delta P_s/\rho)^{1/2} \quad (5)$$

using the mean value of discharge coefficient C_d = 0.65 obtained by Harper [15]. Harper plotted measured discharge coefficients C_d against clearance. His values varied between 0.56 and 0.70. No details of geometry or Reynolds number were given.

Seal leakage was measured for the radial and axial seals and two types of tangential seals on a parallel plate sensible heat regenerator (section 1, Fig. 1). The speed of the rotor appeared to have no effect, up to 2 rad/s, on the mean value of C_d for a revolution. On slow rotation fluctuations in C_d were less than 1 percent. The measured discharge coefficients are shown in Fig. 5. The radial and axial seal discharge coefficient in Fig. 5 was measured on the total flow through two axial and two radial seals. In applying these results it is therefore recommended that half the cross sectional area of the axial seals be combined with each radial seal and that the axial seal leakage be otherwise neglected. After the initial measurements were made the tangential seals were modified to reduce leakage by riveting a 9.5 mm × 9.5 mm aluminium extrusion to the housing circumference with a minimum clearance of 1.6 mm from the upstream wheel face. This modification introduced a sharp 90 deg bend in the leakage flow path which reduced the discharge coefficients. Difficulty in measuring seal dimensions reduces the value of these coefficients for predicting leakage in other regenerators. Since underestimating leakage is more serious than overestimating it, C_d = 0.70 is recommended for design purposes.

3.3 Reduction of Measurements to Dimensionless Form. A B.S. 848 cone inlet nozzle [12], calibrated with Pitot-static tube traverses [13], was used to measure the upper flow stream at the test rig inlet. After passing through the regenerator the upper flow stream was turned 180 deg to pass through the lower half of the regenerator and then the fan. The upper and lower duct cross sectional area upstream and downstream of the regenerator, A_d, was constant. The matrix flows were obtained from the inlet nozzle flow and the seal leakage flows, which were calculated using equation (5) and the pressures measured upstream and downstream of the regenerator in the upper and lower duct. The calculated pressure drops at the regenerator inlet, $P_1 - P_2$, and outlet, $P_3 - P_4$, (section 2.3) were subtracted from the measured regenerator pressure drop, $P_1 - P_4$, to give the passage pressure drop $P_2 - P_3$ for both the upper and lower flow stream. If equation (1) is written for the averaged bulk mean

fluid state for a flow stream, f_∞ Re 2 μ_m u_m $L/D_h{}^2$ may be replaced by its value calculated from equation (2) to give

$$\Delta P = \left(P_2 - P_3 - K\frac{\rho_2 u_2{}^2}{2} - \frac{T_3 - T_2}{T_m}\rho_m u_m{}^2\right) \Big/ \left(1 + m\frac{T_3 - T_2}{\Delta T_m}\right) + K\frac{\rho_m u_m{}^2}{2} \quad (6)$$

ΔP calculated from equation (6) is the measured matrix pressure drop with acceleration and variable property effects removed. The values of ΔP and u_m may now be plotted by calculating the dimensionless coordinates $\Delta P D_h{}^2/(2\ \mu_m u_m L)$ and $\mathrm{Re}_m\ D_h/(4L)$ using Mason and Monchick's [16] moist air viscosity data.

Equation (1) may be divided by $2\mu_m\ u_m L/D_h{}^2$ to give

$$\frac{\Delta P D_h{}^2}{2\mu_m u_m L} = f_\infty\ \mathrm{Re} + K\frac{\mathrm{Re}_m D_h}{4L} \quad (7)$$

Equation (7) shows that, if the theory in section 2 agrees with the experiments, the dimensionless coordinates calculated from the measurements as described in the previous paragraph should lie on a straight line with intercept f_∞ Re on the ordinate and slope K.

4 Pressure Drop Results and Discussion

If the error in conical inlet discharge coefficient is assumed ±2 percent, the errors in pressure measurement ±1 percent and other errors neglected, the error in measuring $\Delta P\ D_h{}^2/(2\ \mu_m u_m L)$ is ±2.35 percent. These error bands are shown by the broken lines in Figs. 6, 7.

Figure 6 shows the results of two series of measurements on the parallel plate sensible heat regenerator (section 1) in dimensionless form. Three flows were used for each series. The winter series was made with no heat or mass transfer and the unmodified tangential seals. The summer series was made with the modified seals and up to 30 K temperature difference between the regenerator inlets. No effect of rotational speed on the average value of the measurements was detected up to 2 rad/s.

Figure 7 shows the results of a single series of measurements on the parallel plate total heat regenerator (section 1). This series was made with no heat or mass transfer and the total heat rotor installed in the sensible heat regenerator housing. Although the nominal size of the rotors was the same, they were not interchangeable. The tangential seals were out of adjustment for these tests and no seal leakage measurements were made. The rotor was a manufacturer's prototype and a large proportion of the cloth plates were slack, which tends to increase the matrix flow. Broken fibres were projecting from the cloth into the passages tending to reduce the matrix flow. The deviation of experiment from theory in Fig. 7 is consistent with a seal leakage greater than predicted and a matrix flow less than theory.

Conclusion

Within the ±2.35 percent experimental error, the pressure drop of parallel plate sensible heat regenerators has been shown consistent with equation (1) (section 2.1). This was possible because many precautions were taken and in particular: Approximate corrections were made for variable property effects (section 2.2), for inlet and outlet pressure drop (section 2.3) and to the minimum free flow area (section 2.4); The matrix plate spacing b (section 3.1) and seal discharge coefficients section 3.2) were carefully measured.

The pressure drop of parallel plate total heat regenerators (section 1.2) may be predicted using the theory described in this paper (sections 2, 3) within ± 4 percent. Further investigations could improve the accuracy of prediction for total heat regenerators.

Acknowledgments

Financial support was received from the Australian government under grant number F 74/15117 awarded by the Australian Research Grants Committee. The regenerators tested were donated by Rotary Heat Exchangers Pty. Ltd. of Melbourne.

References

1 Maclaine-Cross, I. L., "A Theory of Combined Heat and Mass Transfer in Regenerators," Ph.D. thesis, Department of Mechanical Engineering, Monash University, Melburne, 1974.

2 Dunkle, R. V., and Maclaine-Cross, I. L., "Theory and Design of Rotary Regenerators for Air Conditioning," *Mechanical and Chemical Engineering Transactions of the Institution of Engineers,* Australia, Vol. MC 6, No. 1, May 1970, pp. 1-6.

3 Deutscher, K. O., Dunkle, R. V., and Megler, V. R., "A Fundamental Study of Heat, Mass and Momentum Transfer in a Parallel Passage Evaporative Cooler Pad," First Australasian Conference on Heat and Mass Transfer, Monash University, Melbourne, May, 1973, Section 5.2, pp. 7-14.

4 Cornish, R. J., "Flow in a Pipe of Rectangular Cross-Section," *Proceedings of the Royal Society,* Vol. A120, 1928, pp. 691-700.

5 Kays, W. M., and London, A. L., *Compact Heat Exchangers,* 2nd ed., McGraw-Hill, New York, 1964.

6 Beavers, G. S., Sparrow, E. M., and Magnuson, R. A., "Experiments on Hydrodynamically Developing Flow in Rectangular Ducts of Arbitrary Aspect Ratio," *International Journal of Heat and Mass Transfer,* Vol. 13, 1970, pp. 689-702.

7 Lundgren, T. S., Sparrow, E. M., and Starr, J. B., "Pressure Drop due to the Entrance Region in Ducts of Arbitrary Cross Section," ASME *Journal of Basic Engineering,* Vol. 86, No. 3, Sept. 1964, pp. 620-626.

8 Han, L. S., "Hydrodynamics Entrance Lengths for Incompressible Laminar Flow in Rectangular Ducts," ASME *Journal of Applied Mechanics,* Vol. 27, Sept. 1960, pp. 403-409.

9 Tuan, N. V., "Combined Forced and Free Convection between Parallel Plates," Ph.D. thesis, School of Mechanical and Industrial Engineering, University of New South Wales, Sydney, 1979.

10 Kays, W. M., and Perkins, H. C., "Internal Flow in Ducts," *Handbook of Heat Transfer,* Rohsenow, W. M. and Hartnett, J. P. ed., McGraw-Hill, New York, 1973, pp. 7-155 to 7-167.

11 Bird, R. B., Stewart, W. E., and Lightfoot, E. N., *Transport Phenomena,* International ed., Wiley, New York, 1960, pp. 656-668.

12 *B. S. 848 Methods of Testing Fans for General Purposes,* Part 1, British Standards Institution, London, 1963.

13 Ower, E., and Pankhurst, R. C., *The Measurement of Air Flow,* 4th ed., Pergamon, Oxford, 1966.

14 Blake, K. A., "The Design of Piezometer Rings," *Journal of Fluid Mechanics,* Vol. 78, Part 2, 1976, pp. 415-428.

15 Harper, D. B., "Seal Leakage in the Rotary Regenerator and Its Effect on Rotary Regenerator Design for Gas Turbines," *Trans.* ASME, Vol. 79, Feb. 1957, pp. 233-245.

16 Mason, E. A., and Monchick, L., "Survey of the Equation of State and Transport Properties of Moist Gases," *Humidity and Moisture,* Wexler, A. ed., Vol. 3, Reinhold, New York, 1965, pp. 257-272.

T. Iino
H. Sato
Researchers,
H. Miyashiro
Chief Researcher,
Mechanical Engineering
Research Laboratory,
Hitachi, Ltd.,
Ibaraki, 300, Japan

Hydraulic Axial Thrust in Multistage Centrifugal Pumps

An experimental and theoretical study is performed with a single stage pump. The influence of the flow rate, the axial displacement of the impeller, and annular seal clearances on the hydraulic axial thrust is investigated. Pressure distributions measured in the space between the impeller and the casing agree with those calculated by the Kurokawa-Toyokura method when the leakage flow is inward in the space. It is clarified that the method is sometimes not available for the outward leakage flow because of the large thickness of the boundary layer in the space. A computer program for calculating the axial thrust in multistage centrifugal pumps is developed based on the method and experimental results. Axial thrusts measured in prototype multistage pumps agree with the calculation.

Introduction

Centrifugal pumps have become larger in size and higher in head, and the hydraulic axial thrust acting on impellers has increased considerably. On the other hand, it has been proved experimentally that the conventional method of calculating the axial thrust is not adequate [1, 2].

Figure 1 shows the pressure distribution around an impeller in multistage centrifugal pumps. In the multistage pumps without balancing holes, the direction of leakage flow in the front space between the impeller and the casing wall is opposite to that in the back space.

When a control surface is considered around the impeller, the estimation of the axial thrust is simplified to the following two problems: 1 The estimation of the axial momentum difference between the inlet and the outlet flow crossing the control surface. 2 The estimation of the pressure distribution in the space between the impeller and the casing walls.

The axial momentum change described in the problem 1 is small compared with the thrust caused by the pressure distribution. Therefore, for calculation of the axial momentum change, an assumption that the inlet flow is uniform and the outlet flow is radial would yield results of acceptable accuracy.

In order to estimate the pressure distribution, it is necessary to know the value of the pressure and the fluid angular velocity in the space at the impeller outlet diameter as well as the pressure change in the space along the radius. The conventional method of estimation of the pressure change is based on an assumption that the fluid in the space rotates at half the angular velocity of the impeller. A. Verba and G. Sebestyén [1] proved that the axial thrust calculated on this assumption was considerably smaller than that measured in a multistage pump. U. Domm and H. Zilling [2] proposed a method of calculating the pressure change, considering the influence of through-flow rate. Recently new methods were proposed to analyze the flow in the space in consideration of the velocity distributions in the boundary layers and a potential core in the space [3, 4, 5].

On the other hand, there have been few studies on the

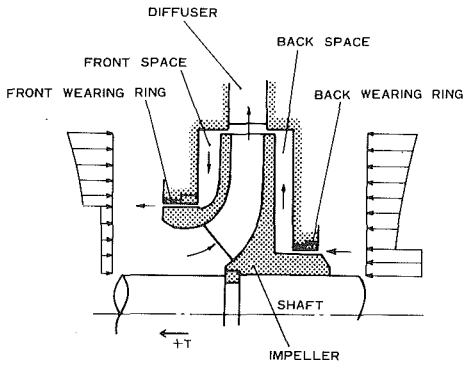

Fig. 1 Pressure distribution around an impeller

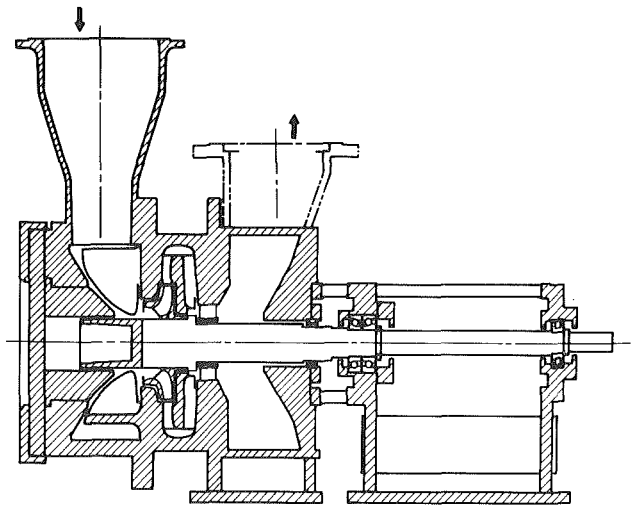

Fig. 2 Test pump

Contributed by the Fluids Engineering Division for publication in the JOURNAL OF FLUIDS ENGINEERING. Manuscript received by the Fluids Engineering Division, March 31, 1979.

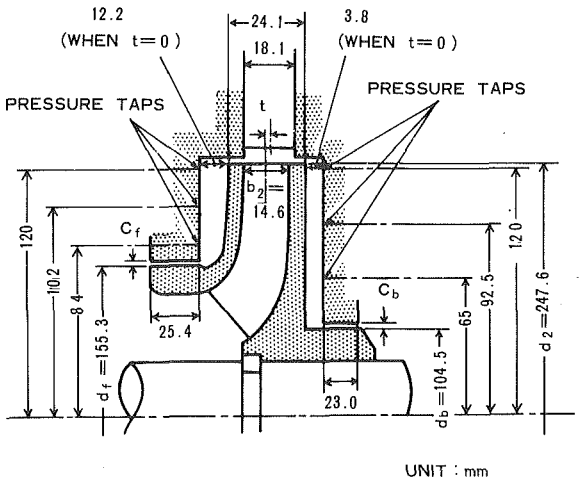

Fig. 3 Test impeller A

boundary values of the pressure and the fluid velocity in the space, especially in the region of low flow rates.

U. Domm and H. Zilling investigated experimentally the influence of the impeller axial position on the axial thrust with a single stage pump [2]. A. Verba and G. Sebestyén attributed the difference between the measurement and the calculation to the impeller axial displacement. However, the relation between the pressure distribution and the impeller axial displacement has not been studied.

This paper deals with the axial thrust in multistage centrifugal pumps with vaned diffusers. Pressure distributions around impellers are measured under several conditions of flow rate, impeller axial displacement, and wearing ring clearances. The pressure and the fluid angular velocity at the impeller outlet diameter as well as the pressure change in the space are investigated.

Test Pumps and Method of Experiments

Test Pumps. The test pump A is shown in Figs. 2 and 3. Table 1 shows the performance of the test pumps A and B. In order to measure the pressure distribution in the space between the impeller and the casing walls, four pressure taps were fitted on each pitch circle shown in Fig. 3.

Table 1 Performance of test pumps

Pumps	Speed rpm	Flow m^3/min	Head m	n_s (m,m^3/min, rpm)
A	3000	2.25	74.8	177
B	3000	2.70	66.3	212

Method of Experiments. Experiments were carried out under several conditions of the flow rate, axial displacement of the impeller, and annular clearances at the wearing rings. The axial spacing between the impeller and the casing walls changed with t, the axial displacement of the impeller against the diffuser. Transducers of strain gauge type were used for pressure measurements. Flow at the impeller outlet, at the diffuser inlet, and in the space was also investigated by means of an oil film technique.

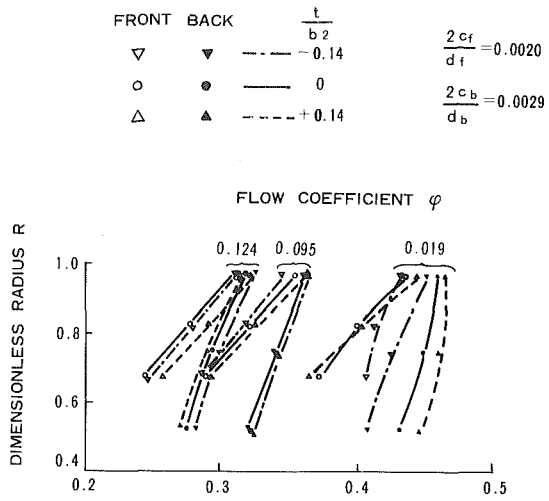

Fig. 4(*a*) Influence of the axial displacement of the impeller

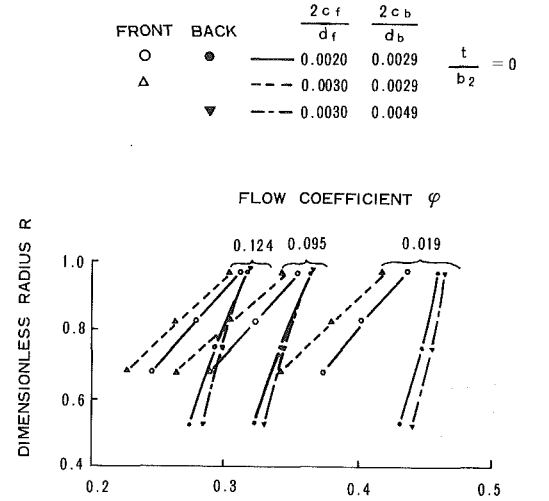

Fig. 4(*b*) Influence of the annular clearances at wearing rings

Fig. 4 Pressure distribution in the space between the impeller and the casing of the test pump A. Uncertainty: R ± 0.5 percent, φ ± 1.5 percent, C_p ± 0.5 percent, t/b_2 ± 5.2 percent, $2c_f/d_f$ ± 3.2 percent, $2c_b/d_b$ ± 3.3 percent.

Experiments

Experimental Results. Figs.4(*a*) and (*b*) show the influence of the impeller axial displacement and the wearing ring

Nomenclature

A = Boussinesq factor, Pa. s
b_2 = impeller width at the outlet diameter, m
c = radial clearance at annular seals, m
C_p = pressure coefficient ($=p/(\rho u_2^2)$)
C_{pD} = pressure coefficient ($=(p-p_0)/(\rho u_2^2)$)
C_T = thrust coefficient ($=T/(\rho S u_2^2 n)$)
C_{TB} = thrust bearing load coefficient ($=T_b/(\rho S u_2^2 n)$)
d = diameter at annular seals, m
d_2 = impeller outlet diameter, m
K = angular velocity coefficient ($=\beta_c/\omega$)
n = number of stages
n_s = specific speed defined in units m, m^3/min, and rpm
p = pressure, Pa
Q_l = leakage flow rate, m^3/s
r = radius, m
R = dimensionless radius ($=2r/d_2$)
S = area difference ($=\pi(d_f^2-d_b^2)/4$)
s = axial spacing between the impeller and the casing wall, m
T = axial thrust, N
T_b = load on the thrust bearing, N
T_d = axial thrust acting on a balancing device, N

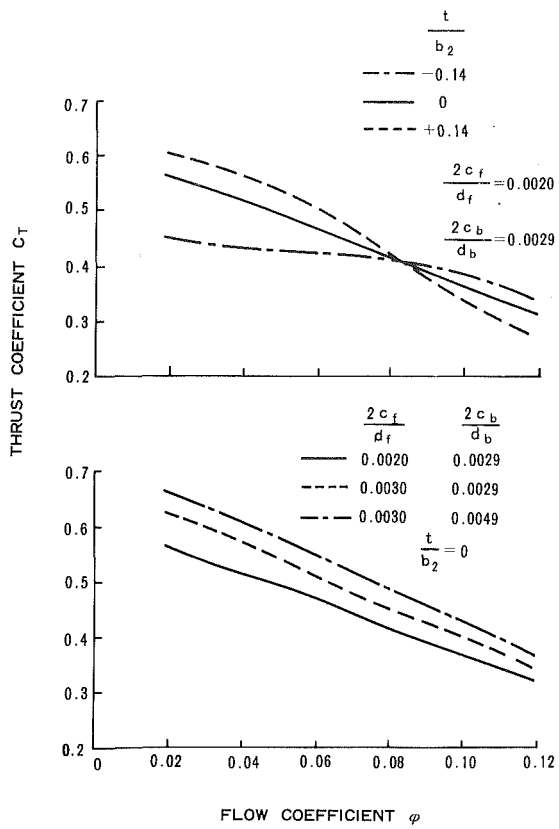

Fig. 5 Axial thrust calculated from the pressure distribution of the test pump A. Uncertainty: C_T ± 1.1 percent, φ ± 1.5 percent, t/b_2 ± 5.2 percent, $2c_f/d_f$ ± 3.2 percent, $2c_b/d_b$ ± 3.3 percent.

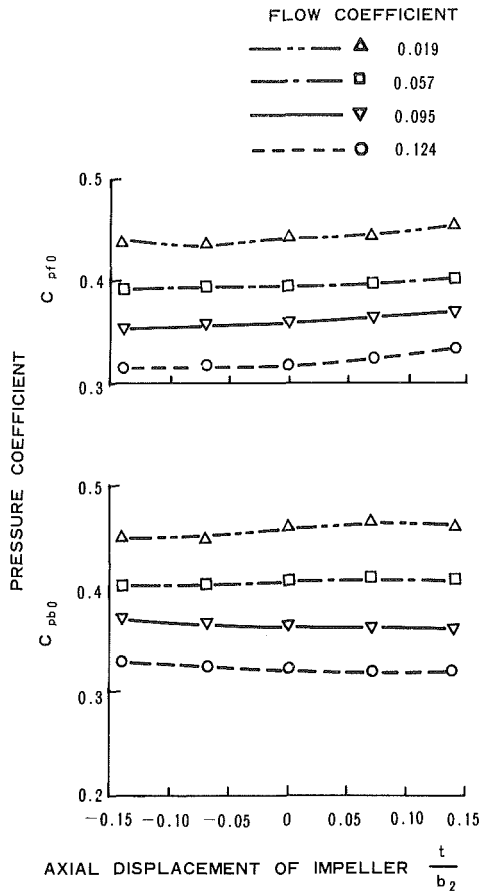

Fig. 6 Pressure coefficient in the space at the impeller outlet diameter of the test pump A. Uncertainty: C_{pfo} and C_{pbo} ± 0.5 percent, φ ± 1.5 percent, t/b_2 ± 5.2 percent.

clearances, respectively, on the pressure distribution in the spaces.

The impeller axial displacement t had a great influence on the pressure distributions in both spaces, especially in the region of small flow coefficient, as shown in Fig. 4(*a*). When t was made negative in the region of small flow coefficient, the pressure coefficient C_p in the front space increased, and C_p in the back space decreased. This change had a great influence on the axial thrust.

The influence of the wearing ring clearances was great, but did not depend much on the flow coefficient. When the front wearing ring clearance increased, C_p in the front space decreased considerably. On the other hand, C_p in the back space increased with the increase of the back wearing ring clearance.

Figure 5 shows the axial thrust calculated from the pressure distributions. The axial momentum change of the flow through the impeller, though it was small, was added to the axial thrust. The impeller axial displacement of the value between ± 0.14 caused the maximum thrust change of about 40 percent of the thrust at the best efficiency point. The thrust curves intersected at a flow coefficient of about 0.08. The increase of the wearing ring clearances caused the thrust change of about 30 percent within the experimental range of clearance variation. The thrust curves were almost parallel.

Influences of the Impeller Axial Displacement. Pressure coefficients in the spaces at the impeller outlet diameter were estimated by making extrapolations from the measurements of pressure distributions to the very location of the outlet. Figure 6 shows those boundary values. They did not change much with the impeller axial displacement. The result that the boundary values in the back space C_{pbo} were a little higher than those in the front space C_{pfo} could be explained as follows. The through-flow in the back space is outward and passes from the space to the impeller outlet through the clearance between the impeller tip and the cylindrical wall of the casing.

Therefore, C_{pbo} is a little higher than the pressure coeffi-

Nomenclature (cont.)

T_i = axial thrust acting on impellers, N
t = impeller axial displacement; displacement in the direction of the impeller eye is designated as positive, m
u_2 = peripheral velocity of impeller, m/s
v_{m2} = radial component of fluid velocity at the impeller outlet, m/s
β = fluid angular velocity at an arbitrary radius in the space, rad/s
$\bar{\beta}$ = fluid angular velocity coefficient ($=\beta/\omega$)
β_c = equivalent angular velocity of fluid in the space, rad/s
λ = friction coefficient
ν = kinematic viscosity, m^2/s
ρ = density, kg/m^3
φ = flow coefficient ($= v_{m2}/u_2$)
ω = angular velocity of rotating parts, rad/s

Subscripts

b = in the space between the impeller back shroud and the casing wall
f = in the space between the impeller front shroud and the casing wall
o = at the impeller outlet diameter in the space

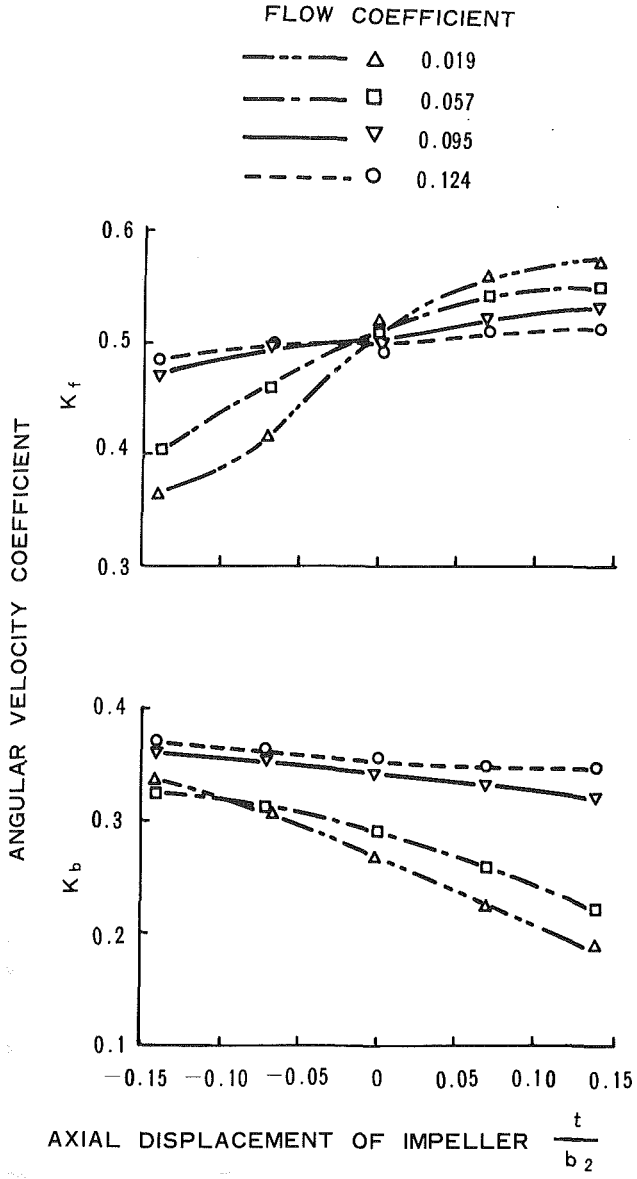

Fig. 7 Angular velocity coefficient of fluid in the space of the test pump A. Uncertainty: K_f and K_b ± 1.3 percent, φ ± 1.5 percent, t/b_2 ± 5.2 percent.

cient at the impeller outlet. The inward through-flow in the front space has the opposite effect.

Pressure coefficients at the impeller outlet at the flow coefficient of 0.095 were calculated on an assumption that the impeller hydraulic efficiency was 95 percent. The pressure coefficients calculated with the slip factors proposed by Stodola and by Wiesner [6] were 0.386 and 0.391, respectively. These coefficients were a little higher than the coefficients C_{pfo} and C_{pbo} shown in Fig. 6.

Figure 7 shows the fluid angular velocity coefficients K calculated from the pressure distribution on the following assumptions.

1 The fluid contained in the space rotates as a solid body at an angular velocity $K\omega$.

2 The pressure distribution for the solid body rotation

$$p(r) = p_0 - \frac{1}{2}\rho(r_2^2 - r^2)K^2\omega^2$$

yields a force to the impeller, which is equal to the force calculated from the actual pressure distribution.

The angular velocity coefficients were greatly influenced by the impeller axial displacement in the region of small flow

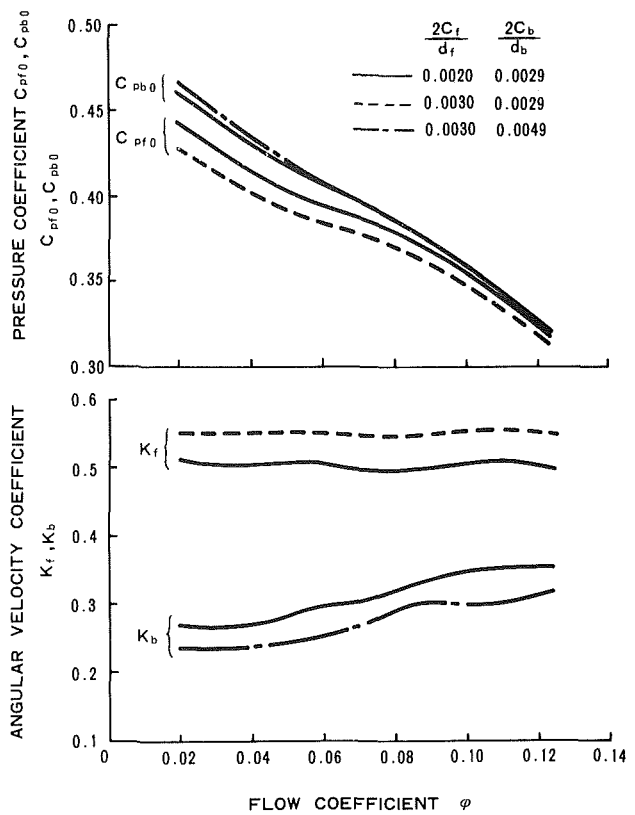

Fig. 8 Influence of wearing ring clearances on the pressure coefficients and the angular velocity coefficients of the test pump A. Uncertainty: C_{pfo} and C_{pbo} ± 0.5 percent, K_f and K_b ± 1.3 percent, φ ± 1.5 percent, $2c_f/d_f$ ± 3.2 percent, $2c_b/d_b$ ± 3.3 percent.

coefficient. With the increase of t/b_2, the coefficient in the front space K_f increased, but K_b decreased. Therefore, a great increase of the axial thrust was caused by the increase of t/b_2.

It turned out from visualization experiment by means of the oil film technique that there existed a reverse flow from the diffuser when t/b_2 was negative and the flow rate was small. This is likely to be the cause of small values of K_f in that region.

Influences of Wearing Ring Clearances. Fig. 8 shows the influences of the wearing ring clearances on the pressure coefficients C_{pfo} and C_{pbo}, and on the angular velocity coefficients K_f and K_b.

Reduction of C_{pfo} with increasing the front wearing ring clearance would be explained by the behavior of the through flow in the front space. The rate of inward through-flow naturally increases as the clearance is widened. This in turn helps to reduce the pressure at the impeller outlet. An increase in through-flow rate also causes an increase of loss in the clearance between the impeller tip and the cylindrical wall of the casing.

The coefficient C_{pbo} did not depend on the back wearing ring clearance.

Increase of K_f with increasing the front wearing ring clearance would also be explained by the behavior of the through-flow in the front space. As stated above, the rate of inward through-flow increases as the clearance is widened. This causes the increase of the angular momentum carried into the front space.

Reduction of K_b brought by the increase of the back wearing ring clearance is the result of increased outward through-flow which carries the angular momentum out of the back space.

Comparison Between Calculation and Measurement of the Pressure Change in the Space. The pressure change measured

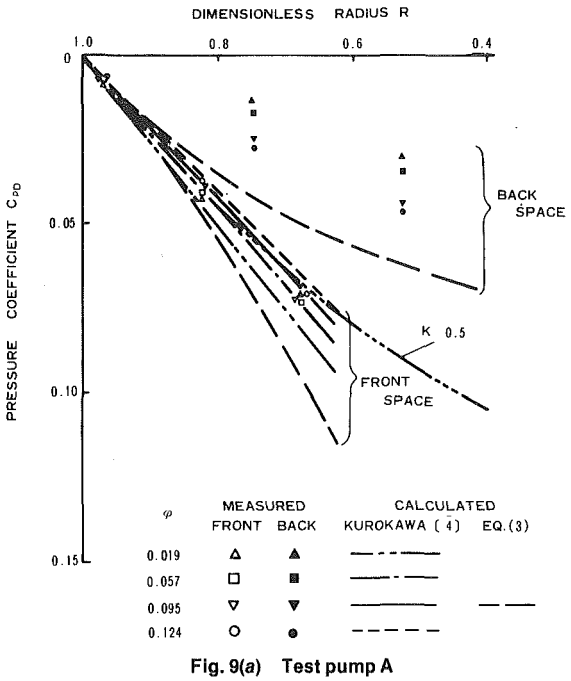

Fig. 9(*a*) Test pump A

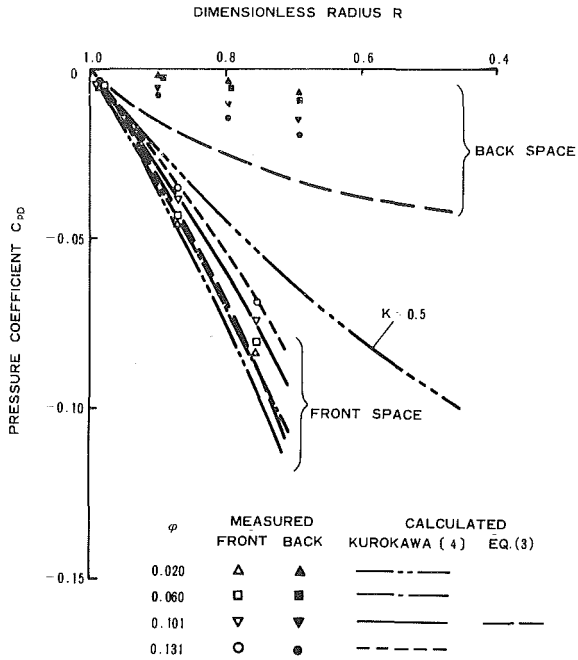

Fig. 9(*b*) Test pump B

Fig. 9 Pressure change in the space between the impeller and the casing. Uncertainty: C_{pD} (measured) ± 1.0 percent, R ± 0.5 percent, φ ± 1.5 percent.

in the spaces were compared with that calculated by the following two methods, as shown in Figs. 9(*a*) and (*b*). One method was based on equation (1) presented by U. Domm and H. Zilling [2].

$$d\beta = \frac{\dfrac{\pi\lambda\omega r^2}{2Q_l}\left\{\beta - \left(\frac{\omega}{2} + \frac{8As}{\rho\lambda r^3}\frac{\beta}{\omega}\right\} - \frac{2\beta}{r}\right.}{1 + \dfrac{8\pi As}{\rho Q_l}} dr \qquad (1)$$

$$dp = \rho r\beta^2 dr$$

The friction coefficient λ was calculated with equation (2) proposed by Y. Yamada [7] for calculation of the torque resistance coefficient for the flow between rotating coaxial cylinders.

$$\lambda = 0.243 R_\omega^{-0.24} \qquad (2)$$

where

$$R_\omega = \frac{sr\omega}{\nu}$$

Equation (2) was substituted into equation (1), and the Boussinesq factor A was neglected. The result was rewritten in the dimensionless form, as shown in equation (3).

$$d\bar{\beta} = \left\{\frac{0.191 R_{\omega 0}^{-0.24} R^{-1.76}(2\bar{\beta} - 1)}{C_q} - \frac{2\bar{\beta}}{R}\right\} dR \qquad (3)$$

$$dC_{pD} = R\bar{\beta}^2 dR$$

where

$$R_{\omega 0} = \frac{sd_2\omega}{2} \text{ and } C_q = \frac{Q_l}{\left(\frac{d_2}{2}\right)^3 \omega}$$

The boundary values of the pressure and the angular velocity, and the leakage flow rate, which were required to perform the calculation, were given by the experimental results. The values of C_{pD} calculated by equation (3) were considerably small compared with the measurements, as shown in Fig. 9.

The pressure change in the spaces was also calculated by the method proposed by J. Kurokawa and T. Toyokura [4]. In the front space, the calculated C_{pD} agreed well with the measurements, as shown in Fig. 9. However, this method was not adequate to calculate the pressure change in the back space with the outward through-flow because of the large thickness of the boundary layer on the casing wall.

Calculation of the Axial Thrust in Multistage Pumps

Axial Thrust in Multistage Centrifugal Pumps. Multistage centrifugal pumps without balancing holes are usually equipped with a balancing drum or disk and a thrust bearing. Figure 10 shows a multistage centrifugal pump equipped with a balancing drum. The thrust bearing must bear the residual axial thrust T_b expressed by equation (4).

$$T_b = T_i - T_d \qquad (4)$$

The bearing capacity is usually 10 to 20 percent of the impeller axial thrust T_i. Therefore the accurate estimation of the axial thrust is necessary to keep the residual thrust within the bearing capacity.

Calculation of the Axial Thrust. A method for calculation of the axial thrust in multistage centrifugal pumps was developed. The impeller axial displacement and annular seal clearances were treated as variable quantities in this method. The outline of the method is explained as follows.

1 In the front space of each impeller and the back space of the last stage one, the pressure distribution is calculated by the Kurokawa-Toyokura method with the boundary values based on the experimental results.

2 In the back space of each stage except the last one, the pressure distribution is calculated based on the experimental results.

3 The pressure distribution on the balancing drum is

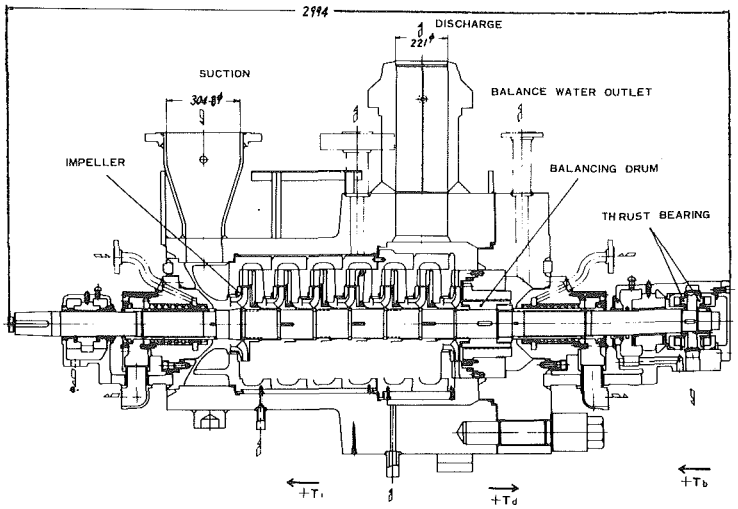

Fig. 10 Prototype multistage centrifugal pump

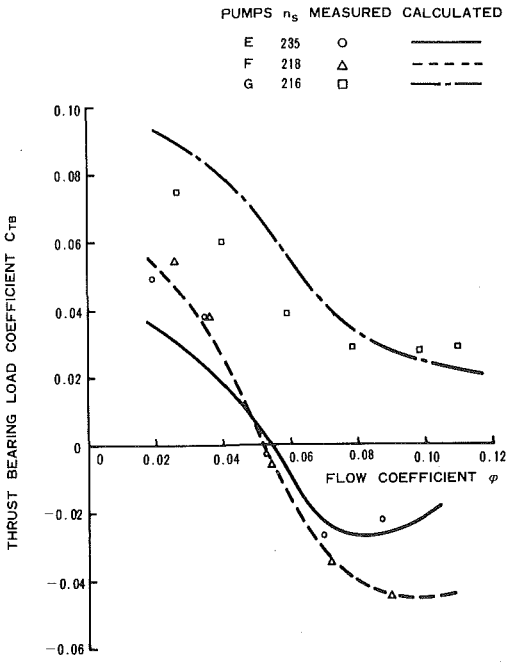

Fig. 11 Axial load on thrust bearings of prototype multistage pumps. Uncertainty: C_{TB} (measured) ± 1.7 percent, C_{TB} (calculated) ± 6.3 percent, φ ± 1.5 percent.

calculated on the assumption that the fluid rotates at half the angular velocity of the rotor.

4 The leakage flow rate through the annular seal clearances is calculated by using the friction coefficient proposed by Y. Yamada [8] and assuming the inlet loss coefficient of 0.5 and the outlet loss coefficient of 1.0.

5 The pressure distribution between the impeller and the casing walls is calculated iteratively until the calculated leakage flow rate agrees with that assumed previously.

A computer program was developed based on the study.

Axial Thrust in Prototype Pumps. Loads acting on the thrust bearings of the three prototype pumps E, F, and G were measured and compared with the calculation. The calculation agreed well with the measurements, as shown in Fig. 11.

Conclusions

An experimental and theoretical study was performed to investigate the hydraulic axial thrust in multistage centrifugal pumps. The following conclusions are deduced.

1 The pressure at the impeller outlet diameter in the space between the impeller and the casing walls was not influenced much by the impeller axial displacement. When the impeller was moved backward, the fluid angular velocity in the front space decreased considerably, but on the contrary the angular velocity in the back space increased.

2 The increase of the front wearing ring clearance reduced the pressure at the impeller outlet diameter and increased the fluid angular velocity in the front space. The increase of the back wearing ring clearance reduced the angular velocity in the back space.

3 In the front space, the pressure distribution calculated by the Kurokawa-Toyokura method agreed well with the measurements. This method was not adequate for the calculation of pressure distribution in the back space where the through-flow was outward.

4 A computer program for calculating the axial thrust in multistage centrifugal pumps was developed. Axial thrust measured in prototype pumps agreed well with the calculation.

Acknowledgments

The authors wish to express their gratitude to Messrs. K. Kamata and K. Komatsu of Tsuchiura Works, Hitachi, Ltd. for their valuable advice.

References

1 Verba, A., and Sebestyén, G., "Contribution to the Calculation of Axial Thrust of Multistage Pumps," *Preprint for the IAHR Symposium "Pumps in Power Stations,"* Braunschweig, 1966, pp. J35-J42.

2 Domm, U., and Zilling, H., "Axial Thrust in Centrifugal Pumps," *Preprint for the IAHR Symposium "Pumps in Power Stations,"* Braunschweig, 1966, pp. J23-J34.

3 Altmann, D., "Contribution to Calculating the Turbulent Flow in the Axial Gap Between Impeller and Casing of Centrifugal Pumps," *Proceedings of 4th Conference on Fluid Machinery*, Budapest, 1972, pp. 37-50.

4 Kurokawa, J., and Toyokura, T., "Study on Axial Thrust of Radial Flow Turbomachinery," *Proceedings of the Second International JSME Symposium Fluid Machinery and Fluidics,* Tokyo, Vol. 2, Sept. 1972, pp. 31-40.

5 Senoo, Y., and Hayami, H., "An Analysis on the Flow in a Casing Induced by a Rotating Disk Using a Four-Layer Flow Model," ASME JOURNAL OF FLUIDS ENGINEERING, Vol. 98, No. 2, June 1976, pp. 192-198.

6 Wiesner, F. J., "A Review of Slip Factors for Centrifugal Impellers," ASME *Journal of Engineering for Power,* Vol. 89, No. 4, Oct. 1967, pp. 558-572.

7 Yamada, Y., "Torque Resistance of a Flow Between Rotating Co-Axial Cylinders Having Axial Flow," *Bulletin of The Japan Society of Mechanical Engineers,* Vol. 5, No. 20, Nov. 1962, pp. 634-642.

8 Yamada, Y., "Resistance of a Flow Through an Annulus with an Inner Rotating Cylinder," *Bulletin of The Japan Society of Mechanical Engineers,* Vol. 5, No. 18, May 1962, pp. 302-310.

A Quasi-Standing-Wave Phenomenon Due to Oscillating Internal Flow

D. Rockwell
Professor.
Mem. ASME

A. Schachenmann[1]
Visiting Assistant Professor.
Assoc. Mem. ASME

Department of Mechanical Engineering and Mechanics,
Lehigh University,
Bethlehem, Pa. 18015

The objective of this investigation is to characterize a quasi-standing-wave pattern having a wavelength two orders of magnitude smaller than the corresponding acoustic wavelength, and relate it to the presence of: a) a downstream travelling wave due to vortical structures generated in a free shear layer, and b) downstream and upstream propagating acoustic waves. In this experiment, the vortical structures were generated by flow past an axisymmetric cavity and their influence extended downstream through the exhaust pipe. The amplitudes of the acoustic waves were associated with Helmholtz resonance of the upstream settling chamber. A linear theory models well the measured amplitude and phase distributions of the fluctuating velocity in the core flow. As system resonance is approached, the ratio of vortex wave amplitude to acoustic wave amplitude decreases. The consequence is an increase in the magnitude and gradient of the phase change across the node, or amplitude minimum, of the resultant standing-wave pattern. In addition, the peak-to-peak amplitude of the quasi-standing-wave increases. A variety of internal (and external) flow systems, including unsteady phenomena in wind tunnels, may be subject to this flow mechanism when the frequency of coherent vortex formation in the test section lies near the Helmholtz resonance frequency of the upstream settling (or plenum) chamber.

Introduction

Many internal flow systems include complex duct-settling or plenum chamber arrangements upstream/downstream of the region of primary interest (e.g. the test section). Aside from lumped parameter analysis of the gross system behavior, little attention has been given to the manner in which resonance of these settling chambers influences the detailed flow dynamics throughout the entire system. Yet, the results of several recent investigations [1, 2, 3, 4, 6] strongly suggest that formation of coherent structures in the presence of a high intensity acoustic field, usually associated with some sort of resonant condition, can produce a quasi-standing-wave behavior.

In experiments aimed towards determining the acoustic reflection coefficient at a sudden expansion, Ronneberger [1] detected peaks and valleys in the streamwise distribution of fluctuating pressure, which he hypothesized to be associated with the formation of vortices downstream of the sudden expansion. The peak-to-peak amplitude of these distributions was enhanced by increasing Mach number (M) and decreasing frequency (f) of forcing by the upstream loudspeaker. For the case of a free jet excited by sound, Pfizenmaier [2] extensively measured fluctuating pressure and velocity distributions, which had shapes similar to those of Ronneberger; in addition, some phase data were acquired but their interpretation was complicated by the measurement method. By superimposing downstream travelling instability and sound waves, he modelled several features of the streamwise distributions of amplitude.[2] In a comprehensive study of flow through a Helmholtz resonator, Morel [3] mentions detection of a standing-wave-like pattern along the centerline of the resonator, but no corresponding data are given. For the situation of a relatively high Mach number ($0.60 \lesssim M \lesssim 0.95$) jet impinging on a wall, Schlieren photos of Wagner [4] exhibit a stationary wave pattern, which he hypothesized to be due to downstream travelling vortices and acoustic disturbances propagating upstream from the stagnation point at impingement - no data were reported for the fluctuating velocity or pressure along the jet. In the case of Parker-mode-resonance [5] generated by flow past a flat plate, the measurements of Morkovin et al. [6] show peaks and valleys in the streamwise distribution of fluctuation velocity. This pattern was related to the downstream propagation of vortices shed from the leading edge of the plate. For this variety of internal and external flows, the overall nature of the flow unsteadiness, and the time mean character of the flow as well, can be related to the flow mechanisms producing these quasi-

[1] Sulzer Bros. Inc., Winterthur, Switzerland; on leave from position of Research Engineer, Fluid Mechanics Laboratory.

Contributed by the Fluids Engineering Division and presented at the Winter Annual Meeting, New York, N. Y., December 3-7, 1979, of THE AMERICAN SOCIETY OF MECHANICAL ENGINEERS. Manuscript received by the Fluids Engineering Division, March 26, 1979. Paper No. 79-WA/FE-24.

[2] The authors wish to thank a reviewer, who pointed out a paper of Davis [19]. He reports on experiments and results very similar to those of Ronneberger, and on modelling the corresponding wave pattern in the spirit of Pfizenmaier [2].

sinusoidal patterns of fluctuating pressure and velocity. Indeed, the intimate interaction between vortex formation and pressure waves incident upon the sensitive region of the shear layer near separation is of central importance for maintenance of self-sustaining oscillations as described herein, and in noise generation and mixing as well (Rockwell and Naudascher [7, 8], Morkovin and Paranjape [9], Bechert and Pfizenmaier [10]).

To date, the stationary wave patterns described above have been typically part of an investigation focussing on other features of the flow field. With the exception of the unconfined jet study of Pfizenmaier [2], which involved only downstream propagating acoustic and instability waves, these patterns have not been pursued in sufficient detail to describe their underlying mechanics. In order to attain an understanding of self-sustaining oscillations of internal flow, both phase *and* amplitude distributions of fluctuation parameters (velocity/pressure), along with an appropriate theoretical model, are called for. The relation between amplitudes of the waves due to sound (acoustic waves) and the wave due to vortex formation in the shear layer (vortex wave) should strongly influence the phase and magnitude distributions of the overall wave pattern. Yet, the central aspects of phase distributions and the manner in which they are associated with the corresponding amplitude distributions of the overall wave pattern have not been pursued. This investigation reveals the relation between the strength of self-sustained oscillations of a typical internal flow system and the corresponding amplitude and phase distributions of the standing wave pattern. Features of peak to peak amplitude of the amplitude distributions, overall phase changes and local phase gradients at amplitude minima, and extent of phase "jitter" at amplitude maxima and minima are linked to the degree of resonant coupling of the flow system.

Experimental System

To allow accessibility for hot wire and pressure transducer measurements, a settling chamber-test section (cavity)-pipe system was chosen. Oscillations of this system are self-sustaining; that is, coherent oscillations occurring in the test section (cavity) couple with the resonance characteristics of the upstream ssettling chamber. The resultant flow pattern involves a quasi-standing-wave phenomenon having a wavelength two orders of magnitude smaller than the corresponding acoustic wavelength. This pattern extends

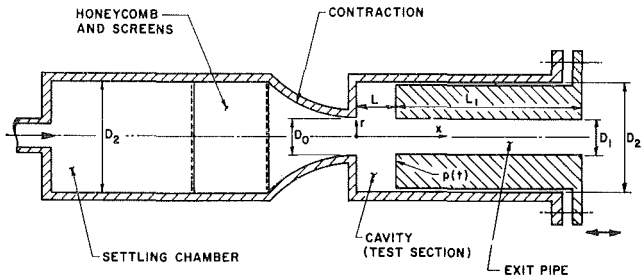

Fig. 1 Test section goemetry

throughout the entire flow region downstream of the settling chamber, and the local flow behavior in the test section is strongly influenced.

An essential aspect of this unsteady flow pattern is a self-excited or self-sustained oscillation of flow in the test section. Among the basic types of self-sustaining oscillations is the flow past a cavity (see Fig. 1), which has been reviewed by Rockwell and Naudascher [7, 8]. As evidenced by several investigations, it is possible to generate strongly coherent oscillations even the the absence of acoustic standing waves within the cavity - i.e., even when the acoustic wavelength is much longer than the cavity length. On the other hand, if cavity resonance does occur, the oscillation can be substantially enhanced. This resonance can take the form of standing waves within the cavity (East [11]) or Helmholtz resonance of the cavity (Wilson, et al. [12]; Morel [3]). In the present investigation, care was taken to ensure that both the Helmholtz and standing-wave resonance frequencies of the cavity were at least an order of magnitude higher than the frequency of interest, thereby eliminating local resonance effects within the cavity test section. This condition substantially eases interpretation and analysis of the overall phenomenon described herein, although, in concept, the same flow mechanisms could interact effectively in cases where the self-sustaining and resonance frequencies have the same order of magnitude.

As shown in Fig. 1, a turbulent pipe flow entered the stilling chamber in the form of a jet, expanded in the chamber (D_2 = 152.4 mm), and passed through a series of honeycomb and screens before experiencing acceleration in the axisymmetric nozzle (D_0 = 48.3 mm). Separation of flow past the cavity (0 $\leq L \leq$ 180 mm) generated organized vortical structures,

Nomenclature

D_0 = nozzle diameter (mm)
D_1 = exit pipe diameter (mm)
D_2 = cavity diameter (mm)
$\mathbf{D}$ = complex amplitude of acoustic waves
$\mathbf{F}$ = complex amplitude of vortex waves
L = cavity length (mm)
L_1 = exit pipe length (mm)
M = Mach number
R = pipe radius (mm)
U = jet centerline velocity at separation (m/s)
c_a = speed of sound (m/s)
c_v = propagation speed of vortex wave (m/s)
f = frequency (Hz)
f_0 = oscillation frequency of system with flow (Hz)
f_r = resonant frequency of system without flow (Hz)
f_{0_r} = resonant oscillation frequency of system with flow (Hz)
$i = \sqrt{-1}$
$k_a = \frac{2\pi}{\lambda_a}$ = acoustic wavenumber (mm^{-1})
$k_v = \frac{2\pi}{\lambda_v}$ = vortex wavenumber (mm^{-1})
p = pressure (N/m^2)
r = radius coordinate (mm)
t = time (s)
u = velocity (m/s)
$\mathbf{u}$ = complex velocity (m/s)
x = coordinate along centerline (mm)
λ = wavelength (mm)
λ_a = acoustic wavelength (mm)
λ_v = vortex wavelength (mm)
λ_{sw} = standing-wave wavelength (mm)
ω = radian frequency (Hz)
θ = momentum thickness (mm)
θ_0 = momentum thickness at separation (mm)
δ_0^* = displacement thickness at separation (mm)
ϕ = phase angle
ϕ_0 = phase angle at $x = 0$
$\pi = \pi$

Subscripts

rms = root mean square value
r = real part
i = imaginary part

Superscripts

( ) = time mean value

which, in turn, were associated with organized flow disturbances transported downstream through the exit pipe (D_1 = 50.8 mm; L_1 = 210 mm). The cavity length (L) was varied using the illustrated piston arrangement. To provide checks on axisymmetry, this arrangement could be rotated through angles up to 90 degrees.

Two DISA 55D01 hot wire anemometer systems (with linearizers) were used to measure flow velocities inside the cavity and the exit pipe. One hot wire was mounted radially inside the cavity; the other reached into the exit duct from the downstream end. These hot wires could be traversed radially and axially, respectively. Linear potentiometers served as position transducers for traverses. Extensive checks were made for probe interference effects by taking measurements at the same location with different probe orientations. For measurements reported here, there were no discernible interferences.

A DISA 51F32 microphone pressure transducer (Bruel and Kjaer No. 4135 (6.35 mm) microphone) was mounted 10 mm below the impingement edge of the cavity. The pressure tap diameter was 3 mm, and the overall frequency response of the volume between the face of the tap and the transducer surface was calculated to be flat up to 3000 Hz, which is two orders of magnitude higher than the frequencies examined herein. Checks on axisymmetry of the pressure fluctuations, which were made by rotating the entire downstream part of the cavity (see Fig. 1), showed undetectable phase and amplitude variations, in accord with the long acoustic wavelength.

The principal objectives of the unsteady data processing were acquisition of pressure and velocity amplitude spectra, which indicated the organized oscillations present, and phase and amplitude distributions of pressure and velocity fluctuations. Both of these requirements can be met with an Ortec two-phase lock-in amplifier with a vector computer module. Two modes of operation can be used: spectrum analyzer and phase sensitive lock-in amplification. In the spectrum analyzer mode, the reference signal is provided by a frequency ramp generator. The lock-in amplifier is used as a swept bandpass filter (with a very high Q factor), with its center frequency determined by the frequency operator. The amplifier output (the rms value of the signal at that particular center frequency) is then plotted on an XY recorder (Y = amplifier output, X-frequency analog from ramp generator). If the lock-in amplifier is used as a phase sensitive detector, a suitable reference signal must be provided; here, it is the amplified and filtered output of the pressure transducer. Care was taken to compensate for phase shifts through the filter and associated electronics. The lock-in amplifier educts the rms values of the measured signal at the frequency given by the reference signal and also indicates the phase angle between the measured and reference signals.

Results

An extensive diagnostics program, carried out at the onset of the experiments, involved characterization of: frequency spectra of velocity fluctuations just downstream of the settling chamber inlet, at the cavity inlet, in the cavity shear layer, and in and at the end of the exit duct, and spectra of pressure fluctuations at impingement (see Fig. 1). These measurements were made in conjunction with other revealing studies, such as extensions of the exit pipe (L_1), placing vortex-inhibiting grids just downstream of the exit pipe, and measuring the response of the entire system to acoustic excitation with and without mean flow.

In essence, these initial forays showed that the predominant frequency of the cavity oscillation (triggered by the hydrodynamic instability of the free shear layer of the cavity [7, 8]) coincided with the Helmholtz resonance frequency of the settling chamber to produce the relatively large amplitude oscillations of the cavity-settling chamber system, which is the subject of this paper. Calculations were carried out using the coupled-resonator theory of Rayleigh [12] in order to examine possible acoustic coupling of the settling chamber-cavity combination. However, since the resonant frequencies were sufficiently different (settling chamber ~ 40 Hz; cavity ~ 287 Hz), the overall acoustic character of the system was that of a single resonator. The settling chamber oscillated in the Helmholtz mode, and the cavity and downstream pipe acted as the resonator neck. In this respect, the large ratio of acoustic wavelength to cavity diameter (λ_a/D_2 ~ 55) made the cavity shape and diameter ratio (D_2/D_1) inconsequential. Since Helmholtz frequencies are typically low compared to those producing classical acoustic standing waves, this limiting (and simplifying) condition is likely to occur often in practice.

Additional results of the diagnostics program, which should be noted here, involve the apparent lack of influence of the jet at the entrance of the settling chamber and the jet at the exit of the pipe ($x = L + L_1$). In the case of the former, detailed spectra in the jet shear layer showed broad-band turbulence and no organized components related to the Helmholtz frequency of the settling chamber; although broad-band excitation of Helmholtz resonance of the settling-chamber (by the jet) may have been present to some degree, predominant excitation was associated with self-sustaining oscillations of the cavity. For the latter, it was originally anticipated that vortex growth in the jet shear layer would couple with the upstream pipe flow. Use of numerous grids and screens to attenuate this vortex growth did not affect the overall system oscillation.

For data reported here, the experiments were conducted at a jet centerline velocity U = 2.75 m/s, resulting in a Mach number M = 7.95×10^{-3} and a Reynolds number based on D_0 of R_e = 8855. The Helmholtz resonance frequency of the system with no flow applied was measured to be 40.8 Hz.

Figure 2 illustrates the variation of dimensionless frequencies (f_r/f_{o_r} and f_o/f_{o_r}) with impingment length (L/θ_0) with and without mean flow. (As discussed by Rockwell and Naudascher [7, 8], it is the characteristic shear layer thickness θ_0 that is associated with the instability of the separated shear layer). The symbol f_0 designates the frequency of the self-sustaining oscillation of the system at a given length (L/θ_0), and f_{0_r} represents its value at the length giving maximum amplitude response (i.e. amplitude at L/θ_0 = 97.6 in Fig. 3). Resonance of the system in the absence of flow, due to Helmholtz resonance of the settling chamber, was determined by loudspeaker excitation; this frequency is f_r. The normalizing momentum thickness (θ_0) of the mean flow experiments also was used to non-dimensionalize data taken in absence of mean flow. Agreement of the no-flow theory (described above) with data is good. These data were obtained by observing the maximum response to loudspeaker excitation over a range of frequencies. It is evident that the presence of mean flow severely increases the slope of the frequency versus length variation. Aside from possible modification of the Helmholtz frequency by mean flow through the neck of the resonator, it is primarily the frequency associated with self-excited oscillation of the cavity that produces this increase in slope. In fact, comparison of this slope ($d(f_0\theta_0/U)/d(L/\theta_0)$) with recent cavity experiments in a water tunnel where no system resonance occurred (Rockwell and Knisely [12]) shows that this slope is nearly the same for the same average value of dimensionless frequency ($\bar{f}_0\theta_0/U$). That is, the inherent instability of the cavity shear layer, an in [12], has a strong influence in triggering the oscillation of the system. Even though variations in length (L/θ_0) shift the settling chamber away from its optimum resonance condition, substantial, but reduced, oscillation amplitudes still persist (see Fig. 3 and amplitudes at x/D_0 = 0 in Fig. 5).

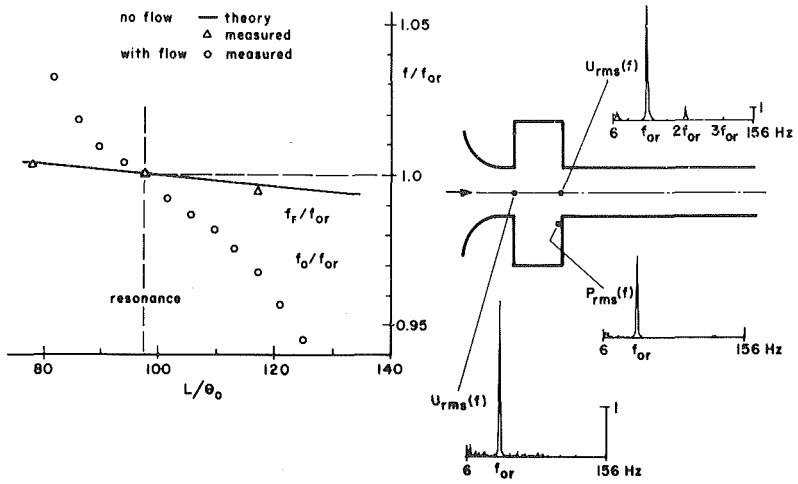

Fig. 2 Variation of dimensionless frequency (f/f_{or}) with cavity length (L/θ_o). Frequency spectra ($u_{rms}(f)$ and $p_{rms}(f)$) at system resonance ($f=f_{or}$), $R_{e\theta o}$ = 94

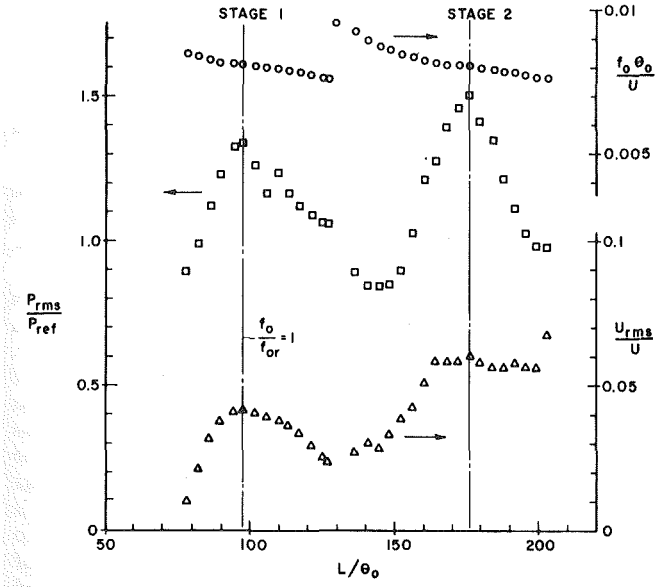

Fig. 3 Variation of Strouhal number ($f_o\theta_o/U$), pressure (p_{rms}/P_{ref}) and velocity (u_{rms}/U) amplitudes with cavity length (L/θ_o). $Re_{\theta o}$ = 94

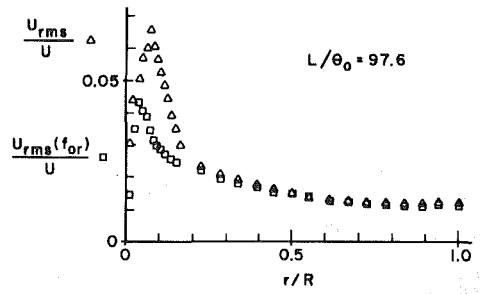

Fig. 4 Velocity amplitude u_{rms}/U and organized oscillation amplitude $u_{rms}(f_{or})/U$ as a function of radius (r/R) at separation (x/D_o = 0). $R_{e\theta o}$ = 94

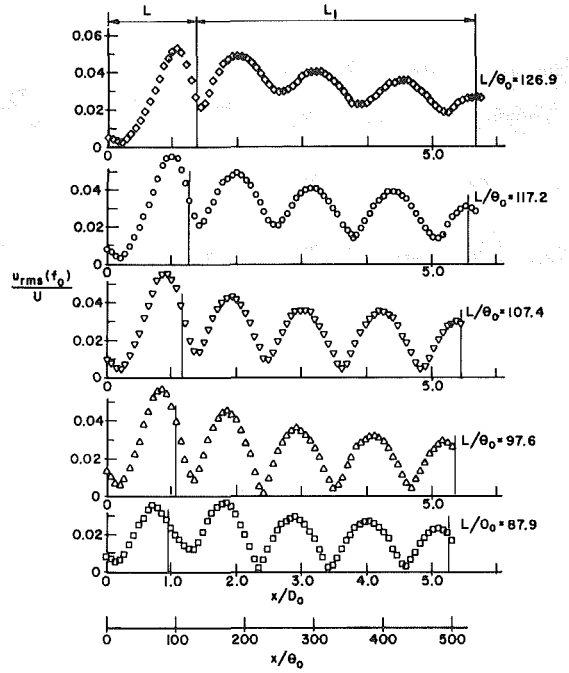

Fig. 5 Velocity amplitude at cavity oscillation frequency $u_{rms}(f_o)/U$ along the duct centerline (r/R = 0) in the streamwise direction (x/D_o) for several values of cavity length (L/θ_o). $R_{e\theta o}$ = 94

Also shown in Fig. 2 are typical amplitude spectra of the velocity fluctuations. At the nozzle exit (x/L = 0), essentially all of the energy is concentrated at the resonant frequency (f_{0_r}). At the cavity exit (x/L = 1), there are contributions from the first and second harmonics. According to the free shear-layer experiments of Miksad [15], this presence of harmonics indicates that the nonlinear process of vortex formation is well underway. In subsequent discussion, the corresponding downstream travelling wave will be called a "vortex wave"; in a more general sense, it could be termed an instability wave. This would accommodate the possibility that unstable disturbance growth, without concentration of vorticity into vortical structures, can also characterize the downstream propagating wave.

As shown in Fig. 3, variation of cavity length (L) produces the above-mentioned changes in oscillation frequency of the system (f) (see references [7, 8] for discussion of similar variations), pressure amplitude at impingement (P_{rms}) and velocity amplitude on the centerline at impingement (u_{rms} at x = L, r = 0). Minimum amplitudes occur approximately at the location of the frequency jump, while maximum amplitudes occur near the middle of each stage of oscillation. Comparison of the location of pressure and velocity amplitude maxima (at L/θ_0 = 97.6) in Fig. 3 with the location of the curve intersection (L/θ_0 = 97.6) in Fig. 2 show that they occur at the "resonance" condition of the system. Moreover,

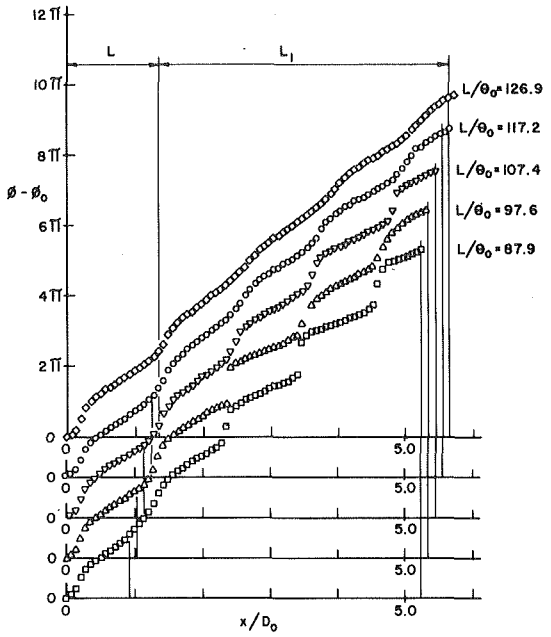

Fig. 6 Phase variation of velocity signal (ϕ-ϕ_0) at cavity oscillation frequency (f_0) along the duct centerline ($r/R = 0$) in the streamwise direction (x/D_0) for several values of cavity length (L/θ_0). $R_{\theta\theta 0} = 94$

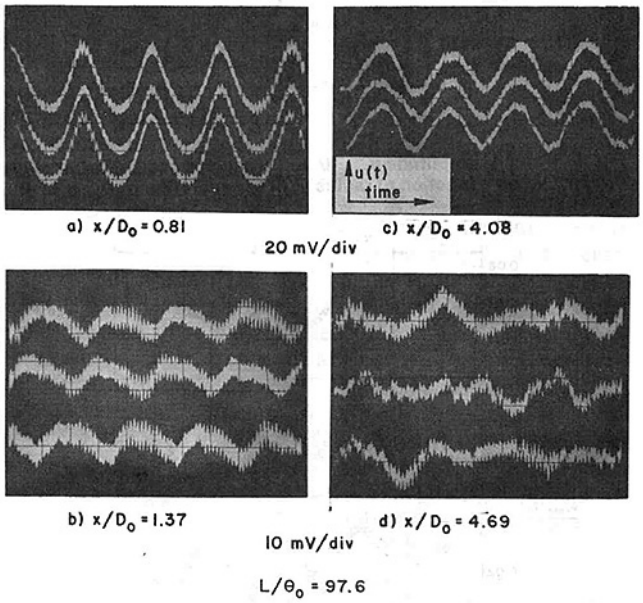

Fig. 7 Velocity traces at velocity antinodes (*a, c*) and nodes (*b, d*) illustrating phase "jitter." $L/\theta_0 = 97.6$, $r/R = 0$, $R_{\theta\theta 0} = 94$. (Correspond to amplitude and phase variations of Figs. 5 and 6)

the average oscillation frequency ($f\theta/U \simeq 0.016$ where $\theta/\theta_0 = 1.95$) agrees well with that predicted by Michalke [16] for an axisymmetric jet. As in the investigation of Crow and Champagne [17], the boundary layer was tripped just upstream of the nozzle exit, and according to Michalke [14], it is most appropriate to use a charateristic momentum thickness evaluated at a reference station downstream of separation. Here, θ was determined at $x = L/2$.

As shown in Fig. 4 ($L/\theta_0 = 97.6$), the velocity amplitude of the organized oscillation ($u_{rms}(f_{or})/U$) at separation ($x/D_0 = 0$) varied from about 0.013 in the free stream to 0.045 in the boundary layer. In fact, the distributions of turbulence intensity (u_{rms}/U) and mean velocity ($\bar{u}/U$) at separation are similar to those of Crow and Champagne [15], where a loudspeaker system located in the upstream settling chamber

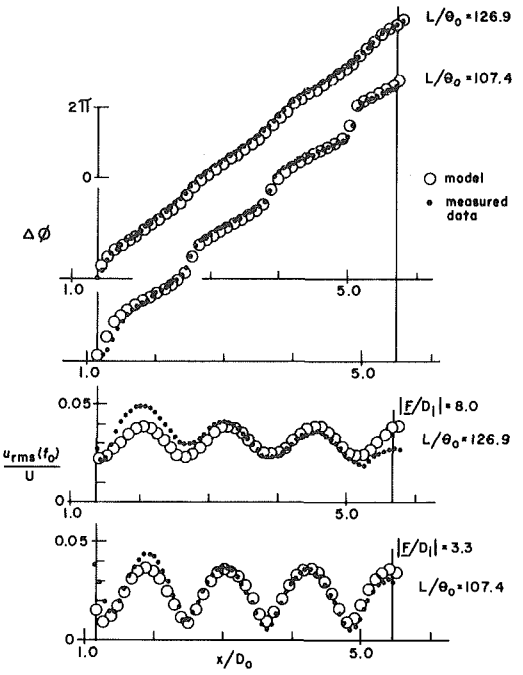

Fig. 8 Comparison of measured velocity amplitude ($u_{rms}(f_0)/U$) and phase ($\Delta\phi = \phi_0$) with values predicted by model

forced oscillations of a jet flow. Mean flow momentum and displacement thickness, corresponding to the data of Fig. 4 (and subsequent figures), were: $\theta_0/D_0 = 0.0106$ $\delta_0^*/D_0 = 0.026$. Reynolds numbers were $Re_{\theta 0} = 94$ and $Re_{D0} = 8855$.

Figure 5 shows velocity amplitude at the oscillation frequency ($u_{rms}(f_0)/U$) measured along the centerline as a function of distance downstream of the nozzle exit (x/D_0). Not given in Fig. 5 are the amplitude variations upstream of the nozzle exit; traverse revealed that the amplitude was constant upstream of the exit at least a distance of D_0. This finding reaffirms the assumption that the nozzle acts as the "neck" of the settling chamber resonating in the Helmholtz mode. For each cavity length (L/θ_0), the disturbance is substantially amplified within the cavity to an order of five to ten times its original amplitude at separation. This degree of amplification is in accord with that attained by Crow and Champagne [15] in their forced jet study, where their forcing amplitudes ($u_{rms}(f_0)/U$) were of the same order. For the range of cavity lengths investigated, the first peak amplitude is consistently reached at $x/L \simeq 0.75$, followed by a rapid decrease in amplitude, which persists into the entrance region of the pipe. Within the pipe, there are only mild changes in the peak amplitude of the quasi-standing-wave pattern with increasing streamwise distance. The most remarkable characteristic of all amplitude distributions is their short wavelength ($\lambda/D_0 \sim 1$), in comparison with the corresponding acoustic wavelength ($\lambda_a/D_0 \sim 175$). For values of L/θ_0 at, or close to, resonance (i.e., $L/\theta_0 = 97.6$ in Fig. 3), the amplitude minima, or "nodes," in Fig. 6 approach zero. On the other hand, high values of L/θ_0 (= 117.2, 126.9), which are not close to the resonance condition, possess smaller peak to peak amplitudes and amplitude minima as high as 0.02 U. Furthermore, at these high values of L/θ_0, the pipe exit corresponds to a maximum in the velocity amplitude. In a strictly acoustical sense (in absence of mean flow), this is expected at the frequencies studied here: velocity antinode and pressure node at the exit. However, at lower values of L/θ_0 (at and near the resonance condition), this is not the case.

The time-averaged phase distributions of Fig. 6 correspond to the amplitude distributions of Fig. 5. Particularly in-

teresting are rapid changes in phase (i.e. large $d\phi/dx$) at several streamwise stations for a given value of L/θ_0. Comparison of the velocity minima in Fig. 5 with these regions of large $d\phi/dx$ shows that they occur at the same values of x/D_0. Both the overall magnitude of the phase change due to negotiating a velocity minimum *and* the rate of change of the phase ($d\phi/dx$) at the velocity minimum is a function of L/θ_0. That is, at values of L/θ_0 near resonance (near $L/\theta_0 = 97.6$ in Fig. 4), large changes in phase occur, and $d\phi/dx$ is very large. In fact, in some cases, a phase jump is approached. In contrast, at the extreme value of L/θ_0 (= 126.9), mild phase variations occur.

Determination of the phase at locations of velocity minima was, for cases near resonance, complicated by substantial phase "jitter," which is illustrated in Fig. 7. For each of the photos, three consecutive sweeps of the instantaneous velocity fluctuation were made on a storage oscilloscope. Comparison of the values of x/D_0 for these photos with Figs. 5 and 6 shows that Figs. 7 (*a*) and (*c*) correspond to locations of velocity maxima, while Figs. 7 (*b*) and (*d*) correspond to velocity minima and regions of large $d\phi/dx$. It is evident that at velocity maxima, there is little variation in phase, whereas at velocity minima, severe jitter occurs. In contrast, cases away from resonance ($L/\theta_0 = 117.2$, 126.9), though not illustrated here, exhibited negligible jitter. The corresponding values of $d\phi/dx$ at locations of velocity minima are mild (see Figs. 5 and 6).

The extent of one-dimensionality of the oscillation was determined by acquiring amplitude distributions, similar to those of Fig. 5, at various values of r/R. Up to $r/R \simeq 0.4$, distributions along the entire length of the system followed closely those at $r/R = 0$, justifying a one-dimensional model for the central region of the pipe.

Theory

If the central features of the quasi-standing-wave pattern depicted in Figs. 5, 6, and 8 are considered to be approximated by superposition of upstream and downstream travelling waves, contributions from acoustic waves and waves due to vortex formation and propagation must, in general, be accommodated. The acoustic, or sound, waves will be assumed to possess an essentially one-dimensional character as they propagate through the core flow of the system. Likewise, the wave induced in the core flow by the passage of a ring vortex (formed in the free shear layer of the cavity) will be assumed to be quasi-one-dimensional. Since the formation and propagation of the ring vortices can, in concept, be described by stability theory, the propagation speed of the resultant "vortex wave" follows. In general, this wave will propagate at some fraction of the mean flow speed, as contrasted with the sound speed of the acoustic waves. Although both of these classes of waves (hereafter referred to as acoustic and vortex waves) are associated with the same frequency, their wavelengths differ by about two orders of magnitude (for this experiment) due to their different propagation speeds.

The exit of the Helmholtz resonator (i.e. exit of the nozzle downstream of the settling chamber) generates a downstream propagating wave. Due to its long wavelength ($\lambda_a/D_0 \sim 175$), this wave will be almost totally reflected from the exit of the pipe (at $x = L + L_1$ in Fig. 1) as shown by Ronneberger [1]. Consequently, contributions to the resultant wave velocity from downstream and upstream travelling acoustic waves must be accounted for:

$$\hat{u}_a = \mathbf{D}\{e^{i(\omega t - k_a x)} + e^{i(\omega t + k_a x)}\} \text{ where } k_a = \frac{2\pi}{\lambda_a} \tag{1}$$

In this expression, it has been assumed that the velocity fluctuations of the incident and reflected waves are in phase and, for the time being, that both waves have the same wave number. This is valid only if $M << 1$, which is the case for the experiment carried out here ($M = 7.95 \times 10^{-3}$). In contrast to the reflected acoustic wave, the wave resulting from vortex formation and propagation, which travels at a fraction of the mean flow velocity and has a relatively short wavelength ($\lambda_v/D_0 \sim 1$), is completely transmitted. Therefore, only a downstream propagating "vortex wave" must be modelled:

$$\hat{u}_v = \mathbf{F}e^{i(\omega t - k_v x)} \text{ where } k_v = \frac{2\pi}{\lambda_v} \tag{2}$$

Superposing all contributions to the wave field,

$$\hat{u} = \hat{u}_a + \hat{u}_v = \mathbf{D}e^{i\omega t}\{e^{-ik_a x} + e^{ik_a x}\} + \mathbf{F}e^{i\omega t}\{e^{-ik_v x}\} \tag{3}$$

and writing in time-independent form, the resultant velocity becomes

$$\mathbf{u}(k_a, k_v, x) = \mathbf{D}\{e^{-ik_a x} + e^{ik_a x}\} + \mathbf{F}e^{-ik_v x} \tag{4}$$

where $D = D_r + iD_i$ and $\mathbf{F} = F_r + iF_i$. Clearly, $\mathbf{F}$ will rapidly increase just downstream of the nozzle exit as the shear layer disturbance is amplified and the vortex is formed (see Pfizenmaier [2]). In the spirit of this approximate analysis, changes in $\mathbf{F}$ in the near field will be neglected, and it will be assumed that $\mathbf{D}$ and $\mathbf{F}$ are invariant with x. This approximation is most accurate downstream of the pipe inlet (see Fig. 5).

Dividing by $\mathbf{D}$, and letting $\mathbf{D} \to D_i$, which means that the phase angle of the acoustic wave becomes 90 deg and serves as a reference for subsequent calculations, the normalized equation becomes

$$\frac{\mathbf{u}(x)}{D_i} = e^{-ik_a x} + e^{ik_a x} + \frac{\mathbf{F}}{d_i}e^{-ik_v x} \tag{5}$$

This expression can be divided into real and imaginary parts:

$$\left\{\frac{\mathbf{u}}{D_i}\right\}_i = 2\cos(k_a x) + \frac{F_i}{D_i}\cos(k_v x) - \frac{F_r}{D_i}\sin(k_v x) \tag{6}$$

$$\left\{\frac{\mathbf{u}}{D_i}\right\}_r = \frac{F_r}{D_i}\cos(k_v x) + \frac{F_i}{D_i}\sin(k_v x) \tag{7}$$

Since the acoustic wavelength (λ_a) is, for this experiment, much larger than typical values of x, $k_a x << 1$, and $\cos(k_a x) \sim 1$. Consequently, *the resultant wave pattern will be influenced only by the amplitude of the acoustic waves and the amplitude and wave number of the vortex wave.* The amplitude and phase angle of the resultant quasi-standing-wave are

$$\left|\frac{\mathbf{u}}{D_i}\right| = \left\{\left|\frac{\mathbf{u}}{D_i}\right|_i^2 + \left|\frac{\mathbf{u}}{D_i}\right|_r^2\right\}^{1/2} \quad \phi = \arctan\left\{\frac{(\mathbf{u}/D_i)_i}{(\mathbf{u}/D_i)_r}\right\} \tag{8}$$

In general, it would be possible to calculate the amplitude and phase distributions as follows: estimate k_v from shear-layer stability theory for the specified frequency (f_0) of oscillation; determine k_a from $k_a = 2\pi f_0/c_a$ (provided $M << 1$); and specify the amplitude ratio of the vortex wave to acoustic wave $|\mathbf{F}/D_i|$. Although equations (6) and (7) require values of F_i and F_r, it can be shown that the effect of specifying different F_i and F_r (which together produce the same resultant $|\mathbf{F}|$) is simply to translate both the predicted amplitude and phase patterns in the x direction provided $L_1/\lambda_a << 1$. This means that if the ratio F_r/F_i is unknown, it is only necessary to impose, for example, the location of the

velocity maximum at, or near, the pipe exit (see Fig. 5). That is, this exit restraint fixes the axial location of the amplitude and phase patterns. Since the primary objective of this model is to examine the effect of wave amplitude ratio $|\mathbb{F}/D_i|$ on the distributions of velocity amplitude and phase exhibited in Figs. 5 and 6, λ_{sw} was determined from Fig. 5, thereby allowing direct calculation of k_v. Alternatively, k_v could have been estimated from the fact that the vortex wave travels at a fraction ($\sim$0.5 to 0.7) of the free stream velocity. More precisely, this wave speed can be calculated if the dimensionless oscillation frequency is known (Michalke [16], Betchov and Criminale [18]). The wave number k_a was evaluated from the observed frequency of the oscillation and the speed of sound at operating conditions. So, in summary, this model requires only the ratio of vortex wave to acoustic wave amplitude $|\mathbb{F}/D_i|$ as an input. Other parameters can be reasonably estimated using concepts of hydrodynamic stability and acoustic wave theories.

Fig. 8 shows comparison of the model with data for two extreme cases - near and away from resonance (see Figs. 2 and 3). For $L/\theta_0 = 126.9$, minimum values of velocity amplitude are predicted to be relatively large ($\sim$0.023) and gradients in the phase distribution are mild. On the other hand, at $L/\theta_0 = 107.4$, minimum values of velocity amplitude approach "nodes," the peak to peak amplitude is larger, and gradients in the phase distribution are large at locations of velocity minima. All of these features are modelled well, and it is evident that the nature of the standing wave pattern strongly depends on the ratio of vortex wave to acoustic wave amplitude $|\mathbb{F}/D_i|$. As this ratio increases, the peak to peak amplitude of the standing wave decreases. On the basis of this trend, it is apparent that the strength of the acoustic field induced during a self-sustaining oscillation must be sufficiently large, relative to disturbances induced by vortex formation, if a standing wave pattern is to appear.

Close inspection of the patterns portrayed in Fig. 5 reveals that λ_{sw} is not constant, but increases slightly in the streamwise direction. From the relations $\lambda_{sw} \sim c_v/f$ and $c_v = f/d\phi/dx$,

$$\lambda_{sw} \sim 1/(d\phi/dx)$$

which means that the phase gradient should decrease in the streamwise direction. The phase distributions of Fig. 6 show that the local phase gradients at locations corresponding to velocity minima (see Fig. 5) do, in an overall sense, decrease in the direction of flow.

In the event that higher speed flows are considered, and the condition $M << 1$ does not hold, it is necessary to consider different wave numbers for downstream (k_{a+}) and upstream (k_{a-}) propagating waves by accounting for the respective wave speeds, $C_a(1+M)$ and $C_a(1-M)$. Furthermore, the complex amplitudes of the reflected waves must be determined using the incident wavenumber and pipe radius (Ronneberger [1]). If these aspects are accounted for, the superposition approach (equation (4)) can be employed to determine the overall features of the standing wave pattern.

Conclusions

The self-excited oscillations of a settling chamber-cavity combination, which is a typical geometry encountered in internal flow systems, can lead to a quasi-standing-wave pattern having a very short wave-length; this pattern extends well downstream of the settling chamber. For oscillations occurring at very low Mach number, it can be shown that the standing-wave characteristics are determined by the wavenumber of the vortex wave and the ratio of the vortex wave and acoustic wave amplitudes. The effect of amplitude of the vortex wave relative to the acoustic wave can be approximated using a linear model. Predicted amplitude minima and streamwise phase gradients of the wave pattern agree well with data both at and away from the resonant state of the self-sustaining oscillation.

When the entire system (settling chamber - test section (cavity) - pipe) is operating at resonance, the amplitude minima of the quasi-standing-wave approximate nodes, and the phase distributions exhibit very large gradients ($d\phi/dx$) at locations of these approximate nodes. In addition, successive sweeps of instantaneous velocity taken at these nodal points show large jitter in phase of the local fluctuations. On the other hand, at the velocity antinodes, the fluctuations display negligible phase jitter.

Operation of the system sufficiently far away from the resonance condition results in a larger ratio of vortex wave to acoustic wave amplitude. Corresponding gradients in phase ($d\phi/dx$) are much smaller, and only very mild phase jitter occurs at locations of the amplitude minima.

In concept, it appears that this type of quasi-standing-wave pattern can occur in any flow situation where vortical structures propagate downstream in the presence of upstream/downstream travelling acoustic waves, provided the acoustic wave has sufficient amplitude. Either acoustic standing-wave resonance or Helmholtz-induced resonance could enhance the amplitude of these acoustic waves during self-sustaining oscillations.

Acknowledgments

The authors would like to express their gratitude to the National Science Foundation and the Volkswagen Foundation for financial support of this investigation. Professors Eduard Naudascher and Mark V. Morkovin encouraged pursuit of this phenomenon; discussions with MVM and the unsteady wind tunnel investigation of reference [6] stimulated consideration of the vortex-acoustic wave field superposition.

References

1 Ronneberger, D., "Experimentelle Untersuchungen zum akustischen Reflexionsfaktor von unstetigen Querschnittsänderungen in einem luftdurchstroemten Rohr," *Acustica,* Vol. 19, 1967/1968, pp. 222-235.

2 Pfizenmaier, E., "On the Instability of a Sound-Influenced Free Jet," Report No. DLR-FB 73-69, DFVLR, TU Berlin, Jan. 1975.

3 Morel, T., "Experimental Study of a Jet-Driven Helmholtz Oscillator," General Motors Research Laboratories Research Publication-GMR-2362, July 1977.

4 Wagner, F. R., "Zum Schall-und Stroemungsfeld eines axialsymmetrischen Freistrahls beim Auftreffen auf eine Wand," *Z. Flugwiss.,* Vol. 19, 1971, pp. 30-44.

5 Parker, R., "Resonance Effects in Wake Shedding from Parallel Plates: Calculation of Resonant Frequencies," *J. Sound Vibr.,* Vol. 5, 1967, pp. 330-343.

6 Morkovin, M. V., Loerhrke, R. I., and Fejer, A. A., "On the Response of Laminar Boundary Layers to Periodic Changes in Free-Stream Speed," IUTAM Symposium on Unsteady Boundary Layers, Quebec, 1971.

7 Rockwell, D., and Naudascher, E., "Self-Sustaining Oscillations of Impinging Free Shear Layers," *Annual Review of Fluid Mechanics,* Vol. 11, 1979, pp. 67-94.

8 Rockwell, D., and Naudascher, E., "Review - Self-Sustaining Oscillations of Flow Past Cavities," ASME JOURNAL OF FLUIDS ENGINEERING, Vol. 100, June 1978, pp. 152-165.

9 Morkovin, M. V., and Paranjape, S. V., 1979, "On Acoustic Excitation of Shear Layers," *Z. Flugwiss.,* Vol. 19, 1971, pp. 328-335.

10 Bechert, D., and Pfizenmaier, E. 1973, "Optische Kompensationsmessungen zur instationären Abflussbedingung an einer Düsenaustrittskante. Eine Untersuchung im Zusammenhang mit dem Schalldurchgang bei durchströmten Düsen," DFVLR Forschungsbericht 73-93, Institut Für Turbulenzforschung, Berlin.

11 East, L. F., "Aerodynamically Induced Resonance in Rectangular Cavities," *Journal of Sound and Vibration,* Vol. 3, No. 3, 1966, pp. 277-287.

12 Wilson, T. A., Beavers, G. S., DeCoster, M. A., Holger, D. K., and Regenfuss, M. D., "Experiments on the Fluid Mechanics of Whistling," *Journal of the Acoustical Society of America,* Vol. 50, No. 1, Part 2, 1971, pp. 366-372.

13 Rayleigh, J. W. S., *The Theory of Sound,* Dover, New York, 1945.

14 Rockwell, D., and Knisely, C., "Low Frequency Self-Modulation of Flow Past a Cavity," submitted for publication.

15 Miksad, R. W., "Experiments on the Nonlinear Stages of Free-Shear-Layer Transition," *Journal of Fluid Mechanics,* Vol. 56, Part 4, 1972, pp. 695-719.

16 Michalke, A., "Instabilitaet eines kompressiblen runden Freistrahls unter Beruecksichtigung des Einflusses der Strahlgrenzschichtdicke," *Z. Flugwiss.,* Vol. 19, 1971, pp. 319-328.

17 Crow, S. C. and Champagne, F. H., "Orderly Structure in Jet Turbulence," *Journal of Fluid Mechanics,* Vol. 48, Part 3, 1971, pp. 547-591.

18 Betchov, R., and Criminale, W. D., *Stability of Parallel Flows,* Academic Press, New York, 1967.

19 Davies, P. O. A. L., "Bench Test Procedures and Exhaust System Performance Prediction," *Proceedings of Surface Transportation Exhaust Noise Symposium,* Oct. 11-13, 1977, EPA, Office of Noise Abatement and Control, Washington, D. C. 20460. EPA Doc. No. 550/9-78-206.

On the Relevance of Inviscid Subsonic Flow Calculations to Real Centrifugal Impellers Flow

D. Adler

Y. Krimerman

Faculty of Mechanical Engineering,
Technion Israel Institute of Technology,
Haifa, Israel

The results of a fully three-dimensional inviscid compressible calculation technique for the flow field inside centrifugal impellers are compared to optical measurements in an open, radial exit impeller. It is concluded from this comparison that as long as viscous influence, including its displacement effects (manifested mainly in the jet-wake flow structure), are not too big, the inviscid method applied can be used with confidence. When the viscous influence is such that it distorts the flow field in certain regions but displacement effects are still insignificant, the inviscid method can be used outside regions of viscous dominance. This situation occurs about halfway downstream, through the impeller. Only when displacement effects resulting from viscous flow field distortions, become big and the jet-wake profile becomes fully developed, does the inviscid method fail to predict the correct flow field. This happens at the exit of the impeller investigated here.

Introduction

A great deal of effort was invested in the last two decades in the development of methods to predict the flow field inside centrifugal impellers. Because of the complexity of viscous flow models (turbulent flow in rotating curved passages) most of the theories developed so far included the assumption that the flow is not viscous. It is the aim of this article to discuss the severity of this assumption and to try to find out under which conditions inviscid theories, which are relatively simple and inexpensive to use, can be used with confidence.

The inviscid flow theories can be classified into a number of groups. On a geometrical basis, a possible classification is: Hub-to-Shroud theories (H-S), Blade-to-Blade theories (B-B), quasi three-dimensional theories and three-dimensional theories. The calculation methods in each of these groups can be further classified on the basis of the computational scheme used: singularity methods, streamline curvature methods, finite difference methods or finite element methods.

Historically, H-S streamline curvature techniques were the first to be developed. Being based on first order ordinary differential equations they required relatively modest computer storage and simple numerical schemes. The price paid for this simplicity was the loss of ellipticity. Examples of these technics were published by Katsanis [1], Novak [2, 3], Davis [4], Smith [5], and Adler and Iberg [6]. H-S finite difference methods were based in most cases on Wu's theory [7]. Typical solutions were developed by Wu [8], Marsh [9], Davis [10], Katsanis and McNally [11, 12]. All these finite difference technics are physically more correct than stream-line curvature methods because they are elliptic and therefore mathematically compatible with the subsonic elliptic flow field they ought to describe. The same is true for the H-S finite element methods which are also based on Wu's formulation [7]. Here three methods can be mentioned: Adler and Krimerman [13], Oates [14], and Hirsch and Warzee [15].

Solution on the B-B stream surface are essentially not much different from H-S methods because the differential equations of the B-B surface are basically analogous to the H-S equations. The major difference is that on B-B surfaces the domains in which the solutions have to be found lack well defined boundaries at the inlet to, and exit from the blade passages. These boundaries are given on the H-S surface by the hub and shroud extensions in up, and down-stream directions. In contrast, the B-B boundaries in form of the leading and trailing edge stagnation streamlines, are determined in the course of the solution.

B-B singularities methods avoid the boundaries problem. The best known methods were developed by Martensen [16], Wilkinson [17], Rauchman [18], Von der Braembussche [19] and Ogawa and Murata [20, 21]. B-B streamline curvature techniques were published by Katsanis [22] and Wilkinson [23, 24].

Most frequently used in the B-B flow problem are finite difference solutions. Stanitz was a pioneer in this approach [25, 26, 27], followed by Katsanis and McNally [28, 29, 30] and Smith and Frost [31].

Recently, Deshpande improved the original computation scheme of Katsanis and was able to reduce computer time considerably [32]. As on the H-S surface the B-B partial differential equation can also be solved with the finite element method. Two finite element methods were published so far, one by Adler and Krimerman [33] and the second by Price [34].

A number of quasi three-dimensional inviscid com-

Contributed by the Fluids Engineering Division for publication in the JOURNAL OF FLUIDS ENGINEERING. Manuscript received by the Fluids Engineering Division, April 30, 1979.

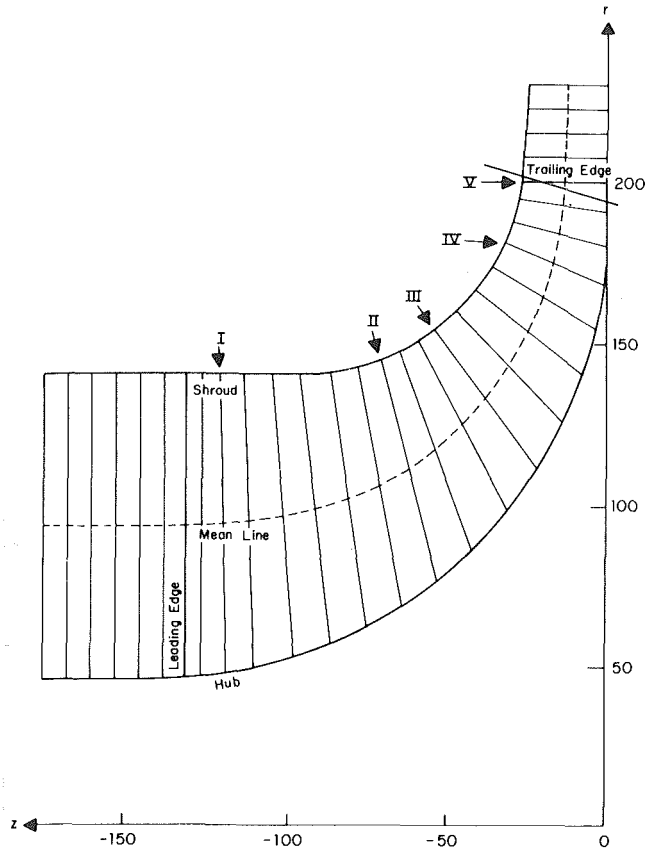

Fig. 1 The quasi orthogonals in the meridional cross section of Eckardt's impeller (roman numerals indicate surfaces of reference)

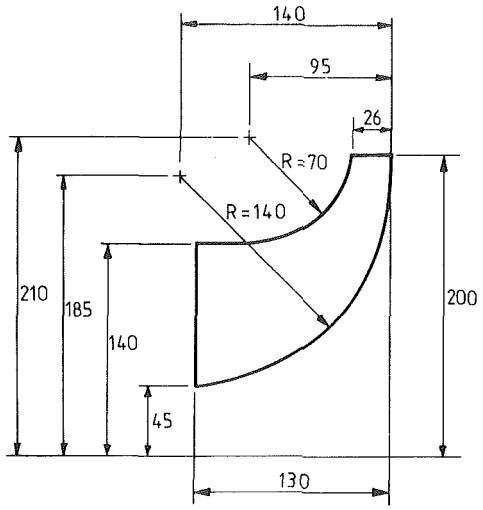

Fig. 2 Meridional geometry of Eckardt's impeller

Table 1 Polar angle of radial blade elements as function of axial distance measured from the hub toward the impeller inlet

Axial distance from the hub	Polar angle of radial blade elements
mm	degrees
0	0
10	.2
20	.9
30	2.1
40	3.8
50	5.9
60	8.6
70	11.8
80	15.5
90	19.9
100	24.9
110	30.7
120	37.3
130	44.8

putations were published in recent years. Each included a single or more restricting simplifications. These simplifications cause the techniques not to be fully three-dimensional. In 1971 Katsanis published his method [35], a combination of streamline solutions, restricted by linear variation of curvature normal to streamlines as well as constant radius and flow angle along B-B orthogonals. Senoo and Nakase [36], Bosman and El-Shaarawi [37], and Novak and Hearsey [38] all developed quasi three-dimensional methods restricted by B-B stream surfaces that were surfaces of revolution. Real B-B surfaces deviate considerably from axi-symmetric surfaces. Hirsch and Warzee [39] published a finite element method in which the interaction between the H-S and the B-B solutions was stronger than in the previous methods because in this method the stream sheet thickness and the stream angle were transferred from the H-S solution to the B-B solution. But, nevertheless the B-B stream surfaces were still always axi-symmetric and the H-S solution, although corrected by computed fluctuation terms resulting from the B-B solution, was still carried out on a single surface.

These shortcomings were not present in Krimerman's and Adler's method [40]. Their finite element method did not include all the classical simplifying restrictions as B-B surfaces of revolution and single representative H-S stream surface. In their method the interaction between the H-S and the B-B stream surface was as strong as it could be using Wu's theory [7] and no geometrical restrictions were imposed on the shape of any stream surface. There was also no restriction on the number of H-S and B-B surfaces used for the solution. The computation of the flow on a number of H-S flow surfaces is especially important for proper representation of the circumferential variation of the flow field. Krimerman's and Adler's results were restricted only by the inviscid nature of the fluid and by the fact that passage corners were assumed to be streamlines.

Being an advanced three-dimensional inviscid computation technique with minimum simplifying assumptions, Krimerman's and Adler's method [40] was chosen in this study to serve as the instrument to produce the inviscid results which are compared to measurements. This comparison can

Nomenclature

b = impeller passage width in axial direction
C_m = meridional velocity component
PS = pressure side of passage
SS = suction side of passage
t = impeller passage width in circumferential direction
u_2 = impeller tip velocity
y = coordinate in circumferential direction defined in Fig. 8
z = coordinate in axial direction defined in Fig. 8
$\Delta\beta$ = deviation angle (blade angle relative to circumferential direction minus flow angle)
μ = normalized circumferential coordinate defined inFig. 8
ν = normalized axial coordinate defined in Fig. 8

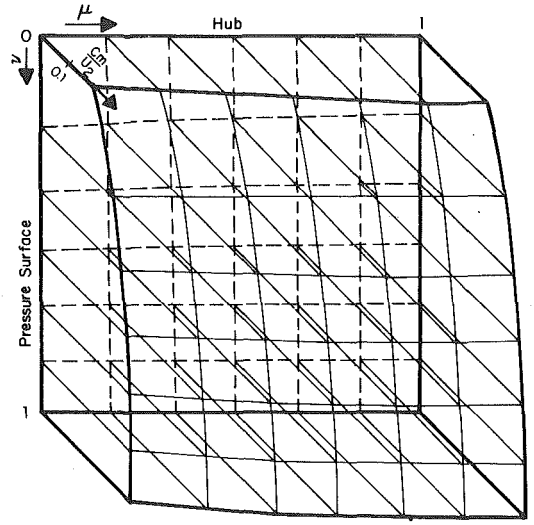

Fig. 3 Calculated normalized meridional velocity distribution on reference plane I (the broken lines on the base are intersection lines between the plane of reference and the H-S and B-B stream surfaces)

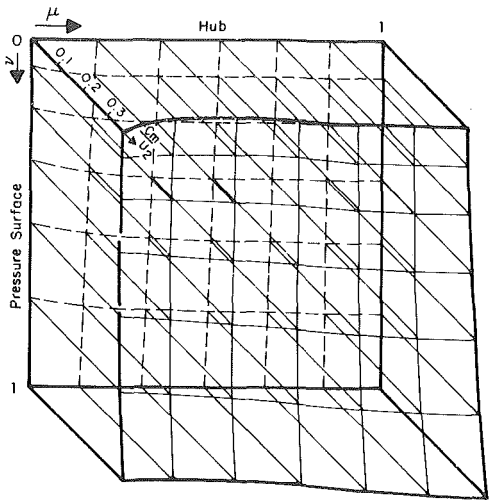

Fig. 5 Calculated normalized meridional velocity distribution on reference plane V (the broken lines on the base are intersection lines between the plane of reference and the H-S and B-B stream surfaces)

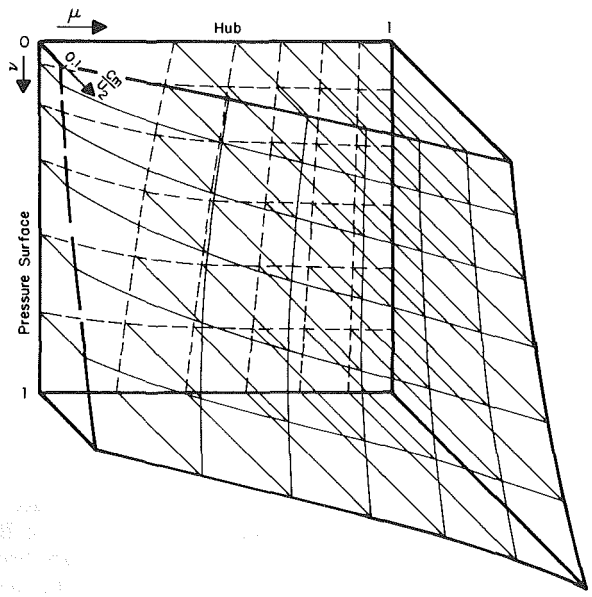

Fig. 4 Calculated normalized meridional velocity distribution on reference plane IV (the broken lines on the base are intersection lines between the plane of reference and the H-S and B-B stream surfaces)

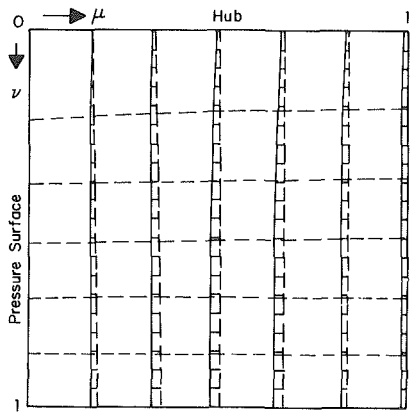

Fig. 6 Calculated deviation angles $\Delta\beta$ on reference surface I drawn on the intersection lines with H-S surfaces (in this figure the values of $\Delta\beta$ are negative)

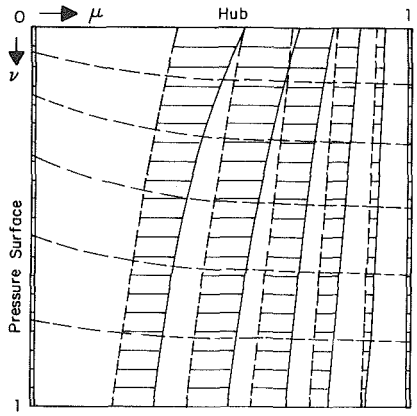

Fig. 7 Calculated deviation angles $\Delta\beta$ on reference surface IV drawn on the intersection lines with H-S surfaces (in this figure the values of $\Delta\beta$ are positive)

throw some light on the ability of inviscid subsonic methods to represent the real impeller flow.

Comparison Between Measurement and Calculation

One of the most extensive experimental studies in centrifugal compressors impellers is Eckardt's work [41]. Eckardt published his work on the optical measurement of flow in a high speed open radial exit impeller in 1976. The measurements were carried out close to the design point of the impeller. The tip velocity was about 300 m/s. Eckardt used Schodl's L2F technique [42] and was able to obtain the internal impeller flow field details. His results show the development of a well established jet-wake structure from an almost uniform inlet flow field into a highly distorted exit flow field. Unfortunately the geometry of Eckardt's impeller was not published by him, so that his results could not be used for analysis by other investigators. Luckily the missing information was furnished by J. Moore [43], who reconstructed Eckardt's flow passage using available data. Analyzing Eckardt's measured flow field one discovers well pronounced, and certainly not negligible viscous effects. These effects are dominating the flow field even at the design point at which separation should not occur and viscous influence is anticipated to be smaller than at off design points of operation. Being dominant as they are the question arises: are not viscous effects too strong to be neglected; do they render all inviscid calculation methods to be invalid?

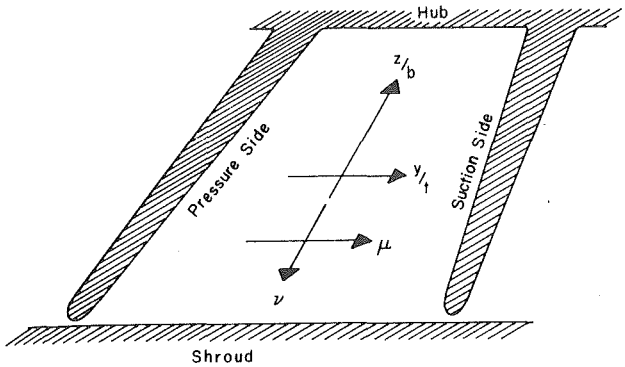

Fig. 8 The coordinate systems of Eckardt and of the present method

To answer this question Eckardt's impeller geometry as published by Moore [43] (See Fig. 2 and Table 1) was used as data, together with operation point specifications as published by Eckardt [41] to compute the inviscid flow field using the method described in [40]. The computation of the results presented here were carried out on an IBM 370/168 computer using its PL/1 compiler. A memory of 150 K was required for compilation of the program. Seven hub to shroud and seven blade to blade stream surfaces, together with 29 quasi orthogonal surfaces along the direction of the principal flow were used to generate the three dimensional grid used for discretization of the continuous flow field. With this grid a working volume of about 150 K was needed. The maximum convergence error on the relative velocity was 2 percent. Under these conditions the duration of the entire computation was about 6 minutes. The grid used in the computation is shown in Fig. 1. Results of the computation are given for the five reference planes I to V shown in Fig. 1. These reference planes are perpendicular to the direction of the main flow. Figs. 3 to 5 give the dimensionless meridional velocity component and Figs. 6 and 7 show the deviation angle distribution $\Delta\beta$. The computed and the measured flow fields are compared in Figs. 9 and 10 in coordinates as defined by Eckardt and illustrated in Fig. 8.

The computed velocity distributions of Figs. 3 to 5 show the dominating basic potential influence as anticipated from results of an inviscid theory. This potential influence is strongly affected by compressibility, by nonzero vorticity and by three-dimensional effects. All these effects are well represented in the mathematical model and its solution method as used here. Despite these distortions however, the theoretical flow is basically healthy and orderly. The flow field distortion is considerably reduced as the exit is approached (Fig. 5) due to the elliptic effect of the far downstream uniform boundary conditions.[1]

The broken lines on the basis of the diagrams in Figs. 3 to 5 are the intersections of the reference plane in question and the computed H-S and B-B stream surfaces. The deviation of these broken lines from straight lines is the effect of the three-dimensional nature of the present calculation technique. Were the B-B surfaces axisymmetric, and H-S surfaces represented by a single mean surface, the broken lines on the basis would have been straight. The calculated deviation angle distribution $\Delta\beta$ is given on the intersection lines between the reference planes and the H-S and B-B stream surfaces (the broken lines in Figs. 6 and 7). Again the deviation of these broken lines from straight horizontal and vertical lines is the three dimensional influence on the flow as represented in the model of reference [40].

The deviation angle inside the passage is insignificant as can be seen in Fig. 6. It should be pointed out that $\Delta\beta$ is negative inside the passage, i.e., the flow angle is steeper than the blade. This negative deviation angle increases towards the exit and then reverses to become positive in agreement with well known and observed slip phenomena (Fig. 7).

The calculated meridional velocity components are compared with Eckardt's measurements in Figs. 9(*a*) to 9(*e*). In each figure three velocity profiles on the reference plane are given. One close to the shroud (small z/b value) the second in the middle of the passage and the third close to the hub. On surfaces I and II (Figs. 9(*a*) and 9(*b*)) agreement between experiment and calculations is good. On surface III, however, a considerable disagreement, due to the beginning of the suction side wake, can be observed near the shroud. In this figure the profiles given are closer to the shroud to show this disagreement. The wake on this plane is still very narrow and does not stretch as far as $z/b = 0.1$. The wake increases in size in a downstream direction as can be seen in Fig. 9(*d*) which shows the velocity profiles on surface IV. Here a trace of the wake penetrates as far as $z/b = 0.5$. Outside the wake, where inviscid effects are dominant the agreement between measurements and calculation is good as is evident from both Figs. 9(*c*) and 9(*d*). Displacement effects, caused by the wake are still not very big. On surface V at the impeller exit where the wake reaches its maximum size, disagreement between calculation and measurements are largest (Fig. 9(*e*)). Here the wake occupies approximately 25 percent of the cross section with an average velocity of about 40 percent of the almost uniform velocity in the jet. Consequently, the displacement effect of the wake is clearly visible in the healthy jet regions of the passage. Further in these healthy regions the almost uniform velocity profile imposed on the elliptic flow by its downstream boundary conditions is visible both in the calculated and the measured profiles (although a level difference because of displacement exists). This is an indication that the uniform downstream boundary conditions and their assumed location as applied in the calculations are basically correct.

The deviation angle $\Delta\beta$ is shown in Figs. 10(*a*) and 10(*b*). On surface III (Fig. 10(*a*)) the wake is still insignificant and the shroud clearance flow is still small, therefore, agreement between calculation and experiment is good. The situation is different further downstream on surface IV (Fig. 10(*b*)), considerable secondary flow components were measured close to the shroud. The secondary flow increased towards the direction of the suction side corner. In the region of the secondary flows agreement between calculations and measurements is poor. Along the shroud the predicted deviation angles disagree not only in their values but also in their direction.

This is not surprising because viscous effects and shroud clearance leakage influence are not represented at all in the inviscid computation model which yields almost symmetric $\Delta\beta$ profiles on this surface. Inside the passage towards the hub, as shroud clearance effects decrease, the agreement between prediction and reality is better. The predicted direction of the secondary flow components is correct though smaller than measured values are calculated. This indicates that at least partially there is an inviscid contribution to secondary flows (an observation that is not new) but that even advanced inviscid theories can not represent the entire phenomenon. Unfortunately, no comparison could be carried out at the impeller exit, the "slip surface," because Eckardt did not publish data on the deviation angle distribution on this surface.

Conclusions

It is dangerous to draw general conclusions on the relevance

[1] For details of boundary conditions see references [13, 30, and 40].

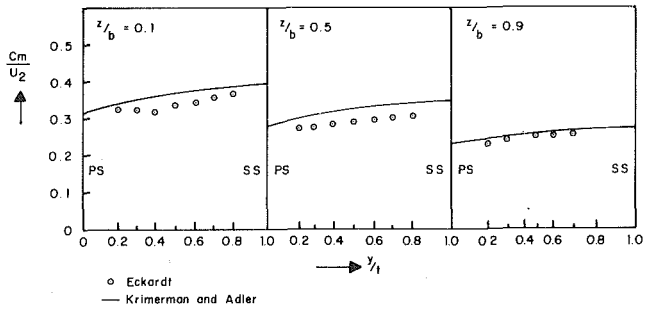

Fig. 9(a)

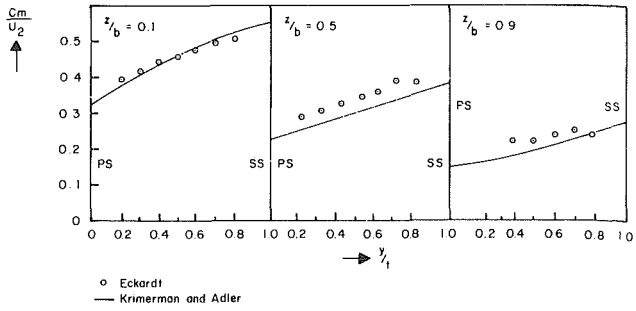

Fig. 9(b)

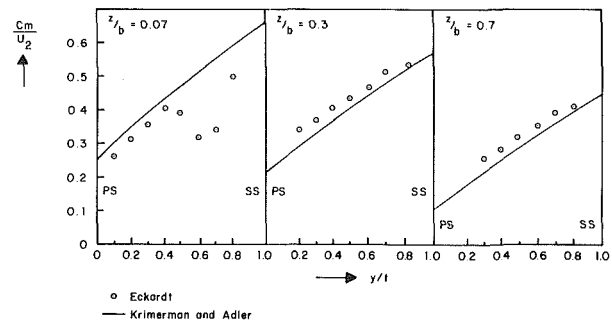

Fig. 9(c)

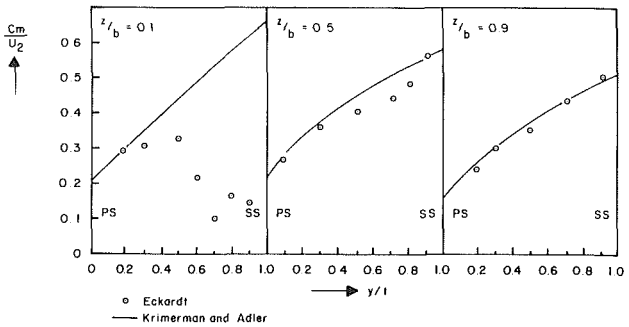

Fig. 9(d)

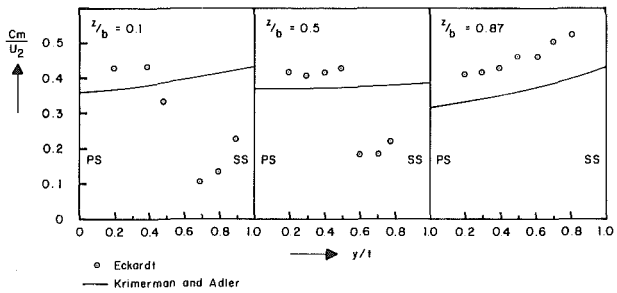

Fig. 9(e)

Fig. 9 Comparison between Eckardt's velocity measurements and the present calculation (a-surface I, b-surface II, c-surface III, d-surface IV, e-surface V)

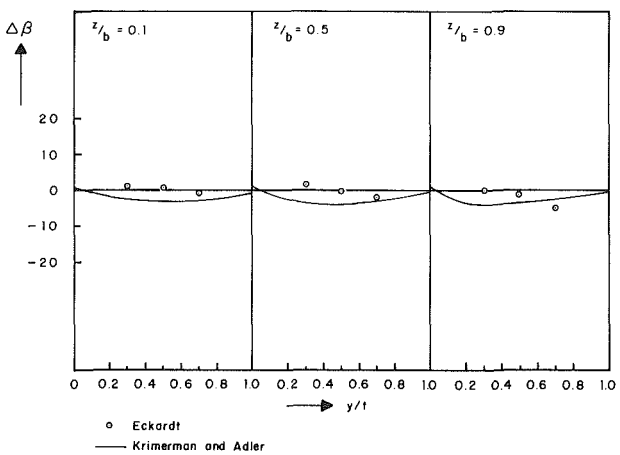

Fig. 10(a)

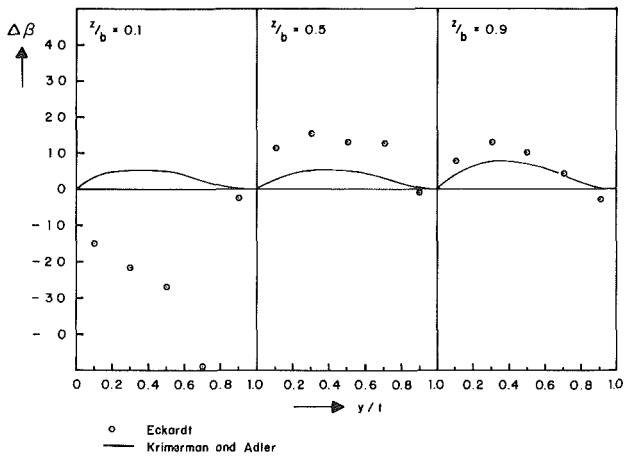

Fig. 10(b)

Fig. 10 Comparison between Eckardt's devialton angle measurements and the present calculation (a-surface III, b-surface IV)

of inviscid theories to real centrifugal impeller flow on the basis of a single comparison. It is clear that more comparative studies similar to the present one are required before a general comprehensive conclusion can be drawn. Especially, comparative studies are necessary for impellers operating at different tip speeds, for impellers with backswept blades, for closed impellers with no shroud clearance and for impellers with splitter blades (where inlet shocks into the splitter blades can cause regions of separated flow). Despite all this the present study can serve as a source of important information and as a starting point.

At the impeller inlet (surfaces I and II) the agreement between the predicted and the measured flow fields was good. In this region boundary layers are still thin, no wake is yet developed and viscous phenomena have negligible effect on the flow field. The same observation is also true for surface III except for a narrow region near the open shroud where the initial development of a wake can be detected. Further downstream on surface IV agreement between the calculation and the experiment is still good in the region outside the wake. The reason is the relatively small displacement effect of the wake which on this plane occupies about five percent of the total area with an average velocity of approximately 40 percent of the average velocity in the jet. Only on surface V where the displacement effects of the wake on the jet are considerable, are the predicted results totally inaccurate everywhere in the flow field: in the jet as well as, obviously, in the wake.

It can, therefore, be concluded that for the present case: (*a*) when regions of viscous influence are small, and the jet-wake structure is not yet developed, the prediction method applied will yield fairly accurate results, (*b*) when regions of viscous influence are present but are small enough as not to cause considerable displacement effects, the prediction method will deliver fairly accurate results outside the region of viscous influence only. This is true in regions where the jet-wake profiles begin to develop. (*c*) when regions of viscous effects are relatively large as to cause considerable displacement influence, as in locations where the jet-wake flow is fully developed, inviscid methods will not be accurate over the entire flow field. In these regions an entirely viscous flow model has to be used because of the considerable displacement effects of the wake. A boundary layer approach, combined with an inviscid core model will most probably fail to predict the flow properly in this region.

This does not mean that inviscid prediction techniques cannot be used any more with confidence. They can be safely utilized in all cases where there is strong reason to believe that considerable suction side wakes and other domains of viscous influence are not present. Examples are axial rotors or centrifugal impellers with backswept blades in which the jet-wake flow structure in the impeller is not present. Further, inviscid methods can play an important role in patching techniques (inner-outer solutions) where they can be used in the inviscid methods can play an important role in patching techniques (inner-outer solutions × whee they can be used in the inviscid region coupled with a viscous solution in the rest of the passage where viscous influence is dominant.

References

1 Katsanis, T., "Use of Arbitrary Quasi-Orthogonals for Calculating Flow Distribution in the Meridional Plane of a Turbomachine," NASA TN D-2546, 1964.

2 Novak, A., "Stream Line Curvature Computing Procedures for Fluid Flow Problems," Trans. ASME, 1967.

3 Novak, R. A., "The Mean Stream-Sheet Momentum Continuity Solution Techniques for Turbomachinery," Iowa State University, July 15-25, 1975.

4 Davis, W. R., "A Comparison of Different Forms of the Quasi-Three-Dimensional Radial Equilibrium Equation of Turbomachines," Carleton University Report No. ME/A 68-1, 1968.

5 Smith, L. H., "The Radial Equilibrium Equation of Turbomachinery," ASME *Journal of Engineering for Power,* Vol. 88, 1966, pp. 1-12.

6 Adler, D., and Ilberg, M., "A Simplified Method for Calculation of the Flow Field at the Entrance of a Radial or a Mixed Flow Impeller," ASME Paper No. 70-FE-36, 1970.

7 Wu, C. H., "A General Theory of Three-Dimensional Flow in Subsonic and Supersonic Turbomachines of Axial- Radial- and Mixed Flow Types," *NACA* TN 2604, 1952.

8 Wu, C. H., and Curtis, A., et al., "Analysis of Flow in a Subsonic Mixed Flow Impeller," *NACA* TN-2749, 1952.

9 Marsh, H., "A Digital Computer Program for the Through-Flow Fluid Mechanics in an Arbitrary Turbomachine Using a Matrix Method," R&M No. 3509, 1968.

10 Davis, W. R., "Axial Flow Compressor Analysis Using a Matrix Method," Carleton University, Report No. MW/A 73-1, 1973.

11 Katsanis, T., and McNally, W. D., "Fortran Program for Calculating Velocity and Streamlines on the Hub-Shroud Mid Channel Flow Surface of an Axial- or Mixed Flow Turbomachine," *NASA* TN D-7343, 1973.

12 Katsanis, T., and McNally, W. D., "Revised Fortran Program Calculating Velocity and Streamlines on the Hub-Shroud Mid Channel Stream Surface of an Axial-, Radial-, or Mixed Flow Turbomachine or Annular Duct," *NASA* TN D-8430/1, 1977.

13 Adler, D., and Krimerman, Y., "The Numerical Calculation of the Meridional Flow Field in Turbomachines Using the Finite Elements Method," *Israel Journal of Technology,* Vol. 12, 1974, pp. 268-274.

14 Oates, G. C., Knight, C. J., and Carey, G. F., "A Variational Formulation of the Compressible Through Flow Problem," ASME Paper No. 75-GT-32, 1975.

15 Hirsch, C., and Warzee, G., "A Finite Element Method for Through Flow Calculation in Turbomachines," ASME JOURNAL OF FLUIDS ENGINEERING, Vol. 98, 1976, p. 403.

16 Martensen, G. E., Juris Verlag, Prom. No. 3042, 1964.

17 Wilkingon, D. H., Aeronautical Research Council, R&M 3545, 1968.

18 Rauchman, B. S., "Blade Cascade on Axisymmetric Flow Sheet of Variable Thickness of Subsonic Flow," Energomachinostroenie N11, 1972, (in Russian).

19 Von Der Braembussche, "Transonic Flow in Turbomachinery" Von Karmon Institute Lecture Series, Lecture 59, 1973.

20 Ogawa, T., and Murata, S., "On the Flow in the Centrifugal Impeller with Arbitrary Airfoil Blades," *Bulletin of the JSME,* Vol. 17, 1974, p. 713.

21 Ogawa, T., and Murata, S., "On the Flow in the Centrifugal Impeller with Arbitrary Airfoil Blades," *Bulletin of the JSME,* Vol. 17, 1974, p. 723.

22 Katsanis, T., "Use of Arbitrary Quasi-Orthogonals for Calculating Flow Distribution on a Blade-to-Blade Surface in a Turbomachine," *NASA* TN D-2809, 1965.

23 Wilkinson, D. H., "Calculation of Blade-to-Blade Flow in a Turbomachine by Streamline Curvature," Aeronautical Research Council, R&M No. 3704, 1972.

24 Wilkinson, D. H., "Streamline Curvature Methods for Calculating the Flow in Turbomachines," English Electric Co., Report No. W/M (3F), 1969.

25 Stanitz, J. D., "Two Dimensional Compressible Flow In Conical Mixed Flow Compressors," NACN TN 1744, 1948.

26 Stanitz, J. D., "Two Dimensional Compressible Flow in Turbomachines with Conical Flow Surfaces," NACA TR 935, 1949.

27 Stanitz, J. D., and Ellis, G. O., "Two Dimensional Compressible Flow in Centrifugal Compressors with Straight Blades," *NACA* TR954, 1950.

28 Katsanis, T., "Computer Program for Calculating Velocities and Streamlines on a Blade-to-Blade Stream Surface of a Turbomachine," *NASA* TN-4525, 1968.

29 Katsanis, T., and McNally, W. D., "Fortran Program for Calculating Velocities in a Magnified Region on a Blade-to-Blade Stream Surface of a Turbomachine," *NASA* TN D-5091, 1969.

30 Katsanis, T., and McNally, W. D., "Fortran Program for Calculating Velocities and Streamlines on a Blade-to-Blade Stream Surface of a Tandem Turbomachine," *NASA* TN D-5044, 1969.

31 Smith, D. J. L., and Frost, D. H., "Calculation of the Flow Past Turbomachine Blades," *Proc. Institution of Mechanical Engineers,* Vol. 184, Part 3G (II), 1969/1970.

32 Deshpande, R. B., "A New Algorithm for the Solution of Turbomachinery Flow Problems," ASME JOURNAL OF FLUIDS ENGINEERING, Vol. 97, 1975, pp. 372-374.

33 Adler, D., and Krimerman, Y., "Calculation of the Blade-to-Blade Compressible Flow Field in Turbo Impellers Using the Finite-Element Method," *Journal of Mechanical Engineering Science,* Vol. 19, 1977, pp. 108-112.

34 Prince, T. C., "Prediction of Steady Inviscid Compressible Flow on a Blade-to-Blade Surface by Finite Element Method," AIAA paper 78-244, 1978.

35 Katsanis, T., "Fortran Program for Quasi-Three-Dimensional Calculation of Surface Velocities and Choking Flow For Turbomachine Blade Rows," *NASA* TN D-6177, 1971.

36 Senoo, Y., and Nakase, Y., "An Analysis of Flow Through a Mixed Flow Impeller," ASME *Journal of Engineering for Power,* Vol. 94, 1972, pp. 43-50.

37 Bosman, C., and El-Shaarawi, M. A. I., "Quasi-Hsec-Dimensional Numerical Solution of Flow in Turbomachines," ASME JOURNAL OF FLUIDS ENGINEERING, Vol. 99, 1977, pp. 132-140.

38 Novak, R. A., and Hearsey, R. M., "A Nearly Three-Dimensional Interblade Computing System for Turbomachinery," ASME JOURNAL OF

FLUIDS ENGINEERING, Vol. 99, 1977, pp. 154-166.

39 Hirsch, C., and Warzee, G., "An Integrated Quasi-3-D Finite Element Calculation Program for Turbomachinery Flows," ASME *Journal of Engineering for Power,* Vol. 101, 1979, pp. 141-148.

40 Krimerman, Y., and Adler, D., "The Complete Three-Dimensional Calculation of the Compressible Flow Field in Turbo Impellers," *Journal of Mechanical Engineering Science,* Vol. 20, 1978, pp. 149-158.

41 Eckardt, D., "Detailed Flow Investigation within a High Speed Centrifugal Compressor Impeller," ASME JOURNAL OF FLUID ENGINEERING, Vol. 98, 1970, p. 390.

42 Schodl, R., "A Laser Dual-Beam Method for Flow Measurements in Turbomachines," ASME paper, No. 74-GT-157, 1974.

43 Moore, J., "Eckardt's Impeller — A Ghost From Ages Past," University of Cambridge, Report CUED/A-Turbo/TR 83, 1976.

Flow in the Initial Region of Axisymmetric Turbulent Jets

S. M. N. Islam
Assistant Professor,
Department of Mechanical Engineering,
University of Engineering and Tech.,
Dacca, Bangladesh
Now on deputation to
University of Windsor

H. J. Tucker
Associate Professor,
Department of Mechanical Engineering,
University of Windsor,
Windsor, Ontario N9B 3P4, Canada

In the initial region of axisymmetric turbulent jets a core of uniform velocity is assumed to exist, bounded by an annular free shear layer. An empirical model for axial mean velocity is found from experimental measurements using a length scale which forces self-preservation in the central part of the free shear layer. This model is applied to the integral form of the momentum and energy equations, subject to the boundary layer simplifications, to obtain an approximate solution for the development of jets where the thickness of the mixing layer at the nozzle exit is assumed negligible. The differential form of momentum and continuity equations are also solved by a finite difference technique of DuFort-Frankel type using a typical boundary layer type of velocity profile at the exit of the nozzle. The results of this method are compared with those of the empirical velocity method, and the present and existing experimental results. Prandtl's mixing length is shown to be a slightly nonlinear function of the axial distance and is used to define the eddy diffusivity for this region.

Introduction

When an incompressible turbulent jet discharges into still air, the shear layer grows continuously with the entrainment of ambient air. For convenience it is usual to divide the turbulent jet into three Principal regions: initial region, transition region, and developed region. The initial region applies to jets with an initial core of uniform velocity or potential core and extends until the core disappears. This region starts from the exit plane of the nozzle and shows three distinguishable layers – 1) outer layer, 2) mixing layer and 3) potential core as shown in Fig. 1. The axial mean velocity changes in the mixing layer from efflux velocity at the potential core side to near zero velocity at the outer layer side. This variation of mean velocity is due to the transfer of momentum from the potential core to the outer layer. The transition region starts after the initial region. Further downstream there exists a developed region where the eddy structure becomes such that the flow quantities, i.e., mean velocity, turbulent intensity etc., become self-preserving.

Much work has been done both theoretically and experimentally in the developed region by Heskestad [1], Wygnanski, et al. [2], Rotta [3], Schlichting [4] and others. Much less work has been done in the initial region except lately in relation to noise by Bradshaw, et al. [5], Davies, et al. [6] and Ko and Davies [7]. Also Hatta and Nozaki [8] have developed some theoretical models and Von-Frank [9] has made extensive measurements of mean velocity in the initial region.

The aim of the present research was to determine experimentally both mean velocity and turbulent quantities in the initial region of a turbulent jet of uniform core velocity and thin mixing layer at nozzle exit, and from these measurements develop satisfactory theoretical models. This paper establishes the mean velocity field and jet boundaries both by measurement and by solving the differential momentum and continuity equations of flow. The results will be used in future work to develop a turbulence model for the initial region.

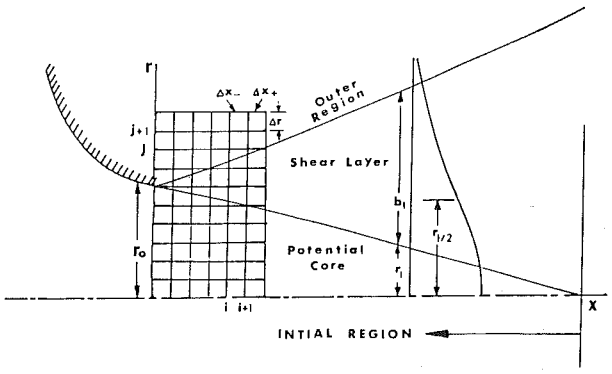

Fig. 1 Jet geometry and finite difference grid

The existing self-preserving models of mean velocity given by Townsend [10] and Schlichting [4] for the developed region of jets do not apply to the initial region. The present authors have developed an empirical and universal expression of the axial mean velocity defining the similarity variable $\eta = (r - r_{1/2})/b$, where b is a length scale proportional to the width of mixing layer and expressed by the following equation,

$$\frac{b}{r_0} = -\frac{1.0}{\left.\dfrac{\partial(u/u_0)}{\partial(r/r_0)}\right]_{r=r_{1/2}}} \tag{1}$$

where r_0 is the jet exit radius, $r_{1/2}$ is the radial distance for

Contributed by the Fluids Engineering Division for publication in the JOURNAL OF FLUIDS ENGINEERING. Manuscript received by the Fluids Engineering Division, December 4, 1978.

$u/u_0 = 0.5$, and u_0 is the efflux velocity. The coordinate $r_{1/2}$ and the length scale b were chosen as the most convenient for establishing the self-preserving qualities of the jet in the initial region and for ease of plotting experimental data.

All the calculations reported in this paper used the turbulent eddy diffusivity in terms of Prandtl's mixing length which is shown here, and also by Madni and Pletcher [11] to apply satisfactorily to the initial region. The jet has been analyzed by the following two methods:

1) Empirical velocity method.
2) Numerical method.

The first method is preferable in the sense of ease of calculation, but can only be applied to a jet with a thin mixing layer at the nozzle exit. The second method, although more time consuming, allows an arbitrary initial velocity profile and thus could be applied to a jet having a thick mixing layer at the nozzle exit. The numerical method is also the more accurate.

Methods of Analysis

1. Empirical Velocity Method. Using the present mean velocity measurements, which will be presented later in the paper, a third order polynomial for the main portion of the mixing layer, and superimposing Townsend's [10] hyperbolic tangent velocity profile at the outer layer side the following composite velocity profile was established.

$$\left.\begin{aligned} \frac{u}{u_0} &= 1.0, \qquad \eta \le -0.736 \\ \frac{u}{u_0} &= 0.5 - \eta + 0.05\,\eta^2 + 0.66\,\eta^3, \\ &\quad -0.736 \le \eta \le 0.5 \\ \frac{u}{u_0} &= A[1 - \tanh B(\eta - 0.5)] \quad \eta \ge 0.5 \end{aligned}\right\} \tag{2}$$

The constants $A = 0.095$ and $B = 4.79$ were determined by using continuity of velocity and matching the slope of the velocity profile at $\eta = 0.5$. This composite profile behaves asymptotically at the outer part of the jet with RMS deviation of $(\Delta u/u_0)_{\text{RMS}} = 0.0112$. The inner radius r_1 corresponds to $\eta = -0.736$ where $u/u_0 = 1.0$ and the outer radius r_2 is defined here as corresponding to $\eta = 0.8$ where $u/u_0 = 0.01$. So, the inner and the outer radii of the shear layer in terms of $r_{1/2}$ and b are,

$$r_1 = r_{1/2} - 0.736b \tag{3a}$$

$$r_2 = r_{1/2} + 0.8b \tag{3b}$$

The width of the shear layer b_1 can be obtained by subtracting r_1 from r_2 in the following form

$$b_1 = 1.536b \tag{4}$$

From the basic mass and momentum conservation equations of flow in a constant pressure region without contacting solid surfaces and subject to boundary layer approximations, the integral momentum and energy equations are,

$$\frac{\partial}{\partial x}\int_0^\infty r\,u^2\,\partial r = 0 \tag{5}$$

$$\frac{1}{2}\frac{\partial}{\partial x}\int_0^\infty r\,u^3\,\partial r = -\int_0^\infty \nu_T\, r\left(\frac{\partial u}{\partial r}\right)^2 \partial r \tag{6}$$

The turbulent eddy diffusivity ν_T expressed in terms of Prandtl's mixing length L and mean velocity gradient is:

$$\nu_T = L^2\left|\frac{\partial u}{\partial r}\right| \tag{7}$$

where L is assumed to be a function of x only. Introducing equation (7) in equation (6), transforming the variable r to η, and using empirical velocity equation (2) into fundamental equations (5) and (6), and integrating, the following two ordinary differential equations are obtained:

$$\frac{\partial}{\partial x}\left[\frac{r_1^2}{2} + 0.548\quad r_{1/2}\,b - 0.215\quad b^2\right] = 0 \tag{8}$$

$$\frac{1}{2}\frac{\partial}{\partial x}\left[\frac{r_1^2}{2} + 0.451\quad r_{1/2}\,b - 0.203\quad b^2\right] = \frac{L^2}{b^2}\left[-0.658\quad r_{1/2} + 0.0131\quad b\right] \tag{9}$$

These equations are subject to boundary conditions:

$$\text{at } x = 0,\ b = 0,\ r_1 = r_0.$$

Physically these boundary conditions mean that at the exit of the nozzle the potential core fills the nozzle and the length scale $b = 0$ approximates a very thin mixing layer at the nozzle exit. Integrating equation (8) with the boundary condition at $x = 0$ and using equation (3a), the following relation is obtained:

$$\frac{r_{1/2}}{r_0} = 0.188\quad b/r_0 + \sqrt{1.0 - 0.0754\quad (b/r_0)^2} \tag{10}$$

Equation (8) and equation (10) are used in equation (9) to obtain,

Nomenclature

A, B = constants in equation (2)
b = scale for linear distance
b_1 = width of the shear layer
L = Prandtl's mixing length
r = radial distance measured from jet axis
r_1 = radius of potential core
r_2 = radius of jet for $u/u_0 = 0.01$
Re = exit Reynolds number based on nozzle diameter
u = axial velocity
u' = fluctuating velocity in x-direction
v = radial velocity
v' = fluctuating velocity in r-direction
w' = fluctuating velocity in z-direction
x = axial distance measured from the exit plane of jet
ν = laminar kinematic viscosity
ν_T = turbulent kinematic viscosity
η = similarity variable = $(r - r_{1/2})/b$
ρ = density of air
Δ = difference between calculation and measurement or between two solutions
δ^* = displacement thickness

Subscripts

0 = exit condition
RMS = root mean square

$$\frac{d(b/r_0)}{d(x/r_0)} = 2(L/b)^2 \left[0.658 \quad -0.0496 \quad (b/r_0)^2 + 0.1109 \quad b/r_0\sqrt{1-0.0754 \quad (b/r_0)^2}\right] \Big/ \left[0.0965 \quad -0.0145 \quad (b/r_0)^2 + 0.0121 \quad b/r_0\sqrt{1-0.0754 \quad (b/r_0)^2}\right] \tag{11}$$

The ratio L/b was determined experimentally by measuring the shear stresses and velocity gradients, and using the following relation,

$$\overline{u'v'} = L^2 \left|\frac{\partial u}{\partial r}\right| \frac{\partial u}{\partial r} \tag{12}$$

Transforming the variable r into η, equation (12) is written as:

$$(L/b)^2 = \frac{\overline{u'v'}}{\left|\frac{du}{d\eta}\right| \frac{du}{d\eta}} \tag{13}$$

The experimental values of L/b presented later in the paper, lie within the range 0.099 and 0.109 with an average,

$$L/b = 0.106 \tag{14}$$

Using equation (14), equation (11) can be integrated numerically with the starting condition at $x = 0$, to obtain b and hence r_1, r_2 and b_1 from equations (3*a*), (3*b*) and (4) as functions of x.

2 Numerical Method. Madni and Pletcher [11] solved the differential momentum and continuity equations for the mean velocity by using finite difference technique starting with uniform exit velocity at the nozzle. The same type of finite difference technique was used here to determine the mean velocity and the goemetry of the turbulent jet in the initial region. The differential momentum and continuity equations were solved using the actual exit velocity profile which consists of a uniform core with a very thin boundary layer. Comparisons of the finite difference results with measurements and the results of the empirical velocity method are presented.

The governing equations are as follows:

The continuity equation,

$$\frac{\partial(ur)}{\partial x} + \frac{\partial(vr)}{\partial r} = 0 \tag{15}$$

Neglecting pressure gradients, the axial momentum equation is,

$$u\frac{\partial u}{\partial x} + v\frac{\partial u}{\partial r} = \frac{1}{r}\frac{\partial}{\partial r}(r\ \tau/\rho) \tag{16}$$

The shear stress τ includes both viscous and turbulent contributions,

$$\frac{\tau}{\rho} = \nu\frac{\partial u}{\partial r} - \overline{u'v'}$$

where ν is molecular diffusivity, u', v' are fluctuating components of velocity. Expressing the turbulent shear stress in terms of Prandtl's mixing length and the gradient of axial mean velocity,

$$\frac{\tau}{\rho} = \nu\frac{\partial u}{\partial r} - L^2\left|\frac{\partial u}{\partial r}\right|\frac{\partial u}{\partial r} \tag{17}$$

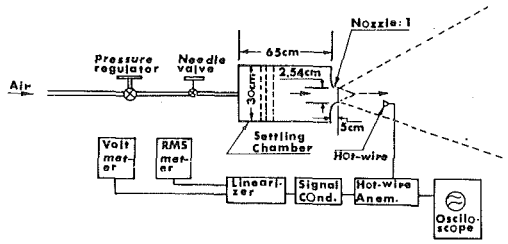

Fig. 2 Schematic diagram of experimental setup

where L is given by equation (14). The appropriate boundary conditions are:

$$\frac{\partial u}{\partial r}(x,0) = 0,\ v(x,0) = 0,\ \text{Lim}_{p\to\infty}\ u(x,r) = 0 \tag{18}$$

In addition the measured initial distribution for $u(x,r)$ is used,

$$u(x_0,r) = f(r) \tag{19}$$

The properties ν, ρ are assumed constant.

Equation (16) associated with boundary conditions (18) and (19) were solved by an explicit finite-difference technique of the Dufort-Frankel type as Madni and Pletcher [11] used for axisymmetric jets. Examples of how the derivatives are approximated for this method and the truncation errors, are given in reference [12] and are not repeated here. The finite difference grids used for the calculation are shown in Fig. 1. The computer program developed for this purpose had the capability of handling nonuniform grid spacings in both directions. This calculation was made with uniform grid spacing in the r-direction. It is necessary to use very small grid spacings in this region to attain convergence of the solution. The calculations were performed by dividing the discharge radius into 30 equal increments. Von Newman's method of stability analysis [13] showed that the finite difference equation suffered a mild stability constraint. The finite difference equation and its constraint are shown in the Appendix.

Experimental Facilities and Measurements

A one-in. diameter nozzle was attached to a 12-in. diameter settling chamber containing flow straighteners and screens, and supplied with air from a high pressure laboratory line through a pressure regulator and needle valve to produce an axisymmetric jet with uniform central core velocity. The exit Reynolds number based on nozzle diameter was 1.53×10^5. The schematic diagram of the experimental setup together with pertinent dimensions are shown in Fig. 2. A line filter, not shown, followed the pressure regulator to remove particles 1 micron or larger.

The mean axial velocity was measured by using a DISA Constant temperature hot-wire anemometer (type 55M10) with a linearizer (type 55D10), signal conditioner (type 55D31), digital voltmeter (type 55D31), and a DISA miniature probe (type 55P11) with a 5μ tungsten normal wire (0.005mm dia) of an approximate length 1mm. The hot wire configuration is shown in Fig. 2, and it was traversed up and down by a motor operated traversing mechanism with a scale of precision 0.0254mm. The shear stress was measured by using the same normal wire and a single 5μ slanting wire (0.005mm dia) with a DISA Probe (type 55P12).

The hot-wire anemometer was calibrated by using a Pitot tube with a micromanometer in the uniform core of the jet. The nonlinear output of the anemometer was linearized by passing the signal through a linearizing circuit. The low velocity calibration was performed as outlined in the DISA instruction manual for Linearizer Type 55D10. The repeatability of the calibration curve was found to be ±1

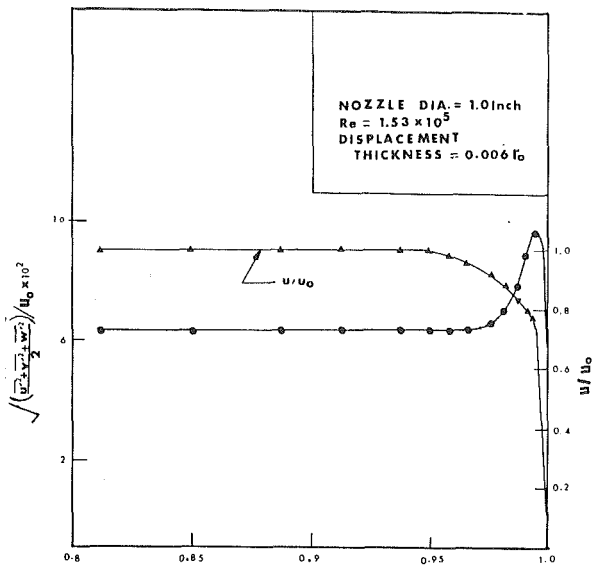

Fig. 3 Measured velocity distribution at exit plane. Uncertainty of u/u_0 is ± 1.5 percent, 20:1 odds.

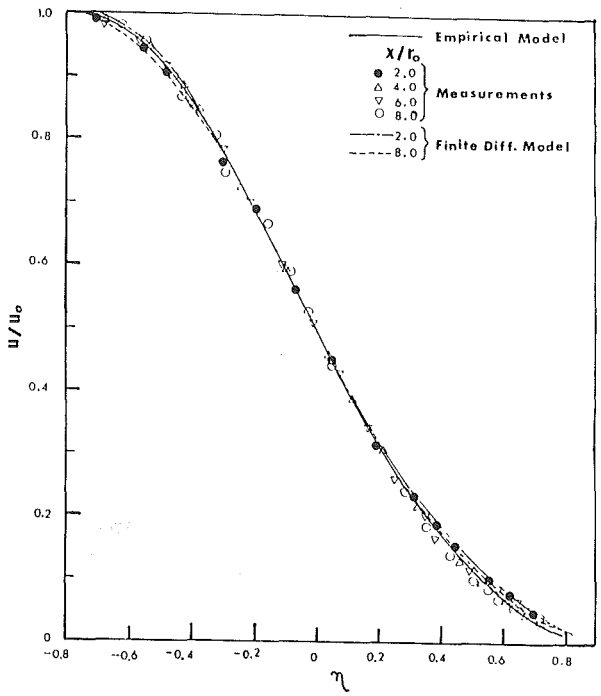

Fig. 4 Self-preserving velocity profile in the initial region. Uncertainty of u/u_0 is ± 1.5 percent, 20:1 odds, for u > 6m/s, and ± 4 percent, 20:1 odds, for $u \leq$ 6m/s.

percent, 20:1 odds, following the procedure given in reference [14]. The angle of inclination of the slanting wire was measured by positioning the probe in a slide projector and projecting the wire image on a paper screen. To minimize image distortion, the wire was located near the centre of the lens and the screen was positioned perpendicular to the projector. Twenty values of the angle of the slanting wire fell within the range 45 deg ± 36′.

The uncertainty of the measurements of mean velocity and shear stress are influenced by variations of ambient temperature, the characteristics of the linearized circuit, contaminations of the hot wires during the experiments, the accuracy of the angle of inclination of the hot wire to the mean flow direction and the accuracy of the calibrating equipment. In the calibration unit the uncertainty of mean velocity u/u_0 was estimated to be ± 0.3 percent, 20:1 odds. The mean velocities u/u_0 which were obtained by using a linearized circuit showed uncertainty of ± 1.5 percent in the main region and ± 4 percent in the outer region where velocity is less than 6 m/s. The shear stress was calculated by using the standard Kramer's relation given in reference [15]. The uncertainty of $\overline{u'v'}/u_0^2$ was estimated to be less than ± 4.5 percent, 20:1 odds, neglecting wire angle uncertainty. The angular uncertainty of the slanting wire caused an additional uncertainty in $\overline{u'v'}/u_0^2$ of ± 3 percent, 20:1 odds, bringing the total uncertainty to less than ± 8 percent for the major portion of the shear layer where the mean axial velocity is greater than 6 m/s. This value is exceeded at the outer layer side where the mean velocity is less.

The repeatability of mean velocity and shear stress were tested by taking 300 readings at each of nine locations in the mixing layer at three planes normal to the axis of the jet and at distances of x/r_0 = 4, 6 and 8 from the nozzle. Repeatability of measurements was estimated to be ± 5 percent by drawing frequency distribution curves and using 20:1 odds.

The micromanometer readings and the hot wire traversing were within the precision of 0.0254 mm. The temperature variation was noted to be ± 0.3°C.

Results and Comparisons

The present limited measurement of velocity within the boundary layer shown in Fig. 3 gives the displacement thickness δ^*/r_0 = 0.006 at the nozzle exit. From the mean velocity and turbulence measurements of Fig. 3 it was assumed that the present jet contained a very thin turbulent boundary layer at x = 0. The measured velocity distribution at the nozzle exit in Fig. 3 supplemented by 1.0/6.66 power law for velocity inside the boundary layer was used to start the finite difference solution.

Fig. 4 shows that the measurements of the axial mean velocity in the initial region have an approximate self-preserving distribution when plotted against the similarity variable $\eta = (r - r_{1/2})/b$. It also shows that the empirical velocity profile as expressed by a composite equation (2) is in reasonable agreement with measurements. The overall RMS deviation of the combined experimental data at sections x/r_0 = 2, 4, 6 and 8 from the empirical profile was calculated to be $(\Delta u/u_0)_{\text{RMS}} = 0.0112$. The axial mean velocity obtained from the finite difference solution is also approximately self-preserving in the u/u_0 versus η plane. The results of the finite difference solutions at sections x/r_0 = 2 and 8 are plotted in Fig. 4 to show a comparison with the empirical model. The RMS deviation of empirical model and finite difference model from the experimental data are shown in Table 1.

Table 1 A comparison of RMS deviation

Axial distance x/R_0	Finite-diff. solution $(\Delta u/u_0)_{\text{RMS}}$	Empirical equation $(\Delta u/u_0)_{\text{RMS}}$
2.0	0.0067	0.0154
4.0	0.0119	0.0137
6.0	0.0150	0.0101
8.0	0.0180	0.0098

The similarity variable η was chosen to force agreement with experimental measurements and to produce self-preservation in the central region of the mixing layer. It is not surprising that the slight disagreement between the measurements and the model shows up in the outer part of the mixing layer, from whence comes the major part of the RMS deviation shown in Table 1. The comparison shows that equation (2) describes the

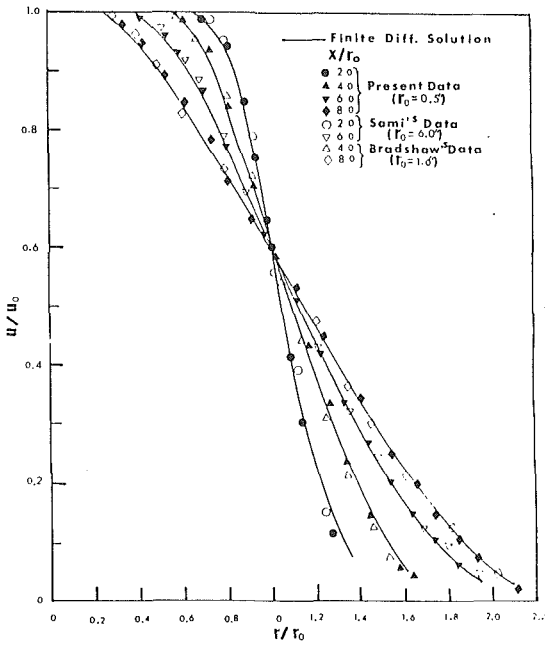

Fig. 5 Calculated and experimental mean axial velocity distribution. Uncertainty of u/u_0 is ± 1.5 percent, 20:1 odds, for $u > 6$m/s, and ± 4 percent, 20:1 odds, for $u < 6$m/s.

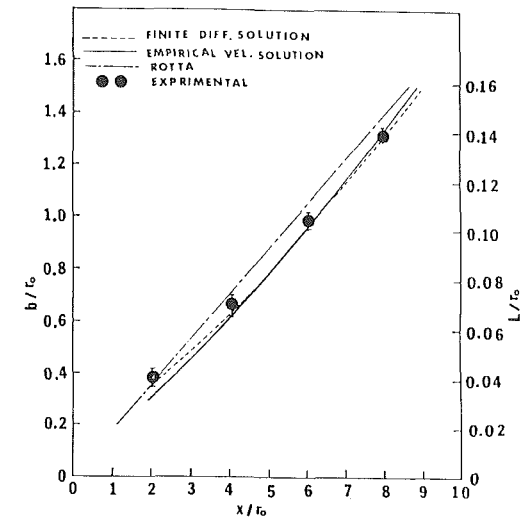

Fig. 6 Length scale b/r_0 and Prandtl's mixing length L/r_0. Uncertainty for b/r_0 is ± 2 percent, 20:1 odds.

axial mean velocity in the initial region with a deviation from the experimental values of not more than ± 1.5 percent. It is interesting to note that the conventional variable $(r\text{-}r_0)/x$ does not produce satisfactory self-preservation in the present experimental measurements or those of Bradshaw, et al. [5] and Sami, et al. [16].

The axial mean velocity calculated by the finite difference technique is plotted against the radial distance r/r_0 in Fig. 5 to show comparison with the measurements of Bradshaw, et al. [5]. Sami, et al. [16] and the present measurements. Satisfactory agreement is shown.

Simpson's integration rule is used to calculate the scale b/r_0 from the first order differential equation (11) with starting condition at $x = 0$. These results together with measurements and those obtained from the finite difference solution are shown in Fig. 6. The root mean square deviation of the results of equation (11) from those of the finite difference solution was found using values of 100 points equally spaced along the

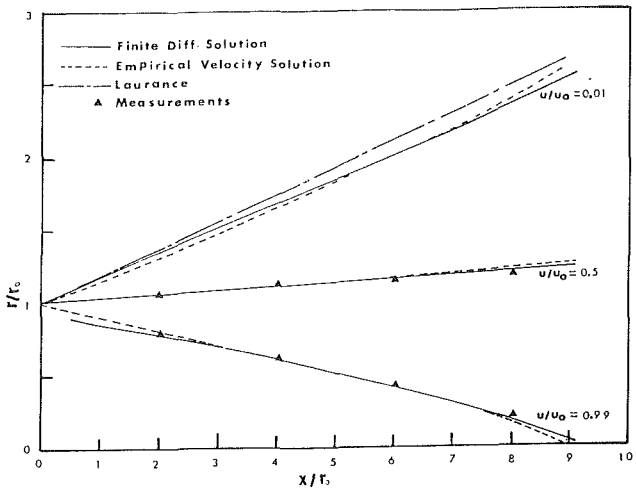

Fig. 7 Calculated and experimental iso-velocity lines. Uncertainty of u/u_0 is ± 1.5 percent, 20:1 odds.

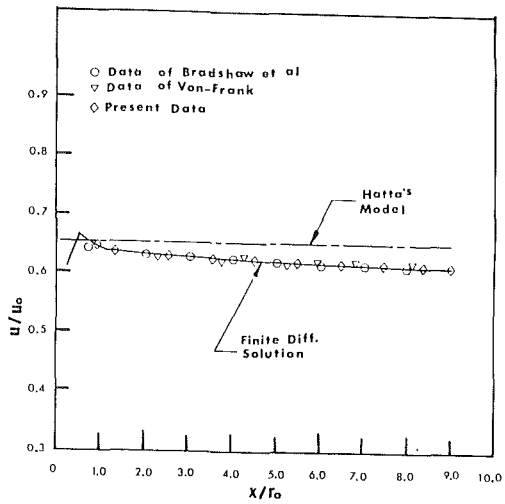

Fig. 8 Calculated velocity at $r/r_0 = 1$ and its comparison with Hatta's model and experiments. Uncertainty of u/u_0 is ± 1.5 percent, 20:1 odds.

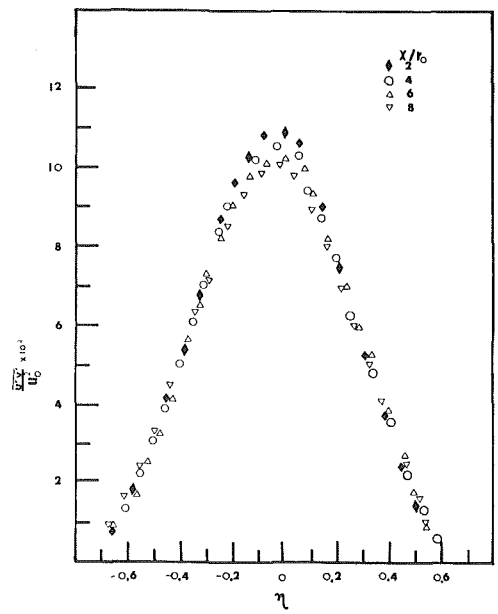

Fig. 9 Turbulent shear stress distribution. Uncertainty of $\overline{u'v'}/u_0^2$ is ± 8 percent, 20:1 odds.

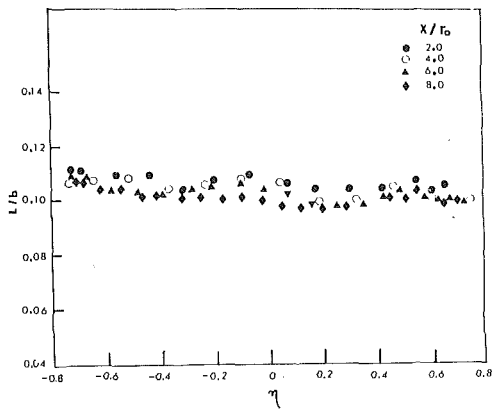

Fig. 10 Experimental values of *L/b*. Uncertainty of *L/b* is ± 5.5 percent, 20:1 odds.

axial direction in the mixing layer. The resulting values are: $(\Delta b/r_0)_{RMS} = 0.00128$ and $(\Delta r_{1/2}/r_0)_{RMS} = 0.000953$. Fig. 6 shows that the scale b is only approximately a linear function of x. The nonlinearity of b would generate the width of shear layer b_1, and the Prandtl's mixing length L, as nonlinear functions of x. The linear approximation of Prandtl's mixing length given by Rotta [3] has also been compared with the present results and measurements in Fig. 6.

The radii for $u/u_0 = 0.5$, $u/u_0 = 0.99$ and $u/u_0 = 0.01$ were calculated by using equations (10), (3*a*), and (3*b*), and plotted in Fig. 7 to show a comparison with measurements and the results of finite difference solution. The isovelocity lines $u/u_0 = 0.99$ and $u/u_0 = 0.5$ obtained from the results of finite difference solution are in good agreement with measurements and the deviation from that of the empirical velocity method is insignificant for the major part of the shear layer. The deviation that is observed in the outer and inner boundaries in Fig. 7 may be expressed in terms of RMS difference which was calculated by choosing 100 points at equally spaced intervals and found to be $(\Delta r_2/r_0)_{RMS} = 0.0193$ for outer boundary and $(\Delta r_1/r_0)_{RMS} = 0.00215$ for inner boundary. Here it is noted that the jet boundaries are not quite linear with the axial distance x. Laurence's [17] approximation of outer boundary is also drawn in Fig. 7 to show a comparison with the present outer boundary for $u/u_0 = 0.01$. The major contribution to uncertainty in the velocity measurement occurred in the outer layer. If one wishes to compare theoretical results with experimental values it is preferable not to formulate in terms of outer radius and the width of the mixing layer of the jet as Abramovich [18] did. Hatta and Nozaki [8] assumed the eddy diffusivity to be proportional to the width of the shear layer and the center-line velocity and developed a self-preserving model of axial mean velocity in terms of r_1 and r_2 which predicts constant velocity at $r/r_0 = 1.0$ for any axial distance in this region. Fig. 8 shows the shortcoming of Hatta and Nozaki's [8] model and the agreement of present calculation and measurements with the experimental measurements of Bradshaw, et al. [5] and Von-Frank [9]. The present calculations assume the eddy viscosity is equal to the radial velocity gradient and the square of the mixing length. The length of initial region calculated by the finite difference method was close to $x/r_0 = 9.0$, which agrees with the prediction of Madni and Pletcher [11]. It was calculated here to be $x/r_0 = 8.8$ by the empirical velocity method. Albertson, et al. [19] measured its value to be less than 10.0 and Davies, et al. [6] found it to be 9.0.

The experimental measurements plotted in Fig. 9 show that the shear stress is also approximately self-preserving in the initial region. Here it is repeated that the uncertainty of shear stress measurements is about ± 8 percent in the main part of mixing layer and may be higher in the outer boundary where axial mean velocity is less than 6 m/s. The present measurements of shear stresses were used to calculate L/b from equation (13) for axial distances $x/r_0 = 2, 4, 6, 8$ and their variations with radius as shown in Fig. 10 and it is observed that L/b lies in the range between 0.099 and 0.109 for the initial region of the jet. The calculations presented in this paper used $L/b = 0.106$ as an average of all observations for $x/r_0 = 2, 4, 6, 8$. Satisfactory results for mean velocity and jet boundaries already discussed were obtained using this value.

Summary and Conclusion

1) A suitable length scale and coordinate system were chosen to develop an empirical self-preserving model for axial velocity of the mixing layer in the initial region. The ratio of Prandtl's mixing length to this length scale was found constrant throughout the whole mixing layer.

2) Development of the jet was predicted by the empirical velocity method using Prandtl's mixing length as a function of x only and satisfactory agreement was found with measurements.

3) Differential momentum and continuity equations were solved by finite difference technique and the results were found to be in good agreement with the measurements and the results of the empirical velocity method.

4) Prandtl's mixing length is only approximately a linear function of x and its dependency on radius is negligible in the initial region.

Acknowledgments

The authors wish to thank Dr. K. Sridhar and Dr. R. H. Pletcher for their cooperation. The work was financially supported by the Association of Universities and Colleges of Canada and a grant by the National Research Council of Canada.

References

1 Hekestad, G., "Hot-wire Measurement in a Radial Turbulent Jet," ASME *Journal of Applied Mechanics*, Vol. 33, June 1966, pp. 417-424.

2 Wygnanski, I., and Fiedler, H., "Some Measurements in the Self-Preserving Jet," *Journal of Fluid Mechanics*, Vol. 38, Part 3, 1969, pp. 577-612.

3 Rotta, J. C., "Prediction of Turbulent Shear Flow Using the Transport Equations for Turbulent Energy and Turbulence Length Scale," Lecture presented at Von Karman Inst., Belgium, No. VKILS 76, Mar. 1975.

4 Schlichting, H., *Boundary Layer Theory*, 6th. Ed. McGraw-Hill, New York, N. Y., 1968, pp. 699-702.

5 Bradshaw, P., Ferriss, D. H., and Johnson, R. F., "Turbulence in the Noise-Producing Region of a Circular Jet," *Journal of Fluid Mechanics*, Vol. 19, 1964, pp. 591-624.

6 Davies, P. O. A. L., Fisher, M. J., and Barratt, M. J., "The Characteristics of Turbulence in the Mixing Region of a Round Jet," *Journal of Fluid Mechanics*, Vol. 15, 1963, pp. 337-367.

7 Ko, N. W. M., and Davies, P. O. A. L., "The Near Field Within the Potential Cone of Subsonic Cold Jets," *Journal of Fluid Mechanics*, Vol. 50, Part I, 1971, pp. 49-78.

8 Hatta, K., and Nozaki, T., "Two-Dimensional and Axisymmetric Jet Flows with Finite Initial Cross Sections," *Bulletin of the J. S. M. E.*, Vol. 18, No. 118, 1975, pp. 349-357.

9 Von-Frank, E., "Turbulence Characteristics in the Mixing Region of a Perturbed and Unperturbed Round Free Jet," M.S. thesis, Department of Aero Engineering, Penn. State University, 1970.

10 Townsend, A. A., *The Structure of Turbulent Shear Flow*, Cambridge University Press, 1956, pp. 175-177.

11 Madni, I. K., and Pletcher, R. H., "Prediction of Turbulent Jets in Coflowing and Quiescent Ambients," ASME JOURNAL OF FLUIDS ENGINEERING, Vol. 97, Dec. 1975, pp. 558-567.

12 Pletcher, R. H., "On a Finite-Difference Solution for the Constant Property Turbulent Boundary Layer," *AIAA Journal*, Vol. 7, No. 2, 1969, pp. 305-311.

13 O'Brien, G. G., Hyman, M. A., and Kaplan, S., "A Study of a Numerical Solution of Partial Differential Equations," *Journal of Mathematical Physics*, Vol. 29, 1951, pp. 223-251.

14 Kline, S. J., and McClintock, F. A., "Describing Uncertainties in Single-Sample Experiments," *Mechanical Engineering*, Vol. 75, Jan. 1953, pp. 3-8.
15 Tucker, H. J., "The Distortion of Turbulence by Irrotational Strain," Techn. Report No. 70-7, Mechanical Engineering Research Laboratories, McGill University, Montreal, Dec. 1970, pp. 157-165.
16 Sami, S., Carmady, T., and Rouse, H., "Jet Diffusion in the Region of Flow Establishment," *Journal of Fluid Mechanics*, Vol. 27, Part 2, 1967, pp. 231-252.
17 Laurence, J. C., "Intensity, Scale and Spectra of Turbulence in Mixing Region of Free Subsonic Jet," NACA, Rep. No. 1292, Apr. 1956.
18 Abramovich, G. N., *The Theory of Turbulent Jets, Translation by Scripts Technica*, MIT Press, 1963.
19 Albertson, M. L., Dai, Y. B., Jensen, R. A., and Rouse, H., "Diffusion of Submerged Jets," *ASCE Trans.*, Vol. 115, 1950, pp. 637-697.

APPENDIX

The equations (15), (16), and (17) were transformed into nondimensional forms using the following nondimensional variables:

$$X = \frac{x\,u_0}{\nu}, \qquad R = \frac{r\,u_0}{\nu},$$

$$L^* = \frac{L\,u_0}{\nu}, \text{ and } U = \frac{u}{u_0}$$

The explicit finite difference equations for the nondimensional momentum and continuity equations are written as:

$$\frac{U_{i,j}}{\Delta X}(U_{i+1,j}-U_{i,j})+\frac{V_{i,j}}{\Delta R}(U_{i,j}-U_{i,j-1})=\frac{1}{R_j}\frac{2}{\Delta R_+ +\Delta R_-}$$

$$\left\{\frac{R_j+R_j+1}{2}\left[1+L_i^{*2}\,|\,\frac{U_{i,j+1}-U_{i,j}}{\Delta R_+}\,|\right]\right.$$

$$\frac{U_{i,j+1}-U_{i,j}}{\Delta R_+}-\left[1+L_i^{*2}\,|\,\frac{U_{i,j}-U_{i,j-1}}{\Delta R_-}\,|\right]$$

$$\left.\frac{R_j-R_{j-1}}{2}\,\frac{U_{i,j}-U_{i,j-1}}{\Delta R_-}\right\} \tag{20}$$

$$\frac{R_{j+1}}{4\,\Delta X}\left[U_{i+1,j}-U_{i,j}+U_{i+1,j+1}-U_{i,j+1}\right]+$$

$$\frac{R_{j+1}V_{i+1,j+1}-R_jV_{i+1,j}}{\Delta R}=0 \tag{21}$$

These equations start the solution with information at the previous streamwise station.

After calculating the necessary information at the second station, the following finite difference equation of Dufort-Frankel type, that require information from two previous streamwise stations, start calculation.

$$\frac{U_{i,j}}{\Delta X_+ +\Delta X_-}(U_{i+1,j}-U_{i-1,j})+\frac{V_{i,j}}{\Delta R_+ +\Delta R_-}$$

$$(U_{i,j+1}-U_{i,j-1})=\frac{1}{R_j}\frac{2}{\Delta R_+ +\Delta R_-}$$

$$\left\{\left[1+L^{*2}_i\left|\frac{U_{i,j+1}-0.5(U_{i+1,j}+U_{i-1,j})}{\Delta R_+}\right|\right.\right.$$

$$\left.\frac{R_j+R_{j+1}}{2}\,\frac{U_{i,j+1}-0.5(U_{i+1,j}+U_{i=1,j})}{\Delta R_+}\right]$$

$$-\left[1+L_i^{*2}\left|\frac{0.5(U_{i+1,j}+U_{i-1,j})-U_{i,j-1}}{\Delta R_-}\right|\right.$$

$$\left.\left.\frac{R_j+R_{j-1}}{2}\,\frac{0.5(U_{i+1,j}+U_{i-1,j})-U_{i,j-1}}{\Delta R_-}\right]\right\} \tag{22}$$

$$\frac{R_{j+1}+R_j}{4(\Delta X_+ +\Delta X_-)}(U_{i+1,j+1}+U_{i+1,j}-U_{i-1,j+1}-U_{i-1,j})$$

$$+\frac{R_{j+1}V_{i+1,j+1}-R_{j-1}V_{i+1,j-1}}{\Delta R_+ +\Delta R_-}=0 \tag{23}$$

In this scheme the axial mean velocity $U_{i+1,j}$ is calculated first by using equation (22) and then the radial velocity $V_{i+1,j+1}$ from equation (23). Von-Neuman's method [13] of stability analysis with terms of degree one in variation and uniform radial grids develops the following stability criterion.

$$(\Delta X_+ +\Delta X_-)\le U_{i,j}\Delta R\Big/\left|V_{i,j}+(L_i^*/\Delta R)^2\right.$$

$$\left.\frac{2U_{i,j}-U_{i,j-1}-U_{i,j+1}}{2}(1-\Delta R/2R_j)\right| \tag{24}$$

M. D. Kelleher
Associate Professor.
Mem. ASME

D. L. Flentie
Lieutenant Commander, USN.

R. J. McKee
Lieutenant, USN.

Mechanical Engineering Department,
Naval Postgraduate School,
Monterey, Calif. 93940

An Experimental Study of the Secondary Flow in a Curved Rectangular Channel

The Taylor-Gortler vortex pattern in a curved rectangular channel of high aspect ratio has been examined using hot wire anemometry. Using a two dimensional traversing mechanism, velocity surveys have been made at several radial locations across the channel for several values of Dean number. The velocity measurements show that the periodic secondary motion undergoes a phase shift as the hot wire probe crosses the midplane between the concave and convex walls. The measurements also indicate that the secondary flow wave number is constant over the range of Dean numbers examined. Complementary flow visualization photographs of the secondary motion have also been obtained.

Introduction

Secondary flow due to centrifugal forces induced by streamline curvature has become an important area of investigation in a broad range of disciplines from geophysics to aerodynamics. Recently it has been shown [1, 2, 3] that wall curvature can have a significant effect on the performance of film cooling over turbine blades. It has also been hypothesized that centrifugally induced secondary motion due to streamline curvature may play an important role in the cross-hatching phenomenon observed on reentering missiles [4]. It is apparent that there are many areas of fluid mechanics from the high temperature, high speed flow in rocket nozzles to the flow in heat exchangers, where the secondary motion due to streamline curvature could profoundly effect engineering design considerations.

The flow in a rectangular channel which is curved in the streamwise direction provides an excellent configuration for studying this form of secondary flow due to streamline curvature. If the span of the channel is large compared to the channel spacing in the radial direction, the secondary flow will be in the form of regularly spaced vortices whose axes are in the direction of the mean motion.

In 1916 Lord Rayleigh [5] showed that flows with curved streamlines are stable under the condition that the circulation always increases with radial distance. G. I. Taylor [6, 7] published an extensive analytical and experimental study of the flow of a viscous fluid contained in the gap between a stationary outer cylinder and a concentrically rotating inner cylinder. Gortler [8] investigated the secondary flow in the boundary layer along a concave wall. He also found that the secondary motion is in the form of streamwise vortices. A. M. O. Smith [9] has performed an extensive numerical analysis of the flow in a curved boundary layer.

Contributed by the Fluids Engineering Division and presented at the Joint ASME/CSME Applied Mechanics, Fluids Engineering, and Bioengineering Conference, Niagara Falls, N. Y., June 18-20, 1979, of THE AMERICAN SOCIETY OF MECHANICAL ENGINEERS. Manuscript received by the Fluids Engineering Division, March 12, 1979. Paper No. 79-FE-6.

The flow of a viscous fluid in a curved channel was first studied by W. R. Dean [10]. He determined that the secondary flow would appear only if the parameter $(Ud/\nu)\sqrt{d/R_i}$ were greater than a critical value of 36.

The parameter $(Ud/\nu)\sqrt{d/R_i}$ is now referred to as the Dean number, where U is the mean velocity in the channel, ν is the kinematic viscosity, d is the spacing between the inner and outer walls of the channel and R_i is the radius of curvature of the inner wall. Reid [11] has made more accurate calculations which confirm the results obtained by Dean.

As pointed out by Yih and Sangster [12] the flow in a curved channel behaves like a stratified flow. The centrifugal force coupled with the velocity gradient near the wall causes a stratification not in density but in specific weight. In the region near the concave wall this stratification is unstable. It is the instability of this stratification which leads to the formation of the familiar Taylor-Gortler vortex pattern.

It is the purpose of this paper to present the results of a hot wire anemometer study of the structure of the secondary flow in a curved channel of large aspect ratio. The study is similar to that of Tani [13] for the boundary layer on a concave wall.

Description of Experiment

Experimental Apparatus. The apparatus for the present study is shown schematically in Fig. 1. It consists of a plexiglass channel with a contraction inlet followed by a straight section 1.22 m long. This is then followed by the curved test section. The air flow is maintained by suction from a centrifugal blower. A rotometer is installed between the outlet of the test section and the blower. The flow cross-section is 6.35 mm by 254.0 mm for an aspect ratio of 40. The straight section immediately down stream of the inlet nozzle is of sufficient length for the flow to be fully developed before entering the curved section. With the high aspect ratio of the flow cross-section the flow is essentially two dimensional Poiseuille flow before entering the curved section.

The curved section of the channel turns through 180 degrees

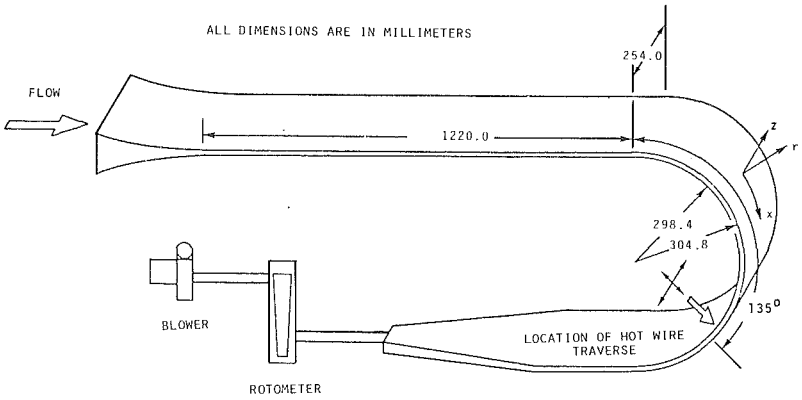

Fig. 1 Schematic of curved channel

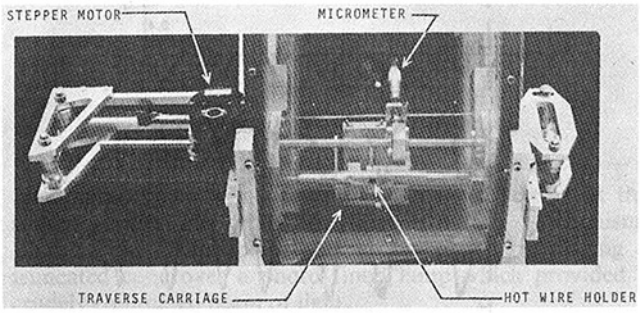

Fig. 2 Photograph of hot wire traverse mechanism

with the radius of curvature of the outer (concave) wall being 304.8 mm and the radius of the inner (convex) wall being 298.4 mm. The hot wire anemometer traverse is mounted through the convex wall at a location 135 degrees downstream of the start of the curved section.

At this location a 25 mm wide section running in the spanwise direction was removed from the convex wall. This section was replaced by a movable belt of flexible vinyl plastic. The hot wire probe was mounted through a small hole in this movable wall section. The hot wire probe was supported by a cylindrical brass plug which was cemented at one end to the flexible wall while the other end was mounted in a two dimensional traversing mechanism.

The brass plug supporting the hot wire probe allows the probe to slide freely in the radial direction. The ends of the flexible movable wall section are supported by a system of tension adjusting rollers and then attached to the traverse mechanism. This system permits the hot wire probe and the flexible wall section to move as a unit in the spanwise direction while the probe itself can move independently in the radial direction. Fig. 2 is a photograph of the traverse mechanism. Additional details of the construction of the experimental apparatus can be found in the theses of McKee [14] and Flentie [15].

The probe movement in the spanwise direction is controlled by a d-c Stepper motor and sweep drive unit. With this system, the speed of traverse could be controlled over a very wide range. For these experiments the spanwise traverse was run at a speed of 0.85 mm/s. The output from the sweep drive unit also served as a linear displacement transducer which indicated the spanwise position of the hot wire probe. The movement in the radial direction is controlled by a hand operated micrometer unit. The hot wire probe was a subminiature, single wire, boundary layer type probe. The wire was 0.75 mm long and 0.0038 mm diameter. All measurements were taken with the wire oriented parallel to the spanwise direction. With the wire in this orientation, the measurements represent the magnitude of the vector sum of the streamwise and radial velocity components. Although the traverse mechanism was capable of sweeping 152 mm in the spanwise direction, during the actual measurements it was found that a 50 mm traverse gave good results. Fig. 3 is a cross-section of the channel in which the actual area over which the velocity surveys were taken is indicated. With the relatively slow traverse speed of 0.85 mm/s a single traverse required approximately one minute.

The velocity surveys were made as follows: the blower for the channel was set to provide the desired flow-rate. With the traverse set at the initial spanwise position, the hot wire probe was set at the desired radial position by means of the micrometer. After the initial position of the hot wire probe had been established, the sweep drive mechanism was turned on to begin the automatic traverse of the hot wire across the channel. When the 50 mm traverse was completed, the traverse was reversed to return the probe to its original position. The radial position was then moved 0.635 mm by adjusting the micrometer setting and a new traverse was begun. The procedure was continued until the probe was at a position of 0.635 mm from the concave wall. This was the closest position for traversing the hot wire probe. The data were recorded directly on an x-y plotter. The output from the sweep drive unit representing spanwise displacement was recorded on the x axis and the linearized signal from the hot wire probe representing velocity was recorded on the y axis. Each sweep of the traverse mechanism was continuously recorded as a velocity profile across the channel. It should be noted that the data were always recorded with the traverse moving in the same direction. Data were never taken while the

Nomenclature

d = spacing between concave and convex wall
De = Dean number, $(Ud/\nu)\sqrt{d/R_i}$
Re = Reynolds number, Ud/ν
R_i = radius of curvature of the inner or convex wall
R_0 = radius of curvature of the outer or concave wall
U = mean flow velocity in the streamwise direction
r = radial coordinate measured outward from the center of curvature
x = streamwise coordinate
Y = $(R_0 - r)/(R_0 - R_i)$
y = transverse coordinate measured radially inward from the concave wall
z = spanwise coordinate
α = wave number, $2\pi(d)/\lambda$
λ = width in the spanwise direction of a single vortex
ν = kinematic viscosity

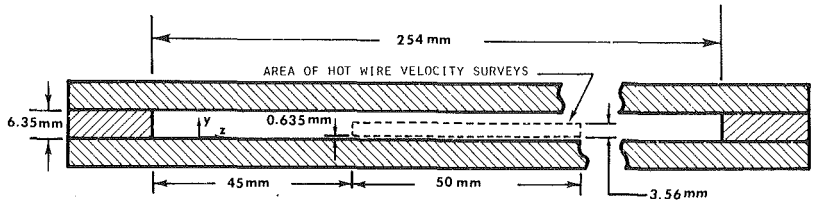

Fig. 3 Cross-section of channel

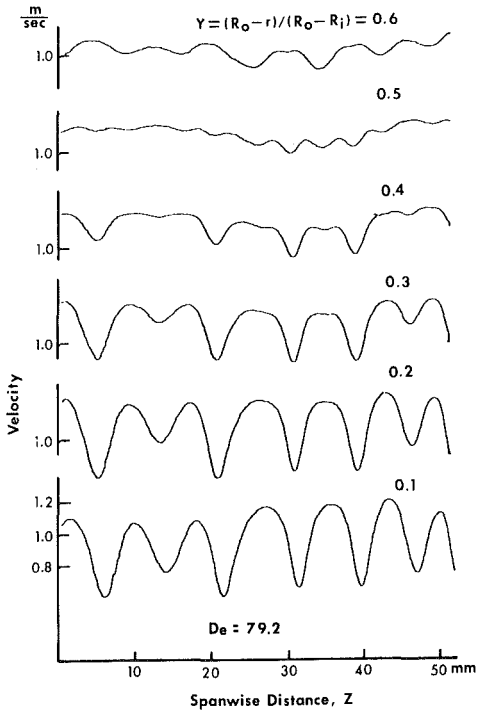

Fig. 4 Velocity profiles for Dean number = 79.2

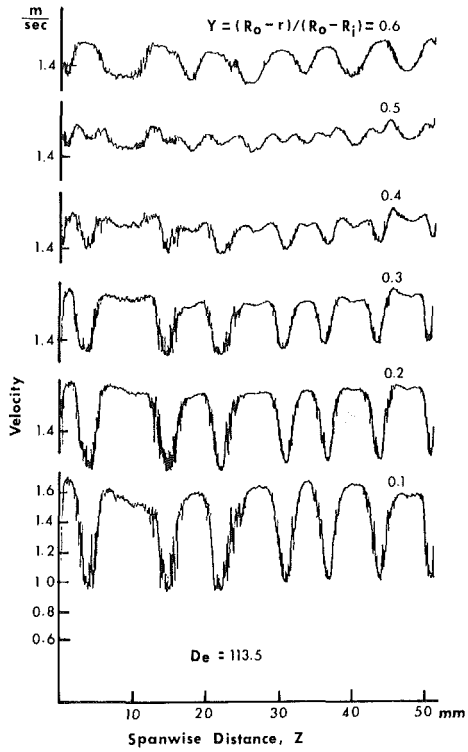

Fig. 6 Velocity profiles for Dean number = 113.5

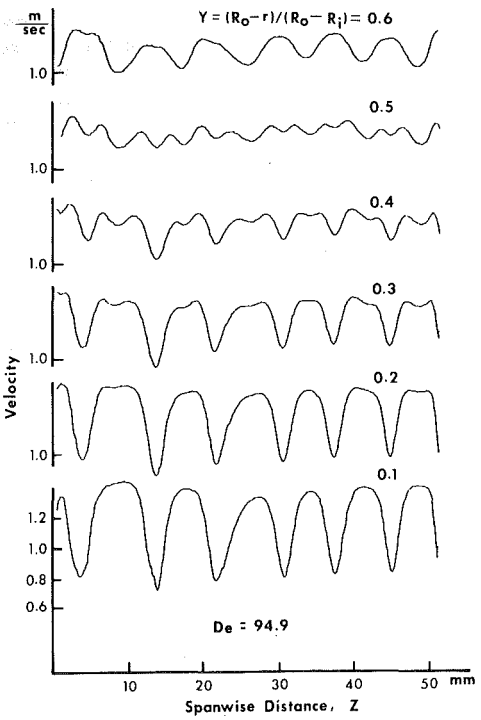

Fig. 5 Velocity profiles for Dean number = 94.9

traverse was being reserved. This was done to negate any uncertainty in traverse position due to mechanical backlash. These velocity surveys were conducted for three different flow rates corresponding to Dean numbers of 79.2, 94.9, and 113.5. In each of these cases spanwise velocity traverses were made at six different radial positions.

Flow Visualizations. Photographs of the secondary flow were taken by using a flow visualization system employing a flow indicator consisting of an aerosol mist of di (2-ethylhexyl) phthalate (usually referred to as DOP). The aerosol generation system is very simple to construct and requires only the DOP liquid and a compressed air supply for operation. Further details on the construction and operation of this system can be found in the works by Griffin and Votow [16] and Griffin, et al. [17]. The use of the aerosol mist as a flow indicator has several advantages over smoke. Combustion is not required for the aerosol as it is for smoke and since only a compressed air supply is required the aerosol flow indicator can be produced continuously for very long periods of time. This ability to run for extended periods of time proved to be extremely helpful since the process of lighting and photographing proved to be a tedious trial and error procedure.

The aerosol mist was injected into the flow stream at the contraction inlet section through several small diameter tubes. The visualization was accomplished by illuminating a narrow plane in the flow field perpendicular to the mean motion. This

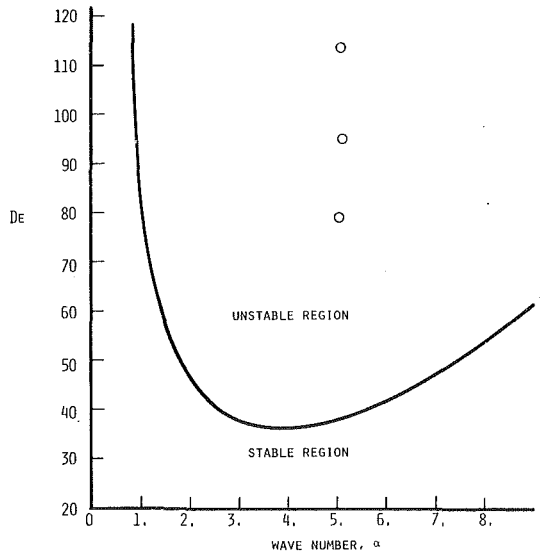

Fig. 7 Dean number versus wave number

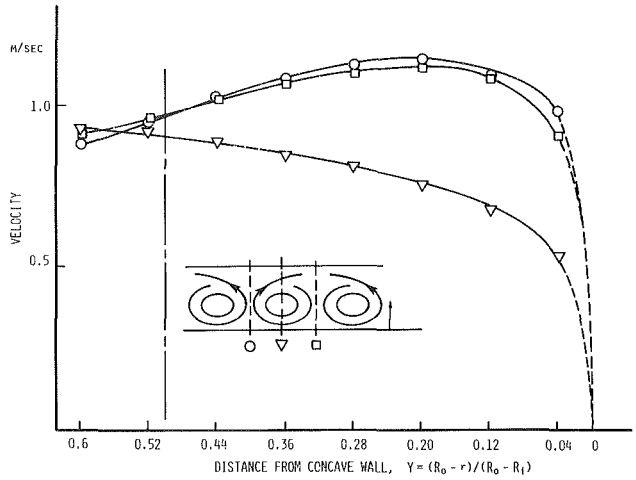

Fig. 8 Velocity profiles across the channel

illuminated plane was located in the curved section at the same position as the hot wire traverse mechanism. Illumination of the plane was accomplished by placing a truncated cone over a photo flood lamp which provided a crudely collimated beam of light.

The outside of the convex wall was made opaque by covering it with strips of black photographic tape except for a narrow slit approximately 1 mm wide. The beam of light was passed through this slit to illuminate the flow field. The camera was mounted so that its optical axis was tangent to the flow direction at the location of the illuminated plane.

Results and Discussion

The resulting velocity surveys are shown in Figs. 4 to 6. The periodic nature of the secondary flow is clearly illustrated. As would be expected the amplitude of the periodic motion is greatest in the region close to the concave wall, decreasing as the channel mid-line is approached. The profile between adjacent peaks represents the velocity distribution across a single vortex with the minimum between peaks corresponding to the region near the core of a vortex. The top three curves in each of these figures represent velocity traces at the mid-plane between the concave and convex walls and at 0.635 mm on either side of the mid-plane. It is interesting to note from the top curve, that the velocity profile on the convex side is 180 degrees out of phase with the velocity profile on the concave side of the mid-plane. This is similar to the phenomenon observed by Schubauer and Skramstad [18] in their measurement of the Tollmien-Schlichting waves in the boundary layer on a flat plate. In their measurements, the Tollmien-Schlichting waves undergo a 180 degree phase shift as the hot wire is moved across the critical layer. The Tollmien-Schlichting waves are, of course, longitudinal two dimensional waves periodic in time. The Taylor-Goertler waves in the present study are three dimensional waves periodic in the spanwise spatial coordinate. For a channel, such as the one used in the present study, with small spacing and large radius of curvature, the basic undisturbed velocity profile will be approximately the parabolic Poiseuille profile with the velocity maximum located at the mid-plane. This base flow on the side of the mid-plane near the concave wall is unstable according to Rayleigh's criterion while the flow near the convex wall is stable. This simplistic description is used to indicate that the mid-plane has more than merely goemetric significance to flow. In the sense that it is the location across which the phase reversal takes place, it is similar to the critical layer for Tollmien-Schlichting waves. As can be seen from the figures the phase shift is present at all three Dean numbers.

Average values of the wave number were calculated from the velocity profiles for the three Dean numbers in Figs. 4 to 6. These values of wave number are shown in Fig. 7 together with the neutral stability curve from Reid [11]. As would be expected for all three of these values, the wave number falls in the unstable or amplified region of the neutral stability diagram. It is interesting to note that the wave number is approximately 5.1 for all three values of Dean number. This seems to agree with Tani's [13] observations with respect to the secondary flow in a curved boundary layer, that the wave number is independent of flow velocity. It should be pointed out that the wave numbers reported here are the average values over the total 50 mm of the velocity traverse. As can be seen from the velocity profiles in Figs. 4 to 6, the actual wave length of a single cycle shows a great deal of variation around the average value.

Velocity profiles across the channel gap have been measured at three spanwise locations. The location of the first profile is determined by setting the traverse mechanism at the location of a maximum in the periodic velocity distribution; this is interpreted to be the outer edge of a single vortex. By means of the micrometer adjustment velocity measurements were taken at intervals of approximately 0.5 mm across the channel gap starting at 0.25 mm from the concave wall. When this profile had been recorded the traverse was moved to the adjacent velocity minimum; this location is interpreted to be a line passing through the vortex core. The velocity profile was t n measured along this line. The third profile was obtained by moving the traverse mechanism to the next velocity maximum. This location was interpreted to be the outer edge of the same vortex. Again the velocity profile was measured. These three velocity profiles are shown in Fig. 8. They represent velocity profiles across the channel at three different locations covering one complete cycle of the spanwise periodic motion. It is interesting to note the high degree of congruence of the velocity profiles taken at the two distinct velocity maxima. Also apparent is the marked departure from the parabolic form of the undisturbed Poiseuille profile.

Fig. 9 shows photographs of the secondary flow taken at two different Reynolds numbers. In these photographs the concave wall is at the bottom and the mean flow is into the page. Fig. 9(a) is at a Reynolds number of 529 (Dean number 77.2). As can be seen from the photographs the secondary vortices cover the full width of the channel from the concave wall to the convex wall.

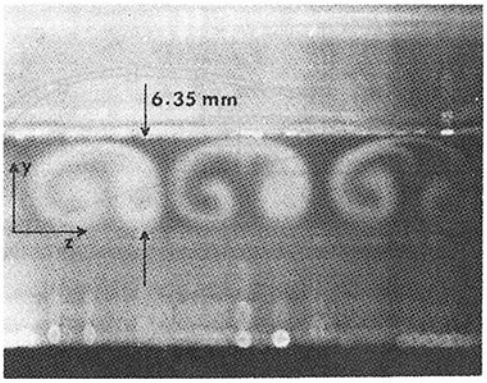

Fig. 9(a) Dean number = 69.3

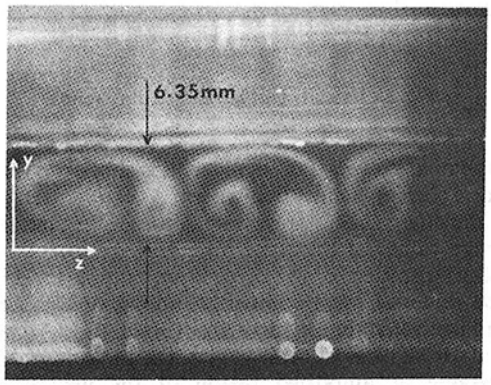

Fig. 9(b) Dean number = 77.2

Fig. 9 Photograph of vortex pattern for Dean number

Although at the higher Reynolds number the vortex pattern is somewhat distorted, the average vortex size is about the same in each case indicating again that the channel geometry and not the flow Reynolds number seems to control the wave number or vortex size. Observations of the flow patterns at much higher Reynolds number (of the order of 1700) indicated that the flow took on a streamwise periodicity in the form of longitudinal waves superimposed on the secondary flow which would travel down the vortices in direction of flow. This condition preceded the fully turbulent flow in the channel.

Experimental Uncertainty

A detailed investigation of the experimental uncertainties associated with the results presented here has not been attempted since the purpose of the results was not to deduce predictive relations but to explore certain phenomena associated with the flow with curved streamlines. Notwithstanding the nature of these experiments, estimates have been made of the uncertainties in the reported experimental quantities. Uncertainties in the measured values of the Reynolds numbers arise from fluctuations in the rotometer used to measure flow. It is estimated that the maximum identifiable uncertainty in Reynolds numbers is of the order of 3 percent. The uncertainty in the hot wire velocity measurement is estimated from the linearized calibration to be approximately 4 percent at a velocity of 0.5 m/s. At higher velocities this uncertainty is lower. The uncertainty in the radial position of the hot wire probe is due to mechanical tolerances in the traverse mechanism as well as uncertainty in reading the micrometer. It is estimated that uncertainty in radial position is of the order of 3 percent. In assessing the uncertainty in the spanwise position of the probe, the significant distance is considered to be of the order of a single vortex spacing. The dominant factor in the uncertainty in spanwise position is considered to be half the sensor wire. This gives an uncertainty of about two percent.

Acknowledgment

The authors would like to thank Dr. Thomas M. Houlihan for his valuable discussions during the course of this work. The authors also wish to acknowledge the support of the Naval Postgraduate School Foundation Research Program.

References

1 Mayle, R. E., Kopper, F. C., Blair, M. F., and Bailey, D. A., "Effect of Streamline Curvature of Film Cooling," ASME *Journal of Engineering for Power,* Vol. 99, No. 1, Jan. 1977, pp. 77-82.

2 Folayan, C. O., and Whitelaw, J. H., "The Effectiveness of Two-Dimensional Film-Cooling Over Curved Surfaces," ASME Paper No. 76-HT-31.

3 Nicolas, J., and LeMeur, A., "Curvature Effects on a Turbine Blade Cooling Film," ASME Paper No. 74-GT-156.

4 Tobak, M., "Hypothesis for the Origin of Cross-Hatching," *AIAA Journal,* Vol. 8, No. 2, Feb. 1970, pp. 330-334.

5 Lord Rayleigh, "On the Dynamics of Revolving Fluids," *Proceedings of the Royal Society of London,* Series A, Vol. 93, 1916, pp. 148-154.

6 Taylor, G. I., "Stability of Viscous Liquid Contained Between Two Rotating Cylinders," *Philosophical Transactions of the Royal Society* (London), Vol. 223, 1923, pp. 289-343.

7 Taylor, G. I., "Distribution of Velocity and Temperature Between Concentric Rotating Cylinders," *Proceedings of the Royal Society of London,* Series A, Vol. 151, 1935, pp. 494-512.

8 Goertler, H., "On the Three-Dimensional Instability of Laminar Boundary Layers on Concave Walls," NACA TM 1375, 1942.

9 Smith, A. M. O., "On the Growth of Taylor Goertler Vortices Along Highly Concave Walls," *Quarterly of Applied Mathematics,* Vol. 13, No. 3, 1955, pp. 233-262.

10 Dean, W. R., "Fluid Motion in a Curved Channel," *Proceedings of the Royal Society of London,* Series A, Vol. 121, 1928, pp. 402-420.

11 Reid, W. H., "On the Stability of Viscous Flow in a Curved Channel," *Proceedings of the Royal Society of London,* Series A, Vol. 244, 1958, pp. 186-198.

12 Yih, C. S., and Sangster, W. M., "Stability of Laminar Flow in Curved Channels," *Philosophical Magazine,* Series 8, Vol. 2, 1957, pp. 305-310.

13 Tani, I., "Production of Longitudinal Vortices in the Boundary Layer Along a Concave Wall," *Journal of Geophysical Research,* Vol. 67, No. 8, 1962, pp. 3075-3080.

14 McKee, R. J., "An Experimental Study of Taylor-Goertler Vortices in a Curved Rectangular Channel," Engineers thesis, Naval Postgraduate School, Monterey, Calif., June 1973.

15 Flentie, D. L., "An Experimental Study of Taylor-Goertler Vortices in a Curved Rectangular Channel," M. S. thesis, Naval Postgraduate School, Monterey, Calif. Mar. 1975.

16 Griffin, O. M., and Votaw, C. W., "The Use of Aerosols for the Visualization of Flow Phenomena," *International Journal of Heat and Mass Transfer,* Vol. 16, 1973, pp. 217-219.

17 Griffin, O. M., Ramberg, S. E., Votaw, C. W., and Kelleher, M. D., "The Generation of Liquid Aerosols for the Visualization of Oscillatory Flows," *Proceedings of the International Congress on Instrumentation in Aerospace Simulation Facilities,* Pasadena, Calif., Sept. 1973 (IEEE Publication 73 CHO 784-9 AES).

18 Schubauer, G. B., and Skramstad, H. K., "Laminar Boundary-Layer Oscillations and Stability of Laminar Flow," *Journal of the Aeronautical Sciences,* Vol. 14, No. 2, 1947, pp. 69-78.

Mitsukiyo Murakami
Professor.

Kouji Kikuyama
Lecturer.

Department of Mechanical Engineering,
Nagoya University,
Furocho, Chikusaku,
Nagoya, Japan

Turbulent Flow in Axially Rotating Pipes

Experimental results concerning the flow pattern and hydraulic resistance in a rotating pipe are described. A fully developed turbulent flow was introduced into a long smooth pipe rotating about its axis, and changes of the flow pattern, together with hydraulic loss within the pipe, were examined by measuring the velocity and pressure distributions across sections at various distance from the pipe entrance. Increase of pipe rotation continuously reduces the hydraulic loss and gradually changes the axial velocity profile from a turbulent type to a laminar one. Governing factors for these changes are discussed.

1 Introduction

When fluid enters a pipe rotating about its axis, tangential forces acting between the rotating pipe wall and the fluid cause the fluid to rotate with the pipe, resulting in a rather different flow pattern from that observed in the stationary pipe. Examples are found in several engineering applications; for example, in the inlet part of fluid machines, heat exchangers, and cooling systems of rotors.

Profiles of flow velocity in a rotating pipe were analyzed by Lavan and his co-workers [1], when a fully developed laminar flow was introduced to an axially rotating pipe. A reverse flow was found in the wall region near the inlet section when the swirl rate, defined by the ratio of the tangential velocity of the rotating pipe to the mean axial flow velocity, was sufficiently large.

By measuring the static pressure difference between two pressure tappings located upstream and downstream of rotating pipes, White [2], Levy [3], and Shchukin [4] studied pressure losses in rotating pipes. The magnitude of the loss varies considerably with the swirl rate. As the rotating speed is increased, the loss is increased if the approaching flow is laminar, but is decreased if the approaching flow is turbulent.

By employing a flow visualization technique, Cannon and Kays [5] found that there were two regions in the rotating sections when the swirl rate was sufficiently high – one was a rotating region near the pipe wall, and the other a nonrotating one enclosed in it. It was also found that in the rotating layer the turbulence was suppressed and the burst of turbulence on the boundary of the two regions was diminished with increase of swirl rate.

For turbulent flows in a rotating pipe, Borishenko, et al. [6] measured turbulence intensities by use of hot wire probes and showed that they were suppressed by rotation and that the suppression extended to the central portion of section as the flow proceeded downstream.

Pedley [7] theoretically analyzed the stability of laminar flow in a long pipe and found it unstable at a constant axial flow Reynolds number of 82.9. By using a visualization technique and a hot thermister anemometer, Nagib and his co-workers [8] also confirmed that when a solid body rotation was superposed on an axial velocity profile having a characteristic of pipe saturated regions in a laminar state, the rotation destabilized the flow. The transition Reynolds number decreased continuously as the swirl rate of the flow increased to $N = 4$, and when the swirl rate exceeded this value, the ideal, solid body rotation profile could not be observed.

Apparently rotation has two counter effects on the flow, stabilizing or destabilizing according to the flow conditions in the rotating pipe. The present study is concerned with determination of the governing parameters, the vector velocity fields, and loss coefficients, details of which have been reported in a thesis [9]. Turbulent flow developed fully in a stationary pipe was introduced to rotating straight pipes, and velocity and pressure distributions were measured. Hydraulic losses due to the pipe rotation were found to be closely related to the flow patterns in the rotating pipes.

2 Equipment and Method of Experiment

A schematic outline of the experimental equipment is shown in Fig. 1. Water delivered from the overflow tank was rectified by a honeycomb and led successively to the upstream stationary pipe, rotating pipe, and downstream stationary pipe. The rate of flow was measured by an orifice, as shown. The length of the upstream stationary pipe was 60D or more, in order to obtain a fully developed velocity distribution at the rotating pipe entrance, and the length of the downstream stationary pipe was 200D. Six different rotating pipe lengths were used, namely 30D, 50D, 70D, 120D, 140D, and 160D. The pipes used were drawn brass tubes having a hydraulically smooth surface.

To obtain the overall pressure loss across a rotating pipe, the upstream tapping was placed 10D upstream from the rotating section. The downstream tapping was situated 120D downstream from it (a pipe length necessary for velocity profile recovery was found experimentally to be about 120D).

The rotating pipe was separated in two parts by a narrow stationary ring of 5 mm length, as shown in the inset of Fig. 1.

Contributed by the Fluids Engineering Division for publication in the JOURNAL OF FLUIDS ENGINEERING. Manuscript received by the Fluids Engineering Division, June 7, 1977.

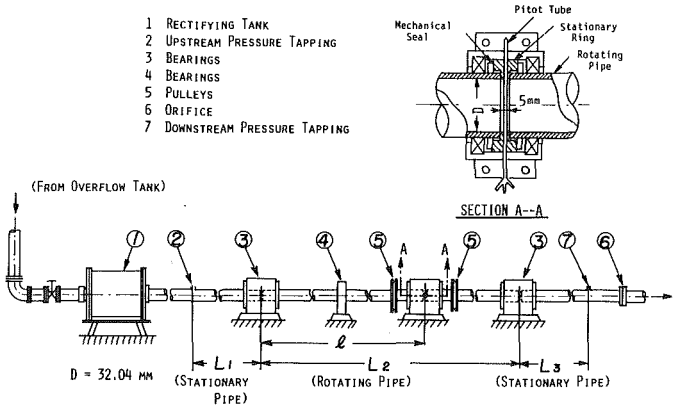

Fig. 1 Schematic outline of experimental equipment

The ends of the rotating parts were supported by ball bearings, and to prevent vibrations due to the rotation the pipe was supported by a series of bearings located at intervals of 20D or 30D. A cylindrical three-hole pitot tube of 2 mm diameter was inserted in the rotating pipe through small holes drilled on the stationary ring, and traversed along the diametral direction to obtain vector profiles across the section.

The moving pipes on both sides of the stationary ring were driven at the same speed by a variable speed motor through belts and pulley systems. Mechanical seals were used for the junctions between the pipes and the ring to prevent any leakage. The experimental range of the axial flow Reynolds number was $10^4 \leqq \mathrm{Re} \leqq 2.0 \times 10^5$, and the rotational Reynolds number was $0 \leqq \mathrm{R}_\theta \leqq 6.5 \times 10^4$.

3 Equations to Predict Experimental Results

The overall hydraulic head loss between two pressure tappings, ② and ⑦ as shown in Fig. 1, was measured at various speeds of rotation and flow rates, and is expressed as

$$H = H_1 + H_3 + H_2 = \lambda \frac{(L_1 + L_3)}{D} \frac{V_m^2}{2g} + \xi \frac{L_2}{D} \frac{V_m^2}{2g} \quad (1)$$

Thus, the coefficient of hydraulic loss of a rotating pipe, ξ, is given by

$$\xi = \left[H - \lambda \frac{(L_1 + L_3)}{D} \frac{V_m^2}{2g}\right] \Big/ \left(\frac{L_2}{D} \frac{V_m^2}{2g}\right) \quad (2)$$

The hydraulic gradient along the rotating and stationary pipes is schematically shown by a solid line in Fig. 2. It is seen that the first term in the right-hand side of equation (1) expresses the hydraulic loss in the stationary pipes upstream and downstream of the rotating pipe, $(H_1 + H_3)$, when the swirling flow component is absent. The second term sums the loss in the rotating pipe itself (H_r) and additional loss (H_a) due to the swirling flow components in the downstream stationary pipe.

If the fluid is considered to be incompressible, and the kinetic energy of eddies is neglected, the sum of the useful mechanical energy of the fluid can be defined by

$$E_t = E_k + E_p \quad (3)$$

where E_k and E_p denote fluxes of the kinetic and pressure energies of fluid

$$E_k = \int_0^R 2\pi\rho r V_z [(V_z^2 + V_\theta^2 + V_r^2)/2] dr \quad (4)$$

$$E_p = \int_0^R 2\pi V_z r (\bar{p} - \bar{p}_0) dr \quad (5)$$

in which $\bar{p}_0$ and $\bar{p}$ denote the static pressures at the inlet section of the rotating pipe and at any point within a downstream section, respectively.

A balance of the surface stresses and momentum fluxes for a control volume of radius r and length dz gives

$$\frac{\tau_{r\theta}}{\rho V_m^2/2} = 2 \frac{V_r}{V_m} \frac{V_\theta}{V_m} + \frac{2}{(r/R)^2} \int_0^{r/R} \left(\frac{r}{R}\right)^2 \frac{\partial}{\partial(Z/R)} \left[\frac{V_\theta}{V_m} \frac{V_z}{V_m}\right] d\left(\frac{r}{R}\right) \quad (6)$$

$$\frac{\tau_{rz}}{\rho V_m^2/2} = 2 \frac{V_r}{V_m} \frac{V_z}{V_m} + \frac{2}{(r/R)} \int_0^{r/R} \frac{r}{R} \frac{\partial}{\partial(Z/R)} \left[\left(\frac{V_z}{V_m}\right)^2 + \frac{\bar{p}}{\rho V_m^2}\right] d\left(\frac{r}{R}\right) \quad (7)$$

where it is assumed that flow is taken to be steady, incompressible and axisymmetric, and also that $\sigma_z \fallingdotseq -\bar{p}$ and $|\tau_{z\theta}| << \rho V_\theta V_z$. The last assumption will be justified from the fact that, in a rotating pipe, the turbulence will be suppressed much by the rotation as is mentioned already and its contribution to the shearing stresses can be considered much less than those in a stationary pipe. Since V_r and V_z reduce to zero on the pipe wall, the values of $\tau_{r\theta}$ and τ_{rz} on the wall are given by

$$\frac{(\tau_{r\theta})_0}{\rho V_m^2/2} = 2 \int_0^1 \left(\frac{r}{R}\right)^2 \frac{\partial}{\partial(Z/R)} \left[\frac{V_\theta}{V_m} \frac{V_z}{V_m}\right] d\left(\frac{r}{R}\right) \quad (8)$$

$$\frac{(\tau_{rz})_0}{\rho V_m^2/2} = 2 \int_0^1 \left(\frac{r}{R}\right) \frac{\partial}{\partial(Z/R)} \left[\left(\frac{V_z}{V_m}\right)^2 + \frac{\bar{p}}{\rho V_m^2}\right] d\left(\frac{r}{R}\right) \quad (9)$$

The rate of pipe rotation is defined by the ratio of the circumferential velocity of the pipe to the mean flow velocity as

$$N = U/V_m = \mathrm{R}_\theta/\mathrm{Re} \quad (10)$$

From equations (8) and (10), $(\tau_{r\theta})_0/(\rho V_m^2/2)$ can be expressed by

Nomenclature

D = pipe diameter (32.04 mm)
E_k = kinetic energy flux across a section (equation (4))
E_p = pressure energy flux across a section (equation (5))
E_t = useful energy flux across a section (equation (3))
H = hydraulic loss between measuring sections located upstream and downstream of rotating pipe
L_1 = axial distance of upstream wall tap measured from the rotating pipe inlet
L_2 = length of rotating pipe
L_3 = axial distance of downstream wall tap measured from the rotating pipe exit
l = axial distance of measuring section from rotating pipe inlet
N = rate of rotation ($= \mathrm{R}_\theta/\mathrm{Re} = U/V_m$), reciprocal of Rossby number
P = dimensionless expression of pressure (equation (17))

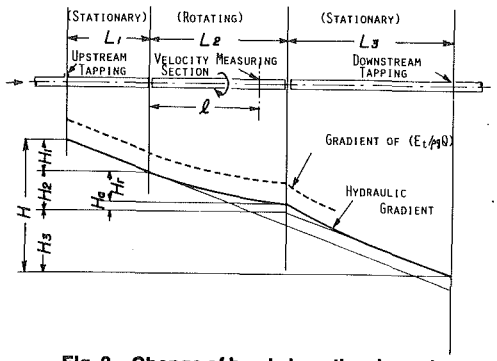

Fig. 2 Change of head along the pipe axis

$$\frac{(\tau_{r\theta})_0}{\rho V_m^2/2} = 2N\int_0^1 \left(\frac{r}{R}\right)^2 \frac{\partial}{\partial(Z/R)}\left[\frac{V_\theta}{U}\frac{V_z}{V_m}\right] d\left(\frac{r}{R}\right) \quad (11)$$

The static pressure at any point $\bar{p}$, can be calculated approximately by the following equation which neglects the radial mean velocity and turbulent fluctuations

$$\bar{p} = \bar{p}_w - \rho\int_R^r (V_\theta^2/r)\,dr. \quad (12)$$

4 Results of Experiment and Discussion

4.1 Loss Coefficient in Rotating Pipes. Data for the coefficient of hydraulic loss, ξ, for various lengths of rotating ducts are shown in Figs. 3(*a*), (*b*), and (*c*). The Reynolds number was always larger than 10^4, so the flow is turbulent when the pipes are held stationary. Therefore, for $N = 0$, the curves of ξ will coincide with those for a smooth stationary pipe, λ, approximated by the Blasius equation, $\lambda = 0.3164\,\mathrm{Re}^{-0.25}$. When rotation begins, it is seen that ξ deviates gradually from λ, decreasing with increase of rotational speed, R_θ, if $\mathrm{Re} < 4 \times 10^4$. This results from suppression of turbulent motion by the swirling flow component. For short rotating tubes, such as $L_2/D = 30$, the reduction is less than that for $L_2/D = 70$ and above, and the rate of reduction is not consistent with the increase of rotational Reynolds number when $\mathrm{Re} < 3 \times 10^4$.

When Re is reduced, the value of ξ also decreases continuously to a minimum, and then increases again. To the left of the minimum points, the curves of ξ tend to be parallel asymptotically to the laminar line, $\lambda = 64/\mathrm{Re}$; turbulence in the flow will be largely suppressed so that viscous effects become dominant. If the rotational Reynolds number, R_θ, is kept constant and the flow Reynolds number, Re, is increased, the values of ξ increase continuously, ultimately exceeding the turbulent friction coefficient of a stationary pipe. The loss caused by the rotating pipe is considered to be composed of the loss experienced in the rotating pipe and an additional loss due to the swirling flow component in the downstream stationary pipe, as shown in Fig. 2. The pipe rotation has an opposite influence of these component losses: the loss within the rotating pipe is decreased but the loss in the stationary pipe downstream of the rotating section is increased. For small rotation rates, the decrease is less than the increase, and ξ becomes larger than λ.

When the rotation rate, N, is increased from a small value, the curves of constant N lie at first nearly parallel to the turbulent λ line, then deviate gradually from it and tend to be horizontal. But for $N > 1.0$, the curves tend to be parallel to the laminar λ line.

Values of ξ relative to λ are shown against the rotation rate, N, in Figs. 4(*a*) and (*b*). For $N < 0.35$, though ξ/λ is slightly larger than 1.0, the effects of pipe rotation on ξ/λ are negligible. ξ/λ decreases with increase of N and reaches to a minimum value which depends on L_2/D. Scattering of the experimental points increases as the rotating length, L_2, decreases, as is seen in Fig. 4(*a*), but this scattering becomes less and ξ/λ becomes almost independent of the pipe length when L_2/D exceeds 100 (Fig. 4(*b*)). The relationships of ξ/λ and N, for $L_2/D \geqq 100$, may be approximated by the following equations:

$$\text{for } N < 0.35, \quad \xi/\lambda = 1.0 \quad (13)$$

$$\text{for } 0.35 \leqq N \leqq 0.8, \quad \xi/\lambda = 0.579N^{-0.52} \quad (14)$$

$$\text{for } 0.8 < N < 1.2, \quad \xi/\lambda = 0.47N^{-1.42} \quad (15)$$

In Figs. 4(*a*) and (*b*) the results obtained by Shchukin [4] by using the experimental data of White ($L_2/D = 232$) and Levy ($L_2/D = 24$) are also shown by a chain line, which exhibits nearly an upper limit of the present results.

With high speed rotation, $N > 1.2$, turbulence in the wall region of the rotating pipe will be largely suppressed, and ξ/λ stops decreasing for larger values of N. Values of the critical flow Reynolds number corresponding to this saturation of ξ/λ increase with N and with L_2/D. From Figs. 3(*b*) and (*c*), they are approximated for $L_2/D \geqq 70$ by

$$\mathrm{Rec} = 1.9\,\mathrm{R}_\theta^{0.90} + 2300, \quad (5\times10^4 > \mathrm{R}_\theta > 10^4) \quad (16)$$

which gives a fair agreement with the relationship between Rec and R_θ obtained by Shchukin [4].

4.2 Velocity Distributions. If the measured coefficient of hydraulic loss of long pipes, including rotating elements, ξ/λ, is plotted against the rotation rate, N, as shown in Fig. 4(*b*), the values of ξ/λ are seen to be governed by a single parameter, N, when $L_2/D \geqq 100$. This can be explained by examining velocity profiles in the rotating pipe. Figure 5 shows the velocity profiles in a rotating pipe of 120D downstream section, when $N = 1.0$. At this section the influence of the pipe rotation on flow is considered to be saturated and all of the velocity profiles are similar.

Velocity profiles change along the pipe. This is shown for

Nomenclature (cont.)

$\bar{p}$ = static pressure
$\bar{p}_0$ = static pressure at the center of the inlet section
$\bar{p}_w$ = pressure on the wall of rotating pipe
Q = rate of flow
R = pipe radius ($= D/2$)
Re = axial Reynolds number ($= V_m D/\nu$)
Re_c = critical value of Re
R_θ = rotational Reynolds number ($= UD/\nu$)
r, θ, z = cylindrical coordinate system
U = circumferential speed of the pipe wall
V_m = mean flow velocity
V_r, V_θ, V_z = mean velocity components in r, θ, z directions, respectively
λ = coefficient of hydraulic friction of stationary pipe
ξ = coefficient of hydraulic loss of rotating pipe (equation (2))
ρ = fluid density
$\tau_{rz}, \tau_{r\theta}$ = shearing stress components (equations (6) and (7))
$(\tau_{rz})_0, (\tau_{r\theta})_0$ = values of τ_{rz} and $\tau_{r\theta}$ on the pipe wall (equations (8) and (9))
ν = kinematic viscosity

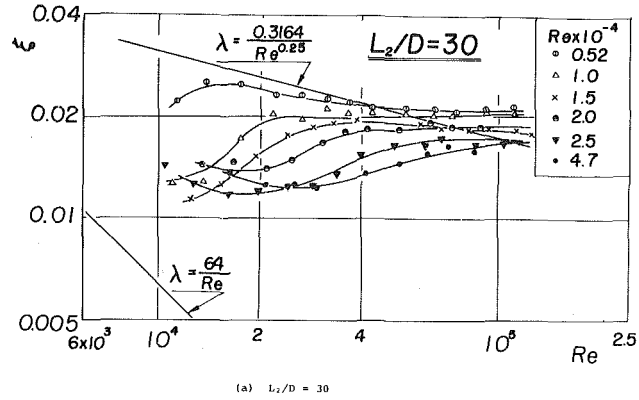

(a) $L_2/D = 30$

Fig. 3(a) Loss coefficients in rotating pipe, $L_2/D = 30$ uncertainty of (Re, ξ) coordinate (2×10^4, 0.015), uncertainty (± 500, ± 0.003), coordinate (10^5, 0.018), uncertainty (± 2500, ± 0.0022)

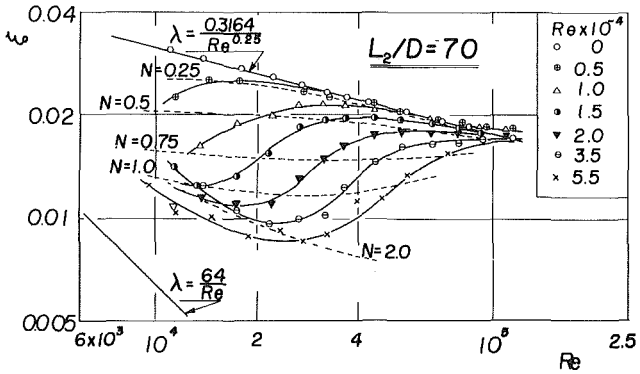

Fig. 3(b) Loss coefficients in rotating pipe, $L_2/D = 70$

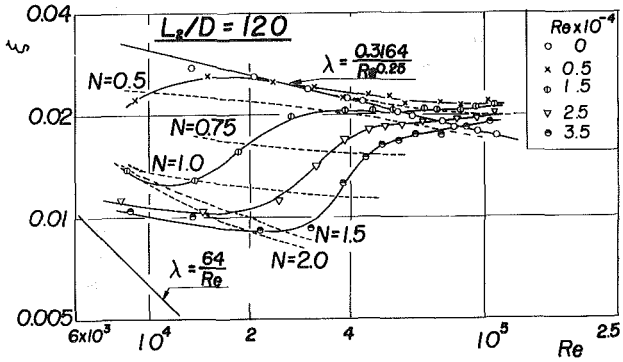

Fig. 3(c) Loss coefficients in rotating pipe, $L_2/D = 120$

various values of N by the data in Figs. 6 (a) and (b). Profiles measured at the section of $l/D = 10$ for $N = 0$ are shown by broken lines. At $l/D = 10$, the axial velocity profile remains flat and the flow in the greater part of the central zone is considered to be still in a turbulent state. As l/D increases, the axial velocity profiles deform gradually, due to a stabilizing effect of the centrifugal force of the swirling flow.

Lavan and his co-workers [1] show theoretically that a reverse flow is to be expected near the wall at entry, for large N. In the present study, a tuft method did not show such a flow, within the range of $N \leqq 5$ and $Re = 10^5$.

At 100D or more downstream, the velocity profile becomes approximately independent of the axial distance from the inlet. For reference, the laminar velocity profile in a stationary pipe is shown by a chain line in Fig. 6(b). To check the effect of the spin ratio, N was increased to 5.8, 6.8, and 8.6 for $Re = 6.1 \times 10^3$, 5.1×10^3 and 4.6×10^3, respectively. The V_θ profiles in these cases did not change ap-

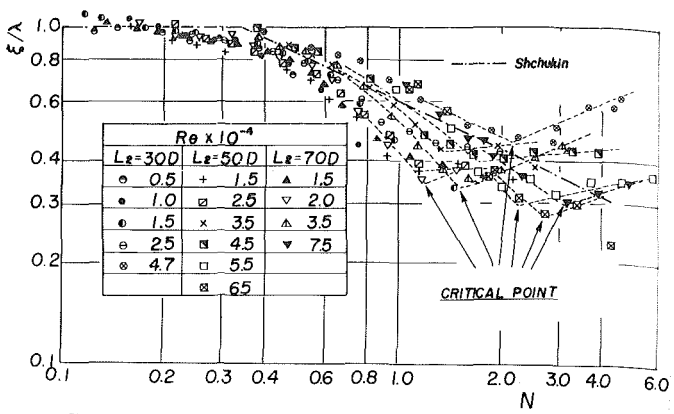

Fig. 4(a) Relation between ξ/λ and N $L_2/D = 30$, 50, and 70

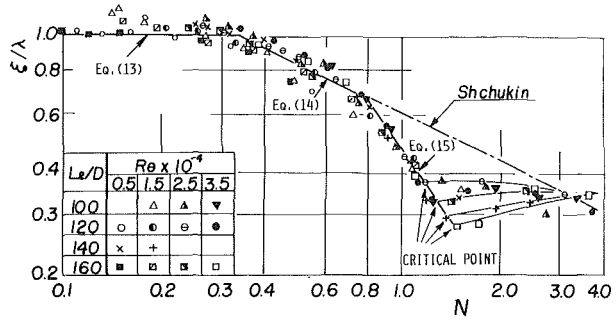

Fig. 4(b) Relation between ξ/λ and N $L_2/D = 100$, 120, 140, and 160

preciably from that shown in Fig. 6(b) for $l/D = 120$; they did not approach a forced-vortex type profile, even at the section far downstream of $l/D = 120$. The V_z profiles remain aproximately the same shape as in the laminar state, with the ratio of V_z to V_m at the pipe center equal to 1.72, 1.79, and 1.85 for $N = 5.8$, 6.8, and 8.6, respectively [9].

4.3 Pressure Distributions. A dimensionless expression of pressure change within the rotating pipe can be given by

$$P = (\bar{p} - \bar{p}_0)/(\rho V_m^2/2) \tag{17}$$

where $\bar{p}$ is a static pressure at any point in the section, and given by equation (12). Changes of pressure on the wall and at the center of the rotating pipe along the axis are shown in Fig. 7. Gradients of the pressure in a stationary pipe at the same Reynolds number are shown for turbulent and laminar conditions. Even with a low spin ratio of $N = 0.25$, the pressure curves are seen to be affected considerably by the rotation, and with increase of the rotation speed, the curve approaches asymptotically that of a laminar flow in a stationary pipe.

4.4 Shearing Stresses. From measured velocities and pressures, shearing stresses can be calculated by use of equations (6) and (7). The results are shown in Figs. 8(a) and (b). The broken line in Fig. 8(a) shows the values of τ_{rz} in the stationary state, the absolute value of which is slightly larger than in the rotating state.

A dimensionless expression of the tangential component of the wall stress, $2(\tau_{r\theta})_0/(\rho V_m^2 N)$, for various values of Re and R_θ is shown in a semilog scale in Fig. 9, showing that $2(\tau_{r\theta})_0/(\rho V_m^2 N)$ decays exponentially along the pipe axis. When N is small, the values are seen to be arranged well by a solid line, irrespective of the values of Re and R_θ. This is to be expected from the fact that $2(\tau_{r\theta})_0/\rho V_m^2$ in equation (11) can be expressed by a product of N and the axial derivative of angular momentum flux in the rotating pipe. From the results

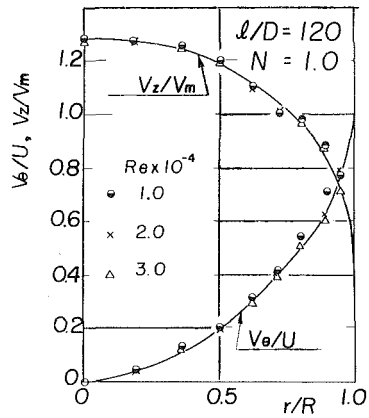

Fig. 5 Similarity of velocity profiles at a constant value of N (N = 1.0)

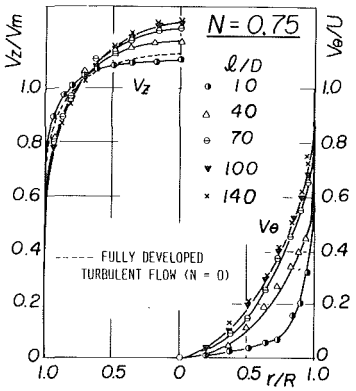

Fig. 6(*a*) Changes of velocity profiles along the pipe N = 0.75 (Re = 2 × 10^4), uncertainty of (r/R, V_z/V_m), coordinate (0, 1.1), uncertainty (±0.02, ±0.022), uncertainty of (r/R, V_θ/V_m), coordinate (0, 0), uncertainty (±0.02, ±0.05)

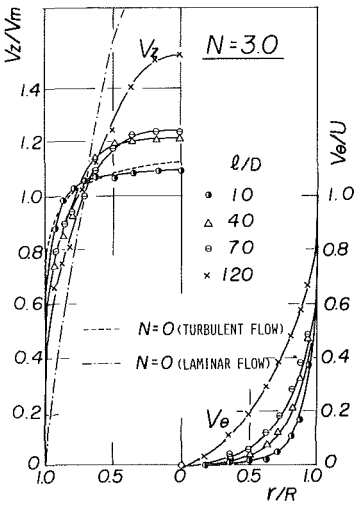

Fig. 6(*b*) Changes of velocity profiles along the pipe N = 3.0 (Re = 2 × 10^4)

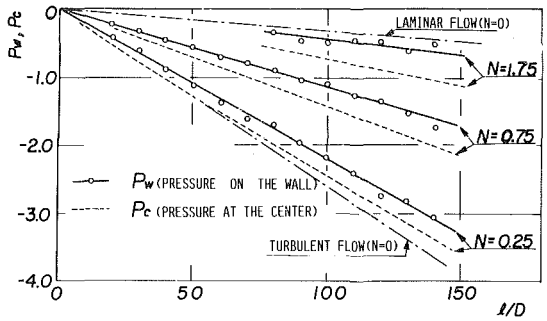

Fig. 7 Changes of pressures on the wall and at the center of rotating pipe (Re = 2 × 10^4), uncertainty of (l/D, P_w), coordinate (100, −2.2), uncertainty (±0.0004, ±0.2)

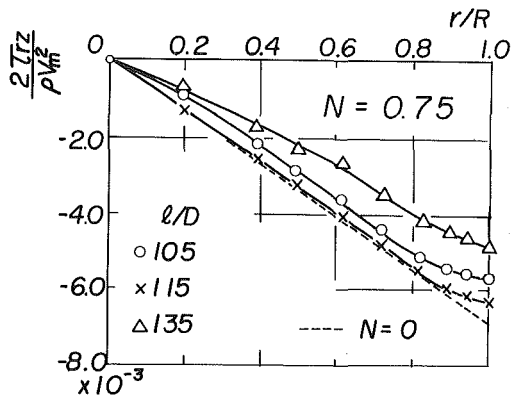

Fig. 8(*a*) Distributions of shearing stresses along the pipe τ_{rz} (Re = 2 × 10^4)

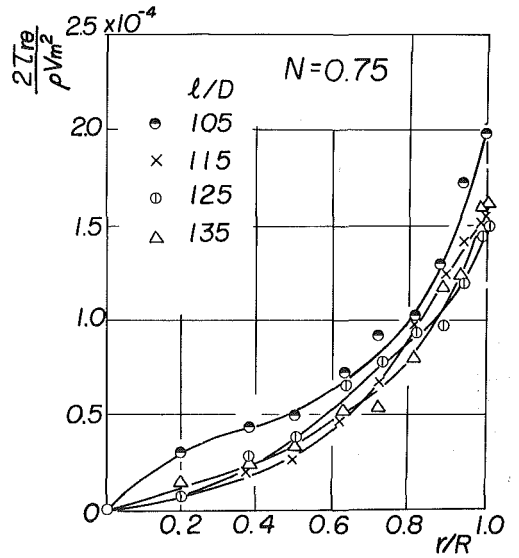

Fig. 8(*b*) Distributions of shearing stresses along the pipe $\tau_{r\theta}$ (Re = 2 × 10^4)

in Fig. 9, $2(\tau_{r\theta})_0/(\rho V_m^2 N)$ can be approximated by, when $N < 0.9$,

$$2(\tau_{r\theta})_0/(\rho V_m^2 N) = 0.00317 \exp[-0.023(l/D)] \quad (18)$$

For $N > 0.9$, an appreciable rate of suppression of turbulence will be expected in the inlet region of the rotating pipe and a larger reduction of $2(\tau_{r\theta})_0/(\rho B_m^2 N)$ will be observed.

4.5 Energy Fluxes in Rotating Pipe. Changes of E_t, E_k, and E_p along the pipe axis are calculated by equations (3), (4), and (5) and the results are shown in Fig. 10. When N is increased, the rate of change in E_p is decreased, while that in E_k is increased. Thus, along the pipe axis the value of E_t is decreased for N = 0.25 and 0.75 but is increased for N = 1.75. This increase in E_t is due to the pipe rotation and it shows that the energy supplied by the pipe rotation is larger than that lost in the pipe. Most of the energies supplied in the rotating pipe is considered to be lost by wall friction in the downstream stationary pipe. Supply and consumption of energy will be performed by pipe wall through friction and both of them, having the opposite sign, may be considered to be roughly in

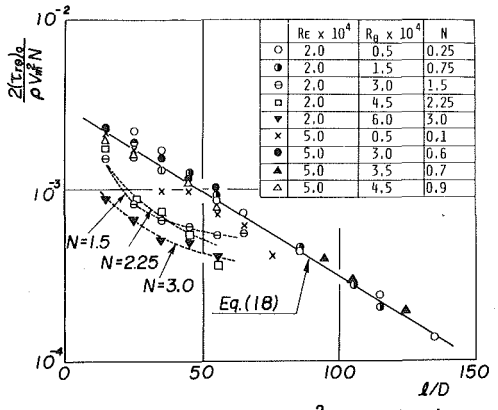

Fig. 9 Change of $2(\tau_{r\theta})_0 l/(\rho N V_m^2)$ along the pipe

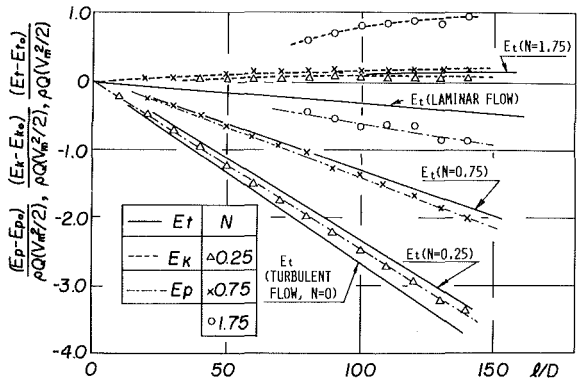

Fig. 10 Changes of E_p, E_k, and E_t along the pipe

the same magnitude, and the effect on the coefficient of hydraulic loss ξ is considered to be considerably small.

Conclusions

Nonswirling turbulent flows were introduced to axially rotating pipes, and flow patterns and resistance in the pipe were investigated experimentally in the ranges of flow Reynolds number $10^4 \leqq Re \leqq 2.0 \times 10^5$ and rotational Reynolds number $0 \leqq R_\theta \leqq 6.5 \times 10^4$.
The results are summarized as follows:

(1) A swirling flow component given by the rotating pipe wall decreases the hydraulic loss undergone in the rotating pipes. The reduction in the hydraulic loss is a function of a parameter, $N = R_\theta/Re$, and the rotating pipe length. When the pipe length is larger than 100D, the ratio of loss coefficient ξ/λ is governed by a single parameter N. In this case ξ/λ decreases as N increases from 0.35 to 1.2, and beyond this range the suppression of the turbulence is saturated and ξ/λ remains substantially unaltered.

(2) Velocity profiles are governed by a parameter N and an axial distance from the rotating pipe inlet. With a constant value of N, the axial velocity distribution approaches the laminar flow profile in the downstream region, but the ultimate flow profile depends on the degree of turbulence suppression. Even when the spin ratio N was increased to 8.6, the measured velocity profiles exhibited neither a wholly laminar profile in the axial component nor a perfectly forced-vortex profile in the circumferential component.

Acknowledgment

The authors wish to express their appreciation to Mr. A. Yokoyama, Mr. T. Noda and Mr. S. Araki for their experimental work and also to Prof. Y. Yamada of Nagoya Institute of Technology for discussion and suggestion on this study.

References

1 Lavan, Z., Nielsen, H., and Fejer, A. A., "Separation and Flow Reversal in Swirling Flows in Circular Ducts," *Physics of Fluids,* Vol. 12, No. 9, 1969, pp. 1747-1757.

2 White, A., "Flow of a Fluid in Axially Rotating Pipe," *Journal of Mechanical Engineering Science,* Vol. 6, No. 1, 1964, pp. 47-54.

3 Levy, F., "Strömungserscheinungen in Rotierenden Rohren," *Vereines Deutscher Ingenieure Forschungsheft,* No. 535, 1929, pp. 18-45.

4 Shchukin, V. K., "Hydraulic Resistance of Rotating Tubes," *Journal of Engineering Physics,* Vol. 12, No. 6, 1967, pp. 782-787 (in Russian).

5 Cannon, J. N., and Kays, W. M., "Heat Transfer to a Fluid Flowing inside a Pipe Rotating about its Longitudinal Axis," ASME *Journal of Heat Transfer,* Vol. 91, No. 1, 1969, pp. 135-139.

6 Borishenko, A. I., Kostikov, O. N., and Chumachenko, V. I., "Experimental Investigation of Turbulent Flow Characteristics in a Rotating Channel," *Journal of Engineering Physics,* Vol. 24, No. 6, 1973, pp. 1103-1108 (in Russian).

7 Pedley, T. J., "On the Stability of Viscous Flow in a Rapidly Rotating Pipe," *Journal of Fluid Mechanics,* Vol. 35, No. 1, 1969, pp. 97-115.

8 Nagib, H. M., Wolf, L., Lavan, Z., and Fejer, A. A., "On the Stability of the Flow in Rotating Pipes," Illinois Institute Technology Report, 1969.

9 Kikuyama, K., "Experimental Investigation of Flow in Rotating Ducts," Doctoral Dissertation of Nagoya University, 1975 (in Japanese).

APPENDIX

Length and Diameter of Pipes. Basic measurements by a dial guage of reading accuracy of ±0.03 mm and a three meters steel measure of reading accuracy of ±0.2 mm

Limits of D: ± 0.1 mm
Limits of L_1, L_2, and L_3: ± 1.0 mm.

Mean Flow Velocity V_m, Peripheral Speed of Pipe U, and Swirl Rate N. The mean flow velocity was determined from the volumetric flow rate measured by an orifice, and the peripheral speed by a tachometer. The manometer could be read to ± 1 mm, and the tachometer to ± 1 rev/min in the range of 100 to 1000 rev/min.

Limits of V_m: ± 2 percent
Limits of U: ± 1 percent

Hence

Limits of N: ± 3 percent.

Local Flow Velocity Components V_z and V_θ. The local flow velocity was measured by a Pitot tube, and its axial and circumferential components were calculated from the measured angle against the rotating pipe axis. The reading accuracy of the manometer associated with the Pitot tube was ± 1.5 mm and that of the measured angle was ± 2.0 deg.

In the central region of a section;
Limits of V_z: ± 2.0 percent
Limits of V_θ: ± 0.05 V_m.

Near the pipe wall, the error in the measurement was increased on account of a steep velocity gradient. To check the measurement, the flow rate obtained by graphical integration of the measured velocity profile over a section was compared with that derived by an orifice meter, and the difference was confirmed to be less than 3 percent.

Loss Coefficient ξ. The coefficient of hydraulic loss was derived by equation (2) from measured values of L_1, L_2, L_3, D, V_m, λ and H. The reading accuracy of H was ± 1.0 percent and the error in the friction factor λ was less than ± 1 percent.

At the lowest value of $L_2(L_2/D = 30)$;

Limits of ξ: ± 20 percent when Re = 2×10^4.
± 12 percent when Re = 10^5.

At the highest value of $L_2(L_2/D = 120)$;

Limits of ξ: ± 6 percent when Re = 2×10^4.
± 5.5 percent when Re = 10^5.

Shearing Stresses τ_{rz} and $\tau_{r\theta}$. Inaccuracy in the calculated shearing stresses was a considerable amount, since each value was obtained by equations (6) and (7) with a set of measured data. But, repeated measurements for each value of the stress have made possible to offer the values on the wall within the error of ± 10 percent.

Flow Over Two Circular Disks in Tandem

T. Morel

M. Bohn[1]

Fluid Dynamics Research Department,
General Motors Research Laboratories,
Warren, Mich. 48090

Placing two or more bluff-bodies in tandem is known to lead, in some cases, to configurations with relatively low overall drag. The present study concerns one particular case where two disks of unequal diameters, normal to the flow, are placed in tandem for the purpose of drag reduction. It shows that very significant drag reductions may be achieved by proper sizing of the disk diameters and of the gap between them. Placing a properly sized disk at an optimum distance ahead of a single reference disk can result in a configuration whose total drag is up to 81 percent lower than that of the reference disk alone. If the additional disk is placed behind into the near-wake of the reference disk, the drag of the two-disk configuration can be up to 70 percent lower than for the reference disk alone. Four different flow regimes have been identified, depending on the diameter ratio of the two disks, two with relatively steady flows and two with unsteady flows. The absolute drag minimum was found to occur in one of the two steady-flow regimes.

Introduction

One of the more intriguing topics in bluff-body aerodynamics is the interaction of two bluff-bodies placed in tandem. The intriguing facet of this topic is that the flow pattern and drag of a tandem configuration cannot be easily predicted from the known flow characteristics of the two individual bodies that form it. The reason for this is that the rear body is exposed to a flow perturbed and substantially altered by the front body and, in addition, there is also some upstream influence of the rear body on the front-body flowfield. There are many examples of flows over bodies in tandem that one can identify in our every day experience; for example, two or more neighboring buildings, and the tractor-trailer combinations one can see on the road.

In the case of neighboring buildings the bodies are not directly connected, and one is interested only in the changes in the flowfield of one building as it is affected by the presence of its neighbors. In cases like that of tractor-trailers, the bodies are directly connected and one is interested in the flowfield of, and forces acting on, the entire system of the connected bodies, as well. The results presented here pertain to one particular combination of two bodies that are directly connected.

Previous Related Experiments

The case of two disks of equal diameters placed in tandem was studied some 70 years ago by Eiffel [1]. His results showed that the combination of two disks separated by not too large a gap produces a smaller drag than a single disk alone, as can be seen from the tabulated data below, obtained at Re = 190,000:

L/D	0.0	0.5	1.0	1.5	2.0	2.5	3.0
$C_{D1} + C_{D2}$	1.12	1.09	0.94	0.81	1.075	1.34	1.57
C_{D2}	–	−0.15	−0.28	−0.43	−0.16	+0.11	+0.37

where C_{D1} and C_{D2} are the drag coefficients of the front and rear disks, respectively. The data are uncorrected for model blockage (the model-to-jet area ratio was 4 percent).

It is striking to see that the rear disk experienced a *negative* drag force (acting forward) over a wide range of gap/diameter ratio. Eiffel pursued this further and let the rear disk slide freely forward on the rod supporting the front disk from behind. For $x/D < 2.26$ the flow field caused the disk to move forward, while for larger gaps the rear disk was pushed backward, away from the front disk.

The drag coefficient of a single disk was also obtained by Fail, et al. [2] at Re = 400,000. Their data gave the same result as Eiffels, $C_D = 1.12$, in this case after a correction, using Maskell's procedure [3], for an area blockage of 1.4 percent (in their closed-jet wind tunnel).

Another related experiment is that of Roshko and Koenig [4], who investigated the effect of diameter ratio and gap length on the drag of a flat-faced circular cylinder preceded by a concentric circular disk. Their data were obtained at Re = 100,000-800,000, and were not corrected for model blockage of 3.4 percent. They found that one optimal configuration, with disk-to-cylinder diameter ratio of 0.75 and gap-to-cylinder diameter ratio of 0.375, produced an amazing drag

[1] Currently with Solar Energy Research, Golden, Colo.

Contributed by the Fluids Engineering Division for publication in the Journal of Fluids Engineering. Manuscript received by the Fluids Engineering Division, June 28, 1979.

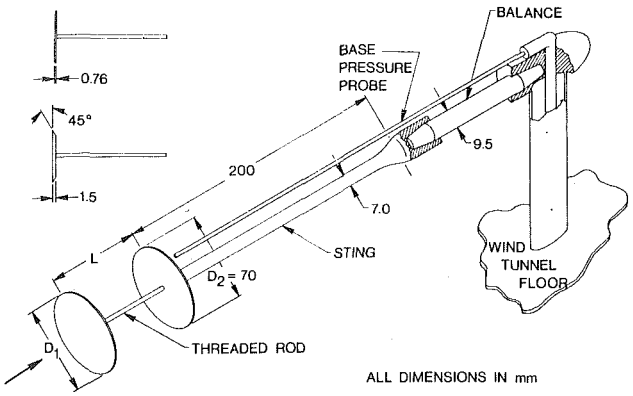

Fig. 1 Experimented arrangement: disk model, force balance, and supporting sting

reduction: while the cylinder's forebody (the cylinder was divided by a transverse cut into a separate short forebody and along afterbody) had $C_{DF} = 0.75$, the addition of the optimum disk reduced the forebody drag coefficient of the configuration to 0.02. The overall drag coefficient reduction from 0.75 to 0.02 is very impressive, especially since it came from the addition of another very bluff body. One may wonder just how close the drag coefficient of the optimum configuration comes to the lower bound of the pressure-drag coefficient which would be experienced if the flow were potential. It has been shown (Morel [5]) that in potential flow the forebody drag coefficient C_{DF} is always negative, tending to zero for forebodies followed by long constant-area afterbodies. For a body like that used by Roshko and Koenig, the potential-flow C_{DF} should have a small negative value. The difference between the measured C_{DF} and this potential flow C_{DF} is then the total drag coefficient due to real flow effects such as flow separation and skin friction.

Experimental Arrangement

The tests were conducted in a 500 × 700 mm wind tunnel. The model used consisted of a thin circular disk, of diameter $D_2 = 70$ mm, attached to a long sting placed on the centerline of the tunnel (Fig. 1). The sting diameter was ten percent of the disk diameter (wake blockage of one percent). The sting was attached to one end of a small strain gage sting balance, the other end of which was clamped in a rigid support. The sting had a threaded internal hole on its axis allowing insertion of a threaded rod carrying another disk of diameter D_1, which could be positioned concentrically at various distances ahead of the fixed disk (up to a gap size $L = 210$ mm $= 3\,D_2$).

The experiment was run for the most part at air speeds of 22 and 44 m/s, giving $\mathrm{Re}_D = 100{,}000$ and 200,000. The model blockage ratio, ratio of the model area to the test section area, was 1.1 percent.

The front disks used in this study varied from 0.25 to 1.2 times the rear disk diameter, and there were 16 different diameters. The larger disks were made of sheet metal 0.76 mm thick ($t/D_2 = 0.011$) with a square side edge. The smaller disks were made of a sheet 1.52 mm thick ($t/D_2 = 0.022$), with a sharp edge beveled from behind at a 45° angle (Fig. 1).

The outputs from the force balance and from the pressure transducer measuring the dynamic pressure were integrated simultaneously over intervals of 2 to 10 seconds, depending on the particular measurement.

No blockage correction was applied to the data presented here, although a study of the blockage effect was made, whose results are discussed below.

Flow Visualization. Flow patterns around the various disk models were made visible by injecting titanium tetrachloride smoke at the rear of the front disk. The smoke was produced by cartridges manufactured by Mine Safety Appliance Co., Pittsburgh, PA. The smoke was injected from a small tube at the rear of the front disk. Light was provided by a spot light or a flashgun aimed through the transparent roof of the wind tunnel. Distracting reflections from the internal wind tunnel surfaces were minimized by covering these with flat-black paper.

Photographs of the smoke were made at two speeds: at a shutter speed of 1/15 second using the spotlight for illumination, and with a flash gun giving exposures of nominally 40 μs. During all visualization experiments, Reynolds number based on 70 mm disk diameter was 100,000. The corresponding flow speed indicated a 1.5 m distance traveled by the mean flow during the slow exposures, while for the fast exposures the distance was only about 1 mm.

Results

The results are presented in terms of drag and pressure coefficients. Their accuracy, based on frequent calibrations, which in the case of pressure transducers were performed prior to every run, as well as on day-to-day repeatability, is C_D within ± 0.003 and C_p within ± 0.001. The measurement of the ratio L/D_2 was accurate to within ± 0.007.

Single Disk. The first configuration studied was a single disk with $D_2 = 70$ mm (the front disk was removed). Its drag coefficient showed only a very small variation with Reynolds number. A least-square fit to data taken in the range $\mathrm{Re}_D = 50{,}000 - 200{,}000$ gave $C_D = 1.150 - 0.0175 \times 10^{-6}\,\mathrm{Re}$, or $C_D = 1.148$ at $\mathrm{Re} = 100{,}000$ and $C_D = 1.146$ at $\mathrm{Re} = 200{,}000$.

It is a well established fact that measurements made in a wind tunnel whose test section is bounded by solid walls do not duplicate exactly a free-stream (unbounded) environment. This is a consequence of the constraining effect of the tunnel walls which makes the wall streamlines follow the wall contours, rather than being shaped by the flowfield around the tested model. This constraining effect is felt at the model itself and results in a modification of the local flow field around it. The larger the model frontal area, as compared to the tunnel cross-section, the stronger is the constraining effect the tunnel walls exert by keeping the wall streamlines straight and, vice versa, the stronger is the influence of this effect back on the flow field around the body.

Nomenclature

C_p = pressure coefficient = $(p - p_\infty)/q_\infty$
$C_{D,1}$ = drag coefficient based on the front-disk diameter
$C_{D,2}$ = drag coefficient based on the rear-disk diameter
D = disk diameter
L = axial spacing between disks (gap)
p = static pressure
q = dynamic pressure
Re = Reynolds number based on disk diameter

Subscripts

1 = front disk
2 = rear disk
∞ = free stream conditions
b = base of rear disk
d = downstream piezometric ring
F = forebody
u = upstream piezometric ring

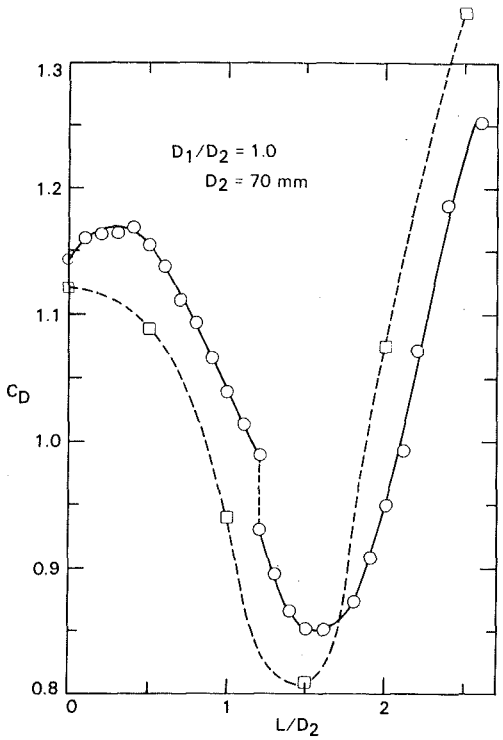

Fig. 2 Drag coefficient versus gap length for two disks of equal diameter, D_2 = 70 mm. – ○ – Re = 100,000, – – □ – – data points and curve taken from Eiffel [1] (Re = 190,000)

This effect and its magnitude have been the subject of many studies. Among them, one of the best known is the analysis performed by Maskell [3], who developed a theory for pressure-drag corrrection for the effects of model blockage. This analysis which is often being applied to a broad range of bluff-body geometries, was in fact developed for the simplest ones — thin plates perpendicular to the flow. Therefore, Maskell's correction is particularly well suited for application to the present configuration, and so it was decided to use it to extrapolate the present data to zero-blockage (infinite stream) conditions. The correction has the following form:

$$\frac{C_D}{C_{Dc}} = 1 + \epsilon C_D b$$

where C_{Dc} is the "correct" (extrapolated) drag coefficient, ϵ is a blockage factor, and b is the ratio of model frontal area to wind tunnel cross-sectional area (model blockage). The extrapolated drag coefficient at zero blockage was found to be C_{DC} = 1.119, using ϵ = 2.75 as recommended by Maskell.

Two Disks of Equal Diameter. The next study involved two disks of equal diameter placed in tandem. The gap between the two disks was increased monotonically in small increments of 0.1 times D_2. The result of this traverse is plotted in Fig. 2, which shows that the drag coefficient of the system has a quite interesting behavior. It increased slightly at first, reaching a maximum at L/D_2 = 0.3, and then it decreased sharply. At L/D_2 = 1.2 the otherwise smooth curve was interrupted by a sharp downward jump in C_D, indicating a change in flow pattern. At this gap length the flow pattern was bistable and the time-average drag coefficient could have a value lying anywhere between the two extremes. Flow visualization later showed that the two possible flow patterns kept switching randomly from one to another so that, because of the finite integration time, some average C_D in between the two limiting values was recorded unless a single pattern persisted during the entire integration period. The two flow patterns are quite well discernible in the smoke photographs presented later.

The system drag coefficient reached a minimum at about L/D_2 = 1.55 with a value C_D = 0.85, which was 26 percent below the single-disk value. Beyond the minimum the drag coefficient increased sharply, going towards its limiting value of twice that of the single disk.

Eiffel's data, mentioned earlier, are included for comparison in Fig. 2. The actual data points are shown by crosses, the broken line is Eiffel's own interpolation. Both curves are seen to be quite similar in shape, but there is a consistent shift between them, which was very puzzling. After careful consideration we wondered whether the shift was caused by the difference in model blockage by the difference in Reynolds number (Re = 100,000 here versus 190,000 for Eiffel), by a difference in the free-stream turbulence level, which was almost certainly substantially higher in Eiffel's simple wind tunnel than in ours (less than 0.1 percent). Any of these possibilities would introduce an additional parameter into the problem, so a closer look was taken to sort out the reasons for the differences between Eiffel's and our results.

The first effect looked at was that of blockage, i.e. the constraining effect of the tunnel walls which forces the local wall streamlines to be parallel to the tunnel axis. To this end, a new test was run with $D_1 = D_2$ = 49 mm, giving 50 percent less blockage than the original disks. This test was run at two Reynolds numbers — 100,000 and 178,000 (the latter constituted the upper limit achievable in the wind tunnel with disks of that diameter). The results for Re = 100,000 were found to be in very good agreement with those obtained with D_2 = 70 mm. Thus, the blockage of our model (1.1 percent) did not seem to be the reason for the shift.

On the other hand, there was some evidence of a Reynolds number effect in the results obtained with the smaller disks at Re = 178,000 in the range L/D_2 = 1.0 - 1.8, in particular on the location of the drag discontinuity, which moved to a higher L/D_2 at the higher Re. To investigate this effect, two Reynolds number runs were made with disks $D_1 = D_2$ = 70 mm at two fixed gap widths, L/D_2 = 1.1 and 1.3, in the vicinity of the drag jump. It was found that the drag coefficient was rather sensitive to Reynolds number in a region Re = 180,000 - 215,000 but not elsewhere. At both gap widths the drag coefficient was almost constant except for the localized Reynolds number region near 200,000 where it dropped to lower levels. Thus it appears that the difference between the two curves in Fig. 2 may be partly due to the Reynolds-number sensitivity of the flow.

When the flow is sensitive to Reynolds number then it often turns out to be sensitive in some degree to the level of turbulence in the free-stream as well. Thus a difference in the turbulence level between the two wind tunnels may also have been responsible for some of the difference in C_D. However, this aspect of the problem was considered outside the scope of this study.

In summary, the drag coefficient of a system of two disks of equal diameter placed in tandem exhibits the characteristic behavior seen in Fig. 2: first an increase with increasing gap then a sharp decrease containing an abrupt downward jump, a smooth minimum around L/D_2 = 1.5, and finally a monotonic sharp increase. Comparison to an earlier study of this flow configuration by Eiffel [1] shows basic agreement with his data but, unfortunately, Eiffel's data were too sparse to show whether an abrupt jump on the drag curve was also present in his case. The differences in the C_D values of Eiffel and those of the present investigation seem to be at least partly caused by the Reynolds number sensitivity of the experiment.

Two Disks of Unequal Diameter, D_1/D_2 = 0.25 - 1.2. All of the data presented in this section were obtained at Re =

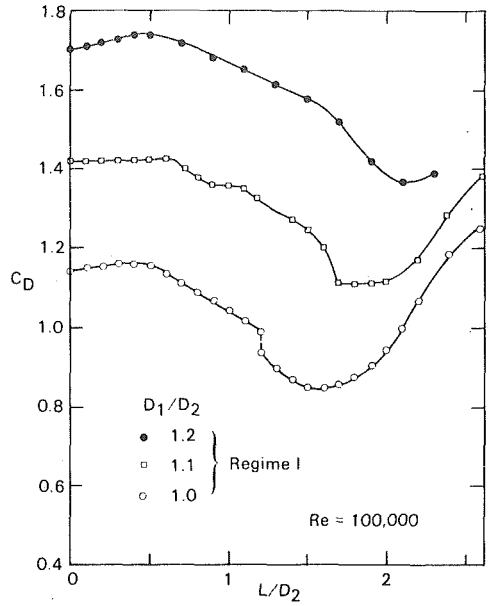

Fig. 3(*a*) Regime I

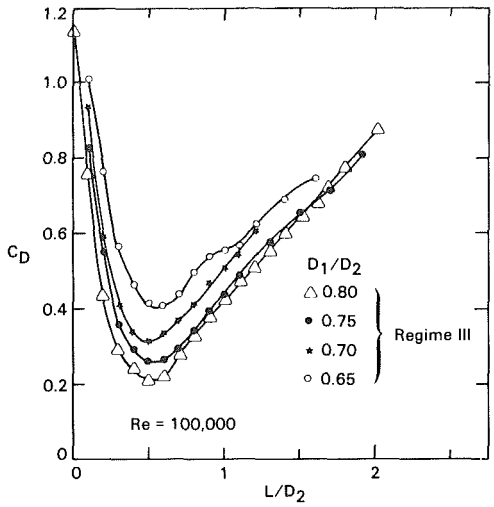

Fig. 3(*c*) Regime III

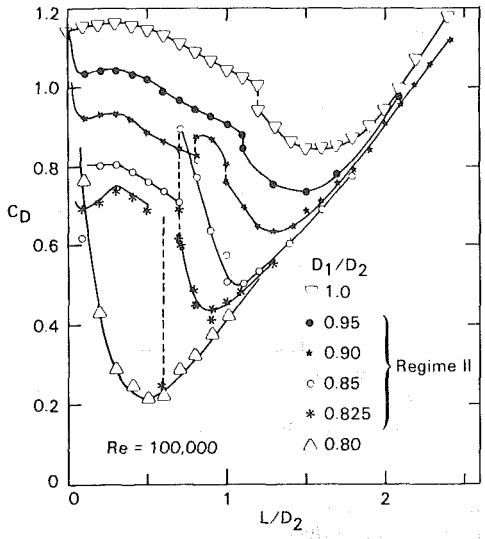

Fig. 3(*b*) Regime II

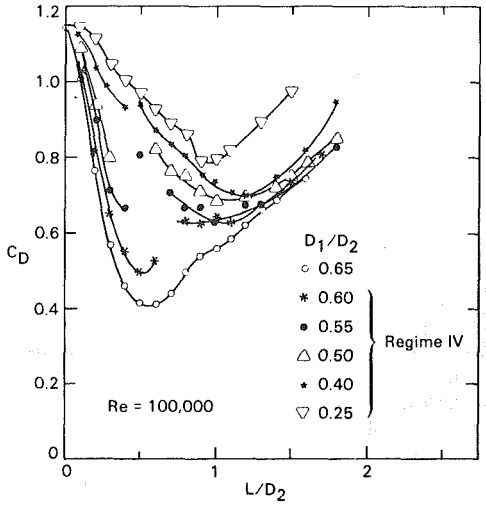

Fig. 3(*d*) Regime IV

Fig. 3 Drag coefficient versus gap length

100,000. A parallel set of data was also obtained for Re = 200,000. For a great majority of the data points the results for the two Reynolds numbers agreed to within $\Delta C_D = 0.01$, but there were some exceptions at isolated data points between $L/D_2 = 0.4$ and 2.2. These exceptions are noted within the text as appropriate. The drag coefficient in this case is based on the total drag acting on both disks, and is referred to the area of the rear disk.

An initial appraisal of all the data for the various diameter ratios led to the conclusions that the data may be conveniently divided into four different groups (regimes), depending on the ratio D_1/D_2, each with a distinct behavior of its own (Fig. 3). Plotting the data separately for each regime highlights the similarities and differences of the regimes, and it aids the clarity of the plots themselves. (Note that the vertical scale in Fig. 3 is several times coarser than in Fig. 2).

The first group, regime I, concerns the cases where the added front disk diameter was larger than or equal to the rear disk, with $D_1/D_2 = 1.0$, 1.1 and 1.2 (Fig. 3(*a*)).

All three curves have a similar behavior, which is the same as that described already in the previous section: C_D first increases with increasing gap, then decreases to a minimum, followed by an increase. The sensitivity to Reynolds number for $D_1/D_2 = 1.0$ was already discussed; for $D_1/D_2 = 1.1$ and 1.2 the sensitivity appeared to be much smaller, with differences between Re = 100,000 and 200,000 being limited to $\Delta C_D \leq 0.02$.

The second group, Regime II, lies in the range $0.8 < D_1/D_2 < 1.0$ (Fig. 3(*b*)). It differs from the first group by two distinguishing features: a sharp initial drop-off in C_D at very small gap lengths, and by a much less smooth behavior, especially at Re = 200,000. The curve $D_1/D_2 = 0.95$ is smooth at Re = 100,000, but at Re = 200,000 one isolated point, $L/D_2 = 0.4$ (not shown) was 0.07 below an otherwise smooth drag curve. As D_1/D_2 decreased further the drag data became increasingly more erratic, as may be seen in the curves for $D_1/D_2 = 0.90$, 0.85 and 0.825. The flow also became rather unsteady and produced model vibration in the region $L/D_2 = 0.3 - 1.1$, in which region the data for the two Reynolds numbers often differed by up to $\Delta C_D = 0.10$. The case of $D_1/D_2 = 0.825$ exhibited a bistable behavior at $L/D_2 = 0.6$, where C_D could be made to switch from a value 0.65,

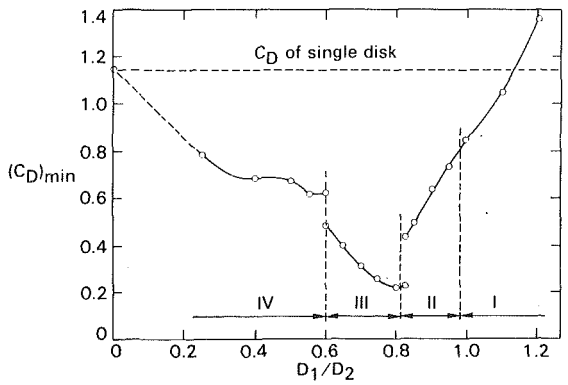

Fig. 4 Minimum drag coefficient versus D_1/D_2

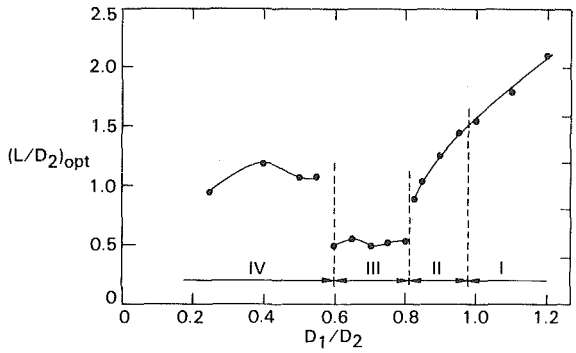

Fig. 5 Disk spacing required for minimum drag versus D_1/D_2

characteristic of Regime II, down to 0.25, a value characteristic of Regime III.

In the third group (Regime III), by contrast, the drag curves were very smooth (Fig. 3(*c*)). In this regime the two-disk configuration experienced the lowest drag, reaching a minimum of $C_D = 0.21$ at $D_1/D_2 = 0.8$ and $L/D_2 = 0.5$. All four curves in this regime were similar in shape. However, the level of flow unsteadiness was not the same for the whole regime, but steadily increased with decreasing D_1. For $D_1/D_2 = 0.8$ and 0.75 the flow was very steady, but for $D_1/D_2 = 0.7$ the model started to vibrate at $L/D_2 = 0.9$ at the higher flow velocity, and for $L/D_2 \geq 1.1$ no data could be taken at that speed because the vibration became so excessive that model failure was feared. A similar behavior was found for $D_1/D_2 = 0.65$, but there the vibrations became excessive (at the higher speed) already at $L/D_2 = 0.7$.

The last group (Regime IV), with $D_1/D_2 \leq 0.60$, differed from the previous one by lack of smoothness in the drag data (Fig. 3(*d*)). It was also beset by model vibration that peaked around $D_1/D_2 = 0.5$. The vibration was sometimes strong enough to prevent measurements, even at the lower flow velocity. For $D_1/D_2 = 0.6$ this occurred at $L/D_2 = 0.65$, for $D_1/D_2 = 0.55$ it was at $L/D_2 = 0.6$ and for $D_1/D_2 = 0.5$ it was at $L/D_2 = 0.4$ and 0.5. Thus, the region of maximum unsteadiness occurred at smaller and smaller gaps as D_1/D_2 was decreased. The same tendency was present at the higher velocity, where the range of L/D_2 where the vibrations were excessive was, of course, much wider.

The salient point on each of the curves in Figs. 3(*a-d*) is the drag minimum occurring at one (optimum) gap length. The dependence of the coordinates of these points, i.e. the minimum C_D and the optimum gap length $(L/D_2)_{opt}$, on the ratio D_1/D_2 is shown in Figs. 4 and 5, respectively. Each of the curves C_{Dmin} and $(L/D_2)_{opt}$ consists of three segments separated by two discontinuities at the boundaries between regimes II, III and IV. There is no discontinuity in either of the curves between regimes I and II. Both curves have their minimum in regime III.

The physical reasons for the discontinuities separating regimes II, III and IV may be speculated on, based on our flow visualization and results known from other related types of separated flows. Both discontinuities can be best analyzed in Fig. 5, showing the gap for minimum drag as a function of disk diameter ratio. In the low-drag regime III the optimum gap is approximately constant with a value of 0.5 D_2. Going toward regime II, as D_1/D_2 increases the flow must turn more sharply if is is to attach itself to or skim just over the shoulder of the rear disk. This requires a lower and lower pressure between the two disks, and at D_1/D_2 slightly more than 0.8 the required pressure differential between the cavity pressure and the ambient pressure becomes too large and the flow separates from the rear disk. The gap then has to be enlarged substantially in order to capture the separated shear layer as it comes back towards the centerline, as it must because the base pressure of the front disk is lower than the ambient pressure.

The changeover from regime III to regime IV, on the other hand, most likely occurs because the front disk diameter becomes too small and the shear layer separating from it can no longer reach all the way to the rear disk perimeter and skim over it. Instead it begins to impact on the front surface of the rear disk, and the flow pattern changes to that associated with regime IV.

In summary, the combination of two disks in tandem often has a drag lower than a single disk alone. More precisely, if the ratio of the front disk diameter D_1 to the diameter of the rear disk D_2 is in the range $D_1/D_2 = 0$ to 1.13 then the drag of the combination, at a proper gap size, will be lower than the drag of the rear disk alone. The upper limit $D_1/D_2 = 1.13$ was obtained from the intercept of the curve of C_{Dmin} and the horizontal broken line $C_D = 1.147$ in Fig. 4. The fact that this upper limit is larger than unity means that the added front disk may be larger than the rear disk and still produce some drag reduction! The absolute drag minimum of 0.21 is obtained with $D_1/D_2 = 0.8$ at a gap $L/D_2 = 0.54$. This minimum is 81 percent below the drag coefficient of a single disk.

The present results may also be intepreted in another way, as pertaining to the reverse problem of adding a disk of diameter D_2 *behind* a disk of diameter D_1, with the purpose of achieving a drag reduction. Replotting Figs. 4 and 5 in terms of $(C_{D,1})_{min} = (C_{D,2})_{min} (D_2/D_1)^2$, i.e. the drag coefficient based on the front disk, and $(L/D_1)_{opt}$ versus D_2/D_1, one obtains the plots in Figs. 6 and 7 which show what happens in the reversed case. There we see that adding a rear disk with $D_2/D_1 = 0 - 1.61$, and adjusting the gap to its optimum size, will reduce the drag of the combination below the drag of the front disk alone. It is somewhat startling to see that the addition of a rear disk with a diameter up to 60 percent larger (2.5 times larger area) can produce a drag reduction! This would seem to be against intuition. The absolute drag minimum in this case is $C_D = 0.35$, obtained with $D_2/D_1 = 1.25$ at a gap $L/D_1 = 0.67$. This minimum is about 70 percent below the drag coefficient of the single disk.

Base Pressure Measurements. The fact that the drag coefficient of the optimum configuration was as low as 0.22 prompted a look at the base pressure behind the rear disk. For a single disk the base pressure is known to be uniform over the rear surface, with $C_{pb} = -0.42$ (Fail, et al. [2]) for a circular disk (uncorrected for wind tunnel blockage of 1.4 percent). Since the minimum drag coefficient of 0.22 is much less than 0.42 it is likely that the base pressure on the optimum configuration was higher than on a single disk, so that part of the drag reduction was caused by an increase in the base pressure of the combination.

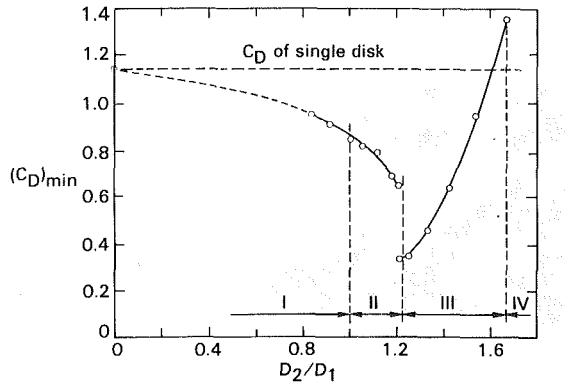

Fig. 6 Minimum drag coefficient (based on upstream disk) versus D_2/D_1

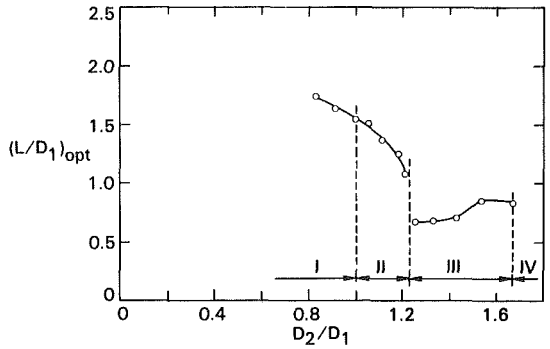

Fig. 7 Disk spacing required for minimum drag versus D_2/D_1

Consequently, it is of interest to consider the two-disk configurations as consisting of two parts: (1) a forebody formed by the front disk plus the front face of the rear disk, and (2) a base – which is just the rear surface of the rear disk. The individual components of the total drag attributable to these two parts can be separated by simultaneous measurements of the total drag coefficient and the base pressure. In this study it was assumed that the base pressure, which is very uniform on a single disk, is also reasonably uniform on the rear surface of the rear disk of a tandem combination. Thus the base pressure was measured at only one location, near the center of the rear disk, and was assumed to be the same over the whole base area.

Of the 16 different disk ratios, three were picked for this study. All three were in the stable regimes I ($D_1/D_2 = 1.0$ and 1.2) and III ($D_1/D_2 = 0.8$). The remaining diameter ratios in these two regimes were expected to behave similarly to the chosen representatives of their particular regimes.

In the case of two disks of equal diameters (Fig. 8(*a*)) the results showed that all the drag reduction (except for $L/D_2 = 1.3$) was due to base pressure increase. The curves of C_{DF} and C_{pb}, in particular the former, suggested an abrupt change of flow pattern at $L/D_2 \approx 1.25$. Up to that point C_{DF} was fairly constant, but beyond it there was a steep increase.[2] The value of C_{DF} for $L/D_2 = 0$ is 0.714, which is quite close to the pressure drag coefficient on the front face of a blunt-faced circular cylinder aligned with the flow, where $C_D = 0.74$ as measured by Roshko and Koenig [4]. The base pressure increased monotonically ($-C_{pb}$ decreased) through the region around $L/D_2 = 1.25$ and reached a maximum at $L/D_2 = 2.0$ with $C_{pb} = -0.011$, i.e. very close to the ambient pressure. Faced with these opposing trends of C_{DF} and ($-C_{pb}$) the total drag coefficient reached its minimum at $L/D_2 = 1.55$.

For $D_1/D_2 = 1.2$ the situation was very similar. Here again most of the drag reduction was due to an increase in C_{pb}, which grew monotonically up to the last data point taken ($L/D_2 = 2.54$) where it reached $C_{pb} = -0.034$. The total drag coefficient reached its minimum earlier, at $L/D_2 = 2.1$, again on account of the rise in C_{DF} which in this case set in around $L/D_2 = 1.9$.

The representative of Regime III (two disks with diameter ratio $D_1/D_2 = 0.8$) showed a behavior different from the first two (Fig. 8(*b*)). There the roles of C_{DF} and C_{pb} were reversed, and it was C_{DF} that accounted for more of the variation in the total C_D. This case was similar to the previous two in that the base pressure maximum (minimum base drag) was reached at

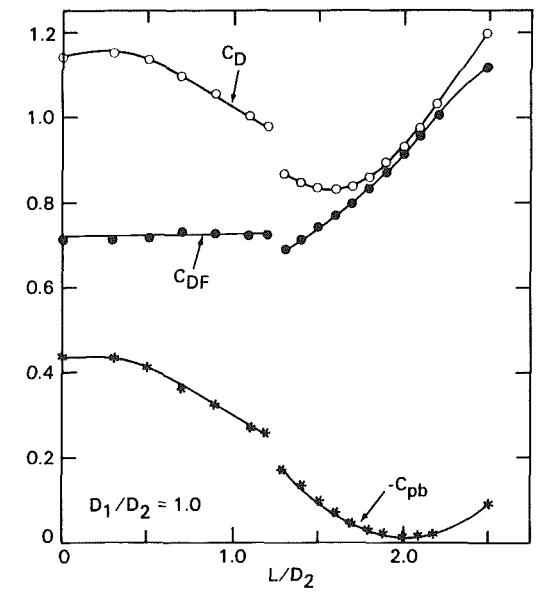

Fig. 8(a) Drag coefficient, "forebody" drag and base pressure versus gap length, $D_1/D_2 = 1.0$

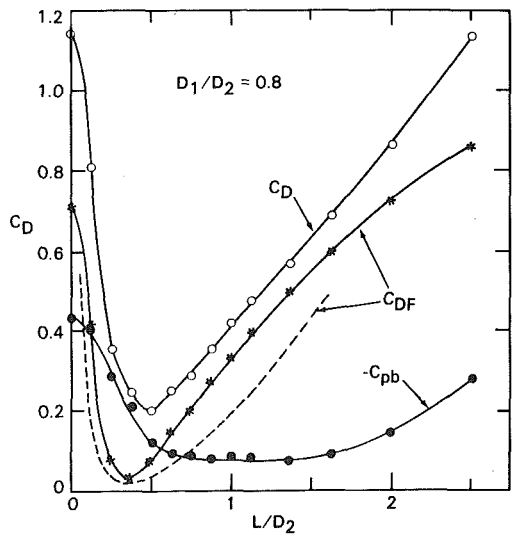

Fig. 8(b) $D_1/D_2 = 0.8$, ——— optimum configuration of Roshko and Koenig [4] with $D_1/D_2 = 0.75$

gaps where the forebody drag coefficient was already increasing sharply. Consequently, the minimum of the total C_D occurred well before the base pressure reached its maximum. The minimum forebody drag coefficient was recorded at $L/D_2 = 0.375$ with a value $C_{DF} = 0.033$. This last result

[2] This behavior may be correlated with the smoke photographs, to be discussed in the next section, which show that at $L/D_2 = 1.23$ the flow that separated from the front disk abruptly closes in and the separated shear layer impinges on the rear disk perimeter.

compares very favorably with the data of Roshko and Koenig [4] who found, for a parallel-sided afterbody (circular cylinder) of diameter D_2 preceded by a circular disk with $D_1/D_2 = 0.75$, the forebody drag coefficient to have a minimum at $L/D_2 = 0.375$ with $C_{DF} = 0.02$. Their data for the optimum configuration are shown by a broken line in Fig. 8(*b*)).

Smoke Visualization

Single Disk. The time-mean picture of the smoke (Fig. 9), obtained with a 1/15 second exposure, shows the flow separating at a steep angle to the oncoming stream, generating a wide separated region, and closing up about 3 disk diameters downstream. At the widest point the separated region had a diameter of about 1.65 times the disk diameter (measured to the center of the band of dense smoke which is presumed to indicate the location of the shear layer).

Two Disks of Equal Diameter. The next series of 3 photographs (Fig. 10) shows a very interesting situation occurring at $L/D_2 = 1.23$, where the flow switches between two flow patterns. The pattern in Fig. 10(*a*) is similar to the previous one in that a wide wake is formed, which here passes above the rear disk.

The flow could stay in this pattern for several tens of seconds before switching to the other pattern that could also persist for a similar period of time. This second pattern is shown in Fig. 10(*b*) and it differs from the first one in that the shear layer coming from the front disk no longer passes above the rear disk but is pulled in, skims over the rear disk perimeter, and forms a narrow wake behind it. This change in flow pattern is accompanied by a reduction in C_D and a change in the trends of C_{pb}, C_{DF} and C_D (Fig. 8(*a*)). The attachment of the shear layer to the rear disk perimeter also brings about a strong increase in recirculation beween the two disks (Fig. 10(*b*)). The last picture in this series (Fig. 10(*c*)) differs from all other photographs taken, and it probably captures the transient situation in which the flow changes form the lower-drag pattern to the higher drag one by ejecting some of the recirculating fluid from between the two disks.

At the drag minimum, $L/D_2 = 1.6$, the flow (Fig. 11) is basically of the same type as the second flow pattern discussed in the previous paragraph: the separated shear layer appears to still basically skim over the edge of the rear disk, and a relatively narrow wake is produced.

Two Disks With $D_1/D_2 = 0.8$. The flow pattern around the minimum-drag configuration with $L/D_2 = 0.5$, is shown in Fig. 12. The picture shows a vortex in between the two disks and the wake behind the rear one narrowing down very substantially. It is very interesting to note that on this minimum-drag configuration the dividing streamline between the two disks is not parallel to the free stream when it attaches to the rim of the second disk. Instead, it comes down towards the rim, steering the outside flow toward the centerline; this contributes to the observed narrowing of the wake behind the rear disk.

Conclusions

1 Experiments with two disks of different diameters placed in tandem and connected together showed that very significant drag reductions from that of a single disk may be achieved by proper sizing of the disk diameters and of the gap between them.

2 Placing a second disk of diameter D_1 *ahead* of a single disk of interest with diameter D_2, and choosing $D_1/D_2 = 0.8$ and the distance between them 0.54 D_2, results in a configuration with total drag coefficient $C_D = 0.21$ as compared to $C_D = 1.15$ for the single disk alone. This represents an 81 percent drag reduction.

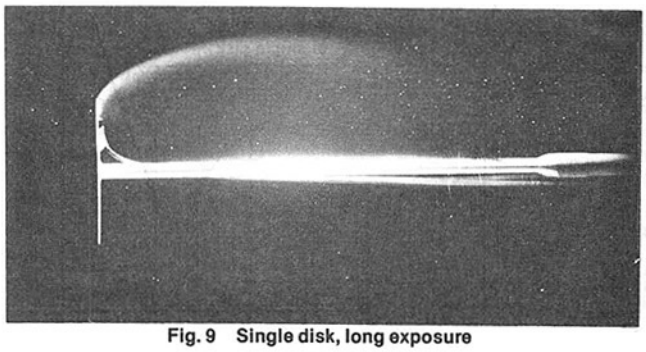

Fig. 9 Single disk, long exposure

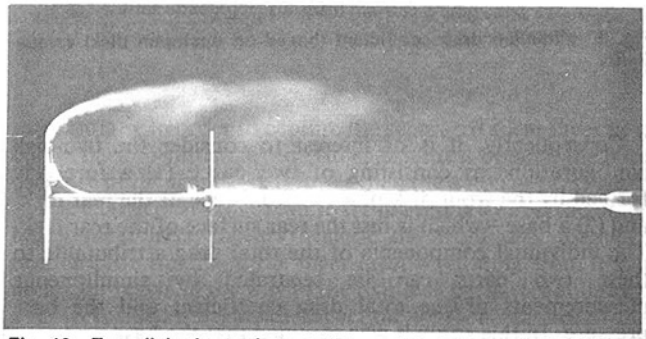

Fig. 10 Two disks in tandem, $D_1/D_2 = 1.0$, $L/D_2 = 1.23$ (*a*) Short exposure, higher C_D

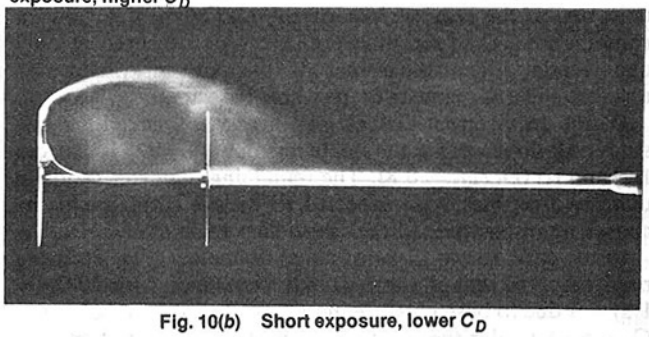

Fig. 10(*b*) Short exposure, lower C_D

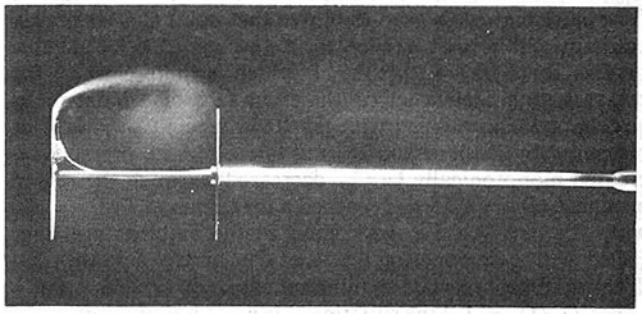

Fig. 10(c) Short exposure, switching of flow patterns

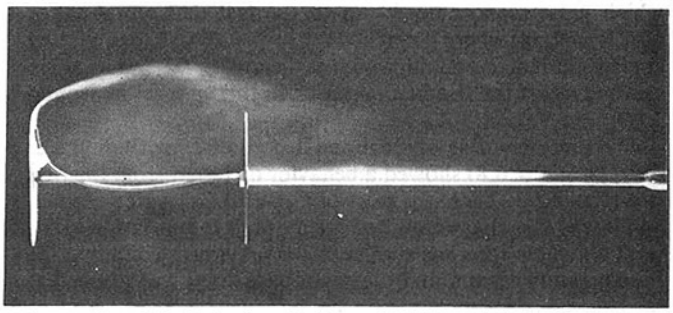

Fig. 11 Two disks in tandem, $D_1/D_2 = 1.0$, $L/D_2 = 1.6$, short exposure

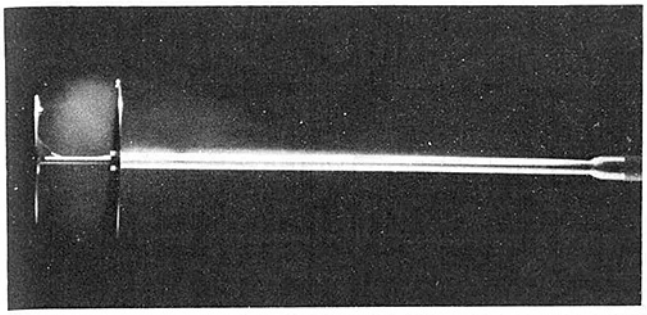

Fig. 12 Two disks in tandem, $D_1/D_2 = 0.8$, $L/D_2 = 0.5$, short exposure

3 Total drag can also be reduced by placing a second disk of diameter D_2 *behind* a single disk of interest with diameter D_1, and choosing $D_2/D_1 = 1.25$ and the distance between them $0.67\ D_1$. In this case the addition of the rear disk results in a 70 percent drag reduction, and it is worth emphasizing that this is achieved by the addition of a disk larger than the original one. In fact, drag reduction was achieved by the addition of larger rear disks with up to 2.5 times larger frontal area than that of the original single disk.

4 Detailed investigation of the two-disk configuration led to identification of four different operating regimes, depending on the disk diameter ratio. Among them, the most important is regime III ($0.65 \leq D_1/D_2 \leq 0.80$) where the most significant drag reductions were observed (at gaps lengths around $0.5\ D_2$).

5 The total drag on the two-disk configurations may be split into two parts: one acting on the "forebody" consisting of the front disk plus the front surface of the rear disk, and the second being the base-pressure drag on the rear surface of the rear disk. For the case of two equal disks it is shown that practically all of the drag reduction caused by the addition of the front disk is due to reduction of the base-pressure drag (increased base pressure). On the other hand, in the case of the minimum-drag configuration with $D_1/D_2 = 0.8$ both parts of the total drag contribute to the large drag reduction.

References

1 Eiffel, G., *The Resistance of the Air and Aviation,* Constable and Co., London, 1913.

2 Fail, R., Lawford, J. A., and Eyre, R. C. W., "Low Speed Experiments on the Wake Characteristics of Flat Plates Normal to an Air Stream," A. R. C. R&M 3120, June 1957.

3 Maskell, E. C., "A Theory of the Blockage Effects on Bluff Bodies and Stalled Wings in a Closed Wind Tunnel," A. R. C. R&M 3400, Nov. 1963.

4 Roshko, A., and Koenig, K., "Interaction Effects on the Drag of Bluff Bodies in Tandem," *Proceedings of the Symposium on Aerodynamic Drag Mechanisms,* Ed. G. Sovran, T. Morel and W. T. Mason, Jr., Plenum Press, New York, 1978.

5 Morel, T., "Theoretical Lower Limits of Forebody Drag," *The Aeronautical Journal,* Jan. 1979, pp. 23-27.

W. R. Martindale

Assistant Professor,
Montana State University,
Bozeman, Mont.

R. V. Smith

Professor,
Wichita State University,
Wichita, Kan. 67208

Pressure-Drop and Sonic Velocity in Separated Two-Phase Flow

Introduction

This paper reports constant area pressure gradient data for air-water vertical flows in the separated-phase (annular and annular-mist flows or gas-continuous flows). The reported data substantiate the previous hypothesis of this paper's authors (reference [1]) concerning the flow pattern transition from annular flow to the churning froth flow regime where the gas flow can no longer be considered as a continuum flow. The combined results of these data and the previous sonic velocity data are discussed, particularly with respect to the churning-froth flow pattern transition as the liquid-flow fraction is increased. Additionally, the data for pressure drop between measurement stations are discussed with respect to gas velocity and their suggestion of wave effects.

Pressure Drop and Sonic Velocity Data Combined

Fig. 1 shows the combined pressure gradient and sonic velocity data. These data were obtained from the vertical, upward flow of air-water mixtures in the experimental apparatus shown in Fig. 2. The sonic velocity values were obtained by measuring the time required for a shock wave to travel between two fixed points in the flow stream. The shock waves or pressure disturbances were created by rupturing a thin plastic or aluminum diaphragm downstream of the test section. Two quartz crystal type pressure transducers were utilized to sense the arrival of the shock wave front. Each transducer was connected to a charge amplifier which in turn was connected to an events-per-unit-time counter which was operating in the start-stop mode. The time of travel between a 30.5 cm fixed distance established the absolute velocity of the shock wave through the duct. The propagation speed is a function of the pressure difference across the diaphragm and the flow velocity. This functional dependence was correlated and applied to the indicated experimental speeds. Test conditions for these experiments are tabulated in Table 1. Superficial gas velocities (gas velocities computed as though the gas were flowing alone, $\dot{m}_g/\rho_g A_{\text{duct}}$) were used in the reduction of these data. The most striking result in comparing the pressure gradient and sonic velocity data is that a flow pattern transition (annular to churn froth) is distinctly indicated at approximately the same quality. This transition is

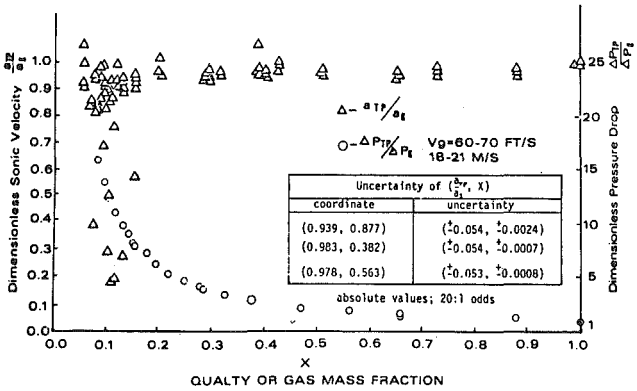

Fig. 1 Sonic velocity ratio and pressure drop ratio versus quality

shown by the near-vertical rise in the pressure gradient data and in the discontinuity for the sonic velocity data at the low-quality end of the plot in Fig. 1. These changes in sonic velocity and pressure gradient at the transition have not been demonstrated previously. The data also show that the sonic velocity is a sensitive indicator of the flow pattern transition from annular to churning froth because of its essentially discontinuous behavior at that point.

Sonic Velocity Data

The sonic velocity data are shown in Fig. 3, together with a plot of the predicted sonic velocity using a homogeneous, thermal equilibrium model. The gas velocities used in the reduction of these data were superficial gas velocities, corrected by an empirically determined blockage factor (reference [2]) which is intended to account for the blockage of the gas flow by the liquid phase. The blockage factor, as used in this context, accounts for an additional blockage of the gas flow by the wavy geometry of the liquid film and by dead regions behind droplets (wakes). Consideration of these lower-velocity gas volumes, changes the superficial gas velocity somewhat from a calculation using void fractions only. Further description of this blockage factor and the empirical method used to determine its value are discussed in reference [2]. The experimental results show that the sonic velocity in this flow-pattern region is far from that predicted by the homogeneous, thermal equilibrium model and, indeed, is essentially that of the sonic velocity in the gas alone. This

Contributed by the Fluids Engineering Division for publication in the JOURNAL OF FLUIDS ENGINEERING. Manuscript received by the Fluids Engineering Division, November 2, 1976.

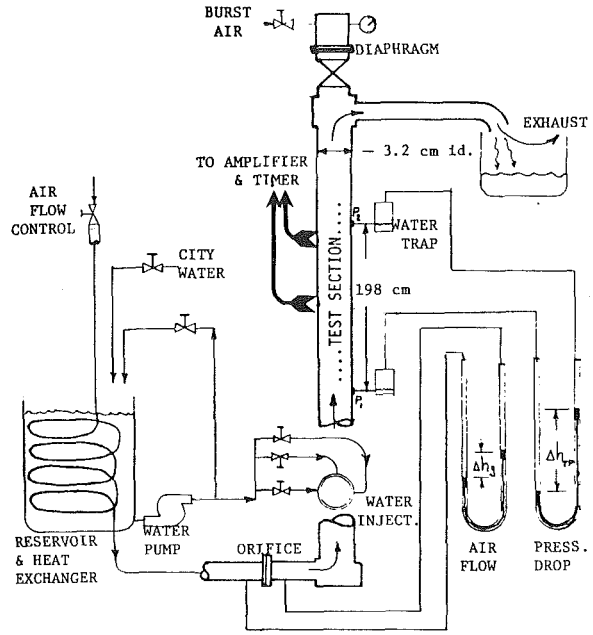

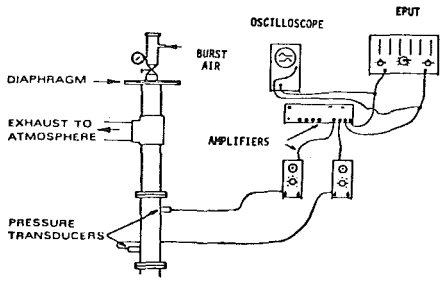

Fig. 2 Schematic of experimental system

Table 1 Experimental test conditions

SYSTEM TEMPERATURE	21 - 27 °C
SYSTEM PRESSURE	102 - 27 kPa
GAS VELOCITIES	12 - 21 m/sec
WATER FLOW RATES	0 - 34 kg/min

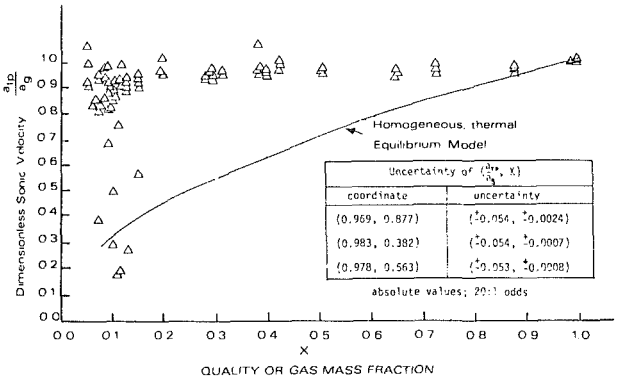

Fig. 3 Sonic velocity ratio data and homogeneous thermal equilibrium model versus quality

indicates that at this shock wave velocity (or at this rate-of-change of pressure) the energy transport processes are essentially negligible. In a two component system, the energy transport between the phases necessary to maintain thermal equilibrium would, for example, represent a substantial gas density change which would, in turn, predict a substantial reduction in sonic velocity as the quality was decreased. This is indicated by the results from the homogeneous, thermal equilibrium model (Fig. 3). These data also tend to support the concept and use of a separated flow model in that they show that the two-phase flow behavior, under these conditions, is primarily the behavior in the gas phase alone. Reference [1] compares the sonic velocity data with predictions from other reported expressions.

Pressure Drop Data

The complete pressure-drop data from the experimental program are shown in Fig. 4. Superficial gas velocities were used in the reduction of the data. The data, which are plotted nondimensionally as the ratio of two-phase drop in pressure to the gas only (superficial velocity) drop in pressure, show a surprising behavior of this ratio with respect to gas velocity.

One would expect that for a constant quality an increase in the gas velocity (gas mass flow rate increase) would produce a higher ratio of two phase to gas only drop in pressure due to an increased acceleration in the gas velocity and an additional increase in liquid (mass) flow rate. However the opposite is seen to occur. The authors believe that the most likely explanation is the effect of liquid-gas interfacial waves and, particularly of the formation of large disturbance waves which are on the annular liquid film next to the wall and travel at a velocity substantially higher than the mean velocity of the liquid in the wall film. Somewhat similar findings of pressure-drop behavior, which may be a result of the behavior of waves, have been reported in references [3, 4, and 5].

Note that the dimensionless pressure drop behavior does not appear to approach a value of 1.0 at quality of 1.0 for the case of the lowest gas velocity band. The reasons are not obvious from the data presented. The velocity range of 12–14 m/s is closely bordering on an unstable, pulsating type flow which makes pressure readings difficult. Further, at lower gas velocities the data are more sensitive to gas velocity changes and the chosen band of velocities was too wide to include in a single curve which would show an extrapolated $(\Delta p_{TP}/\Delta p_g)$ considerably greater than one. If curves for the 12–14 m/s band were to be drawn over the entire quality range there should be one curve through the data from $0.33 < x < 0.45$ (at the higher end of the gas-velocity band), another for $x \simeq 0.63$ (middle of the gas velocity band), and finally a curve for $x \simeq 0.88$ (at the lower end of the velocity band). These three curves would have similar slopes to the curves for the higher velocity bands shown.

Nomenclature

a_{TP}/a_g = the ratio of the two-phase sonic velocity to the sonic velocity computed in the gas alone

$\Delta p_{TP}/\Delta p_g$ = the ratio of the two-phase pressure-ratio over a measured distance in a constant area circular duct to the pressure-drop computed for the gas flowing alone

v_g = gas velocity

x = the quality or gas-mass-fraction of the flow in the two-phase mixture

ρ_g = gas density

A_{duct} = flow duct cross-sectional area

$\dot{m}_g$ = gas mass flow rate

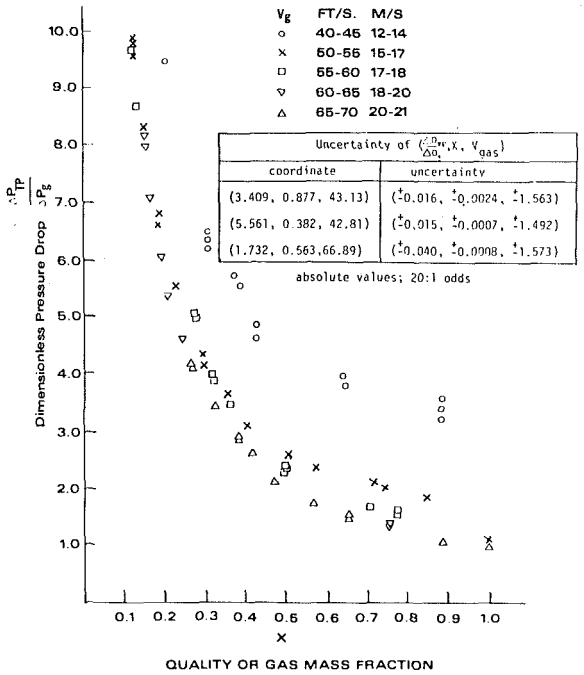

Fig. 4 Dimensionless pressure drop ratio versus quality (superficial gas velocity)

Conclusions

1 A flow pattern transition from annular to churn-froth is indicated by both the pressure-drop and sonic velocity data at essentially the same flow condition. This flow-pattern change is indicated by a marked rise in the pressure-drop data, neither of these experimental indications has been previously reported. The sonic velocity is a particularly sensitive indicator of this flow-pattern change.

2 The sonic velocity data show little or no change in value for the separated flow region from 100 percent quality down to the quality of the flow pattern transition. This indicates that the interface transport processes are essentially negligible in this region and at this rate of wave propagation or pressure change. These data also support the use of the separated flow model for this region. Previously reported data using "homogeneous" fluid velocities tend to show this behavior less sharply.

3 The pressure-drop data show a gas velocity effect which is different than the gas velocity effect one would predict from the use of expressions or models similar to that used for single-phase flow. This gas-velocity effect may be the result of the wave behavior on the liquid film.

Analysis of Uncertainty

The limited-sample uncertainty propagation methods of Kline and McClintock (reference [6]) were used with 20:1 odds. The results are tabulated on the appropriate figures. Possible fixed errors are included in the uncertainty bands given.

References

1 Smith, R. V., Martindale, W. R., and Lindsted, R. D., "Two-Phase Sonic Velocity Measurements for Separated Flow," ASME Paper No. 75-WA/HT-34.

2 Smith, R. V., and Leang, J. T., "Evaluations of Correlations for Two-Phase Flowmeters: Three Current-One New," ASME *Journal of Engineering for Power,* Oct. 1975.

3 Brown, D. J., Jensen, A., and Whalley, P. B., "Non-Equilibrium Effects in Heated and Unheated Annular Two-Phase Flow," ASME Paper No. 75-WA/HT-7.

4 Anderson, G. H., and Mantzouranis, B. B., "Two-Phase (Gas-Liquid) Flow Phenomena - I," *Journal of Chemical Engineering Science,* Vol. 12, 1960.

5 Chien, S. F., and Ibele, W., "Pressure Drop and Liquid Film Thickness of Two-Phase Annular and Annular-Mist Flows," ASME *Journal of Heat Transfer,* Feb. 1964.

6 Kline, S. J., and McClintock, F. A., "Describing Uncertainties in Single-Sample Experiments," *Mech. Engr.,* Vol. 75, Jan. 1953, p. 3.

Journal of Fluids Engineering

Discussion

Prediction of Incompressible Separated Boundary Layers Including Viscous-Inviscid Interaction[1]

H. MCDONALD[2] and W. R. BRILEY.[3] The authors have provided an interesting paper on this difficult flow problem. They have suggested an alternate calculation procedure worthy of consideration, and have also provided further evidence that the behavior of transitional separation bubbles, as commonly occur in practical applications, can be adequately predicted by numerical solution of the boundary layer equations, provided interaction with the free stream is accounted for. It is also gratifying to see that their results for the transitional separation bubble are in good agreement with our solutions (reference [2]) except in the region near transition-reattachment.

The authors twice questioned whether our time-dependent "interacted direct" approach (reference [2]) deals adequately with the "separation singularity," but did not elaborate. We observe that although there are differences in detail, the steady state flow model used by the authors is in essence the same as that we used in reference [2]. The critical feature of this flow model is that in the steady state, the boundary conditions satisfied are neither "direct" nor "inverse" but are "interacted" by means of an iterative solution-dependent "elliptic" correction to the pressure field. In the absence of interaction, the prevailing view (cf. reference [3]) is that solutions of the steady boundary layer equations are singular at separation if the boundary conditions are "direct," but nonsingular if they are "inverse." On this point, our numerical experience was consistent with the results of Klineberg and Steger (reference [28]) in that the singularity, although present in this uninteracted case, is apparently smoothed by low order streamwise truncation error. At the time our study was performed, no other results were available for guidance in the case of interaction, and although our results were not conclusive, it did appear to us that interaction removed the separation singularity. Our interacted boundary layer results were both qualitatively and quantitatively different from the uninteracted results, and we observed nothing resembling the singular behavior with mesh refinement found upstream of separation in numerous uninteracted direct forward marching solutions. For example, the slope of free stream transverse velocity $\partial v_e/\partial x$ at separation should become infinite with mesh refinement if a singularity is present. With interacted boundary conditions, although halving the mesh did cause a change of about 20 percent in this slope, this change is much less than the corresponding 130 percent increase observed without interaction. In turn, this latter increase is both greater than the associated change in mesh spacing and is also of the same order as the increases found by Pletcher and Dancy (reference [12]) in their uninteracted test case. Perhaps more significantly, we were able to show that our interacted boundary layer results were in very good agreement with a corresponding solution of the Navier-Stokes equations using the same grid.

Since the actual boundary condition satisfied by our interacted solutions is the elliptic displacement interaction equation rather than an imposed velocity or displacement thickness, in the steady state our solution procedure is not equivalent to forward marching solution of the steady boundary layer equations with direct boundary conditions. Prior to convergence, difficulty with the (steady) separation singularity is avoided by virtue of time dependence (and interaction). The authors seek the same objective by different means, and their solution procedure (cf. reference [8]) can be characterized as a "direct" iteration procedure (imposing velocity to find displacement thickness) for implementing "inverse" boundary conditions with the steady equations, with further iteration to find the particular set of velocity and displacement thickness distribution which satisfies the final interaction boundary condition. It therefore does not appear to us that the particular algorithm (whether characterized as direct, inverse, time-dependent or iterative) for obtaining numerical solutions of the steady boundary layer equations is relevant to the presence or absence of the separation singularity in the final solution when that solution satisfies interacted boundary conditions. Evidence of the separation singularity is historically limited to solution procedures which do not allow for the elliptic interaction process. In light of the observations given here, we believe that the evidence obtained following our initial study, which tends to confirm that the interacted solution is nonsingular (including that of Carter and Wornom, reference [6], and the present paper) also tends to verify that our reference [2] interacted solutions are nonsingular.

Although in reference [2] our primary interest was to determine if interacted boundary layers could represent an adequate flow model for thin separation bubbles, rather than to find an optimal solution procedure, we originally selected the time-dependent solution procedure in preference to iterated inverse forward marching for two reasons. These were that an adequate iteration procedure for inverse treatment of the displacement interaction was not available at that time, and that forward marching in the reverse flow region requires either further iteration for the streamwise convective term or the computational artifice embodied in variants of the FLARE approximation, such as used by the present authors (see reference [8]). Carter (reference [29]) has

[1] By O. K. Kwon and R. H. Pletcher, published in the December, 1979, issue of the JOURNAL OF FLUIDS ENGINEERING, Vol. 100, No. 4, pp. 460-472.

[2] President and Vice President, respectively, Scientific Research Associates, Inc., Glastonbury, Conn. 06033.

found the FLARE (Flugge-Lotz and Reyhner) approximation adequate for uninteracted laminar flow having small reverse flow velocities (5 percent of the free stream) although he encountered noticeable error in a case having reverse flow of about 10% of the free stream. In transitional-turbulent separation bubbles, the reattachment process is much more abrupt than in Carter's laminar test cases, and there is also experimental evidence of an intense vortex structure near reattachment (Gaster and Young and Horton, cf. reference [2]). Experimental fully turbulent boundary layer separation data (Simpson, reference [30]) also indicates reverse flow velocities greater than 10 percent of the free stream. In view of uncertainties deriving from the FLARE approximation, we preferred not to use it. In our own predictions of the Gault case, we encountered both an intense vortex near reattachment and reverse velocities of about 13 percent of the free stream. Recognizing that the flow near reattachment could be sensitive to details of the transition-turbulence models used, nonetheless we would question whether errors arising from the authors' neglect of negative velocities are significant and might possibly explain the qualitative differences between their solutions and ours, particularly with regard to the local flattening of the wall shear distribution near reattachment in their solution, which was not observed in either our Navier-Stokes or interacted boundary layer solutions.

In addition, the authors noted that when they reduced their mesh by 50 percent they observed a much smaller change in the computed solution than we observed, also with a 50 percent mesh reduction. This is not unexpected however, since their smallest mesh is ten times smaller than the one we used, and both methods have first order streamwise accuracy. Further mesh refinement was not possible in our reference [2] study due to limited computer resources, although our experience suggested that further mesh refinement would not have altered our conclusions.

Finally, the authors estimated that their method is about 10 to 20 times faster than that of reference [2] if the same grid is used, but did not elaborate. These factors are obviously well worthwhile, and the authors' iteration procedure for treating the interaction thus looks promising. Other factors are also present, however, and should be taken into account. Since our time-dependent approach does not require spatial forward marching during the solution process, it was not necessary to introduce either the FLARE approximation in the reverse flow region, or an *ad hoc* streamwise linearization procedure whereby nonlinear coefficients are lagged during forward marching to avoid iteration. Although the linearization error is formally of the same order as the first-order spatial differencing, this error is cumulative in the forward marching process and is not present in the time-dependent approach. Since their comparison of efficiency is based only on the same number of mesh points, it would be interesting to see how their solutions would compare with ours if the same much larger step size were used, since users tend to compute with the coarsest mesh possible, consistent with their accuracy requirements. Although removal of the FLARE and linearization errors might be accomplished simultaneously with the interaction iteration, this might affect convergence and/or convergence rate of the resulting method. Likewise, convergence acceleration techniques have become available since our 1974 study and may prove beneficial in the time-dependent approach (reference [31]), but these various developments will require further study.

Additional References

28 Klineberg, J. M., and J. L. Steger, "On Laminar Boundary Layer Separation," AIAA Paper 74-94, 1974.

29 Carter, J. E., "Inverse Solutions for Laminar Boundary Layer Flows With Separation and Reattachment," NASA-TR-R-447, 1975.

30 Simpson, R. L., "A Review of Some Phenomena in Turbulent Flow Separation," *Turbulent Boundary Layers*, ASME, 1979.

31 McDonald, H., and W. R. Briley, "Computational Fluid Dynamic Aspects of Internal Flows," AIAA Paper 79-1445, 1979.

Authors' Closure

The authors wish to thank the discussers for their interesting and thought provoking comments.

The authors and the discussers apparently disagree on the cause of the singularity in the boundary layer equations at separation. The authors base their observations primarily upon experiences obtained from solving the steady boundary layer equations by space marching techniques whereas the discussers appear to base their comments upon experiences (for separating flows) with the time dependent boundary layer equations. Both groups may be guilty of attempting to draw conclusions about the techniques used by the other by extrapolation. When space marching techniques are employed with the steady boundary layer equations, the preponderance of evidence in the literature [28, 32] suggests that the type of boundary conditions imposed are crucial. Because of the saddle point nature of the singularity, Klineberg and Steger [28] and Leal [32] found that they were unable to obtain a non-singular solution at separation by specifying the pressure gradient even when that pressure gradient corresponded to a completely regular flow field. This suggests that no matter how "interacted" the pressure gradient may be, if it is held fixed during any sweep of a space marching procedure for boundary layer equations, the solution becomes singular at separation. This occurs for numerical, not physical reasons as explained in [28]. It is possible that the time dependent method used by the discussers in [2] is exempt from this behavior, even as steady state is approached. To determine this, the discussers should continue to refine the stream-wise grid in their calculation [2] to establish that their solution is nonsingular.

The discussers point out that the actual boundary conditions satisfied by their solution in [2] was the elliptic displacement interaction equation. This was not clear to us from their paper since equation (2.9) of [2] specifically states that the velocity was fixed as a boundary condition for the boundary layer equations being adjusted *after* each time step according to the inviscid correction procedure. The discussers state that evidence of the separation point singularity is historically limited to solution procedures which do not allow for the elliptic interaction process. This might be because no one has successfully obtained a non-singular solution of the steady boundary layer equations with a fixed pressure gradient through a separated region upon which to base an interaction calculation. Several investigators have used the pressure distribution obtained by solutions to the Navier-Stokes equations [32] or by inverse solutions to boundary layer equations [28] as the boundary conditions for a direct steady boundary layer calculation only to find the solution singular upon careful examination.

Use of a *simultaneous* interaction equation has been observed to remove the singularity [12] for a direct method. The authors are aware of no clear computational evidence that the use of viscous-inviscid interaction alone removes the singularity in a direct finite difference steady boundary layer calculation scheme so long as the pressure gradient is held fixed during each streamwise pass. As mentioned above, the discussers' time-dependent scheme [2] may not display this behavior but there is no computational evidence available to resolve this question.

The estimate that our method was 10-20 times faster than the method of [2] was based on the observation that the method of [2] required about 300 time steps for convergence to a steady state solution whereas our method required less than 20 iterations for convergence for the Gault case. Our grid refinement test (Fig. 9) indicated that our mesh was sufficiently refined for the Gault case but we have no indication as to how much coarser the mesh might be made before serious deterioration in accuracy is observed. Our guess is that the mesh used by the discussers in [2] for the Gault case would be too coarse to provide converged (mesh-size independent) solutions by our method, but the results shown in Fig. 8 of [2] suggest that this same mesh was also too coarse for the method used by the discussers. Here again, further calculations are needed in order to resolve this question.

The FLARE treatment of the streamwise derivative and the linearizing of the equations by lagging the coefficients were approximations which we felt were justified for the flows considered in the present paper. On the other hand, it is believed that these approximations are not essential for the successful and efficient calculation of separation bubbles by an inverse boundary layer-viscous-inviscid interaction procedure. Clearly, the work of Carter [6] and Cebeci [33] indicates that the form of linearization used is not crucial to the success of inverse boundary layer procedures and the work of Cebeci et al. [34] and Arieli and Murphy [35] supports the view that the FLARE approximation might be eliminated from the final few iterations by the use of type-dependent differencing of the streamwise derivative term. It is estimated that such refinements would increase the required computer time by about a factor of two and increase the storage requirements by about 25–30 percent.

The steepness of the wall shear stress distribution near reattachment seems to depend strongly on the transition model used. From Fig. 9 it can be seen that Model A of the present paper gives a distribution flatter than shown [2] whereas Model B gives one which is steeper.

Additional References

32 Leal, L. G., "Steady Separated Flow in a Linearly Decelerated Free Stream," *Journal of Fluid Mechanics*, Vol. 59, Part 3, 1979, pp. 513-535.

33 Cebeci, T., "Separated Flows and Their Representation by Boundary Layer Equations," Report ONR-CR215-234-2, Sept. 1976, Office of Naval Research, Arlington, Va.

34 Cebeci, T., Keller, H. B., and Williams, P. G., "Separating Boundary Layer Flow Calculations," *Journal of Computational Physics*, Vol. 31, 1979, pp. 363-378.

35 Arieli, R., and Murphy, J. D., "Pseudo-Direct Solutions to the Boundary-Layer Equations for Separated Flow," AIAA Paper No. 79-0139, 1979.

Predictions of Induced Air Flows in Hollow Cone Sprays[1]

J. H. STUHMILLER.[2] This paper contributes to the timely study of spray-environment interactions that are so important to combustion, drying, and cooling processes. The qualitative behavior of the smoke tracer in Fig. 1 to the calculated flow patterns in Figs. 5 and 6 is encouraging and the universal nature of the streamfunction contours, when properly normalized, will assist in understanding fuel entrainment. My discussion is directed toward the solution techniques employed.

The gas flow is formulated as a steady-state problem, while the spray droplets are followed individually and in time. It would seem that the convergence to a total steady-state solution would depend upon the number density of drops being followed – only when there are many particles per cell will the fluctuations in time due to cell boundary crossings be small. Would the authors comment on the number of particles followed, number per cell, and the observed effects on reaching steady-state?

The outer edge boundary condition imposed, that both velocity components go to zero as the reciprocal of a power of the radial distance, is an intriguing one. It seems analogous to the radiation boundary conditions used in wave motion calculations. There the radiated flux is estimated from interior points and used to assign boundary values that will preserve the flux. Such a treatment is valid anywhere outside of the region of source generation. The condition applied to the spray flow, however, is only asymptotically true as $R \to \infty$. Would the authors comment on how the size of the computational region influenced the flow, especially in the neighborhood of the outer boundary? Also, what was the variation in the power n, in particular, did n approach 2 on the axis? The problem of simulating an unbounded jet in a finite computational domain occurs in many applications and a good simulated boundary condition would be welcome.

Finally, I would like to call attention to similar research into boiling water reactor cooling sprays being conducted in the Fluid Dynamics Group at JAYCOR for the Electric Power Research Institute. The approach taken is similar, particle differential equations for the gas and ordinary differential for the drops with appropriate interphase coupling, but differs in that it is time-dependent including the affects of compressibility, heat and mass transfer, gravity, and gas pressure gradient forces. The goal is to understand spray collapse in steam environments and the results, including an analysis of the internal and early sheet flow are discussed in a report to be released by EPRI.

Authors' Closure

The authors thank Dr. Stuhmiller for his interest in their paper. When turbulent diffusion is neglected it can be expected that all drops of the same size follow a common trajectory. Therefore, one set of equations (2), (3), (4), and (5) is solved for each size group at the end of a calculation loop. It is true that the fluctuations in time, or in the present case from one loop to the next of the looping iterative solution procedure, due to cell boundary crossings may affect convergence if the particle number density is small. In the present problem, however, the lower limit of the number of particles per cell was on the order of 10^5 and no effect of the fluctuations on this quantity on the rate of convergence was detected.

The outer edge boundary condition employed was inspired by the existence of an exact solution of the Navier-Stokes equations in spherical co-ordinates corresponding to the axially symmetric jet and where the streamfunction is proportional to the distance from the origin [1]. The present form of ψ variation at large R was chosen to make the boundary condition less rigid to suit the present problem. The value of the index is on the axis for $R_{max} = 100$ cms was around 0.9 for most cases. Since the flow inside the spray

[1] By F. Boysan and H. Binark, published in the Sept. 1979 issue of the ASME JOURNAL OF FLUIDS ENGINEERING, Vol. 101, pp. 312-318.

[2] Group Leader - Fluid Dynamics Group, JAYCOR, Del Mar, Calif. 92014.

The estimate that our method was 10-20 times faster than the method of [2] was based on the observation that the method of [2] required about 300 time steps for convergence to a steady state solution whereas our method required less than 20 iterations for convergence for the Gault case. Our grid refinement test (Fig. 9) indicated that our mesh was sufficiently refined for the Gault case but we have no indication as to how much coarser the mesh might be made before serious deterioration in accuracy is observed. Our guess is that the mesh used by the discussers in [2] for the Gault case would be too coarse to provide converged (mesh-size independent) solutions by our method, but the results shown in Fig. 8 of [2] suggest that this same mesh was also too coarse for the method used by the discussers. Here again, further calculations are needed in order to resolve this question.

The FLARE treatment of the streamwise derivative and the linearizing of the equations by lagging the coefficients were approximations which we felt were justified for the flows considered in the present paper. On the other hand, it is believed that these approximations are not essential for the successful and efficient calculation of separation bubbles by an inverse boundary layer-viscous-inviscid interaction procedure. Clearly, the work of Carter [6] and Cebeci [33] indicates that the form of linearization used is not crucial to the success of inverse boundary layer procedures and the work of Cebeci et al. [34] and Arieli and Murphy [35] supports the view that the FLARE approximation might be eliminated from the final few iterations by the use of type-dependent differencing of the streamwise derivative term. It is estimated that such refinements would increase the required computer time by about a factor of two and increase the storage requirements by about 25–30 percent.

The steepness of the wall shear stress distribution near reattachment seems to depend strongly on the transition model used. From Fig. 9 it can be seen that Model A of the present paper gives a distribution flatter than shown [2] whereas Model B gives one which is steeper.

Additional References

32 Leal, L. G., "Steady Separated Flow in a Linearly Decelerated Free Stream," *Journal of Fluid Mechanics*, Vol. 59, Part 3, 1979, pp. 513-535.

33 Cebeci, T., "Separated Flows and Their Representation by Boundary Layer Equations," Report ONR-CR215-234-2, Sept. 1976, Office of Naval Research, Arlington, Va.

34 Cebeci, T., Keller, H. B., and Williams, P. G., "Separating Boundary Layer Flow Calculations," *Journal of Computational Physics*, Vol. 31, 1979, pp. 363-378.

35 Arieli, R., and Murphy, J. D., "Pseudo-Direct Solutions to the Boundary-Layer Equations for Separated Flow," AIAA Paper No. 79-0139, 1979.

Predictions of Induced Air Flows in Hollow Cone Sprays[1]

J. H. STUHMILLER.[2] This paper contributes to the timely study of spray-environment interactions that are so important to combustion, drying, and cooling processes. The qualitative behavior of the smoke tracer in Fig. 1 to the calculated flow patterns in Figs. 5 and 6 is encouraging and the universal nature of the streamfunction contours, when properly normalized, will assist in understanding fuel entrainment. My discussion is directed toward the solution techniques employed.

The gas flow is formulated as a steady-state problem, while the spray droplets are followed individually and in time. It would seem that the convergence to a total steady-state solution would depend upon the number density of drops being followed – only when there are many particles per cell will the fluctuations in time due to cell boundary crossings be small. Would the authors comment on the number of particles followed, number per cell, and the observed effects on reaching steady-state?

The outer edge boundary condition imposed, that both velocity components go to zero as the reciprocal of a power of the radial distance, is an intriguing one. It seems analogous to the radiation boundary conditions used in wave motion calculations. There the radiated flux is estimated from interior points and used to assign boundary values that will preserve the flux. Such a treatment is valid anywhere outside of the region of source generation. The condition applied to the spray flow, however, is only asymptotically true as $R \to \infty$. Would the authors comment on how the size of the computational region influenced the flow, especially in the neighborhood of the outer boundary? Also, what was the variation in the power n, in particular, did n approach 2 on the axis? The problem of simulating an unbounded jet in a finite computational domain occurs in many applications and a good simulated boundary condition would be welcome.

Finally, I would like to call attention to similar research into boiling water reactor cooling sprays being conducted in the Fluid Dynamics Group at JAYCOR for the Electric Power Research Institute. The approach taken is similar, particle differential equations for the gas and ordinary differential for the drops with appropriate interphase coupling, but differs in that it is time-dependent including the affects of compressibility, heat and mass transfer, gravity, and gas pressure gradient forces. The goal is to understand spray collapse in steam environments and the results, including an analysis of the internal and early sheet flow are discussed in a report to be released by EPRI.

Authors' Closure

The authors thank Dr. Stuhmiller for his interest in their paper. When turbulent diffusion is neglected it can be expected that all drops of the same size follow a common trajectory. Therefore, one set of equations (2), (3), (4), and (5) is solved for each size group at the end of a calculation loop. It is true that the fluctuations in time, or in the present case from one loop to the next of the looping iterative solution procedure, due to cell boundary crossings may affect convergence if the particle number density is small. In the present problem, however, the lower limit of the number of particles per cell was on the order of 10^5 and no effect of the fluctuations on this quantity on the rate of convergence was detected.

The outer edge boundary condition employed was inspired by the existence of an exact solution of the Navier-Stokes equations in spherical co-ordinates corresponding to the axially symmetric jet and where the streamfunction is proportional to the distance from the origin [1]. The present form of ψ variation at large R was chosen to make the boundary condition less rigid to suit the present problem. The value of the index is on the axis for $R_{max} = 100$ cms was around 0.9 for most cases. Since the flow inside the spray

[1] By F. Boysan and H. Binark, published in the Sept. 1979 issue of the ASME JOURNAL OF FLUIDS ENGINEERING, Vol. 101, pp. 312-318.

[2] Group Leader - Fluid Dynamics Group, JAYCOR, Del Mar, Calif. 92014.

cone has a dominant direction the outflow boundary condition has little influence downstream. In fact it was found later that putting $n = 1$ does not affect the air flow pattern in and around the spray to a significant degree [2].

Additional References

1 Squire, H. B., *Quart. J. Mech. App. Math.*, Vol. IV, 3-321, 1951.

2 Boysan, F., "Hollow Cone Spray-Air Interaction with and without Evaporation," 2nd Multi-phase Flow and Heat Transfer Symposium, Miami, Apr. 1979.

A Calculation Procedure for Three-Dimensional Viscous, Compressible Duct Flows, Parts I and II[1]

P. M. SOCKOL.[2] I wish to congratulate the authors on what I believe to be a very sensible approach to a very difficult but practical problem. There is now a growing body of evidence which indicates that the pressure field provides the dominant elliptic influence in a wide variety of rotational and viscous flows. In addition to the present work and that of references [I-3] and [I-4], I would like to note two other relevant works. In reference [C-1] the results of a number of parabolized approaches are compared with solutions of the full Navier-Stokes equations for the same two-dimensional problems. These results show that even for separated cases parabolized treatments of the vorticity equation can produce excellent solutions provided that the stream function equation is solved elliptically. In reference [C-2] a general solution is presented for the case of a small rotational perturbation on an arbitrary potential flow. There it is shown that the rotational part of the flow is reducible to quadrature along the streamlines of the base flow, while the perturbed pressure is obtained from a potential, which in turn satisfies an elliptic equation in subsonic flow. Thus, there is good reason to expect good results from parabolized or marching procedures if the pressure is given suitable elliptic treatment.

Before the present procedure is endorsed for general use, however, a couple of points need to be clarified. The comparison between calculated and measured results for the Stanitz elbow is quite impressive, but for this flow the effect of downstream influence does not appear to be significant. Hence, the fully parabolic approaches of references [1–9] and [C-3] might do just as well and be more efficient. A more definitive test case would be a turbomachinery blade row with significant loading of the leading or trailing edge. The second point relates to the three-dimensional pressure correction equation. The numerical technique used for this equation is not adequately described and hence it is difficult to judge how efficiently elliptic effects are spread throughout the domain in cases where they are indeed significant.

Additional References

C-1 Ghia, K. N., Ghia, U., and Tesch, W. A., "Evaluation of Several Approximate Models for Laminar Incompressible Separation by Comparison with Complete Navier-Stokes Solutions," AGARD CP-168 on Flow Separation, May 1975.

C-2 Goldstein, M. E., "Unsteady Vortical and Entropic Distortions of Potential Flows Round Arbitrary Obstacles," *Journal of Fluid Mechanics*, Vol. 89, Part 3, pp. 433-468.

C-3 Briley, W. R., and McDonald, H., "Analysis and Computation of Viscous Subsonic Primary and Secondary Flows," AIAA Paper No. 79-1453, presented at Williamsburg, Va., July 1979.

Author's Closure

The authors wish to thank Dr. Sockol for his thoughtful comments and offer the following discussion in reply.

At any point in Stanitz' duct the elliptic contribution to the local cross-stream pressure gradient *is* small compared with the pressure gradient consistent with the local radius of curvature. This is because Stanitz designed his duct with a gradual increase and a gradual decrease in the radius of curvature. Thus in a sense one could say that the flow in Stanitz duct is nearly parabolic and at least the two dimensional, inviscid, incompressible flow could be calculated fairly well by assuming for each step that the radius of curvature remains constant in a streamwise direction. This is not however what the fully parabolic approach in reference I-9 does; Patankar's fully parabolic approach is like the marching integration part of our duct-flow calculation procedure using a uniform estimated pressure. Fig. A shows that, for a fully parabolic flow calculation, the pressure difference across the duct, as used in the cross-flow momentum equation, is close to the partially-parabolic flow solution. However, because the pressure corrections are separated, the pressure difference across the duct used in the thru-flow momentum equation is zero. Thus the calculated velocity is uniform over each cross section - a poor approximation at the middle of the bend where the velocity actually varies by a factor of two.

If the flow is truly parabolic, with no pressure influences transmitted upstream, then there is no need to use separated pressure corrections. Fig. A shows that a marching

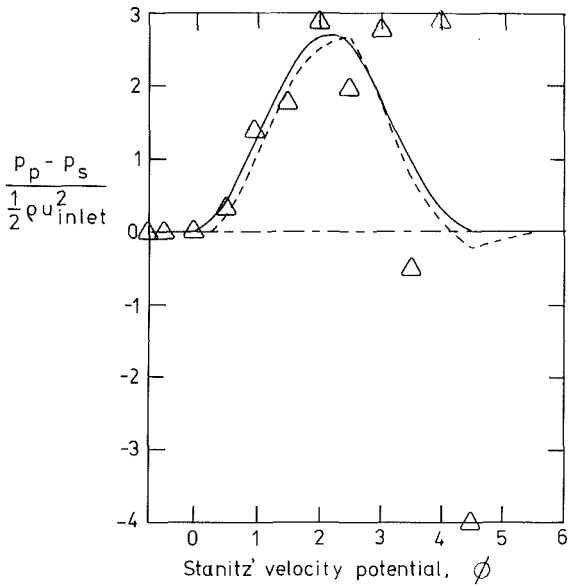

Fig. A The static pressure difference across Stanitz' duct for two dimensional, inviscid, incompressible flow calculated using 13 steps.
___ final solution from partially-parabolic calculation;
– – – – used in u_1 momentum in fully parabolic calculation with separated pressure corrections;
----- used in u_2 momentum in fully parabolic calculation with separated pressure corrections;
Δ parabolic solution using *un*separated pressure correction.

[1] By John Moore and Joan G. Moore, published in the December, 1979, issue of the ASME JOURNAL OF FLUIDS ENGINEERING, Vol. 100, No. 4, pp. 415-428.

[2] Research Engineer, Computational Fluid Mechanics Branch, NASA Lewis Research Center, Cleveland, Ohio.

cone has a dominant direction the outflow boundary condition has little influence downstream. In fact it was found later that putting $n = 1$ does not affect the air flow pattern in and around the spray to a significant degree [2].

Additional References

1 Squire, H. B., *Quart. J. Mech. App. Math.*, Vol. IV, 3-321, 1951.

2 Boysan, F., "Hollow Cone Spray-Air Interaction with and without Evaporation," 2nd Multi-phase Flow and Heat Transfer Symposium, Miami, Apr. 1979.

A Calculation Procedure for Three-Dimensional Viscous, Compressible Duct Flows, Parts I and II[1]

P. M. SOCKOL.[2] I wish to congratulate the authors on what I believe to be a very sensible approach to a very difficult but practical problem. There is now a growing body of evidence which indicates that the pressure field provides the dominant elliptic influence in a wide variety of rotational and viscous flows. In addition to the present work and that of references [I-3] and [I-4], I would like to note two other relevant works. In reference [C-1] the results of a number of parabolized approaches are compared with solutions of the full Navier-Stokes equations for the same two-dimensional problems. These results show that even for separated cases parabolized treatments of the vorticity equation can produce excellent solutions provided that the stream function equation is solved elliptically. In reference [C-2] a general solution is presented for the case of a small rotational perturbation on an arbitrary potential flow. There it is shown that the rotational part of the flow is reducible to quadrature along the streamlines of the base flow, while the perturbed pressure is obtained from a potential, which in turn satisfies an elliptic equation in subsonic flow. Thus, there is good reason to expect good results from parabolized or marching procedures if the pressure is given suitable elliptic treatment.

Before the present procedure is endorsed for general use, however, a couple of points need to be clarified. The comparison between calculated and measured results for the Stanitz elbow is quite impressive, but for this flow the effect of downstream influence does not appear to be significant. Hence, the fully parabolic approaches of references [1–9] and [C-3] might do just as well and be more efficient. A more definitive test case would be a turbomachinery blade row with significant loading of the leading or trailing edge. The second point relates to the three-dimensional pressure correction equation. The numerical technique used for this equation is not adequately described and hence it is difficult to judge how efficiently elliptic effects are spread throughout the domain in cases where they are indeed significant.

Additional References

C-1 Ghia, K. N., Ghia, U., and Tesch, W. A., "Evaluation of Several Approximate Models for Laminar Incompressible Separation by Comparison with Complete Navier-Stokes Solutions," AGARD CP-168 on Flow Separation, May 1975.

C-2 Goldstein, M. E., "Unsteady Vortical and Entropic Distortions of Potential Flows Round Arbitrary Obstacles," *Journal of Fluid Mechanics*, Vol. 89, Part 3, pp. 433-468.

C-3 Briley, W. R., and McDonald, H., "Analysis and Computation of Viscous Subsonic Primary and Secondary Flows," AIAA Paper No. 79-1453, presented at Williamsburg, Va., July 1979.

Author's Closure

The authors wish to thank Dr. Sockol for his thoughtful comments and offer the following discussion in reply.

At any point in Stanitz' duct the elliptic contribution to the local cross-stream pressure gradient *is* small compared with the pressure gradient consistent with the local radius of curvature. This is because Stanitz designed his duct with a gradual increase and a gradual decrease in the radius of curvature. Thus in a sense one could say that the flow in Stanitz duct is nearly parabolic and at least the two dimensional, inviscid, incompressible flow could be calculated fairly well by assuming for each step that the radius of curvature remains constant in a streamwise direction. This is not however what the fully parabolic approach in reference I-9 does; Patankar's fully parabolic approach is like the marching integration part of our duct-flow calculation procedure using a uniform estimated pressure. Fig. A shows that, for a fully parabolic flow calculation, the pressure difference across the duct, as used in the cross-flow momentum equation, is close to the partially-parabolic flow solution. However, because the pressure corrections are separated, the pressure difference across the duct used in the thru-flow momentum equation is zero. Thus the calculated velocity is uniform over each cross section - a poor approximation at the middle of the bend where the velocity actually varies by a factor of two.

If the flow is truly parabolic, with no pressure influences transmitted upstream, then there is no need to use separated pressure corrections. Fig. A shows that a marching

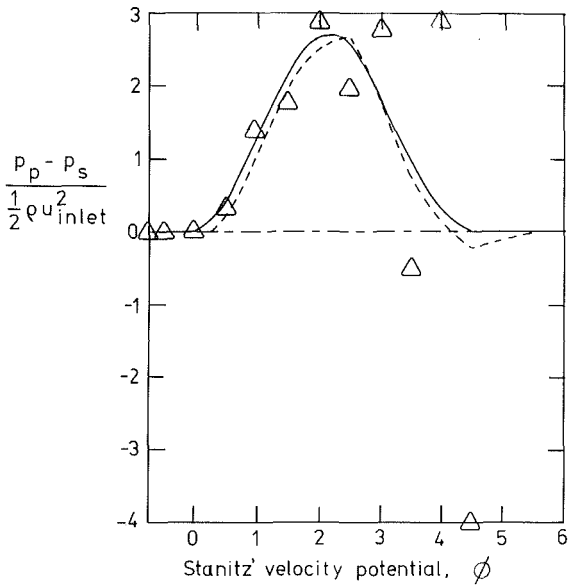

Fig. A The static pressure difference across Stanitz' duct for two dimensional, inviscid, incompressible flow calculated using 13 steps.
___ final solution from partially-parabolic calculation;
– – – – used in u_1 momentum in fully parabolic calculation with separated pressure corrections;
----- used in u_2 momentum in fully parabolic calculation with separated pressure corrections;
Δ parabolic solution using *un*separated pressure correction.

[1] By John Moore and Joan G. Moore, published in the December, 1979, issue of the ASME JOURNAL OF FLUIDS ENGINEERING, Vol. 100, No. 4, pp. 415-428.

[2] Research Engineer, Computational Fluid Mechanics Branch, NASA Lewis Research Center, Cleveland, Ohio.

calculation using an unseparated pressure correction works well over the first few steps. However a growing pressure oscillation occurs at the exit of the bend.

Our duct-flow calculation procedure introduces cross-stream pressure variations into the thru-flow momentum equation only after they have been calculated using the 3-D pressure-correction equation. The point-by-point relaxation procedure used to solve this equation allows elliptic influences to be transmitted throughout the entire flow domain each time the 3-D pressure-correction equation is solved.

An Experimental Study of the Flow-Induced Motions of a Flexible Cylinder in Axial Flow[1]

M. P. PAIDOUSSIS.[2] Although the subject of flow-induced motions of flexible cylinders is axial flow has received considerable theoretical attention, there have been very few experimental studies. Consequently, this study should be applauded both for providing added experimental information and for dealing with a particular application of considerable practical interest.

Concerning comparison between experiment and theory from the point of view of stability, it must be said that the applicability of Païdoussis' theory [1, 2] to these particular experiments is questionable. The reason for this, as the authors suspect, is due to the much higher values of L/D in these experiments, as compared to previous experiments where L/D was much smaller. Here the dynamics of the system are critically dependent on the frictional forces. Therefore, such assumptions as that of a constant value for frictional coefficients over the whole length of the body, which proved to be reasonable for shorter bodies, should be examined carefully. So should the forces at the free end. (It is recalled that in the theory the effect of the shape of the free end was accounted for by a factor f, which is the ratio of the actual lift force on the tapered end to the ideal lift that might arise if three-dimensional flow effects and separation were absent.) It is nevertheless interesting to note that Païdoussis' theory [1, 2] predicts that buckling (divergence) does *not* take place for a cantilevered cylinder with a hemispherical end ($f \leqq 0.5$), if $L/D > 40$. Hence, theory predicts no divergence for the L/D involved in the experiments. This is contrary to the statement made by the authors, that the theory predicts divergence in the range of dimensionless flow velocities $1 < u < 10$; that statement is only true when applied to considerably smaller L/D than were used in Ni & Hansen's experiments.

Moreover, the situation is complicated by the fact that the aforementioned theory neglects the effect of the boundary layer, which for such lengths as those in the experiments must have been quite thick. It was recently shown [3] that the boundary layer has "an insulating effect" on the cylinder and an important stabilizing effect. In other words, when boundary layer effects are considered, divergence is even less likely to develop. In this light, the discusser wonders if the static divergence observed at $u \simeq 30$ for the Tygon tube was real or not, (i) in view of the considerable difficulty that must have been encountered in keeping these long bodies exactly neutrally buoyant and (ii) in view of the tendency of small irregularities, locked-in stresses, and non-uniformities to become exaggerated with increasing flow, as the mean flow tends to counteract the flexural restoring forces. Interestingly, similar experiments by the authors, with a propylene cable, showed no divergence [4], exactly as predicted by theory.

It should be said that the above concern but a small part of the paper and do not distract from its overall value.

Additional References

1 Païdoussis, M. P., "Dynamics of Flexible Cylinders in Axial Flow. Part 1: Theory," *J. Fluid Mechanics,* Vol. 26, 1966, pp. 717-736.

2 Paidoussis, M. P., "Dynamics of Cylindrical Structures Subjected to Axial Flow," *J. Sound and Vibration,* Vol. 29, 1973, pp. 365-385.

3 Hannoyer, M. J., and Païdoussis, M. P., "Instabilities of Tubular Beams Simultaneously Subjected to Internal and External Axial Flows," ASME *Journal of Mechanical Design,* Vol. 100, 1978, pp. 328-336.

4 Hansen, R. J., and Ni, C. C., "An Experimental Study of Flow-Induced Motions of Flexible Cables and Cylinders Aligned With the Flow Direction," ASME Paper 76-WA/FE-15.

Authors' Closure

The authors wish to thank Professor Paidoussis for his observations on their recently reported experimental study of flow-induced motions of a flexible cylinder in axial flow. As he points out, complicating factors such as a cylinder length-to-diameter ratio (L/D) much greater than 40 and a thick boundary layer distinguish his pioneering analytical studies [1, 2] from the present experimental work. Clearly, additional theoretical study is required of the fluid-structure interaction phenomena which prevail in the circumstances considered in the present experiments.

The authors do wish to emphasize that the observed "static divergence" near the downsteam extremity of the flexible cylinder appeared to be a real flow-induced deformation phenomenon and not the result of irregularities or nonuniformities in the test cylinder. The phenomenon was repeatable; the cylinder was neutrally buoyant to an excellent approximation; and permanent set in the tube wall was removed by repeatedly filling it with hot water.

Analytic Derivation of Static Pressure Distribution in Helical Flows[1]

EDWARD SILBERMAN.[2] One of the writer's students has made measurements of turbulence components in a helical flow. The writer has examined their influence on calculated radial pressure distribution using the method described by Kuzay. Data and calculated results are presented in Table 1. The data were obtained in a nominal 1 ft diameter helical corrugated pipe with air flowing. The helix made an angle of 59½ deg with the pipe axis (where 90 deg would be ordinary corrugated pipe). Turbulence measured with a split hot film anemometer was used to examine its effect on Kuzay's

[1] By C. C. Ni and R. J. Hensen, published in the December, 1978 issue of the JOURNAL OF FLUIDS ENGINEERING, Vol. 100, No. 4, pp. 389-394.

[2] Professor and Chairman, Department of Mechanical Engineering, McGill University, Montreal, Canada.

[1] By T. M. Kuzay, published in the June, 1978 issue of the JOURNAL OF FLUIDS ENGINEERING, Vol. 99, No. 2, p. 1.

[2] Professor, St. Anthony Falls Hydraulic Laboratory, University of Minnesota, Minneapolis, Minnesota.

calculation using an unseparated pressure correction works well over the first few steps. However a growing pressure oscillation occurs at the exit of the bend.

Our duct-flow calculation procedure introduces cross-stream pressure variations into the thru-flow momentum equation only after they have been calculated using the 3-D pressure-correction equation. The point-by-point relaxation procedure used to solve this equation allows elliptic influences to be transmitted throughout the entire flow domain each time the 3-D pressure-correction equation is solved.

An Experimental Study of the Flow-Induced Motions of a Flexible Cylinder in Axial Flow[1]

M. P. PAIDOUSSIS.[2] Although the subject of flow-induced motions of flexible cylinders is axial flow has received considerable theoretical attention, there have been very few experimental studies. Consequently, this study should be applauded both for providing added experimental information and for dealing with a particular application of considerable practical interest.

Concerning comparison between experiment and theory from the point of view of stability, it must be said that the applicability of Païdoussis' theory [1, 2] to these particular experiments is questionable. The reason for this, as the authors suspect, is due to the much higher values of L/D in these experiments, as compared to previous experiments where L/D was much smaller. Here the dynamics of the system are critically dependent on the frictional forces. Therefore, such assumptions as that of a constant value for frictional coefficients over the whole length of the body, which proved to be reasonable for shorter bodies, should be examined carefully. So should the forces at the free end. (It is recalled that in the theory the effect of the shape of the free end was accounted for by a factor f, which is the ratio of the actual lift force on the tapered end to the ideal lift that might arise if three-dimensional flow effects and separation were absent.) It is nevertheless interesting to note that Païdoussis' theory [1, 2] predicts that buckling (divergence) does *not* take place for a cantilevered cylinder with a hemispherical end ($f \leqq 0.5$), if $L/D > 40$. Hence, theory predicts no divergence for the L/D involved in the experiments. This is contrary to the statement made by the authors, that the theory predicts divergence in the range of dimensionless flow velocities $1 < u < 10$; that statement is only true when applied to considerably smaller L/D than were used in Ni & Hansen's experiments.

Moreover, the situation is complicated by the fact that the aforementioned theory neglects the effect of the boundary layer, which for such lengths as those in the experiments must have been quite thick. It was recently shown [3] that the boundary layer has "an insulating effect" on the cylinder and an important stabilizing effect. In other words, when boundary layer effects are considered, divergence is even less likely to develop. In this light, the discusser wonders if the static divergence observed at $u \simeq 30$ for the Tygon tube was real or not, (i) in view of the considerable difficulty that must have been encountered in keeping these long bodies exactly neutrally buoyant and (ii) in view of the tendency of small irregularities, locked-in stresses, and non-uniformities to become exaggerated with increasing flow, as the mean flow tends to counteract the flexural restoring forces. Interestingly, similar experiments by the authors, with a propylene cable, showed no divergence [4], exactly as predicted by theory.

It should be said that the above concern but a small part of the paper and do not distract from its overall value.

Additional References

1 Païdoussis, M. P., "Dynamics of Flexible Cylinders in Axial Flow. Part 1: Theory," *J. Fluid Mechanics,* Vol. 26, 1966, pp. 717-736.

2 Paidoussis, M. P., "Dynamics of Cylindrical Structures Subjected to Axial Flow," *J. Sound and Vibration,* Vol. 29, 1973, pp. 365-385.

3 Hannoyer, M. J., and Païdoussis, M. P., "Instabilities of Tubular Beams Simultaneously Subjected to Internal and External Axial Flows," ASME *Journal of Mechanical Design,* Vol. 100, 1978, pp. 328-336.

4 Hansen, R. J., and Ni, C. C., "An Experimental Study of Flow-Induced Motions of Flexible Cables and Cylinders Aligned With the Flow Direction," ASME Paper 76-WA/FE-15.

Authors' Closure

The authors wish to thank Professor Paidoussis for his observations on their recently reported experimental study of flow-induced motions of a flexible cylinder in axial flow. As he points out, complicating factors such as a cylinder length-to-diameter ratio (L/D) much greater than 40 and a thick boundary layer distinguish his pioneering analytical studies [1, 2] from the present experimental work. Clearly, additional theoretical study is required of the fluid-structure interaction phenomena which prevail in the circumstances considered in the present experiments.

The authors do wish to emphasize that the observed "static divergence" near the downsteam extremity of the flexible cylinder appeared to be a real flow-induced deformation phenomenon and not the result of irregularities or nonuniformities in the test cylinder. The phenomenon was repeatable; the cylinder was neutrally buoyant to an excellent approximation; and permanent set in the tube wall was removed by repeatedly filling it with hot water.

Analytic Derivation of Static Pressure Distribution in Helical Flows[1]

EDWARD SILBERMAN.[2] One of the writer's students has made measurements of turbulence components in a helical flow. The writer has examined their influence on calculated radial pressure distribution using the method described by Kuzay. Data and calculated results are presented in Table 1. The data were obtained in a nominal 1 ft diameter helical corrugated pipe with air flowing. The helix made an angle of 59½ deg with the pipe axis (where 90 deg would be ordinary corrugated pipe). Turbulence measured with a split hot film anemometer was used to examine its effect on Kuzay's

[1] By C. C. Ni and R. J. Hensen, published in the December, 1978 issue of the JOURNAL OF FLUIDS ENGINEERING, Vol. 100, No. 4, pp. 389-394.

[2] Professor and Chairman, Department of Mechanical Engineering, McGill University, Montreal, Canada.

[1] By T. M. Kuzay, published in the June, 1978 issue of the JOURNAL OF FLUIDS ENGINEERING, Vol. 99, No. 2, p. 1.

[2] Professor, St. Anthony Falls Hydraulic Laboratory, University of Minnesota, Minneapolis, Minnesota.

Inverse Design of Optimal Diffusers With Experimental Corroboration

T. YANG.[2] I am curious about the results of optimum design provided by the method proposed in this paper as compared to the experimental results listed in the Diffuser Data Book published by Creare Inc.[3] As specific examples, I have considered the cases of blockage parameter of $B = 0.1$ and $B = 0.02$. Two approximations (*a*) $B' \cong B$ and (*b*) $AS = 5 \cong \infty$ were made to avoid interpolating and extrapolating the curves provided by the data book, and one assumption was made that a boundary layer profile of 1/7th power law exists at the inlet of the diffuser. This assumption provides a value of the ratio of the displacement thickness to momentum thickness of 1.285. Now $\mathrm{Re}_D = 214000$ of the data book corresponds to $\mathrm{Re}_{\theta i} = 4533$ for $B = 0.1$ and $\mathrm{Re}_{\theta i} = 1000$ for $B = 0.02$. From Fig. A-1, we find the results correspond to $AR = 2.2$ and $L/W = 3.5$ and Fig. A-2 $AR = 3.25$ and $L/W = 7.6$. The detailed computations for these numbers are given in the Addendum. These two sets of geometrical parameters are apparently much too conservative in projecting the potential pressure recovery. Perhaps the author should elaborate on this comparison.

A second question is one of stability. The diffuser is designed to have $c_f = 0$ at the exit for a given set of inlet conditions. Would the flow in this diffuser separate if there is a disturbance to thicken the inlet boundary layer?

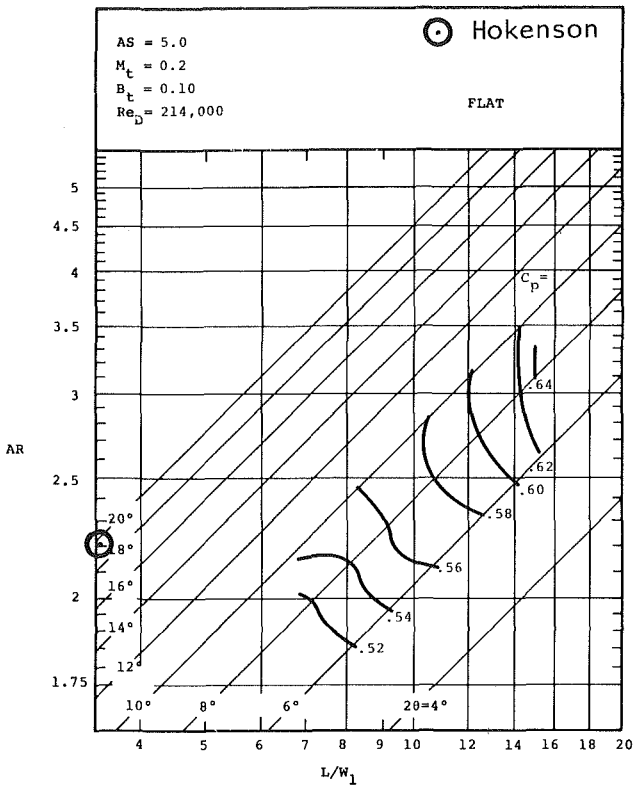

Fig. 1A

Addendum

$B \cong B' = 0.1$

Data Book

$\mathrm{Re}_D = 214{,}000$

$$\frac{\mathrm{Re}_D}{\mathrm{Re}_\theta} = \frac{1.67}{.03536} \cong 47$$

$$\frac{L}{W} = \frac{7.8}{2(1.1)} = 3.5$$

Hokenson

$$\mathrm{Re}_{\theta_i} = \frac{u\theta_i}{\nu} = \frac{u \times .778\delta^*}{\nu}$$

$$= \frac{u \times .778\,(.1)(\tfrac{1}{2}W)}{1.1\nu}$$

$$= 0.03336\,\frac{uW}{\nu}$$

$$\mathrm{Re}_{\theta_i} \cong 4500$$

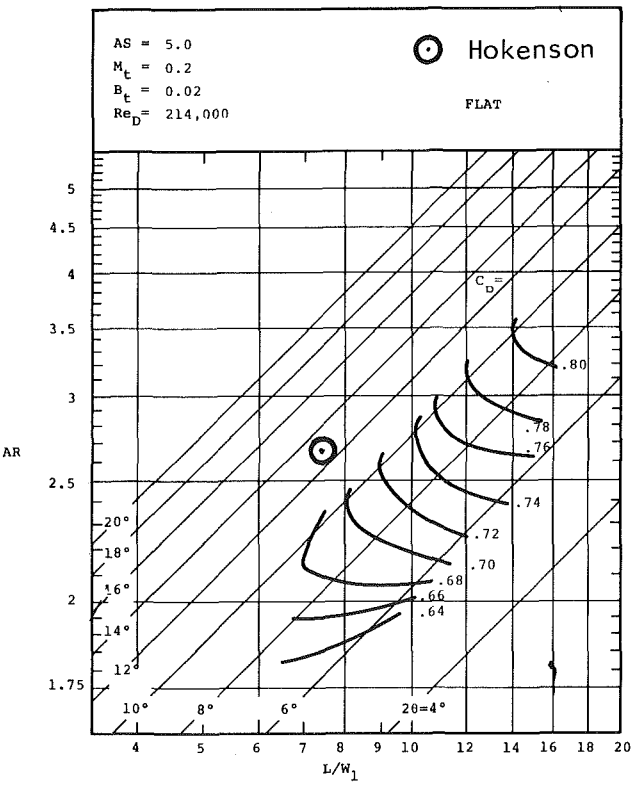

Fig. 2A

[1] By G. Hokenson, published in the December, 1979, issue of the JOURNAL OF FLUIDS ENGINEERING, Vol. 101, No. 4, pp. 478-482.

[2] Mechanical Engineering Department, Clemson University, Clemson, S. C. 29631.

[3] *Diffuser Data Book* by Peter W. Runstadler, Jr., Francis X. Dolan and Robert C. Dean, Jr., TN-186, May 1975, p. 64 and p. 65, Creare Inc.

$$\frac{L}{\theta_i} = 10^2 \qquad L \cong 78\delta^* = 78 \times .1\, h_i$$

$$= 7.8\, h_i$$

From Fig. 2. $\dfrac{W}{h_i} = 2.2.$

$$B \cong B' = 0.02$$

Data Book

$$\frac{h}{W_i} = AS = 5$$

$$D_H = \frac{4Wb}{2W+2b} = 1.67W$$

$$\mathrm{Re}_D = \frac{u\,1.67}{\nu} W$$

$$\frac{\mathrm{Re_D}}{\mathrm{Re}_\theta} \cong \frac{1.67}{7.78 \times 10^{-3}} \cong 214$$

$$\therefore \mathrm{Re}_{DH} = 214{,}000$$

$$\frac{L}{W} = \frac{L}{2h_i(1+B')} \cong 7.6$$

Hokenson

$$\mathrm{Re}_\theta = \frac{u\theta_i}{\nu} = \frac{.778u\delta^*}{\nu}$$

$$= .778\frac{u(0.02)}{\nu} \tfrac{1}{2} W$$

$$= 7.78 \times 10^{-3}\frac{uW}{\nu}$$

Note W in Hokenson's paper is the half widths.

$$\mathrm{Re}_{\theta_i} = 1000$$

$$\frac{L}{\theta_i} = 10^3 \text{ or } L \cong 780\,\delta^*$$

$$B' = .02 = \frac{\delta^*}{h_i}$$

$$\therefore \delta^* = .02\, h_i$$

and $L = 780 \times .02\, h_i = 15.5\, h_i$

From Fig. 3 $\dfrac{W}{h_i} = 3.25$

MICHIHIRO NISHI.[4] The discusser would like to mention the following comments to Mr. Hokenson.

In this paper, although the author emphasizes the optimal skin friction decay for the inverse design of diffusers, his calculated results suggest that the boundary layer growth is sensitive to the pressure gradient. In the decelerating flow, it is proved that the development of boundary layer depends on the freestream velocity gradient (or pressure gradient) rather than skin friction. Therefore, the deceleration rate of freestream with respect to the boundary layer condition is important to treat the optimal diffuser geometry. As a criterion to evaluate the distribution of freestream velocity quantitatively, Senoo and Nishi proposed the deceleration rate parameter θ_1/λ, which is defined as the ratio of momentum thickness to the distance where the freestream velocity is reduced by 10 percent, and recommended $\theta_1/\lambda = 0.02$ where the friction loss is small and the shape factor of boundary layer increases moderately [17]. If one designs a two-dimensional (or axisymmetric) diffuser so that deceleration rate θ_1/λ is kept near 0.02 throughout the diffuser length, the temple bell shape is obtained as the diffuser wall geometry [17]. The author and Huo [18] also show that this is the good diffuser geometry. However, due to the critical design, performance of the temple-bell shape diffuser is very sensitive to the boundary layer blockage at the inlet [19].

In order to achieve high pressure recovery with the shorter diffuser length, I introduce a combined diffuser which consists of the upstream diffuser component with larger divergence angle and the downstream component with smaller divergence angle, considering the facts mentioned above and that simple form diffuser is desirable. The experimental study has been carried out in my laboratory to confirm this design method. Fig. A-3 shows the geometries of test diffusers. The exit-to-inlet area ratio of each diffuser is 3.8. A 9 deg divergence-angle conical diffuser in Fig. A-3(*a*) to use for comparison has the so-called optimum geometry which

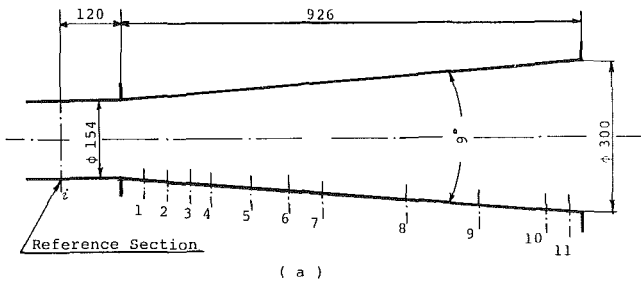

(a)

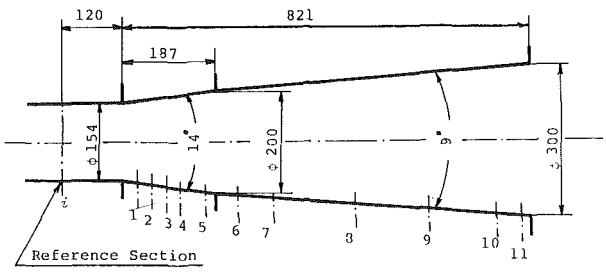

(b)

Fig. A-3

[4]Associate Professor of Mechanical Engineering, Kyushu Institute of Technology, Tobata, Kitakyushu, 804 Japan.

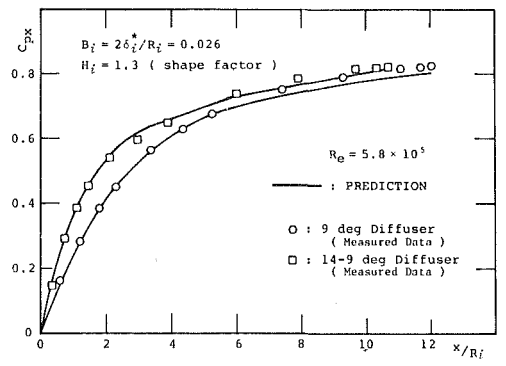

Fig. A-4

produces the maximum pressure recovery in a prescribed diffuser length [4]. Fig. A-3(b) corresponds the the diffuser which is a combination of a 14 deg conical passage and the 9 deg (14-9 deg diffuser). The distributions of local pressure recovery coefficient C_{px} $(=(p_x - p_i)/0.5\rho\bar{u}_i^2)$ in these two diffusers are shown in Fig. A-4 with circular and triangular marks. Solid lines in Fig. A-4 represent the results prediced with Senoo-Nishi method [20]. According to the experimental results, the 14-9 deg diffuser can achieve as high a pressure recovery coefficient as the 9 deg diffuser does, but with 10 percent shorter length.

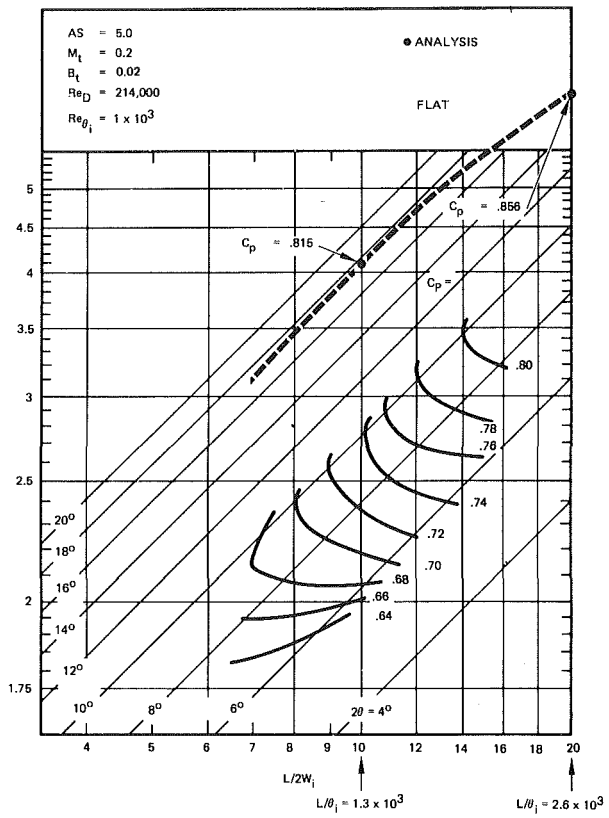

Fig. A-5

Additional References

17 Senoo, Y., and Nishi, M., "Deceleration Rate Parameter and Algebraic Prediction of Turbulent Boundary Layer," ASME JOURNAL OF FLUIDS ENGINEERING, Vol. 99, No. 2, 1977, pp. 390-395.

18 Huo, S., "Optimization Based on Boundary Layer Concept for Compressible Flows," ASME *Journal of Engineering for Power*, Vol. 97, 1975, pp. 195-206.

19 Carlson, J. J., Johnston, J. P., and Sagi, G. J., "Effects of Wall Shape on Flow Regimes and Performance in Straight, Two-Dimensional Diffusers," ASME *Journal of Basic Engineering*, Vol. 89, No. 1, 1967, pp. 151-160.

20 Senoo, Y., and Nishi, M., "Prediction of Flow Separation in a Diffuser by a Boundary Layer Calculation," ASME JOURNAL OF FLUIDS ENGINEERING, Vol. 99, No. 2, 1977, pp. 379-389.

Author's Closure

I sincerely appreciate the interest which Professors Nishi and Yang have shown in my work and welcome this opportunity to respond.

The two sets of experimental data provided by Prof. Yang appear to be sufficiently two-dimensional and incompressible for comparison with analysis. The blockages are 0.02 and 0.10, respectively, with an $Re_D = 214{,}000$ and a range of aspect ratios.

For comparison with analysis B', Re_{θ_i} and L/θ_i must be specified. As Professor Yang suggests, $B' \simeq B = 0.02$ and 0.10 is a good approximation. The relevant Reynolds numbers for the two sets of data may be computed from:

$$Re_{\theta_i} = Re_D \left(\frac{2W}{D}\right) \frac{B}{2H_i}$$

using the terminology in my paper. For a diffuser cross-sectional aspect ratio of 5.0, which is common to both sets of data, the width to hydraulic diameter ratio ($2W/D$) is 3/5. Therefore, $Re_{\theta_i} = 1 \times 10^3$ and 5×10^3 for data sets one and two, respectively. The sensitivity of the analytical results to Re_{θ_i} is not large in this range.

The final parameter which must be established is L/θ_i and may be calculated from:

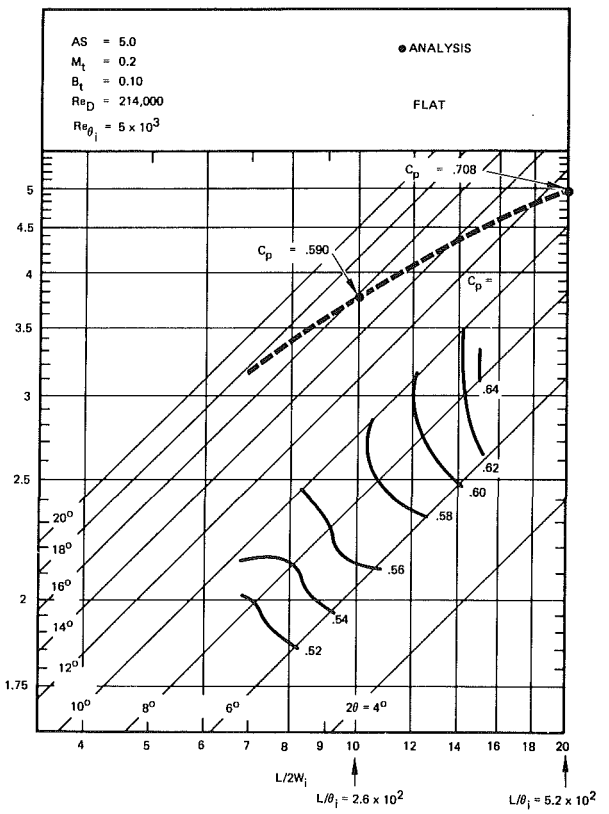

Fig. A-6

$$\frac{L}{\theta_i} = \left(\frac{L}{2W_i}\right)\frac{2H_i}{B}$$

where $L/2W_i$ is the conventional geometric aspect ratio. Therefore, it is possible to superimpose as many analytical points on the experimental data as desired by selecting $(L/2W_i)$ values of interest. For simplicity, $L/2W_i$ is chosen here to be 10 and 20 for both sets of data. In the first data set this leads to $L/\theta_i = 1.3 \times 10^3$ and 2.6×10^3, respectively, whereas $L/\theta_i = 2.6 \times 10^2$ and 5.2×10^2 for the second set of data.

Entering Fig. 1 of my paper with $\mathrm{Re}_{\theta_i} = 1 \times 10^3$ and $L/\theta_i = 1.3 \times 10^3$, 2.6×10^3 leads to C_p $(\equiv 1 - \bar{U}_f^2) = 0.815$ and 0.856, respectively. Following the same procedure with $\mathrm{Re}_{\theta_i} = 5 \times 10^3$ and $L/\theta_i = 2.6 \times 10^2$, 5.2×10^2 results in $C_p = 0.590$ and 0.708.

In order to determine the appropriate area ratios, interpolation of the analytical results is required because of their sensitivity to L/θ_i. For the first set of data at $\mathrm{Re}_{\theta_i} = 10^3$ and $B = 0.02$, the results from Fig. 4 must be *rescaled* to double the blockage. Interpolating between Fig. 3 and a rescaled Fig. 4 at $L/\theta_i = 1.3 \times 10^3$ and 2.6×10^3 leads to area ratios of 4.1 and 6.4, respectively. For the second set of data, the results of Fig. 2 and a rescaled Fig. 3 (converted from $B = 0.02$ to $B = 0.10$) are entered with $\mathrm{Re}_{\theta_i} = 5 \times 10^3$ and interpolated at $L/\theta_i = 2.6 \times 10^2$ and 5.2×10^2, providing area ratios of 3.7 and 4.9.

When these results are plotted on the data set, the same as used by Professor Yang and shown as Figs. A-5 and a-6, it is clear that the analysis bounds the experimental diffuser data and provides realistic performance goals for an *optimally* configured diffuser. The analysis, which provides a different optimally-shaped diffuser at each point along the theoretical curves, does not predict an overall optimum pressure recovery on each figure; as indicated on *some* experimental data plots for a fixed shape diffuser. Instead, since the separation point is analytically tied to the diffuser exit plane, the C_p increases monotonically with increasing L/θ_i for a given $B\,\mathrm{Re}_{\theta_i}$.

Note that the reduction in the analytically-indicated optimal diffuser angle (going from an average of 17 deg in the first data set to 13 deg in the second set, at an $L/2W_i = 15.0$) with *increasing* Re_{θ_i} is due to the exposed increased blockage effect. Also, when converting the analytical results to these type of experimental data correlations, the blockage affects both Re_{θ_i} and L/θ_i, with a different functional dependence. The effect of blockage on these type experimental plots is, therefore, surprisingly complex when compared to its effect on the analysis.

The extent to which the *performance* of these analytically-derived diffusers will be degraded by inlet plane disturbances must be quantified experimentally. The influence of such perturbations on separation is clearly to encourage it, but the time-averaged pressure recovery in a diffuser with transitory stall is an exceedingly complex phenomenon.

Journal of Fluids Engineering

Book Reviews

Boundary-Layer Theory by H. Schlichting, Seventh Edition, (translated by J. Kestin), New York: McGraw-Hill Book Company, xxii + 817 pp., 1979. Price $28.00.

REVIEWED BY ROBERT L. STREET

Boundary-Layer Theory has held a preeminent place in the fluid mechanics literature for almost thirty years. The seventh edition, the first to be published first and only in English, comes eleven years after the sixth edition. I am sure many of us felt that it was "time."

According to the author the principal thrust of the book is "the intent to emphasize and to present theoretical considerations in a form accessible to engineers." In the seventh edition he worked to retain the original character of the book and "provide the reader with a *bird's-eye view* of this important branch of the physics of fluids." These goals are the source of both strength and weakness in the book. It already contained much of the classic essence of the field. Additions and changes had to be balanced against increased heft (now over 800 pages) and loss of important fundamentals. The result is a compromise. There has been a general updating, sharpening of parts of the text, removal of some out-of-date material; many new references were added, and a modest number of new items have been inserted. Some of the additions noted by the author are worth commentary.

The numerical integration of equations is mentioned descriptively (Chap. IV) and discussed for the case of boundary-layer equations for laminar and turbulent flows (Chap. IX, Sec. i). This latter section is new and gives a good description of the numerical technique, leads to the literature, and validation of some specific results. However, I wonder if eight pages among 800 is proper weight for some of the most important methodologies in current practice, an area which has spawned innumerable papers and at least four books.

The sections on the second-order boundary-layer (Chap. VII, Sec. f and Chap. IX, Sec. j) are welcome. The latter is new; the former revised. Together they gave a "first-order" introduction to asymptotic and inner/outer expansions. As always in this book, the feel of these text pieces is comfortable—clear theory, useful examples, numerical results, comparison with experiment, and a sense of the importance of the results.

The treatment of stability in laminar boundary layers has been significantly changed (Chap. XVI) in the light of the direct solutions available for the 4th order Orr-Sommerfeld equation. The previous approach using the inviscid solution (for the 2nd order equation) and a viscous correction has been eliminated. The concluding remark (Sec. f) to the chapter is a fine touch, summarizing the transition process in a boundary layer in words and picture.

In summary, if you do not own an earlier copy of *Boundary-Layer Theory* and your work involves boundary layers, then you should have a copy of the seventh edition. It remains the comprehensive treatise and a major source book for neophytes and veterans. The blend of mathematics, fundamental physics, and experimental results leads the reader to understanding of key features, ideas and approaches. Then, one can branch to the multitudinous in-depth monographs on specific areas.

The tougher issue is, if you own an earlier edition, should you buy the seventh? If you own the sixth, probably not; otherwise, yes.

An Introduction to Viscous Flow by W. E. Hughes, Hemisphere Publishing Corp., New York, 1979, 219 pp., Price: $22.50.

REVIEWED BY WARREN M. HAGIST

This little book, which concentrates on laminar flows in its six chapters, is intended for use at the undergraduate level. In his preface, Dr. Hughes states that it is suitable as a text for a second course (which it is), but the writing is lucid enough so that it could easily be used in a first course if the instructor were willing to supplement chapter 1 with some of the details of the derivations of the integral forms of the basic equations and provide additional material on turbulent flows.

The second chapter begins by discussing and working through the Poiseuille and Couette flows from a free-body diagram of a fluid element. This is followed by derivations of the continuity and momentum equations in differential form and a discussion of the deformation and strain rates, culminating with the Navier-Stokes equations. The chapter concludes with a discussion of non-Newtonian fluids and derivations of the velocity distribution in a circular pipe for both a power-law fluid and a Bingham plastic.

Chapter 3 entitled "Hydrodynamic Lubrication" takes the student through the usual two-dimensional discussions and derivations for the stepped slider, inclined slider, and journal bearings. A rather short fourth chapter introduces the student to the two-dimensional form of the differential energy equation and works out the temperature distributions in Couette and Poiseuille flow. It concludes with a derivation of the general energy equation and the relationship between it and Bernoulli's equation.

The last two chapters are concerned with boundary layers; momentum effects in chapter 5, and thermal effects in chapter 6. After a general discussion of the boundary layer concept and the flow past objects of various shapes, Dr. Hughes proceeds through the two-dimensional order of magnitude development of the boundary layer equations, the Blasius solution, and a third degree polynomial approximate solution. Following this is a section on the turbulent boundary

layer using the 1/7th power velocity profile, and the boundary layer with a pressure gradient. The chapter concludes with short discussions of stagnation point flow and flow around a circular cylinder. The entire treatment is quite good except for the short section entitled "Laminar Sublayer" which might best have been omitted, and a somewhat carelessly drawn Fig. 5.1. Chapter 6 develops the thermal boundary layer equations in both differential and integral form and examines solutions with Prandtl number equal to 1. After a quite thorough discussion of the turbulent boundary layer and Reynolds analogy, the author works out the solution for free convection on a vertical plate. The chapter concludes with a discussion of frictional heating in the boundary layer and aerodynamic heating.

Each chapter includes a small number of problems for the student (and the instructor) to attempt. Since several of the problems say "Discuss. . ." or "What happens if. . ." most adopters might hope that a solutions manual is available. Even though restricted almost entirely to laminar flows this book is a useful addition to the instructional literature in fluid mechanics.

Numerical Methods in Fluid Dynamics, Edited by H. J. Wirz and J. J. Smolderen, McGraw-Hill Book Co., New York, 1978, 399 pp., Price: $35.00.

REVIEWED BY FRANK M. WHITE

This book is very interesting but it is not, as the title implies, a textbook on numerical fluid dynamics. Rather, the added words "Some Aspects of" would put the book in more perspective. It consists of six survey lectures on specialized topics given in 1976 in a short course at the von Kármán Institute. Of these six "chapters," three – more than half the book – are devoted to transonic flow calculations. Then there are three chapters on physiological flows, panel methods, and numerical experiments in the Soviet Union, the latter two of which also cover some transonic flow calculations.

The transonic flow chapters are "Transonic Flow Calculations," by A. Jameson, "Some Recent Progress in Transonic Flow Computations," by W. Ballhaus, and "Progress in Transonic Flow Computations: Analysis and Design Methods for Three-Dimensional Flows," by W. Schmidt. All are interesting but there is considerable overlap and the primary emphasis is on steady, inviscid wing-body flows. Ballhaus briefly treats viscous and unsteady flows.

Chapter 2 on "Application of Numerical Methods to Physiological Flows," by T. J. Mueller, is the best effort at introducing, developing, and "teaching" the subject to the reader. The equations, boundary conditions, and methods are very well discussed along with appropriate biophysical considerations, with detailed applications to heart valves and artery constrictions.

Chapter 4 on "Panel Methods in Aerodynamics," by W. Kraus is a useful review for readers unfamiliar with the technique. A panel method simulates a body shape by distributed source or vortex "panels" and then solves the potential flow equations by an integral technique. It is a special case of the Boundary Integral Method now becoming quite popular in solid mechanics applications. Most of the results presented were developed at the Messerschmitt-Bölkow-Blohm firm in Germany. In these days of Middle East unrest, it is rather disconcerting to see on page 277 a detailed panel-simulated bomber dropping detailed panel-simulated bombs. The figure is euphemistically captioned "Trajectory of a ballistic store." Let's hope the "stores" are merely filled with bread and wine and vitamins for the waiting refugees below.

The final chapter is a 50-page review of Soviet gas-dynamics numerical experiments by O. M. Belotserkovskii. It gives examples of statistical, "large-particle," and continuum simulations conducted recently in the Soviet Union.

The printing and layout of the book are excellent. The publishers have succeeded in printing some three hundred figures – hand-drawn, computer-plotted, artist-inked – with nearly equal quality. Although the topics are specialized, the book is quite useful to readers involved with these topics.

Finite Element Analysis in Fluid Dynamics by T. J. Chung, McGraw-Hill Publishing Company, Inc., 416 pp., New York, Price: $38.00.

REVIEWED BY G. A. KERAMIDAS

Over the past years, the finite element method has been developed to a state-of-art with a large number of applications. A variety of books have been published on the theory and application of the finite element method. These texts have focused primarily on applications for structures, with little or no mention of fluids. A text completely dedicated to fluid problems and their treatment by the finite element method has been long overdue. The *Finite Element Analysis in Fluid Dynamics,* written by Dr. T. J. Chung, successfully gives a uniform and complete presentation of this subject area.

The book is geared toward the graduate level student and can be used as an excellent reference for people working on advanced applications of the finite element method in fluid dynamics.

The mathematical preliminaries presented in the first chapter are useful to establish the basic tools used throughout this text. The concept of the variational methods and the method of weighted residuals are introduced and the derivation of the finite element equations by these methods is given. A first discussion on the accuracy of the method is also given, with a more detailed error analysis found in the chapters to follow.

The second chapter contains complete and detailed presentations of one, two and three dimensional finite element models for linear and higher order interpolations functions. These derivations are of a general nature and the models can be used for solving many types of problems. Thus, specific applications are not given in this chapter.

Mathematical methods for assembling and solving the finite element equations are discussed in the third chapter. Techniques for handling different types of boundary conditions are also presented. Solutions of three types of problems are included and useful examples provide an overall view of the finite element analysis. Of special interest is the derivation of error estimates in the solution of the different types of differential equations.

In the first three chapters, the author succeeds in giving a complete picture of not only the method and how it works, but also its applications for solving various types of general problems. In the subsequent chapters, specific topics in fluid dynamics are presented. A useful review of the theory of fluid